A major purpose of the Technical Information Center is to provide the broadest dissemination possible of information contained in DOE's Research and Development Reports to business, industry, the academic community, and federal, state and local governments.

Although a small portion of this report is not reproducible, it is being made available to expedite the availability of information on the research discussed herein.

ORNL--6053

DE84 016747

GAS-COOLED REACTOR PROGRAMS

HIGH-TEMPERATURE GAS-COOLED REACTOR TECHNOLOGY DEVELOPMENT PROGRAM ANNUAL PROGRESS REPORT FOR PERIOD ENDING DECEMBER 31, 1983

Paul R. Kasten, Program Director

P. L. Rittenhouse, Base Technology Program Manager

D. E. Bartine, Physics and Shielding Program Manager

J. P. Sanders, Component Flow Testing Program Manager

Date Published — June 1984

Prepared by the
OAK RIDGE NATIONAL LABORATORY
Oak Ridge, Tennessee 37831
Operated by
MARTIN MARIETTA ENERGY SYSTEMS, INC.
for the
U.S. DEPARTMENT OF ENERGY
under Contract No. DE-AC05-84OR21400

CREDITS:
Composition and makeup: Debbie LeComte
Editing: Irene Brogden

CONTENTS

FOREWORD ix

SUMMARY xi

1. LEAD PLANT ECONOMIC EVALUATIONS 1

1.1 INTRODUCTION 1

1.2 REVIEW OF *1983 Economic Ground Rules for the HTGR Program*, GCRA 83-008, REV. NO. 0, APRIL 29, 1983 1

1.3 REVIEW OF *Port Arthur Refinery Cogeneration Alternatives Study: Institutional/Economics Assessment*, UE&C/GCRA 83-006, JANUARY 1983, AND *Port Arthur Refinery Cogeneration Alternatives Study: Summary Report*, GCRA 83-007, JANUARY 1983 2

1.4 REVIEW OF *An Economic Evaluation of the Steam-Cycle High Temperature Gas-Cooled Reactor*, GCRA-83-009, JULY 1983 2

1.5 REVIEW OF *HTGR SC/C Lead Plant Design Basis Transient Analysis Report*, HCA-20102/REV. 0, NOVEMBER 1, 1983 3

2. HTR SHIELDING STUDIES 5

2.1 INTRODUCTION 5

2.2 EXPERIMENT 6

2.3 ANALYSIS 12

2.4 REFERENCES 21

3. HTR COMPONENT FLOW TEST LOOP STUDIES 23

3.1 INTRODUCTION 23

3.1.1 Current Application of the Loop 24

3.1.2 Core Auxiliary Heat Exchanger Test 27

3.2 CORE SUPPORT PERFORMANCE TEST 28

3.2.1 Preparation for TEST P-1 29

3.2.2 TEST P-1 Shakedown Operation 31

3.2.3 Preparation for TEST ZERO 33

3.2.4 TEST ZERO Operation 37

3.3 CSPT CHEMISTRY, TEST METHODS, AND SPECIFICATIONS 51

3.3.1 Objectives of TEST P-1 51

3.3.2 Modification of the Impurity Control System 52

3.3.3 Tests of the Impurity Measurement System 52

3.3.4 Moisture Generation and Measurement 52

3.3.5 Leak Rate Measurement and Significance 52

3.3.6 Chemical Behavior of Loop 53
3.3.7 Specifications for Subsequent Tests 54
3.4 CSPT ELECTRICAL DESIGN AND INSTALLATION 54
3.5 CSPT MECHANICAL DESIGN 55
3.5.1 TEST ZERO Graphite Test Structure 55
3.5.2 TEST ZERO Load Post 56
3.5.3 TEST ZERO Graphite Handling Tool 56
3.5.4 TEST ZERO Load Post Handling Tool 56
3.5.5 TEST ONE Graphite Test Structure 58
3.5.6 TEST ONE Structural Loading Device 60
3.5.7 TEST ONE Graphite Handling Tool 62
3.5.8 TEST ONE Test Section Liner Modification 62
3.5.9 TEST ONE Pressure Vessel Modification 62
3.5.10 TEST ONE Stress Calculations 62
3.5.11 Helium Heater Design 63
3.5.12 Helium Circulator Heat Shield 64
3.5.13 Mobile Work Platform 64
3.6 CSPT INSTRUMENTATION AND CONTROLS 64
3.6.1 Loop Instrumentation Modifications 65
3.6.2 Vortex Shedding Flowmeters 66
3.6.3 Electromagnetic Noise 68
3.6.4 Data Aquisition System 69
3.6.5 Impurity Measurement System 71
3.6.6 Impurity Control System 72
3.7 CORE AUXILIARY HEAT EXCHANGER TEST IN THE CFTL 74
3.7.1 CAHE Test Mechanical Design 74
3.7.2 CAHE Test Instrumentation and Controls 83
3.8 REFERENCES 90
4. HTR PHYSICS 93
4.1 INTRODUCTION 93
4.2 CORE PHYSICS ANALYSIS 94
4.2.1 Power Density Study 94
4.2.2 Design Optimization by Depletion Perturbation Theory 97
4.2.3 HTR Reflector Albedo Analysis 99

4.3 THERMAL HYDRAULICS 105
4.4 REFERENCES 106
5. PCRV CONCRETE DEVELOPMENT 107
5.1 ANALYSIS METHODS DEVELOPMENT 107
5.2 CONCRETE PROPERTIES 107
5.2.1 Concrete Behavior Under Uniaxial and Multiaxial States of Stress 108
5.2.2 Development of High-Strength Concrete Mix Designs in Support of HTR-SC-C PCRV Design 108
5.3 MODEL TESTING TECHNIQUE DEVELOPMENT 109
5.4 REFERENCES 113
6. STRUCTURAL CERAMICS TESTING 115
6.1 THERMAL BARRIER HARD CERAMIC MATERIALS 115
6.2 CREEP OF CERAMICS 117
6.3 CHARACTERIZATION OF CORE SUPPORT CERAMICS 117
6.3.1 Fused Silica 118
6.3.2 AD-85 Alumina 119
6.3.3 AD-995 Alumina 120
6.4 REFERENCES 121
7. HTR FUEL MATERIALS QUALIFICATION 123
7.1 INTRODUCTION 123
7.1.1 Irradiation Testing 124
7.1.2 Postirradiation Examination 124
7.1.3 U.S.-FRG Cooperative Program 126
7.1.4 Equipment Development and Maintenance 126
7.2 IRRADIATION CAPSULE ASSEMBLY AND OPERATION 127
7.2.1 Hydrolysis Experiments HRB-17 and HRB-18 127
7.2.2 HRB Thermal Design Code, HRBTAN 130
7.3 POSTIRRADIATION EXAMINATION OF IRRADIATION EXPERIMENTS . . . 131
7.3.1 Capsule HT-35 131
7.3.2 Capsules HRB-11 and -12 142
7.3.3 Capsule HRB-15b 149
7.3.4 Capsule HRB-15a 154
7.3.5 Capsule HRB-16 162
7.3.6 Capsule R2-K13 162

7.4 U.S.-FRG COOPERATIVE PROGRAM 167
7.4.1 PWS FD-1 (Extended) 167
7.4.2 PWS FD-20 168
7.5 EQUIPMENT DEVELOPMENT AND MAINTENANCE 170
7.5.1 Irradiated Microsphere Gamma Analyzer 170
7.5.2 Postirradiation Gas Analyzer 171
7.5.3 X-Radiography Facility 172
7.6 REFERENCES 172
8. FISSION PRODUCT STUDIES 175
8.1 INTRODUCTION 175
8.2 ACTINIDE DIFFUSION IN GRAPHITE 175
8.3 PLUTONIUM VAPOR PRESSURE MEASUREMENT 176
8.4 FISSION PRODUCT RELEASE FROM FAILED FUEL AND DETERMINATION OF CHEMICAL FORMS 180
8.5 REFERENCES 181
9. STRUCTURAL METALS STUDIES 183
9.1 INTRODUCTION 183
9.2 MECHANICAL PROPERTIES OF ALLOYS AND WELDMENTS 183
9.2.1 Creep Testing 183
9.2.2 Effects of Thermal Aging 186
9.2.3 Fatigue Testing 186
9.3 CORROSION AND COMPATIBILITY 193
9.3.1 Decarburization of 2 1/4 Cr-1 Mo Steel 193
9.3.2 Compatibility of Alloys with B_4C Compacts 199
9.4 JOINING TECHNOLOGY 200
9.4.1 Superheater Tube-to-Tubesheet Joints 203
9.4.2 Experimental Welding Equipment 203
9.4.3 Welding Development 206
9.5 FRACTURE TOUGHNESS STUDIES 207
9.5.1 Steels for the PCRV 207
9.5.2 High-Temperature Fracture Toughness Studies 210
9.6 REFERENCES 211
10. GRAPHITE MATERIALS QUALIFICATION 213
10.1 INTRODUCTION 213
10.2 GRAPHITE IRRADIATIONS 214

10.2.1 Irradiation Experiments 214
10.2.2 Results of Irradiation Testing: OC-5 Creep Capsule 216
10.2.3 Results of Irradiation Testing: HFIR Survey Capsules 217
10.2.4 Results of Irradiation Testing: Fracture Mechanics Series 222
10.3 GRAPHITE EVALUATIONS 227
10.3.1 Basic Fracture Mechanics Studies 227
10.3.2 Improved Moderator Graphite, H451I 229
10.3.3 Statistical Analysis of H451 Tensile Strengths . . . 233
10.3.4 Higher Moments of the Weibull Distribution 240
10.4 REFERENCES 244
11. INTERNATIONAL TECHNOLOGY TRANSFER 245
11.1 INTRODUCTION 245
11.2 FUELS 245
11.3 GRAPHITE 245
11.3.1 High-Pressure (HOVA) Loop Tests 245
11.3.2 Fracture Mechanics of Irradiated Graphite 246
11.4 MATERIALS 248
11.5 REFERENCE 249
12. ADVANCED REACTOR SYSTEMS ENGINEERING 251
12.1 INTRODUCTION 251
12.2 CALCULATIONS OF FUEL TEMPERATURES DURING DEPRESSURIZED CORE HEATUP ACCIDENTS IN MODULAR HTRs 251
12.3 ACCIDENT SOURCE TERM ISSUES 253
13. MARKET DEFINITION AND APPLICATION ASSESSMENT 255
13.1 INTRODUCTION 255
13.2 NATIONAL NEEDS STUDY 255
13.2.1 Electrical Energy and the HTR 255
13.2.2 Nonelectrical Energy and the HTR 257
13.3 PROJECTED TOTALS 258
13.4 COMPARISON WITH CAL GROWTH PROJECTION FOR NONELECTRICAL ENERGY 258
13.5 REFERENCES 259

14. ADVANCED SYSTEMS ALLOYS 261
14.1 INTRODUCTION 261
14.2 MECHANICAL PROPERTIES OF ADVANCED NICKEL-BASE ALLOYS 261
14.3 NICKEL-ALUMINIDE ALLOYS 262
15. HIGH-TEMPERATURE DESIGN CRITERIA 263
15.1 INTRODUCTION 263
15.2 REVIEW OF WORK AREA 263
15.3 REFERENCES 264
16. ADVANCED SYSTEMS INTERNATIONAL COOPERATION 265
16.1 INTRODUCTION 265
16.2 BRIEF DESCRIPTION OF THE AVR 267
16.3 AVR PERFORMANCE AND SAFETY EXPERIMENTS 271
16.3.1 Experiments Involving Reactor Shutdown by Stopping Forced Circulation 271
16.3.2 Experiments Involving Sharp Reductions in Primary Coolant Flow with Continued Power Operation 272
16.3.3 Experiments Involving Insertion and Withdrawal of Control Rods 273
16.3.4 Possible Depressurized Loss of Forced-Circulation Experiments 273
16.4 ANALYSES OF AVR RESPONSE TO SELECTED TRANSIENTS 274
16.4.1 Analyses of Flow Reduction and Control Rod Insertion and Withdrawal 275
16.4.2 Analysis of AVR Depressurized Core Heatup Accident 275
16.5 INITIAL IDEAS ON POTENTIAL FUTURE EXPERIMENTS TO FURTHER INVESTIGATE AND DEMONSTRATE INHERENT FEATURES OF THE AVR . . 279
16.6 REACTOR PHYSICS ANALYSIS 280
16.7 REFERENCES 280
ORGANIZATION CHART 281

FOREWORD

The Oak Ridge National Laboratory (ORNL) High-Temperature Reactor (HTR) Technology Program is a part of the national HTR program sponsored by the U.S. Department of Energy (DOE). The major participants in the national program are GA Technologies (GA), which performs the major share of the design and technology development and still intends to be the High-Temperature Gas-Cooled Reactor (HTGR) vendor; Gas-Cooled Reactor Associates (GCRA), an organization sponsored by more than 30 utilities, which gives utility focus to the program and serves as the program coordinator; ORNL, which provides strong support to the technology development effort and serves as a technical reviewer and evaluator for DOE; General Electric Company (GE), which provides design and engineering support in selected HTR areas and emphasizes very high-temperature reactor (VHTR) applications; Combustion Engineering, which provides component expertise, with emphasis on steam generator design and development; and United Engineers and Constructors and Bechtel Group, Inc., which serve as architect-engineers to the program. In addition, other organizations such as Idaho National Engineering Laboratory (INEL) are involved in special studies, analyses, and evaluations.

During the last year, the national program was organized in accordance with a work breakdown structure (WBS) given in a Summary Level Program Plan (SLPP) developed by the national program participants and coordinated by GCRA. The ORNL work is therefore reported in accordance with the WBS number given in the national SLPP; the WBS number is identified at the beginning of each work area.

The ORNL continues to make significant contributions to the national program. In the HTR fuels area, we are providing detailed statistical information on the fission product retention performance of irradiated fuel. Our studies are also providing basic data on the mechanical, physical, and chemical behavior of HTR materials, including metals, ceramics, graphite, and concrete. The ORNL has an important role in the development of improved HTR graphites and in the specification of criteria that need to be met by commercial products. We are also developing improved reactor physics design methods. Our work in component development and testing centers in the Component Flow Test Loop (CFTL), which is being used to evaluate the performance of the HTR core support structure. Other work includes experimental evaluation of the shielding effectiveness of the lower portions of an HTR core. This evaluation is being performed at the ORNL Tower Shielding Facility. Researchers at ORNL are developing welding techniques for attaching steam generator tubing to the tubesheets and are testing ceramic pads on which the core posts rest. They are also performing extensive testing of aggregate materials obtained from potential

HTR site areas for possible use in prestressed concrete reactor vessels. During the past year we continued to serve as a peer reviewer of small modular reactor designs being developed by GA and GE with balance-of-plant layouts being developed by Bechtel Group, Inc. We have also evaluated the national need for developing HTRs with emphasis on the longer term applications of the HTRs to fossil conversion processes.

We anticipate that ORNL will continue to be a key contributor to the successful development of HTRs for commercial applications.

Paul R. Kasten

SUMMARY

1. LEAD PLANT ECONOMIC EVALUATIONS (WBS 3150.03)

Work on lead plant economics involves review of the economic ground rules used in lead plant economic studies and review of selected technical studies. This work provides a peer review of the economic and technical performance of the designs developed by GA Technologies (GA) and Gas-Cooled Reactor Associates (GCRA). We judge the 1983 economic ground rules to be comprehensive and to encompass all the pertinent information needed to perform engineering economic analyses on a consistent and sound basis. We judge the overall lead plant economic and technical studies that we have reviewed to be of excellent quality and comprehensive in scope. Overall, the estimated economic performance is sufficiently attractive to warrant an aggressive lead plant program.

2. HTR SHIELDING STUDIES (WBS 3610.03.1)

Phase I of the High-Temperature Reactor (HTR) Bottom Reflector and Support Block Neutron Streaming Experiment was performed and analyzed. The experiment, which was designed to reduce uncertainties in the predicted neutron exposure rates in the lower regions of the HTR, closely modeled a seven-column cell between the core and the lower plenum. The Oak Ridge National Laboratory (ORNL) Tower Shielding Facility reactor provided the incident neutron source, and integral and spectral neutron flux measurements provided data for comparing with the analytic predictions.

In general, good agreement was achieved between the measurements and the corresponding analyses. This provides partial confirmation of the earlier design analysis, which indicated that the exposure design limit in the lower plenum would be exceeded. Phase II of the experiment should fully resolve this issue.

3. HTR COMPONENT FLOW TEST LOOP STUDIES (WBS 3610.03.2)

The installation of a test vessel with an internal helium heater was completed in the Component Flow Test Loop (CFTL) at the beginning of 1983. The installation of systems to measure and control the concentration of impurities in the circulating helium was completed in January. These facilities are required to conduct a Core Support Performance Test (CSPT).

The purpose of this test is to expose a graphite column with the diameter and geometry of the core support post of the prismatic core HTR to the flow of helium at typical operating temperatures, pressures, and mass velocities. The post will be structurally loaded to simulate the weight of the core and the downward force of the pressure drop across the core.

The concentration of the impurities in the helium will be adjusted so that the amount and the depth of penetration of graphite corrosion anticipated in the reactor during its operating life will be duplicated in a six-month test period.

Shakedown operation was initiated in February to qualify the CFTL and its modifications for this test. Qualification required the completion of two phases of the test plan. Phase I, which required the completion of TEST P-1, was required to demonstrate unattended operation of the CFTL and an acceptably low leak rate from the system. This test was also structured to determine the chemical behavior of principal impurities added or formed during the test of the graphite structure. This TEST P-1 was operated without graphite in the loop to isolate the effect of surface-induced or gas phase reactions on the concentration of these impurities. The test also confirmed the ability of the impurity measurement and control systems to function within their specified limits.

TEST P-1 was completed in May, and the test progressed to Phase II, which required an extended operation of the loop with a graphite structure placed in the test vessel. This structure consisted of four cylindrical segments of off-the-shelf Stackpole 2020 graphite. No structural load was placed on these cylinders, and thermocouples were embedded in the structure so that the graphite temperatures could be correlated with measured gas temperatures. No internal thermocouples can be permitted in the final test structure.

TEST ZERO was initiated in August but was interrupted almost immediately by a short circuit in one of the circulator motors. Repair activities on the motor led to the discovery of excessive erosion in the end rings that house the impellers of each of the three circulators. This erosion apparently resulted from the failure to develop an adherent, protective oxide coating on the type 410 stainless steel end rings following the final machining operation. The high velocity gradients in the impeller enclosure eroded this coating and exposed the metal to subsequent corrosion by oxygen-containing impurities in the helium.

Successive corrosion and erosion of the type 410 stainless steel resulted in the formation of deep grooves in the metal and the distribution of a very fine, black, magnetic powder in the crevices of the circulator housing. This action was terminated by placing rings of the same material in the cavity between the impeller and the end ring. After machining, these rings were heat treated to develop an adherent oxide coating. During this same interval, the stator of the circulator motor that had shorted was removed and rewound on site.

After TEST ZERO was restarted in early October, operation was halted intermittently by problems with the variable-frequency power supplies (VFPSs) that drive the helium circulators. At the end of November, continuous operation for more than 500 h was halted by plugging the full-flow helium filter. During this same operation, temperature measurements indicated a substantial bypass flow around the helium heaters. Inspection of the heaters indicated that the alumina shrouds were cracked and that higher than design temperatures existed in the center alumina mandrels of the heater.

The filter contained a very fine black powder with significant quantities of iron and carbon. It is postulated that the iron came from the erosion of the end ring of the impeller and that the carbon was produced by gas phase reactions with carbon monoxide. The only other source of carbon is the graphite test structure. An in situ examination of the graphite test structure through observation ports did not show significant surface corrosion of the graphite. This off-the-shelf graphite contains trace amounts of iron; however, specimens of a specially refined "nuclear-grade" Stackpole 2020 graphite were inserted in the lowest (upstream) cylinder. This refined graphite contains essentially no iron, and the specimens can be used to detect the deposition of iron particles on the test structure. At the end of the year, TEST ZERO had been interrupted for the installation of a new helium filter and replacement of helium heaters.

Specifications for the test of a full-length 19-tube bundle for the core auxiliary heat exchanger (CAHE) were received from GA. A conceptual design for modifications of the CFTL necessary to conduct this test was completed by staff members of Union Carbide Corporation, Nuclear Division (UCC-ND) Engineering Division and the ORNL Instrumentation and Controls Division. A cost estimate was prepared and included in a conceptual design report, which was submitted to Oak Ridge Operations Office of the Department of Energy (ORO-DOE) for review.

4. HTR PHYSICS (WBS 3610.04)

The analysis of HTRs requires numerical methods capable of modeling the neutronic and thermal-hydraulic characteristics of a large thermal reactor core. The analysis methods must also be capable of simulating various stages in the burnup history of a large core. If options in core burnup or control strategies are to be explored in detail, the analysis must be repeated to determine the effects of changes.

During the past year, the major efforts in HTR physics have been in developing and demonstrating methods to simplify the complex analysis requirements for HTR cores. The ability to perform steady-state thermal-hydraulics analysis for prismatic HTRs has been added to the VENTURE code system. These methods have been applied to study the effects of reducing the power density in a large core. The impact on temperature distributions and core pressure drops was calculated. This information will be used in an assessment of core performance and operating costs as a function of power density. A report covering the prismatic thermal-hydraulics work is forthcoming.

The utility of depletion perturbation theory (DPT) methods was demonstrated in a problem for designing a core loading pattern to obtain a desired power-temperature distribution throughout core life. Least-squares fitting was used with DPT sensitivity coefficients to effect a search for an optimum loading pattern without requiring multiple burnup studies. Finally, the use of reflector albedos was studied to simplify the reflector geometry required for large core neutronic simulations.

Preliminary results indicate that the number of mesh points in large three-dimensional problems may be cut almost in half with little or no error in core flux calculations.

5. PCRV CONCRETE DEVELOPMENT (WBS 3611.01)

The concrete development task consists of generic studies designed to provide technical support for ongoing activities related to the prestressed concrete reactor vessel (PCRV), to contribute to the technological data base, and to provide independent review and evaluation of the relevant technology. During this reporting period activities were conducted in three subtask areas: (1) analysis methods development, (2) concrete properties, and (3) model testing technique development. Highlights of work under each of these subtask areas follow.

Analysis Methods Development

- Completed validation of a set of computer subroutines for finite-element computation of creep effects in concrete structures.

Concrete Properties

- Completed state-of-the-art report on concrete behavior under uniaxial and multiaxial states of stress.
- Completed development of test plan to develop high-strength concrete mix designs in support of HTR-steam cycle (SC) PCRV design.

Model Testing Technique Development

- Completed demonstration of testing techniques developed for circumferentially prestressing and lining PCRV models.

6. STRUCTURAL CERAMICS TESTING (WBS 3611.02)

In the bottom head region of the core outlet plenum, pads fabricated from hard ceramic materials and separated by interface materials are used to support the graphite posts that support the HTR core. Under this activity, candidate ceramic pad materials are being evaluated for their ability to withstand representative thermal gradient and mechanical loading conditions. During this reporting period, 34 tests were conducted as part of the evaluation of ceramic pad materials.

Creep testing of specimens machined from the ceramic pads was also performed, and the specimens were examined after testing to determine dominant creep mechanisms. The transition from primary to steady-state creep in alumina materials was seen to be related to work hardening within the Al_2O_3 grains.

7. HTR FUEL MATERIALS QUALIFICATION (WBS 3650.02)

The HTR Fuel Materials Qualification Program is part of the national HTR fuel development effort being conducted in cooperation with GA. The ORNL program includes irradiation testing of fuel fabricated by GA in

irradiation capsules assembled by ORNL and operated in ORNL reactors. Postirradiation examinations (PIEs) are also conducted on the irradiated fuel in special equipment developed at ORNL for this purpose.

In addition to the cooperation with GA, the ORNL program includes specific cooperative tasks with the German Nuclear Research Center at Jülich [Kernforschungsanlage (KFA) Jülich]. This cooperation is part of the formal agreement between the United States and the Federal Republic of Germany (FRG) for gas-cooled reactor development.

The HTR Fuel Materials Qualification Program is organized around four subtasks: (1) irradiation testing, (2) PIE, (3) U.S.-FRG cooperative work, and (4) PIE equipment development and maintenance. Accomplishments in these four areas are summarized.

1. Irradiation of capsules HRB-17 and -18 was postponed until FY 1984. This experiment is designed to assess the performance of Triso-coated UCO (UO_2 and UC_2 mixture) fissile particles that fail in the presence of moisture. Progress includes completion of subassemblies necessary for capsule construction and assembling and testing the moisture generation system and reactive gas analysis system necessary for capsule operation. Modifications to the in-core portion of capsules were also completed. Bonded fuel specimens and other encapsulated specimens were received from GA. The HRBTAN thermal analysis computer code, which provides an analytical tool for design, operation, and PIE, was documented in the form of a user's manual.

2. Postirradiation examination continued on irradiated coated particles from capsule HT-35. Transmission electron microscopy (TEM) on SiC coatings from irradiated UCO particles indicated significant microstructural differences compared with similar coatings removed from inert particles. Differences are attributed to the higher temperature of the fuel versus the inert particles. Fission products were found in the silicon carbide (SiC) coatings in configurations similar to those observed in out-of-pile experiments. Fission product retention investigations isolated one fissile coating as exhibiting large deficiencies in cesium inventory. Large particle-to-particle variation was observed in silver retention for all SiC coating batches, with mean retention at the 50 to 60% level.

A comparative analysis of the SiC coatings and zirconium carbide (ZrC) coatings from fuel particles irradiated in capsules HRB-11 and -12 indicated failure rates 2 to more than 100 times greater for the ZrC coatings. We attributed these differences to the level of fabrication development for the ZrC design rather than to inherent problems with its irradiation behavior.

Silver release reevaluations on irradiated microsphere gamma analyzer (IMGA)-generated data from capsule HRB-15b support the conclusion that silver and cesium were retained at high levels in all low-enriched uranium (LEU) fissile particle types. Combining the silver release data from capsules HRB-15a and -15b with German data indicates a strong temperature-dependent release above operating temperatures of 1050°C.

Preliminary metallographic examinations on selected capsule HRB-16 fuel rods indicated severe SiC corrosion in coatings from UCO fissile particles. Extent of corrosion was similar to that observed in HRB-15a on a nearly identical coating (from design and production standpoint).

Long-term acid leach investigations of GA fuels from capsule R2-K13 revealed that 0.3 to 1.4% of the fissile UCO particles had total coating failures. For the fertile fuels, the values were 0.1 to 0.4%.

3. The ORNL contribution (report) to the extended project work statement (PWS) FD-1 was completed. This report concentrates on design and fabrication influences on coated particle fuel performance. We completed IMGA examinations on set 2 of irradiated German fuels under PWS FD-20.

4. Availability of the IMGA system at nearly 80% was much improved over the previous year. Maintenance procedures and the addition of another data storage device were responsible. A new pulse height analyzer system to replace the original was purchased and delivered. The postirradiation gas analyzer system progressed to near full operation. The new mass spectrometry equipment was interfaced to a computerized base data acquisition and analysis system, and software was written and implemented.

8. FISSION PRODUCT STUDIES (WBS 3650.03)

Investigations are in progress to obtain data to estimate the rate of transport of important actinides and fission products throughout an HTR under both normal and accident conditions.

An estimated diffusion coefficient of 3.5×10^{-11} cm^2/s was measured for plutonium (initially present as plutonium dioxide) in H451 graphite at 1000°C. The 3.5×10^{-11} cm^2/s value compares with a value of 1.06×10^{-11} cm^2/s obtained previously for uranium under similar conditions.

The vapor pressure of plutonium present as adsorbed plutonium sesquicarbide (Pu_2C_3) on the surface of H451 graphite was measured at 1000, 1200, and 1400°C. The measurements show the vapor pressure to be a function of the plutonium concentration on the graphite surface. At surface concentrations expected in an HTR, vapor pressures of the adsorbed plutonium are orders of magnitude less than are vapor pressures of pure Pu_2C_3.

Tests simulating conditions in an HTR were conducted to determine the chemical forms of cesium and iodine that would be released from failed or defective fuel in the system. Determinations made partly by inference from location and temperature of deposits on graphite thermal gradient tubes (1000→100°C) indicated the presence of several chemical species, including CsI and I_2 along with cesium-rich–low-iodine-content species.

9. STRUCTURAL METALS STUDIES (WBS 3660.01–03)

This task is aimed at filling identified design data needs for HTR structural metal properties and technology. Our long-term creep tests

continued this year, with emphasis on Hastelloy X, 2 1/4 Cr-1 Mo ferritic steel, and Inconel 718. Work on aging and effects of aging also continued in a parallel effort; aging times in excess of 32,000 h were reached.

Low-cycle fatigue testing of Hastelloy X was conducted in both air and simulated HTR-He environments. Major effort was on creep-fatigue interaction, and the data generated were examined by the linear damage summation approach and the strain range partitioning procedure; the latter gave more consistent results. High-cycle fatigue testing of Hastelloy X in air was completed at 760°C.

A study of the decarburization kinetics of 2 1/4 Cr-1 Mo steel in steam-cycle HTR-He was completed. Exposures were up to 7000 h at temperatures between 427 and 650°C. Mean carbon content and carbon gradient were determined following the experiments. Gross decarburization was observed only for the highest temperature, but near-surface carbon loss occurred at all exposure temperatures.

The compatibility of boronated graphite compacts with type 316 stainless steel and alloy 800H was studied by exposing stacks of alternating layers of these materials under load in an HTR-He environment at both 710 and 800°C. Exposures to 6000 h were completed; solid-state reactions are being studied by optical microscopy, scanning electron microscopy, energy-dispersive x-ray analysis, and electron probe microanalysis.

Equipment was developed and assembled for the joining of alloy 800H tubing to a weld-clad alloy 800H tubesheet by internal bore welding. Preliminary welding tests were directed at maximizing penetration of the tube wall while maintaining a controllable weld puddle around the circumference of the tube. Results obtained indicate that a multipass weld with filler metal addition will be required to achieve a satisfactory tube-to-tubesheet weld joint.

Fracture toughness characterization of PCRV liner and penetration steels was completed. The reference fracture toughness curve defined for these materials was essentially identical to the K_{IR} curve currently employed for light-water reactor pressure vessel steels. A task on the high-temperature fracture behavior of HTR alloys was initiated.

10. GRAPHITE MATERIALS QUALIFICATION (WBS 3670.01)

Graphite creep capsule OC-5 was examined and brings the 900°C creep experiments to a total fluence of 4.4×10^{21} (graphite damage fluence) or 5×10^{21} ($E > 50$ keV) neutrons/cm^2. The results are consistent with previous data in this series of irradiations, and we now detect and confirm the tendency for the creep coefficient to decrease as damage becomes more severe.

The first two High Flux Isotope Reactor (HFIR) capsules in the new fracture mechanics series were also examined, and we have our first indication of the effects of damage on fracture mechanics parameters. We anticipated and found a decrease in the critical flaw size. In addition,

however, the strain-energy release rate, G_{IC}, also decreased. Thus, the early assumption that the fracture stress depends only on the Young's modulus changes is certainly not correct.

The effort to improve H451I continued in collaboration with GA and Great Lakes Research Corporation. Results were disappointing in that the molded billets showed major defects. Despite this fact, the picture continues to be promising: the material formulation appears to offer a superior product, but this has not been attained because of forming problems.

We continued our studies of graphite statistical properties, which — like the fracture mechanics — are aimed at the American Society of Mechanical Engineers (ASME) code for structural graphite in nuclear applications. Calculations of the higher moments of the Weibull distribution were virtually completed; these generally lie within the bivariate sample uncertainty contours for normal distributions; it is virtually impossible to distinguish experimentally between the Weibull and normal statistics unless the volume dependence is explicitly sought and found.

11. INTERNATIONAL TECHNOLOGY TRANSFER (WBS 3690.01)

The transfer of technology between the U.S. and the FRG-Switzerland (FRG-CH) gas-cooled reactor programs in the areas of fuels, fission products, graphites, and structural materials was continued during the year. Cooperative activities included examination of irradiated fuels, corrosion of graphite, fracture mechanics of irradiated graphite, and round-robin testing of structural alloys.

12. ADVANCED REACTOR SYSTEMS ENGINEERING (WBS 4108.03)

This task primarily involved a peer review of the modular HTR concept development activities coordinated by GCRA. Areas of review included design and economic ground rules and criteria, capital and fuel cycle cost estimates, reactor performance, and safety. Also, specific technical analyses and assessments were carried out to evaluate important issues. Analyses were performed to investigate and compare heat-transfer mechanisms for prismatic and pebble-bed cores during depressurized loss of forced circulation accidents. Issues involving adequacy of existing data for fission product release from fuel and the primary circuit during a depressurized loss of forced circulation accident were also addressed.

13. MARKET DEFINITION AND APPLICATION ASSESSMENT (WBS 4151.02)

This study relates HTR applications to national needs, projected to the year 2020. The underlying energy projection, based on a cycle-adjusted-logistic methodology, indicates that U.S. energy consumption will grow at a very low rate between 1980 and 2000 and at a very rapid rate between 2000 and 2025, with electrification increasing during the entire 45-year period.

For electrical power generation, the midrange estimate for the year 2020 is an installed HTR capacity of 350 GW(t) [range of 237–462 GW(t)]. This capacity was based on water use considerations only, that is, to the projected need for power plants with advanced (dry or hybrid) cooling in water-deficient areas of the western United States. The low and high estimates correspond to 11 and 22%, respectively, of the projected nuclear capacity additions after the year 2000.

For nonelectrical energy applications of the HTR, four general types of processes that currently use fossil fuels were examined: resource recovery, synthetic fuels production, chemicals manufacture, and delivery of process steam. For these sectors, the total midrange projection for the year 2020 is an installed HTR capacity of 234 GW(t) [range of 103–362 GW(t)].

14. ADVANCED SYSTEM ALLOYS (WBS 4604.01)

This task supports the development of alloys for application in very high-temperature gas-cooled reactors. During the year we continued our evaluation of the creep-rupture properties of several nickel-base alloys developed by GA and of a number of versions of Inconel 617 with modified compositions. A study to assess the potential for use of nickel aluminide alloys was initiated.

15. HIGH-TEMPERATURE DESIGN CRITERIA (WBS 4605.03)

The High-Temperature Design Criteria task is just beginning work toward assessment of the applicability of ASME Code Case N-47 to very high-temperature reactor (VHTR) components. The assessment, which will be completed at the end of FY 1984, will identify areas needing modification and areas in which additional rules will be required to cover the materials and service conditions of the VHTR.

16. ADVANCED SYSTEM INTERNATIONAL COOPERATION (WBS 4607.01)

This effort primarily focused on planning and establishing a cooperative effort between Arbeitsgemeinschaft Versuchs-Reaktor (AVR)-GmbH–KFA-Julich GmbH and ORNL in HTR physics, performance, and safety within the framework of the U.S.-FRG Umbrella Agreement. The basis of the cooperative project derives from the important potential contribution to a second generation of nuclear plants offered by the modular HTR. The objective of this project is to further the understanding of HTR performance and safety and to compare predictions of reactor behavior with experimental data from the AVR. The AVR offers a unique opportunity to further demonstrate and investigate inherent features similar to those of current modular HTR designs. A mutually acceptable PWS was prepared by AVR-KFA and ORNL, and detailed analysis efforts will begin in 1984.

1. LEAD PLANT ECONOMIC EVALUATIONS (WBS 3150.03)

H. I. Bowers

1.1 INTRODUCTION

This activity involves Oak Ridge National Laboratory (ORNL) review of the *Economic Ground Rules for the HTGR Program* developed annually by the Gas-Cooled Reactor Associates (GCRA), comparison of lead plant economic performance with other options, and review of selected technical studies.

1.2 REVIEW OF *1983 Economic Ground Rules for the HTGR Program*, GCRA 83-008, REV. NO. 0, APRIL 29, 1983

This comprehensive set of economic ground rules encompasses all the pertinent information needed to perform consistent and sound engineering economic analyses. This issue of the ground rules is essentially the same as that issued in January 1983 following a meeting in December 1982 at GCRA and reviews of the draft ground rules in which ORNL participated. We have the following four significant points.

1. It would be helpful in understanding the fixed-charge rates if they were separated into their components, for example, capital recovery factor, income tax, investment tax credit, capital replacement, and decommissioning. Fixed-charge rates in future versions of the ground rules should be calculated by the more rigorous method developed in GCRA 83-009, *An Economic Evaluation of the Steam Cycle High Temperature Gas-Cooled Reactor*, which results in a somewhat lower value. Calculations by ORNL methods give a fixed-charge rate for nuclear plants about 1% lower than the 17.9% recommended in the *1983 Economic Ground Rules for the HTGR Program*.

2. The indirect cost rates were developed from the Energy Economic Data Base (EEDB) Phase IV and are significantly lower than those reported in EEDB Phase V, although GCRA has given some consideration to minimizing effects of field backfits on indirect costs.

3. The unit availabilities are optimistic compared with experience. However, they can be considered realistic goals or targets, because experience with light-water reactor and fossil plants has shown that 75 to 80% availability can be achieved. Experience with base-load plants has not shown that availability is synonymous with capacity factor, the measure of performance that should be used in economic comparisons. Because of partial outages and ramp loading during startup and shutdown, the capacity factor will almost always be 5 to 10% lower than availability.

4. The discussion of uncertainty is very general and makes no specific recommendation. As a minimum for the analyses that these ground rules are directed to, sensitivity analyses should be performed on varied capacity factors and capital investment and fuel costs.

1.3 REVIEW OF *Port Arthur Refinery Cogeneration Alternatives Study: Institutional/Economics Assessment*, UE&C/GCRA 83-006, JANUARY 1983, AND *Port Arthur Refinery Cogeneration Alternatives Study: Summary Report*, GCRA 83-007, JANUARY 1983

The *Port Arthur Refinery Cogeneration Alternatives Study* shows that the advantage of the High-Temperature Reactor (HTR) over coal use as the energy source is significant on the basis of the direct comparison of the two; however, the deployment scenario results give a clear mandate for HTR use only in the long term. It is not clear why the deployment scenario results are less favorable to HTR use, unless electricity credits in these scenarios are significantly different from those considered in the direct comparison of energy sources. Additional parameter studies clarifying the above and showing the influence of varying HTR capital investment costs on overall results are recommended.

1.4 REVIEW OF *An Economic Evaluation of the Steam-Cycle High Temperature Gas-Cooled Reactor*, GCRA-83-009, JULY 1983

This is an excellent report and an important contribution to the literature on HTR economics. The elasticity approach to sensitivity

analysis permits presenting the results in a concise manner, but additional work is needed on uncertainty analysis. Although the report makes some recommendations and the nuclear systems seem to be more economic than the coal-base systems, no clear-cut winner is certain. Perhaps uncertainty analysis will help to narrow the field.

Some inconsistency exists in the fixed-charge rate from one part of the report to another. The method described in the appendix appears correct. We believe that the Electric Power Research Institute Technical Assessment Guide method and the use of constant-dollar costs should be avoided; costs should be analyzed in current dollars, including inflation, and then adjusted to constant-dollar costs.

The elasticity approach to sensitivity analysis is excellent, but it could be misleading because it does not address uncertainty in the independent variables. For example, the elasticities for base price and escalation rates for coal fuel indicate that base price is twice as important as escalation rate. However, current coal prices are relatively certain compared with future escalation rates. Thus, the uncertainty in future coal prices depends more on future escalation rates than on today's base prices.

The summary of levelized unit costs for electric-only options gives some surprisingly optimistic results for nuclear options: 39 mills/kWh for the 1 × 800-MW(e) pressurized-water reactor plant, 40 mills/kWh for the 1 × 855-MW(e) HTR plant, and 60 mills/kWh for the 1 × 800-MW(e) coal-fired plant. These values are in 1983 dollars for a common plant startup in 2005. Most current studies show a virtual standoff between light-water reactor and coal-fired plants for startup in the mid-1990s. The nuclear plant capital investment costs in this study are somewhat optimistic, which along with the additional 10-year escalation of coal prices may be enough to make the nuclear option very attractive.

1.5 REVIEW OF *HTGR SC/C Lead Plant Design Basis Transient Analysis Report*, HCA-20102/REV. 0, NOVEMBER 1, 1983

We believe that GA Technologies has postulated a sufficiently wide range of representative transient events to be considered for the design

basis of the HTR steam-cycle cogenerator. From this standpoint, the report is complete. However, a significant number of the analyses have not been completed and are not included in the report. The omissions relate primarily to the more benign transient events. Thus, the more severe and less frequent events have been analyzed and included.

2. HTR SHIELDING STUDIES (WBS 3610.03)

D. E. Bartine, D. T. Ingersoll, C. O. Slater, and
F. J. Muckenthaler

2.1 INTRODUCTION

The lower portion of the High-Temperature Reactor (HTR) core has coolant holes that progressively combine to give large-diameter coolant channels. These coolant channels provide neutron streaming paths that lead to increased neutron fluences at positions where metal materials are located, that is, metal plates covering the prestressed concrete reactor vessel insulation. To lower the neutron source term, boron-containing pins are located near the bottom of the reactor core. However, it is difficult to calculate accurately (1) the influence of using discrete boron pins (as opposed to a homogeneous distribution of boron in graphite) on the effective neutron source term and (2) the influence of neutron streaming in coolant channels on the fluence received by metal cover plates. As a result, a series of shielding experiments was designed to investigate these effects. The experiments were divided into two phases: the first phase emphasizing the effectiveness of the boron pins in reducing neutron penetration into the lower support regions and the second phase emphasizing the neutron streaming in the large coolant holes below the boron pin shields.

Measurements for Phase I of the HTR Bottom Reflector and Support Block Neutron Streaming Experiment were performed at the Oak Ridge National Laboratory (ORNL) Tower Shielding Facility (TSF) and completed this year. The measurements investigated neutron penetration through a prototypic mockup of a cluster of seven hexagonal columns of HTR blocks extending from the upper (near-core) boron pin shield layer to just above the lower shield layer. A detailed description of the test configurations and the measured results are being published.[1] The analysis of the measurements was also completed and is being published.[2]

In general, good agreement was achieved between the measurements and the analytic predictions. Neutron streaming in the first four layers was determined to be as high as a factor of 20, which is only 1% of the total streaming predicted for the lower support region. The remaining streaming is expected to occur in the large coolant channels at the bottom of the support blocks (to be studied in Phase II). Therefore, although the total streaming effect cannot yet be confirmed, the analytic methods used in the earlier design analysis were confirmed for the first half of the total configuration. Additionally, we showed that the effect of doubling the number of boron pins in the upper shield layer results in only a modest 30% reduction in the neutron flux incident on the lower shield layer.

2.2 EXPERIMENT

The experimental program included neutron measurements behind successive segments of graphite, which modeled the lower reflector and core support structure for the reference HTR steam cycle-cogeneration (SC/C) plant. Phase I measurements included only the upper four layers plus a spectrum modifier. The spectrum modifier, which was positioned adjacent to the Tower Shielding Reactor (TSR)-II collimator, was needed to shift the energy spectrum of the TSR-II to correspond approximately to the predicted energy spectrum incident on the lower reflector of the HTR. The first four segments of the test configuration (layers A–D) included the upper boron pin shield layer, the reflector layer, the coolant hole crossover layer, and a coolant hole extension layer.

A plan view of the test configuration is shown in Fig. 2.1. The graphite blocks modeled only a seven-column cluster of hexagonal HTR blocks, as shown in the elevation view of the configuration in Fig. 2.2. The seven-column cluster was made to represent better a larger array by surrounding the blocks with additional pieces of solid graphite and concrete.

The experiment was organized into two parts: part I included the reference pattern of pins in the upper shield layer, and part II included the full pattern of pins. The reference pattern consisted of 738 pure

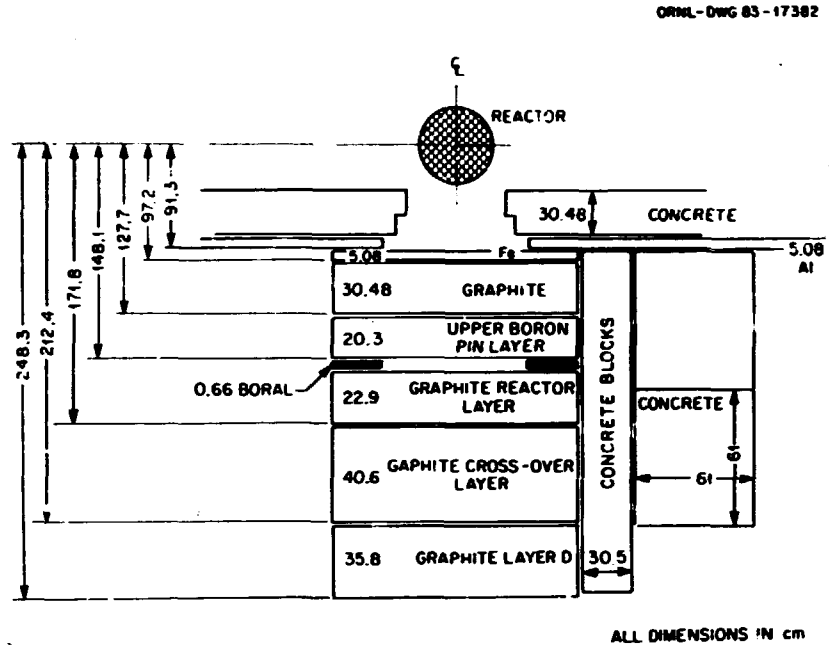

Fig. 2.1. Plan view of the full test configuration investigated in Phase I.

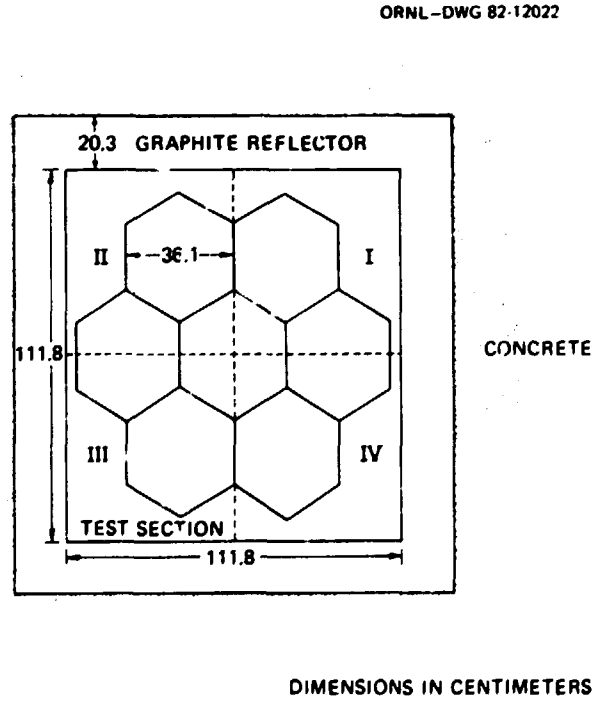

Fig. 2.2. Elevation view of the test configuration showing simulated seven-hex-column cluster and reflector regions.

graphite pins and 770 boronated graphite pins distributed uniformly in the seven-hex-column mockup. For the full pattern, the graphite pins were replaced with boronated graphite pins to provide more effective shielding. Figure 2.3 is a detailed drawing of one quarter of the upper-shield layer and shows the coolant holes and the positions occupied by the graphite and boronated graphite pins.

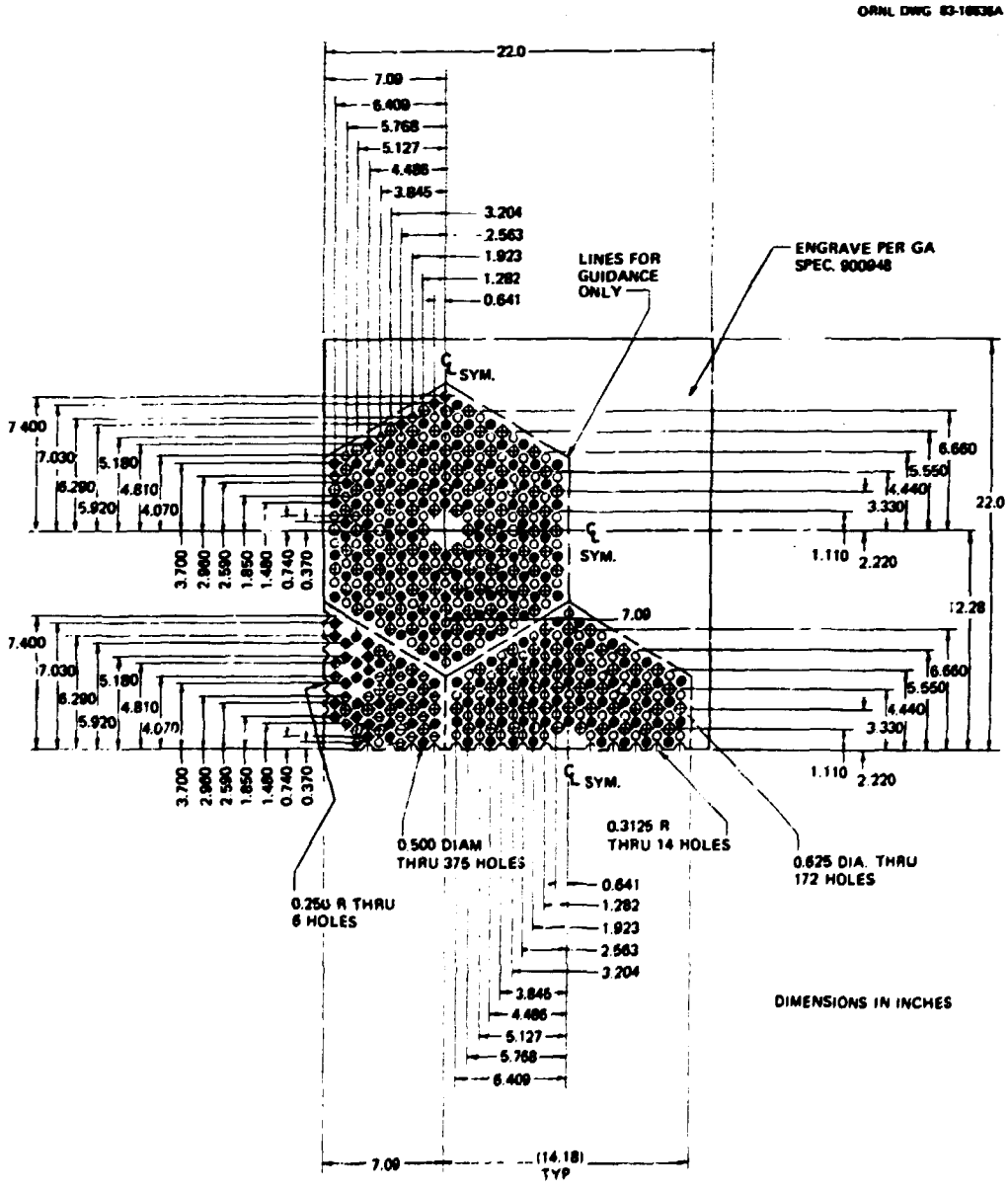

Fig. 2.3. Cross-sectional view of one quarter of the upper boron pin shield layer. One inch = 25.4 mm.

Neutron spectrum measurements were made on centerline behind the spectrum modifier and upper shield layer by use of the NE-213 scintillator and hydrogen-filled proportional counters. Horizontal traverses perpendicular to the reactor configuration centerline were made with the bare and cadmium-covered BF_3 detectors several centimeters behind the spectrum modifier and at each segment as it was added to the configuration. These traverses were repeated at a 30-cm distance along with traverses with the 5- and 10-in. Bonner balls. Centerline measurements were made 300 cm beyond the configuration with the bare and cadmium-covered BF_3 detectors and 5- and 10-in. Bonner balls. Additionally, in situ-type traverses were made with the bare and cadmium-covered detectors in a 15-cm void created between the configuration and the next segment.

Samplings of the count rate profiles measured at 30 cm behind each segment are shown in Figs. 2.4 through 2.7. In Fig. 2.4, the bare detector results are compared for part I (reference pattern in the upper shield layer) and part II (full pattern). Behind the upper pin layer, the flux was slightly decreased when all the pins were boronated graphite. Adding the boral iris and the reflector layer made a big change in the flux intensity, reducing the count rate by a factor of almost 5 for the part I pin arrangement and nearly twice that amount for part II. The count rate behind the crossover layer was essentially the same as that behind the reflector layer in part I, but in part II the count rate increased about 25% over the measurement behind the reflector layer. Behind the next segment (layer D) the counting rates in both parts dropped about the same percentage, with the shapes of the curves changing to reflect the streaming from the large coolant hole.

The results for the cadmium-covered BF_3 detector (see Fig. 2.5) and 5-in. Bonner ball (see Fig. 2.6) are very similar to those for the bare detector. Similar traverses have similar shapes, with the differences between count rates in parts I and II again decreasing as each segment is added. That trend also exists for the 10-in. ball as shown in Fig. 2.7, with no discernible difference between count rates for parts I and II behind the last segment (layer D).

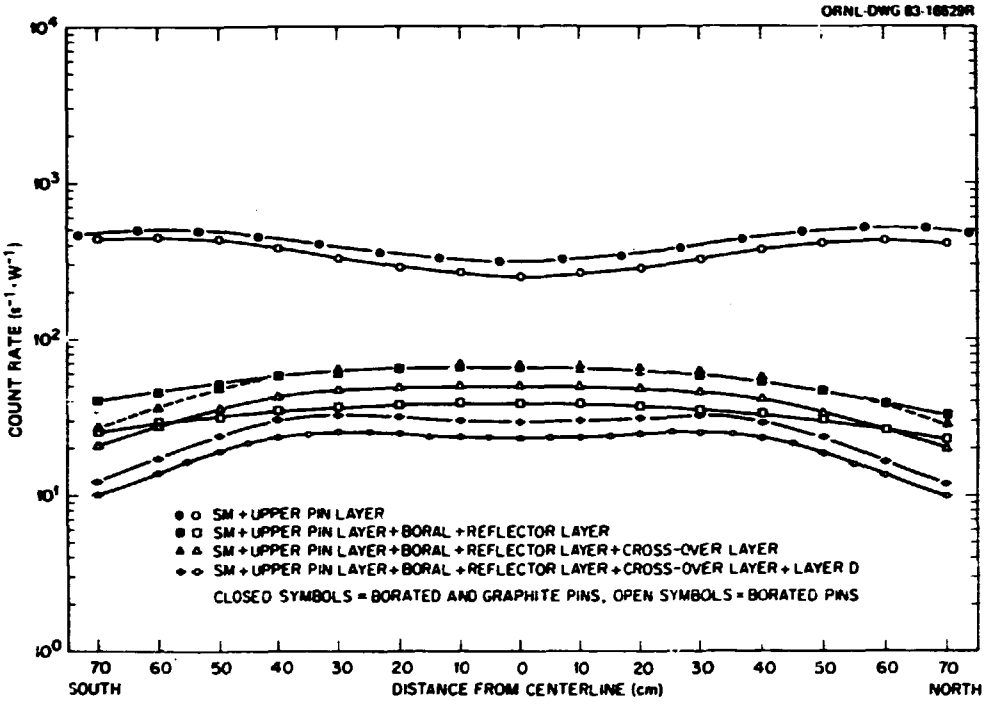

Fig. 2.4. Horizontal traverses with the bare BF_3 detector positioned 30 cm behind the indicated configurations.

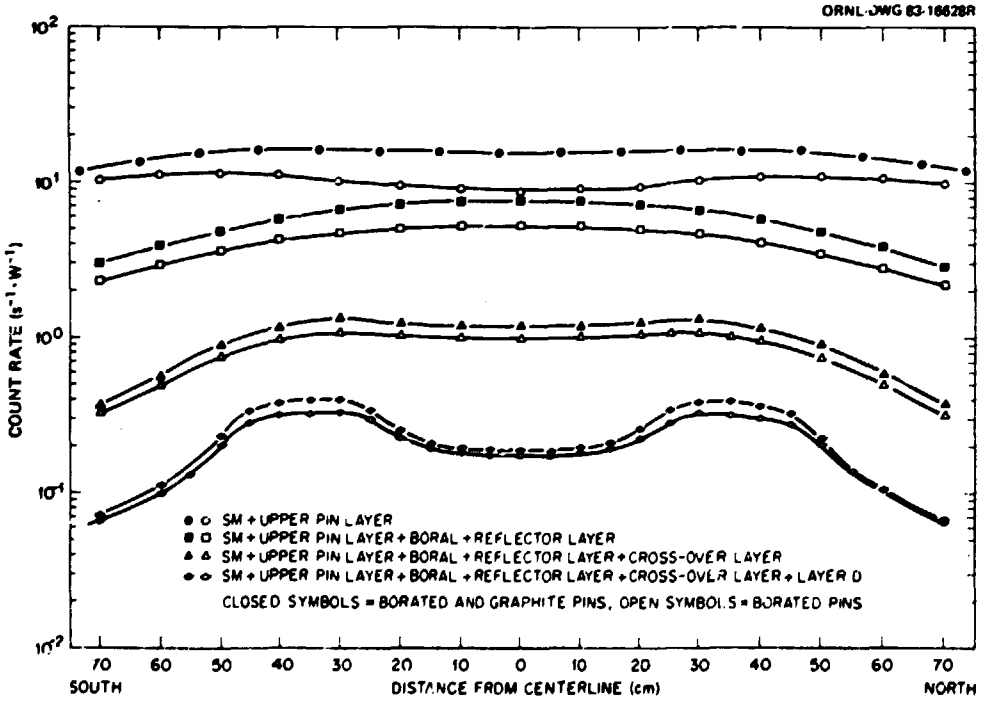

Fig. 2.5. Horizontal traverses with the cadmium-covered BF_3 detector positioned 30 cm behind the indicated configurations.

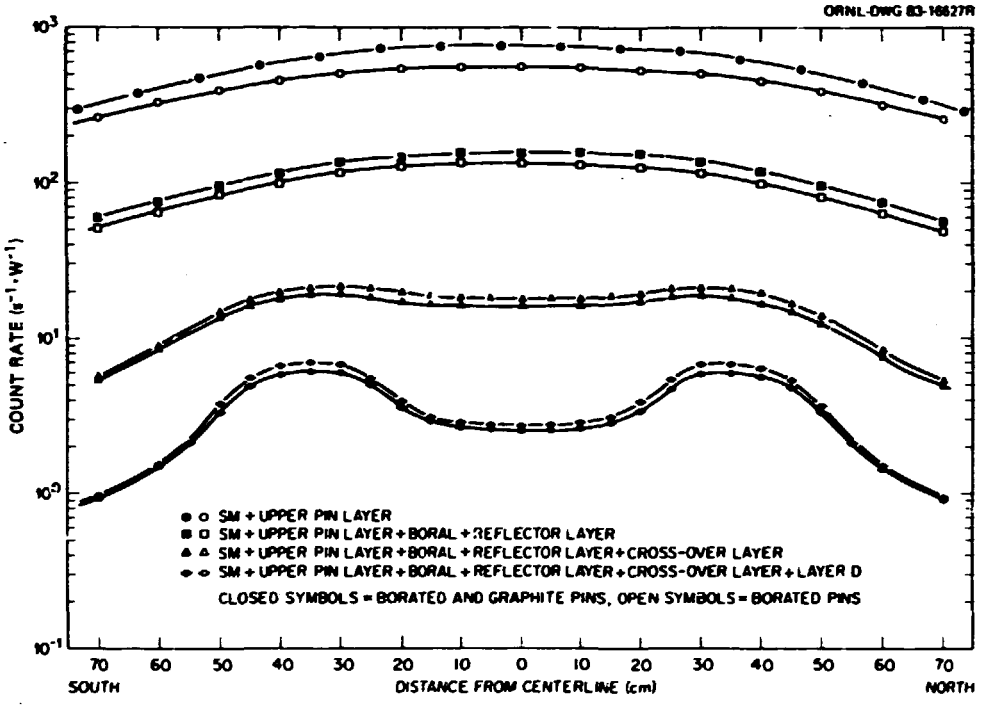

Fig. 2.6. Horizontal traverses with the 5-in. Bonner ball positioned 30 cm behind the indicated configurations.

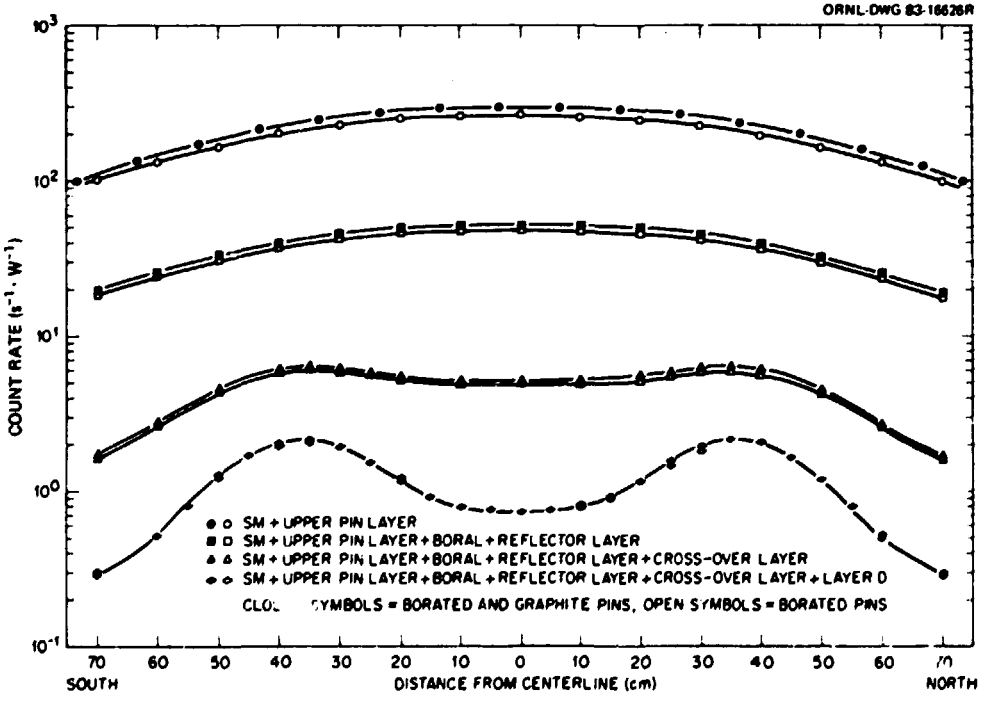

Fig. 2.7. Horizontal traverses with the 10-in. Bonner ball positioned 30 cm behind the indicated configurations.

Data close behind the segments (4–5 cm) display trends similar to that obtained at 30 cm. At this location, with the bare detector, the count rates behind the first three segments are within 50% of each other, with the data behind the crossover layer rising above that obtained behind the reflector layer in the vicinity of the centerline. The shapes follow the same patterns as those for the traverses at 30 cm. Similar responses were found with the cadmium-covered detector, with pronounced peaks behind the large coolant holes and smaller differences between count rates in parts I and II than those obtained with the bare detector.

2.3 ANALYSIS

The analysis effort for the HTR Shielding Studies Program was confined to the analysis of the Phase I measurements of the HTR Bottom Reflector and Support Block Neutron Streaming Experiment.[1] The measurements and analysis were performed for the spectrum modifier and the first four sections (A–D) of the configuration shown in Fig. 2.1. Detailed analysis results are reported in ref. 2.

Selected configurations were calculated with the DOT-IV two-dimensional discrete ordinates code[3] and the MORSE Monte Carlo radiation transport computer code.[4] The MORSE results were used to correct the DOT-IV results for streaming and geometric effects.

The first calculation was the TSF reactor source calculation through the spectrum modifier. Neutron spectra from this calculation were reported in the 1982 annual progress report.[5] However, a new calculation had to be performed when the original 15-group energy structure was found to be inadequate for calculating detector responses. The 15-group structure included only one thermal neutron group ($E < 3.05$ eV), and the weighted thermal neutron response function values had to be representative of the thermal neutron flux both in boron and in graphite. However, the two thermal neutron flux spectra are so different that a single thermal neutron response function value would not be adequate. The new energy structure contained 44 neutron groups and 4 thermal groups. Cross sections and response function values were collapsed from a 227-group master cross-section library.[6]

Boundary fluxes from the TSF source calculation were then transported from the spectrum modifier to detector positions behind it, and the fluxes were folded with BF_3 and Bonner ball detector responses to give calculated count rates. The results were in good to excellent agreement. Figure 2.8 illustrates the good agreement for the bare BF_3 detector.

Not all agreement was good, however. The calculated neutron spectrum was generally lower than the measured neutron spectrum. Calculation-to-experiment (C:E) values ranged from about 0.1 in the top energy group to about 1.0 near 0.1 MeV. The ratio for the integrated flux is 0.77. The calculated and measured $E > 0.005$ MeV neutron spectra are shown in Fig. 2.9.

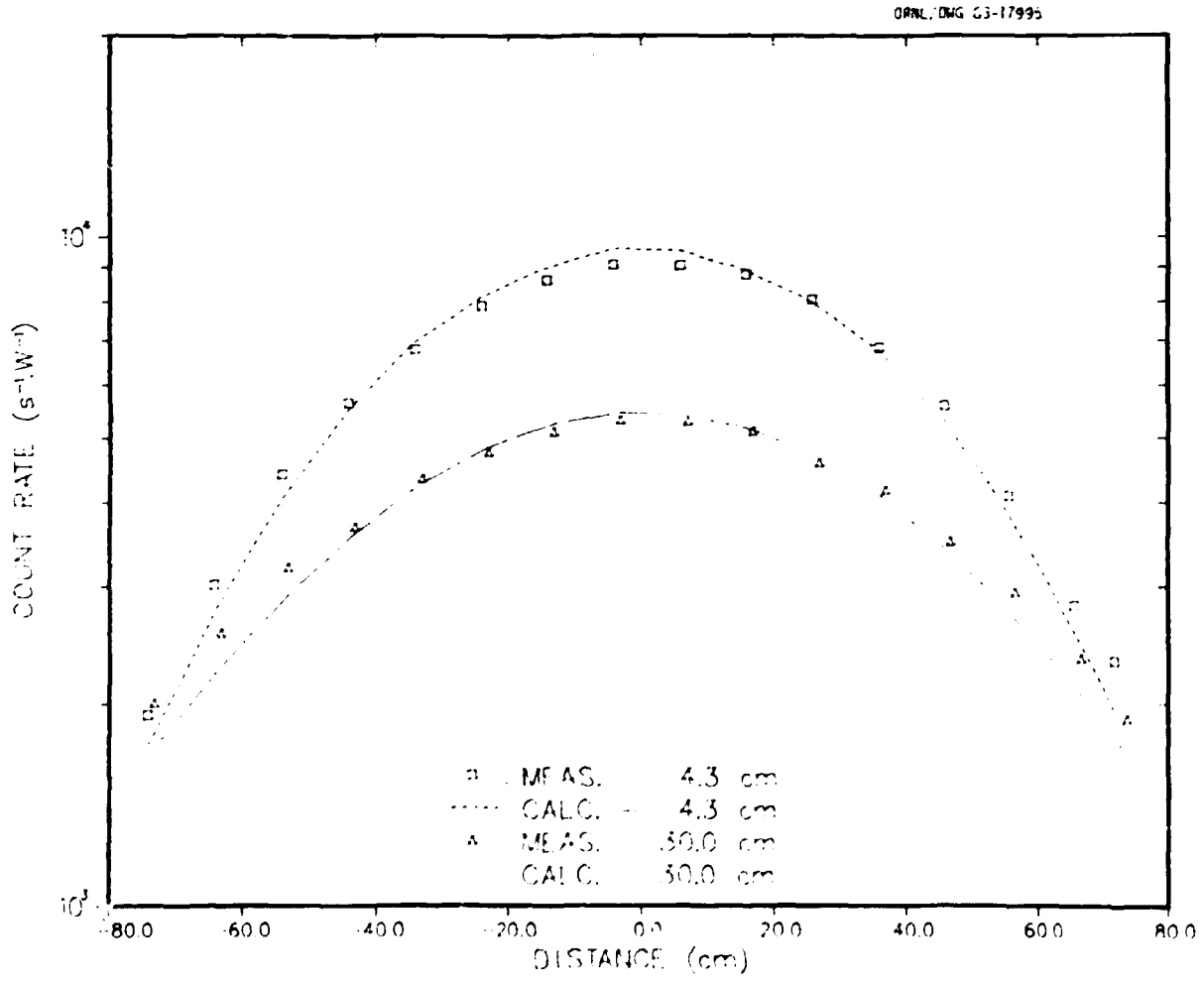

Fig. 2.8. Comparison of calculated and measured bare BF_3 detector count rates for radial traverses 4.3 and 30 cm behind the spectrum modifier for the High-Temperature Reactor Bottom Reflector and Support Block Neutron Streaming Experiment.

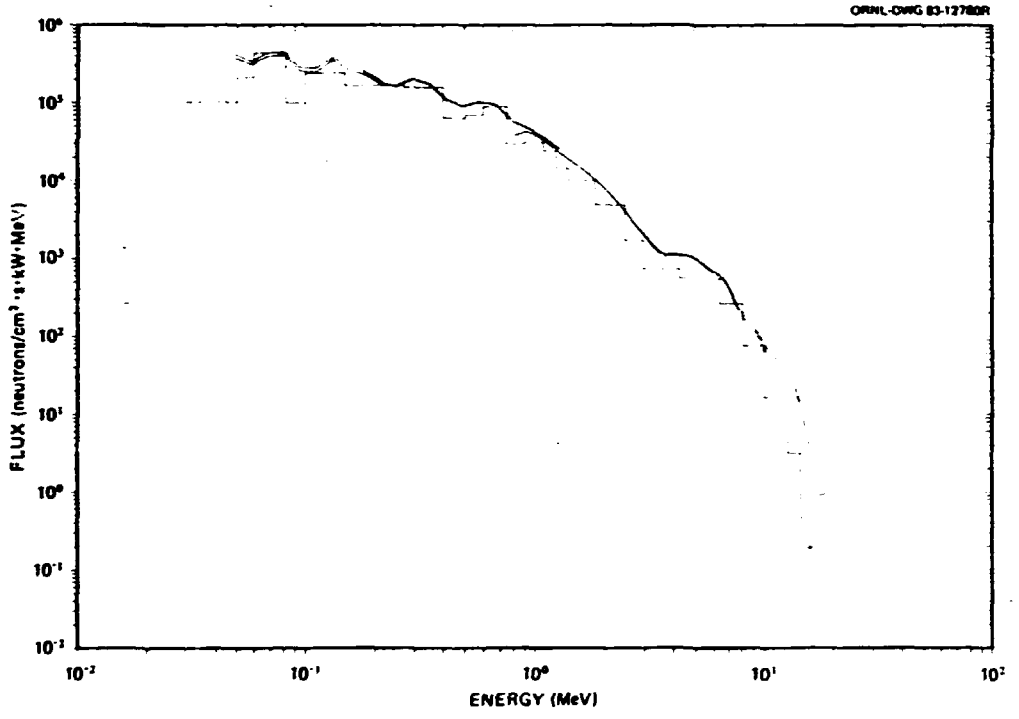

Fig. 2.9. Comparison of calculated and measured neutron spectra 125.3 cm behind the spectrum modifier (NE-213 run 7831A and hydrogen counter runs 1501B to 1503B).

The lack of agreement between the calculated and measured spectra is attributed in part to the iron filter used to reduce the gamma-ray field so that the measurements could be made. A strong case for this view is shown in Table 2.1, which shows that calculated Bonner ball count rates for the case without the iron agree well with the measured results but that those for the case with the iron show C:Es of about that for the integrated neutron flux above 0.05 MeV.

The DOT-IV calculations through the first boron pin layer were performed with homogeneous mockups of the layer. Results from these calculations were compared with the measured results. Near the centerline, measured bare BF_3 detector results were up to 5.0 times the calculated results. This indicated a very significant thermal neutron streaming effect. Results were similar for both boron pin patterns. However, the thermal neutron streaming effect is negated somewhat by the large contribution to the thermal neutron source made by fast and intermediate

Table 2.1. Comparison of calculated and measured Bonner ball count rates at the spectrum measurement position 125.3 cm behind the spectrum modifier

Bonner ball	Count rate ($s^{-1} \cdot W^{-1}$)		Calculated-to-measured ratio
	Measured	Calculated	
	With 15.4-cm iron slab		
3-in.	92	72.4	0.78
6-in.	327	262	0.80
10-in.	131	100	0.76
	Without 15.4-cm iron slab		
3-in.	606	752	1.24
6-in.	1148	1232	1.07
10-in.	419	405	0.97

neutrons, which thermalize in the graphite beyond the boron pin layer. Although the factor of 2 difference in the number of boron pins in the first layer resulted in a factor of 2.2 difference in the thermal flux behind the layer, the thermal fluxes for the two cases differed by a factor of only 1.3 when sections B through D were added. These factors are inferred from the bare BF_3 detector measurements.

The fast neutron spectrum behind the boron pin layer was similar to that behind the spectrum modifier. Calculation-to-experiment values for the detector count rates with and without the iron filter are shown in Table 2.2. The agreement between measured and calculated results clearly follows the same pattern as that behind the spectrum modifier. The agreement is better without the iron filter than with it. Again, the C:E for the integrated flux is about the same as that for the detector count rates when the iron filter is present.

Behind the small coolant hole section (configuration II.B), good agreement was achieved between the measured and calculated detector count rates. Figures 2.10 and 2.11 show results for the bare BF_3 and 5-in.

Table 2.2. Comparison of calculated and measured detector count rates on centerline behind the first boron pin layer

Detector	Count rate ($s^{-1} \cdot W^{-1}$)		Calculated-to-measured ratio
	Calculated	Measured	
At spectrum location behind configuration II.A (no iron)			
Bonner ball, 3-in.	63.0	69.3	0.91
Bonner ball, 6-in.	138.1	157.5	0.88
Bonner ball, 10-in.	53.3	64.4	0.83
At spectrum location behind configuration II.A (with 15.4-cm iron)			
Bonner ball, 3-in.	7.70	10.3	0.75
Bonner ball, 6-in.	33.0	44.7	0.74
Bonner ball, 10-in.	13.5	18.8	0.72
At spectrum location behind configuration III.A (with 15.4-cm iron)			
Bonner ball, 3-in.	6.91	9.16	0.75
Bonner ball, 6-in.	32.5	44.2	0.74
Bonner ball, 10-in.	13.6	20.9	0.65
Three hundred centimeters from boron pin layer of configuration II.A (no iron)			
Bare BF_3	30.8	45.4	0.68
Cadmium-covered BF_3	0.832	1.50	0.55
Bonner ball, 5-in.	29.4	43.0	0.68
Bonner ball, 10-in.	11.1	17.4	0.64

Bonner ball detectors, respectively, behind this configuration (spectrum modifier plus the first boron pin layer with the reference pattern of boron pins plus the boral collar plus the small coolant hole section). With the reference pattern of boron pins, the thermal neutron flux is about 1.8 times that for the one with the full pattern of boron pins, compared with a factor of 2.2 behind the boron pin layer.

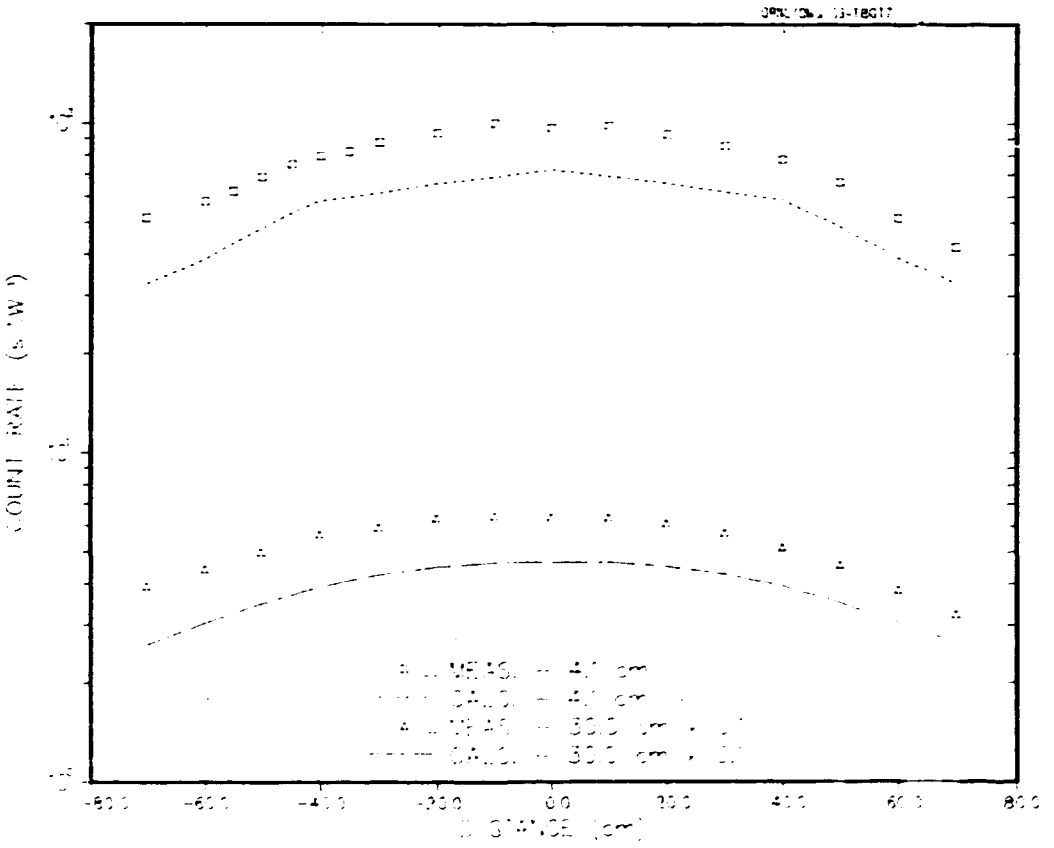

Fig. 2.10. Comparison of calculated (streaming-corrected) and measured bare BF_3 detector count rate radial traverses 4.1 and 30 cm behind configuration II.B (spectrum modifier plus reference pattern boron pin layer plus boral plus section B).

The DOT-IV boundary fluxes were streaming-corrected with MORSE results and transported to the detector locations. The fluxes at the detector sites were folded with the response functions (by use of a weighting over the surface of the detectors) to give the results shown. The streaming-corrected fluxes from this configuration were also used as a source for DOT-IV and MORSE calculations of subsequent configurations, because the calculation through the boron pin layer would thus be avoided.

The DOT-IV and MORSE calculations were also performed on configuration II.C, which contained the spectrum modifier and sections A through C with the reference pattern of boron pins in section A. The source for this configuration was the same as that used for the earlier configurations, rather than a streaming-corrected source from section B as was used for

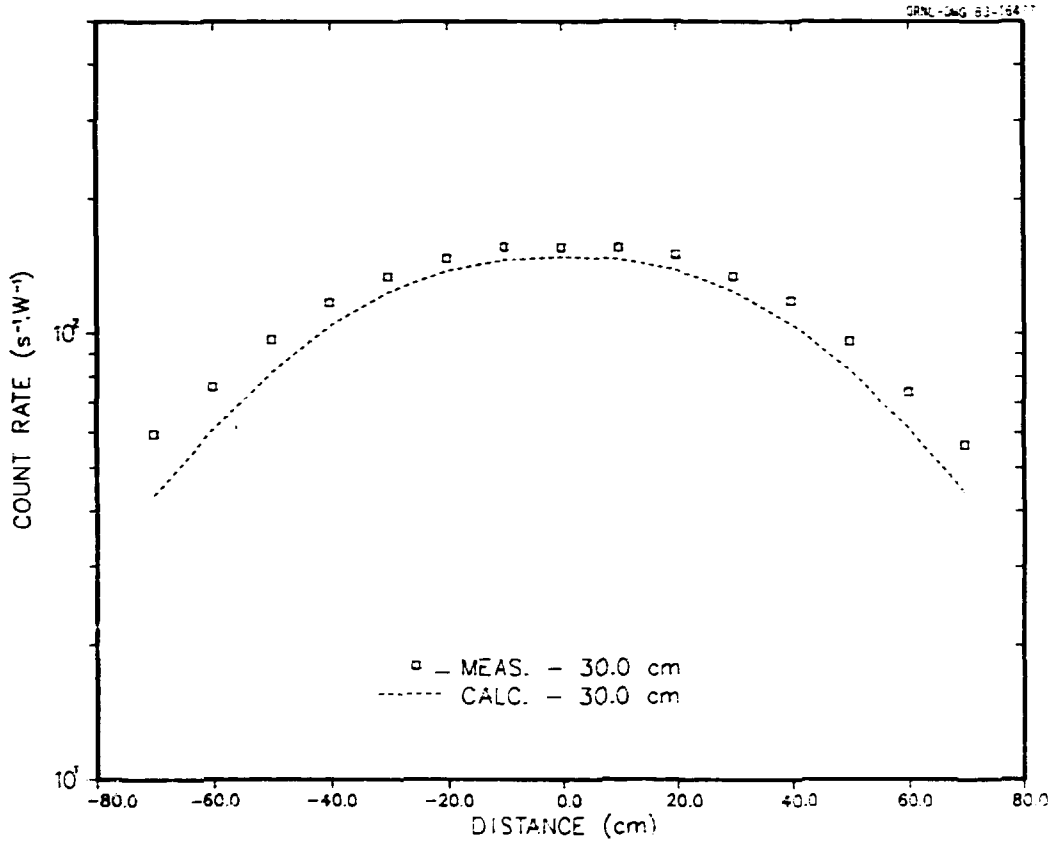

Fig. 2.11. Comparison of calculated (streaming-corrected) and measured 5-in. Bonner ball count rate radial traverses 30 cm behind configuration II.B.

configurations II.D and III.D. This likely accounts for part of the detector count rate underprediction observed. The bare BF_3 detector count rate was underpredicted by 36 to 48%, the cadmium-covered BF_3 detector count rate by 8 to 26%, the 5-in. Bonner ball count rate by 8 to 29%, and the 10-in. Bonner ball count rate by 26 to 44%. Thus, the largest calculational errors were in the thermal (bare BF_3) and the fast (10-in. Bonner ball) neutron fluxes.

Finally, MORSE and homogeneous and heterogeneous DOT-IV calculations were performed for configurations II.D and III.D (see Fig. 2.1) with either the reference (II.D) or full (III.D) boron pin pattern in section A. The streaming-corrected (with MORSE) DOT-IV results were generally in good agreement with the measured results except near the edges of the coolant holes, where the DOT-IV two-dimensional void ring was quite a bit narrower

than the diameter of a large coolant hole. Consequently, the peak is narrower for the calculation than for the measurement. The results for the bare BF_3 and 5-in. Bonner ball detectors, respectively, behind configuration II.D are shown in Figs. 2.12 and 2.13. Results behind configuration III.D are similar.

As stated before, the bare BF_3 detector count rate behind configuration II.D (with the reference pattern of boron pins in section A) is about 1.3 times that for configuration III.D (with the full pattern of boron pins in section A). Hence, although the full boron pin pattern had a shielding

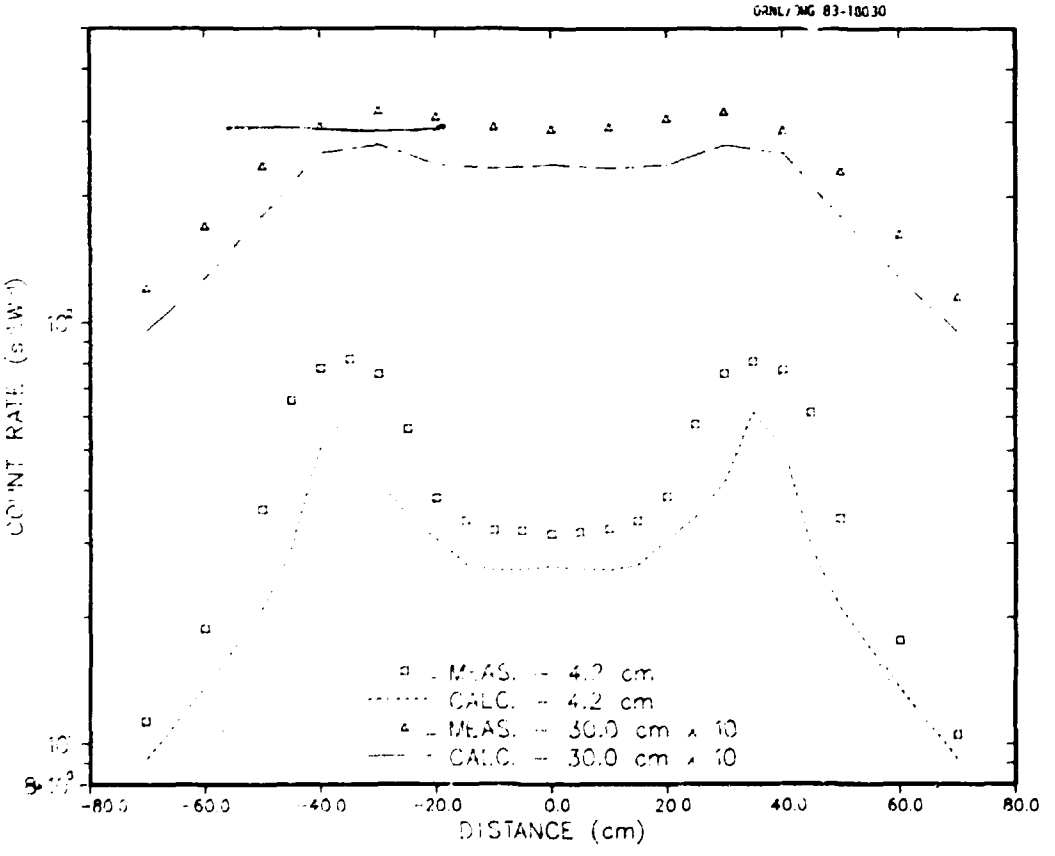

Fig. 2.12. Comparison of calculated (streaming-corrected) and measured bare BF_3 detector count rate radial traverses 4.2 and 30 cm behind configuration II.D (spectrum modifier plus reference pattern boron pin layer plus boral plus sections B through D).

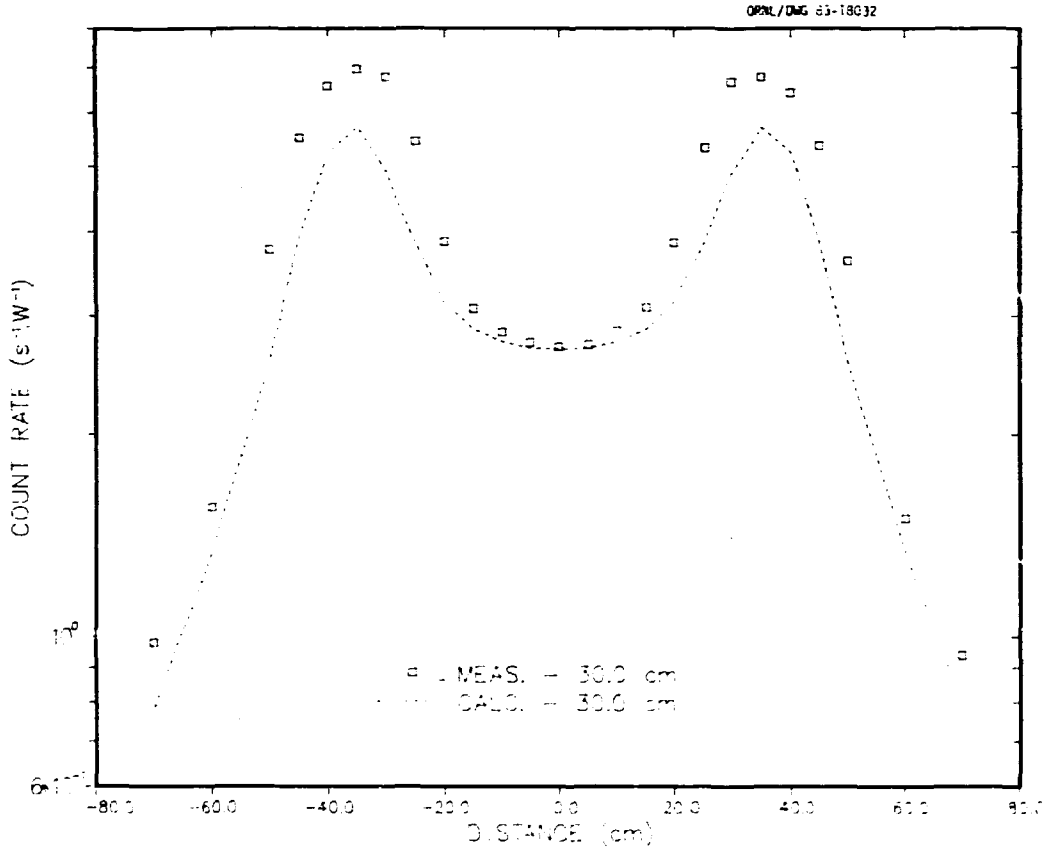

Fig. 2.13. Comparison of calculated (streaming-corrected) and measured 5-in. Bonner ball count rate radial traverses 30 cm behind configuration II.D.

effectiveness more than twice that for the reference boron pin pattern directly behind the pin layer, much of that effectiveness was negated as a result of neutron thermalization in the graphite beyond the layer.

Neutron streaming factors were estimated from the homogeneous and the heterogeneous calculations. Thermal neutron ($E < 3.05$ eV) factors of 2.26 and 1.98 and epithermal neutron ($E > 3.05$ eV) factors of 12.9 and 11.8 were found for configurations II.D and III.D, respectively. Because the heterogeneous results were lower than the measured results, additional streaming is indicated. Thus, maximum streaming factors of 3.0 to 3.4 were estimated for thermal neutrons and 18 to 19 for epithermal neutrons.

These factors are many times smaller than those calculated for the HTR design lower core support regions. However, in the region below the layers studied in Phase I, the coolant holes merge into a much larger coolant channel, which should permit more streaming than that allowed by the preceding six smaller coolant holes. Therefore, the streaming factors calculated for the design[7] cannot be confirmed on the basis of the results obtained thus far.

In summary, the good agreement obtained between calculated and measured results for Phase I of the HTR Bottom Reflector and Support Block Neutron Streaming Experiment, provides partial confirmation of the design calculation results. Likewise, the measured results confirmed the calculated results, which indicated that there was little difference between the thermal neutron flux in the lower bottom reflectors for the reference and full patterns of boron pins in the upper boron pin layer. The full boron pin pattern affords only 30% greater shielding effectiveness than the reference pattern, even though about twice as many boron pins are used.

2.4 REFERENCES

1. F. J. Muckenthaler et al., *Phase I Measurements for the HTGR Bottom Reflector and Support Block Neutron Streaming Experiment*, ORNL/TM-8977, to be published at Oak Ridge National Laboratory.

2. C. O. Slater, *Analysis of Phase I of the HTGR Bottom Reflector and Support Block Neutron Streaming Experiment*, ORNL-6014, to be published at Oak Ridge National Laboratory.

3. W. A. Rhoades et al., *The DOT-IV Two-Dimensional Discrete Ordinates Transport Code with Space-Dependent Mesh and Quadrature*, ORNL/TM-6529, 1979.

4. M. B. Emmett, *The MORSE Monte Carlo Radiation Transport Code System*, ORNL-4972, 1975.

5. C. O. Slater and D. T. Ingersoll, "High-Temperature Reactor Shielding Studies," pp. 132–35 in *High-Temperature Gas-Cooled Reactor Technology Development Program Annual Progress Report for Period Ending December 31, 1982*, ORNL-5960, June 1983.

6. W. E. Ford III et al., *CSRL-V: Processed ENDF/B-V 227-Neutron-Group and Pointwise Cross-Section Libraries for Criticality Safety, Reactor and Shielding Studies*, NUREG/CR-2306 (ORNL/CSD/TM-160), June 1982.

7. C. O. Slater and S. N. Cramer, *Survey Analysis of Radiation Levels in the HTGR Lower Regions*, ORNL/TM-8141, February 1982.

3. HTR COMPONENT FLOW TEST LOOP STUDIES (WBS 3610.03.2)

J. P. Sanders and A. G. Grindell

3.1 INTRODUCTION — J. P. Sanders

The Component Flow Test Loop (CFTL) is a high-temperature, high-pressure, gas-flow loop that has the potential of resolving problems in the design, performance, safety, and licensing of High-Temperature Reactor (HTR) primary system components. The loop can circulate helium with controlled concentrations of impurities at typical primary loop operating conditions for both steady-state and anticipated normal and upset transient conditions. The design operating pressure for the installed components is 7.24 MPa (1050 psia); however, the loop piping, the circulators, and the air-cooled heat exchangers have a maximum operating pressure of 10.7 MPa (1500 psia).

The maximum internal gas temperature that can be tolerated in the impeller cavity of the gas-bearing circulators is 425°C (800°F), and the design operating temperature of the primary pressure boundary is 600°C (1100°F). Higher internal gas temperatures are obtained within the pressure vessel through the use of a helium heater in line with the test item and an annular flow of attemperating gas to limit the temperature of the pressure boundary. Similar operating conditions can be achieved by adding insulation to the interior of the pressure boundary and cooling the exterior surface with air.

The helium heater power is controlled by a 0.5-MW motor-driven induction regulator. Transformers have been installed to supply a total capacity of 5.0 MW for helium heating. An air-cooled heat exchanger that can remove 4.4 MW at normal design operating temperatures is installed in the helium loop.

Flow is provided by three gas-bearing centrifugal circulators installed in series. The speed of the circulators is controlled through the use of three solid-state, variable-frequency power supplies (VFPSs), and the flow is measured with vortex-shedding flowmeters (VSFMs) specifically developed for the CFTL. These flowmeters indicate the flow over a range of 165 with an accuracy of about 1% of the value at pressures ranging over a factor of 45.

3.1.1 Current Application of the Loop

The test vessel, which has been installed in the loop, will accept a full-diameter graphite structure that represents the proposed core support post and post seat for the prismatic HTR core design. To permit relative movement between the post and its seat, each surface has a spherical curvature with a different radius. The concave surface on the post with the larger radius nests into the convex surface of the seat. This geometry results in a small contact area that supports the weight of the core and the downward force of the pressure gradient resulting from the coolant flow. The concentration of forces over a small area is usually denoted as Hertzian stress. A narrow wedge-shaped interface occurs at the junction between these two graphite parts. This interface is exposed to the flow of coolant from the core, which is at the maximum temperature of the primary loop.

This support structure is designed to operate over the lifetime of the reactor, which is specified as 40 actual years or its equivalent of 32 full-power years. Because of the extensive downtime that would be associated with the replacement of this structure and the safety implications related to a possible failure of the structure, an engineering performance test was initiated. This test was designated as the Core Support Performance Test (CSPT).

Only a segment of the post and its associated seat will be represented. GA Technologies (GA) has requested that three combinations of radii be used to provide information to optimize the design choice for these two dimensions.

The operating conditions at the curved interface will duplicate those of the reactor in temperature, pressure, and mass velocity. To limit the time of testing to a practical period, the concentration of impurities in the circulating gas will be increased from those anticipated in the reactor. The concentration and relative ratio of these impurities will be selected and controlled so that both the amount and the nature of graphite corrosion anticipated during the reactor life will be duplicated in the CSPT in a six-month test period. The nature of the corrosion is characterized by the ratio of the amount of material removed from the surface of the graphite to the amount removed from subsurface strata as a result of diffusion of both reactants and corrosion products through the pores of the graphite.

The main objective of the test is to determine the effect of the corrosion process on the specified geometry between the post and its seat. The penetration of the corrosion at the surfaces of the wedge-shaped interfaces and in the areas of the Hertzian stress concentration will be examined, and the effect of this corrosion on structural performance in this critical area will be determined.

The post and seat material that will be used in the final CSPT is a specially refined Stackpole 2020 graphite, which was produced for this test and which has been designated as the preferred material of construction for future HTR plants. This material has been called "nuclear-grade" Stackpole 2020 graphite to provide a special designation; this is not intended to imply that other Stackpole 2020 graphite is not suitable for reactor use. In qualifying tests for the current loop configuration and control systems, we have used test structures that are right-circular cylinders constructed of off-the-shelf Stackpole 2020 graphite.

The CSPT has been divided into three phases as outlined in Fig. 3.1. Both Phase I and Phase II are devoted to qualifying the CFTL for long-term (up to three months of uninterrupted operation with extended periods in an unattended mode) performance and to qualifying the systems that measure and control the low concentrations of impurities in the circulating gas.

- PHASE I
  - SHAKEDOWN TESTS WITHOUT GRAPHITE INSTALLED
  - DETERMINE CATALYTIC EFFECT OF LOOP MATERIALS ON GASEOUS IMPURITIES
  - PROVE ABILITY TO MAINTAIN REQUIRED GASEOUS IMPURITY CONCENTRATIONS
  - PHASE I COMPLETED IN JUNE 1983
- PHASE II
  - OFF-THE-SHELF STACKPOLE 2020 GRAPHITE INSTALLED
  - CONTROLLED LEVELS OF IMPURITIES TO ESTABLISH ACCELERATED OXIDATION RATE
  - PHASE II BEGAN IN AUGUST 1983
- PHASE III
  - ACTUAL TEST OF SIMULATED SEGMENT OF CORE SUPPORT STRUCTURE
  - NUCLEAR-GRADE STACKPOLE 2020 GRAPHITE
  - AXIAL LOADING OF CORE SUPPORT STRUCTURE
  - PHASE III TEST OPERATION TO BEGIN IN FISCAL YEAR 1985

Fig. 3.1. Outline of the Core Support Performance Test.

Phase I, which included an operational sequence designated as TEST P-1, included operation of the loop without a graphite test structure. The purpose of this procedure was to determine the effect of the internal surfaces or the effect of gas phase reactions on the ability to maintain the prescribed concentrations of impurities.

Phase II, which contains a procedure designated as TEST ZERO, included extended operation with the right-circular structure of off-the-shelf Stackpole 2020 graphite. The purpose of this operation was to confirm the capability of the impurity control system (ICS) to maintain adequately the prescribed concentrations of impurities in the presence of graphite. This operation would also determine the corrosion characteristics of the structure and would help to verify the analytical procedures used to specify the concentrations of impurities necessary to produce accelerated corrosion.

Phase III is the actual test of the nuclear-grade Stackpole 2020 graphite with the spherically curved interfaces. This graphite structure will be loaded by use of weights and levers external to the pressure vessel. A loading shaft penetrates the pressure boundary through a bellows seal that has a compensating bellows to eliminate the effect of internal pressure in supporting the load. This test, which will extend for approximately six months, has been designated TEST ONE.

3.1.2 Core Auxiliary Heat Exchanger Test

GA Technologies had originated a test specification to determine the performance characteristics of a representative segment of a full-length tube bundle for the core auxiliary heat exchanger (CAHE). This is a water-cooled bundle located in the lower face of the prestressed concrete reactor vessel (PCRV) to remove the residual heat from the core following a loss of main loop cooling and during refueling operations. The circulator for this auxiliary loop is electrically driven and is located at the upper face of the PCRV.

The CAHE bundle must operate over a range of pressures, temperatures, and flows corresponding to the conditions anticipated in the primary loop during a variety of postulated sequences. The bundle consists of 547 sheath-bayonet tubes with primary system coolant flowing outside the sheath and auxiliary cooling water flowing through the bayonet.

The test was specified to determine the performance of a symmetrical segment of 19 full-length tubes at typical temperatures, pressures, and flows per tube of both primary system gas and cooling water. The test required that the primary system gas contain significant amounts of both air and moisture to simulate air ingress or water ingress accidents.

A conceptual design was completed to determine the modification to the CFTL that would be required to execute this test series. It was determined that an additional low-pressure helium loop would be required to provide the necessary flow under the "depressurized conditions." A comparison indicated that this choice was less costly than a modification of the piping in the existing high-pressure loop.

The conceptual design of a helium heater to meet the required test conditions was prepared, and the specifications of the necessary power control and supply system were developed. A conceptual design of the cooling water system with a pressurizer and heat dump was prepared.

A conceptual design report and an associated cost estimate were prepared and submitted to the Oak Ridge Operations Office (ORO) of the Department of Energy (DOE). These documents were accompanied by a request for directive for construction pending available funding. Because funding was not made available by the end of the year, review by ORO was not initiated.

3.2 CORE SUPPORT PERFORMANCE TEST — H. C. Young

The design capabilities, the historical background, and the status of the CFTL at the end of 1982 are summarized in the previous annual progress report.[1] At the beginning of 1983, the few remaining construction tasks needed to modify the CFTL Stage Alpha to accommodate the CSPT were completed. Shakedown operation was initiated at the beginning of February 1983 to qualify the CFTL for operation with CSPT TEST ONE. Qualification of the facility required the completion of Phase I and Phase II of the test plan.

The shakedown operation consists of two CSPT tests: TEST P-1 and TEST ZERO. TEST P-1, which was completed at the end of May 1983, was operated without a graphite structure. During the test, both satisfactory unattended operation of the CFTL and an acceptable gas leak rate from the helium circulation system were demonstrated, and a general shakedown of the CFTL helium circulation and auxiliary systems was performed.

From June to mid-August the TEST ZERO graphite structure was installed in the CSPT test vessel, the helium heater was cleaned, a new alumina shroud was installed in heater assembly 2, new gland seals were installed in various bulkhead fittings, and other miscellaneous work was performed.

TEST ZERO was initiated in August 1983 but was halted almost immediately by necessary repairs to the stator of one of the circulator drive motors and the concurrent installation of filler rings in the impeller end

ring for all three circulators. After restart in early October, operation was halted intermittently by problems with the solid-state VFPSs for the helium circulators. Then, at the end of November, a run of about 500 h was halted by plugging of the full-flow helium filter. At year's end, TEST ZERO had been interrupted for the installation of a new helium filter and two new heater assemblies being assembled for the helium heater.

3.2.1 Preparation for TEST F-1

By the end of 1982 the CSPT test vessel, vessel liner, and helium heaters were installed. The loop was pressurized, and the circulators were operated briefly in late December 1982. This was almost exactly a year after the brief operation of the three helium circulators signaled the end of construction of the CFTL Stage Alpha configuration.[2]

In January 1983 installation of the protective circuitry for the helium heater and for the cooling air system for the helium-to-air heat exchanger was completed, and functional testing of the protective alarm and scram systems for both attended and unattended operation was continued.

In February the circulators were operated for 81 h; however, problems with the VFPSs prevented operation of the CFTL in the unattended mode. Assistance from a factory representative for the VFPS, Servo-Optic Systems of Dallas, was required on several occasions.

The control circuitry that accomplishes emergency stopping of the VFPSs was revised to avoid electrical overstressing of the large silicon controlled rectifiers. Overstressing appeared to be a problem with the previous method used to stop the circulators rapidly. In the new method recommended by Servo-Optic Systems, controlled deceleration of the circulators is provided by utilizing internal logic circuits of the VFPSs. Our electrical engineering staff made a concerted effort to attain reliable operation of the VFPSs, and from mid-March to the end of May, the VFPSs were operated without failure.

From February to mid-March, the circulators and associated power supplies sustained a large number of unplanned scrams arising from signals provided by the sensors that measure the film thickness in the circulator thrust bearings. The automatic action associated with the film thickness signal was changed from scram to alarm only.

In a separate experience, with only two of the three circulators in operation, the temperature of the impeller end journal bearing and motor stator in the idle circulator quickly reached design limits as a result of the loss of the forced convection heat transport in the motor cavity. To avoid damaging the idle circulator, all three circulators are stopped when one is stopped, for example, by failure of its power supply. An existing differential pressure sensor, which measures total head for the three circulators, was connected to the protective circuitry; a signal from this sensor scrams the other two circulators when any one of the three is stopped. This signal has provided a very reliable method of protecting all circulators from thermal damage whenever any one of the VFPSs fails.

After assuring that the circulators could be operated for 24 h in the unattended mode (which first occurred on March 10, 1983), the helium heater (which consists of two each 250-kW assemblies)[3] was first energized on March 22, 1983. Just before starting the heater, hydrogen was added to the loop helium in a concentration of about 1000 ppm to protect the molybdenum components of the heater from oxidation due to moisture.

The electrical resistance of the heating elements, which are made of HT grade Moly (molybdenum), increases rapidly with an increase in temperature. Initially, the voltage across the heater was increased, and excess helium flow through the heater flow annulus was used to maintain a low heater helium outlet temperature. However, the excess helium flow reduced the operating temperature of the two heating elements and lowered electrical resistance. Under these conditions higher current was required than the heater power supply could sustain, and the helium heater was scrammed. Satisfactory operation was subsequently achieved by maintaining a constant helium flow that permitted operation of the elements at higher temperatures.

On March 31, 1983, unattended operation was attempted with both the circulators and the helium heater at the specified TEST P-1 conditions. The heater was scrammed within 24 h by low helium heater flow. The helium heater is protected against high temperature by alarm and scram based on high heater helium outlet temperature, low helium flow, and low loop

pressure. In addition, to protect both the test structure and the heater against thermal transients due to the flow of cool helium flow on loss of heater power, the valve that controls this helium flow is closed automatically by a signal of low helium temperature or low heater power.

At that time, the following method was tried to control CSPT operation. The heater potential was controlled by varying the position of the pintle in the motor-operated induction voltage regulator in response to a feedback signal from the heater outlet helium temperature. Loop pressure was controlled with a pressure regulator. Helium temperature was controlled with the 4-MW helium-to-air heat exchanger (HX-1) operated at a load of only 0.25 MW by varying the air blower speed on feedback signal from helium temperature at the HX-1 outlet. This control method was unstable.

A very satisfactory control system was evolved during operation. The heater input voltage was placed on manual control. The loop pressure was governed by supplying helium through an electrically controlled open-shut valve (helium supply valve) by use of an upstream pressure regulator set slightly above loop pressure but below the pressure boundary protection provided by the settings of the high-pressure scram and the relief valve. As the loop pressure decreased by continuous slow venting or a small practically unavoidable helium leak from the loop, a pressure limit switch activated the helium supply valve to increase the pressure to the specified level. This method has satisfactorily maintained the loop pressure within a narrow range above and below the 7.24-MPa specified operating pressure. The temperature of the circulating helium was controlled satisfactorily by partially closing both the inlet and outlet air flow dampers to HX-1 to force the air blower to operate at increased speed where it could be controlled tolerably well by feedback from the helium temperature signal at the HX-1 outlet.

3.2.2 TEST P-1 Shakedown Operation

TEST P-1 was initiated in mid-March 1983 and completed on June 2, 1983. A scheduled shutdown was made to simulate an inspection

of the graphite test structure and to demonstrate the return to normal operation. The CFTL was depressurized, and the two 10-cm (4-in.) observation ports in the CSPT vessel were removed and reinstalled.

During evacuation of the system after closing the ports and before resuming TEST P-1, a large helium leak was discovered in the pressure vessel of circulator 3.* After the circulator rotary assembly was removed, inspection revealed electrical damage of the Ceramaseal bulkhead fitting that accommodates the penetration of three electrical power leads through the pressure vessel closure flange to the drive motor. The short circuit had made a small hole in the weld that seals the fitting to the closure flange. A replacement bulkhead fitting was installed and seal welded to the closure flange.

During this time a small quantity of very fine magnetic black powder was found trapped in drilled holes in the inlet of the impeller front shroud. The powder contained iron and iron oxide, and there was considerable speculation about its source, which was not readily resolved.

TEST P-1 was resumed on May 26, and the specified conditions and levels of gaseous impurities were reestablished. The helium heater operation was discontinued on June 1, and the circulators were manually stopped on June 2 to complete TEST P-1. Leak tests were made of the many compression-type seals in the CFTL pressure boundary before the loop was depressurized. The seals for the circulator and Grayloc flanges were satisfactory for reuse. The seals in the Conax fittings, which accommodate test vessel thermocouples and gas sampling tubes, and in the other Conax fittings, which accommodate the four power electrodes for the helium heater, all leaked excessively and were later replaced in preparation for TEST ZERO. These Conax fittings are located in the top and bottom flange closures for the test vessel.

The circulators had been operated for about 1900 h, and the helium heater had been operated for about 1200 h during TEST P-1.

---

*The circulators are connected in series, and the order of the number corresponds to its position in the direction of flow. The variable frequency power supply for each circulator is identified with a corresponding number.

3.2.? Preparation for TEST ZERO

In June 1983 after completion of TEST P-1, the helium heater was removed from the bottom of the CSPT vessel, and the three-piece liner was removed from the top of the vessel.[4] The filter cartridge was removed from the CFTL full-flow-helium filter, and the rotary assemblies for circulators 1 and 2 were removed from their respective pressure vessels. All these components were visually inspected for the presence of the black powder found previously in circulator 3 during TEST P-1.

Most surfaces were coated with a very light film of black powder that would smudge a white glove. A very small amount of black powder was present on the upstream side of the filter. A similarly small amount was present in the impeller inlet region of circulator 1 and slightly more in the same area of circulator 2. A few particles of powder were visible on horizontal surfaces of the liner and on the helium heater support plates that were exposed to low helium velocity. The total found in all the above components was much less than the 2 mL found earlier in circulator 3.

The 1-m-long alumina shroud tube that surrounds the heating element to form the outer boundary of the element flow annulus was cracked near the top of heater assembly 2, as shown in Fig. 3.2. However, the flow passage appeared to be intact. The heating element (HT molybdenum wire) exhibited a very shiny surface adjacent to the cracks in the alumina shroud tube, as shown in Fig. 3.3.

Near the top of the heating elements for both heater assemblies 1 and 2, the normal separation between helical turns had become altered during operation as shown in Fig. 3.4. The normal separation for several turns was reduced to the point of neighboring turns almost touching, and the three or four turns at the top of the element became more separated than normal. The helical turns of the heating element are supported in threaded grooves in the male alumina mandrels, and each turn normally has a uniform separation from its neighbor. However, several of the grooves at the top of the mandrel had been removed to provide for differential thermal expansion between the molybdenum and the alumina. It is in this area of unsupported turns that the change in separation occurred.

CRNL-PHOTO 7146-83

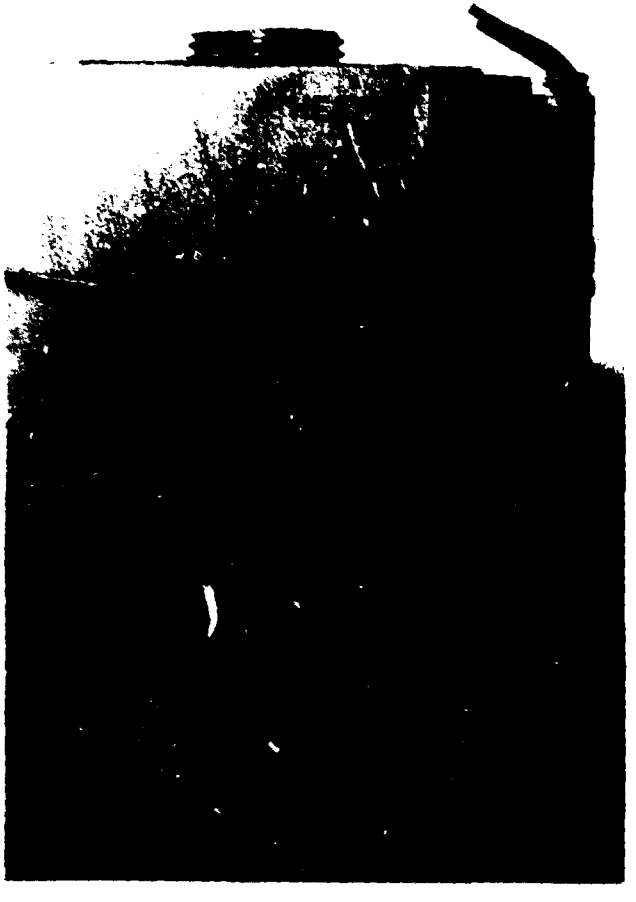

Fig. 3.2. Core Support Performance Test helium heater. Cracked alumina shroud tube for heater assembly 2 after TEST P-1.

ORNL-PHOTO 7142-83

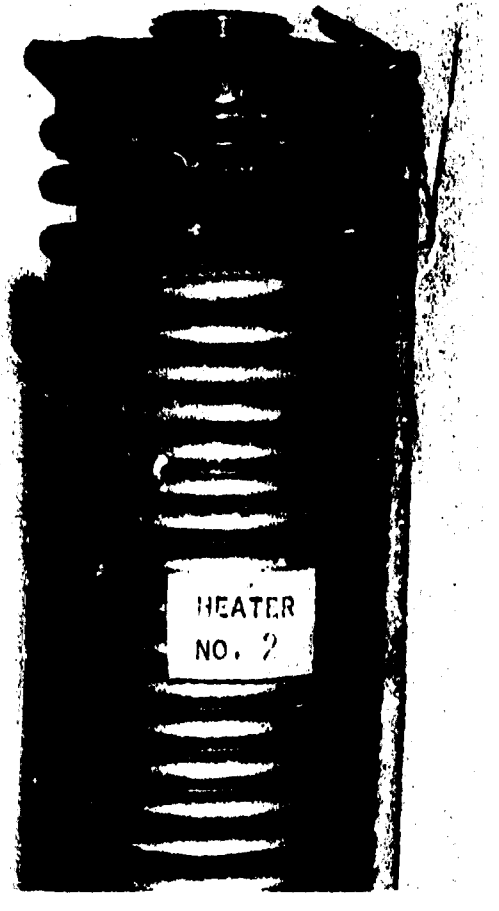

Fig. 3.3. Core Support Performance Test helium heater. Heating element for heater assembly 2, showing normal turn separation near bottom of element, small separation just above the sign, and large separation of turns at the top.

ORNL-PHOTO 7143-83

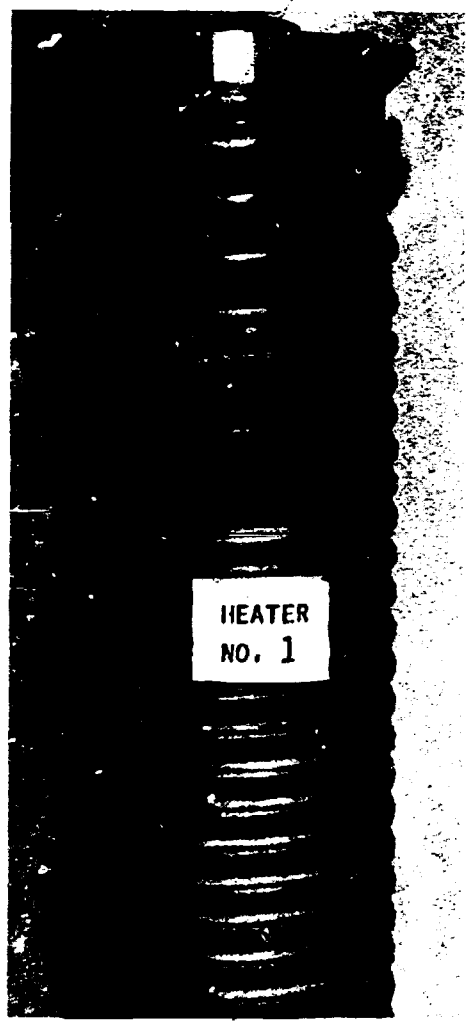

Fig. 3.4. Core Support Performance Test helium heater. Heating element for heater assembly 1, showing same alteration of turn separation as for assembly 2 at end of TEST P-1.

Apparently, during heater operation, arcing between and partial welding of some adjacent turns had occurred in this area, and differential expansion during cooling had increased the separation between the top three or four turns.

Some particles of molten molybdenum apparently were carried up the flow annulus with the flowing helium and then dropped onto the heater support plate. The heater surfaces looked clean, as shown in Fig. 3.5. We decided to repair the heater and reinstall it for TEST ZERO. A new

ORNL-PHOTO 7149-83

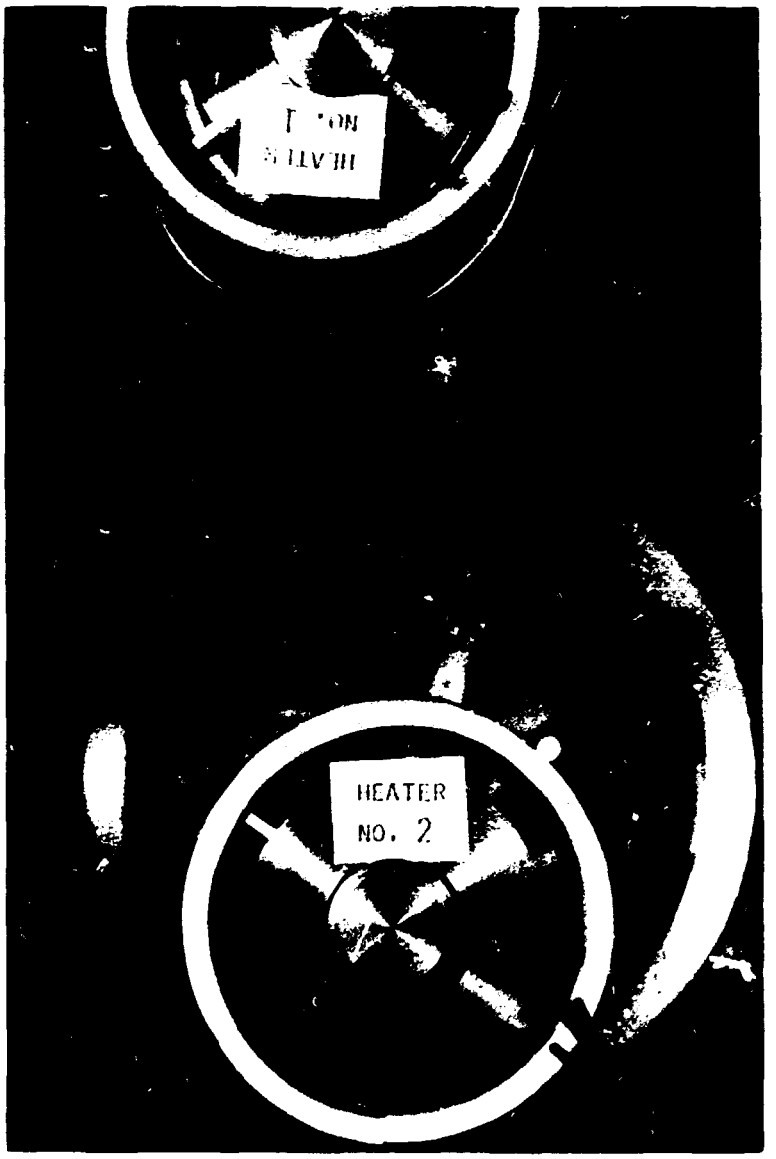

Fig. 3.5. Core Support Performance Test helium heater. Top view of the two heater assemblies that comprise the heater on removal from the test vessel after TEST P-1.

shroud tube was installed on assembly 2. The locations of the junction end of the four thermocouples at the helium exit from each of the two assemblies were repositioned to provide a more uniform indication of helium exit temperature because during TEST P-1 readings of these eight adjacent thermocouples in the gas stream varied by more than 20°C at 700°C operation.

Helium leakage through various bulkhead fittings that penetrate the CFTL pressure boundary became progressively worse during TEST P-1. Crushed boron nitride and crushed lava were used, respectively, as sealants for heater electrode and thermocouple penetrations. As part of the preparation for TEST ZERO, substitute sealants were subjected to testing at full expected pressure and temperature conditions by use of spare bulkhead fittings. Glass-filled Teflon proved to be a good seal for the electrode penetrations, and Viton proved acceptable for the thermocouple and sample tube penetrations. Both were used in appropriate locations for TEST ZERO.

The graphite test structure for TEST ZERO was prepared under the direction of personnel in the Oak Ridge National Laboratory (ORNL) Metals and Ceramics Division. The structure consists principally of four cylinders made from an off-the-shelf Stackpole 2020 graphite. Each piece is 0.201 m (8 in.) in diameter by 0.46 m (18 in.) long and has two axial drilled holes, one at the center and one near the circumference of the cylinder. Six thermocouples are inserted in each hole, and pairs of thermocouples in each hole terminate at each of three different elevations in the structure. A preassembly check was made of the graphite structure as shown in Fig. 3.6.

To quantify the effect of the black powder on the TEST ZERO graphite, 36 samples of nuclear-grade Stackpole 2020 graphite were inserted into an axial slot that was machined in the circumferential surface of the bottom piece of the graphite structure.

The functions of the graphite handling tool were verified with a practice piece of graphite. This piece was inserted into the liner before installation of the liner in the test vessel. Figure 3.7 shows the handling tool during lifting of the practice piece from its cradle. Figure 3.8 shows the practice piece after being lowered down through the liner to a position immediately above the graphite load plate; the two dowel pins are in the graphite load plate.

3.2.4 TEST ZERO Operation

By mid-August the TEST ZERO graphite structure was installed, the pressure boundary was closed, and the preliminary steps required by the

Y-190002

Fig. 3.6. Core Support Performance Test TEST ZERO graphite. Trial assembly of the graphite test structure in the fabrication shop.

ORNL-PHOTO 7240-83

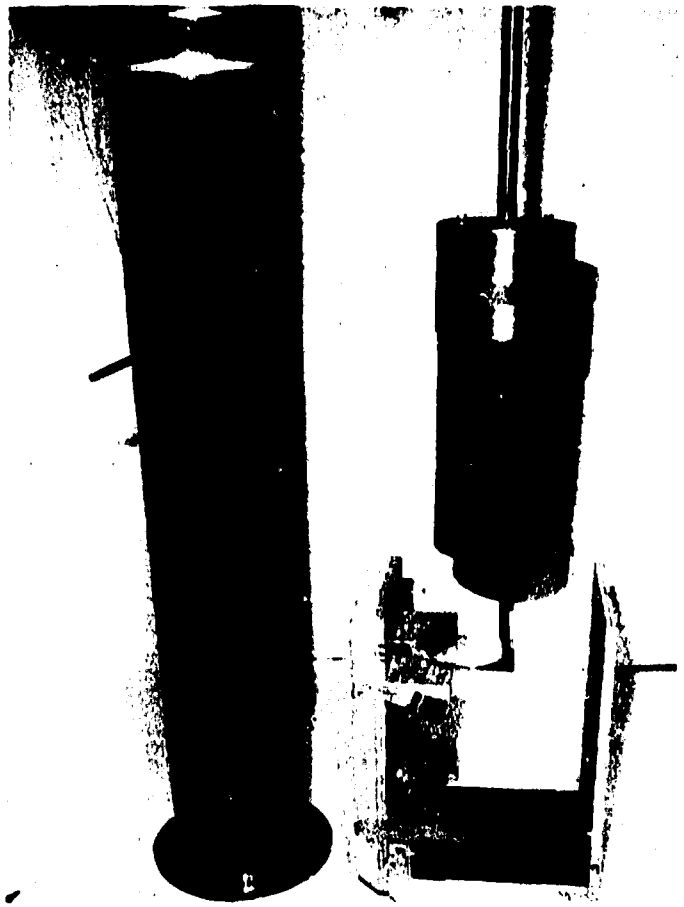

Fig. 3.7. Core Support Performance Test TEST ZERO graphite. *Right*, handling tool used to lift graphite cylinder from cradle. *Left*, view of center section of vessel liner; observation port closure at mid-height of liner.

ORNL-PHOTO 7238-83

Fig. 3.8. Core Support Performance Test TEST ZERO graphite. *Top*, graphite cylinder suspended in center section of vessel liner. *Bottom*, graphite load plate supported on lower section of liner.

specifications for TEST ZERO were begun.[5] Progress was hampered by a large gas leak in the evacuation system across the seat of each of the two isolation (ball) valves that are installed in series and connect the

vacuum pump to the helium circulation system (the loop). We attempted to purchase replacement Teflon seats from the Cameron Iron Works of Houston, the valve manufacturer. The seats were not replaceable, and replacement valves were quoted at $2,500 each and to take several weeks for delivery. Instead, we chose to shut off the two valves at the vacuum pump side with a blind flange following evacuation of the loop.

On August 22, 1983, the circulators were started. After about 5 h of operation, the circulators scrammed. Inspection revealed that the stator winding in the rotary assembly installed in pressure vessel 2 had a short circuit to ground. The assembly installed in vessel 2 at that time was the prototype that had been constructed for circulator development at Mechanical Technology, Inc. (MTI).

It was necessary to heat the motor cooling jacket (made of Inconel) with low-pressure steam to remove the stator, which had been shrink fitted into the jacket. The short circuit had occurred where the stator electrical insulation had been worn by vibration and fretting between the stator and an adjacent corner of the stator iron laminations. The Y-12 Electric Motor Shop rewound the stator, vacuum impregnated it with varnish three times, and baked it after each impregnation for 4 h at 160°C. Epoxy was subsequently added to cover some small chipped places in the varnish observed after delivery. The stator was then rebaked for 24 h at 150°C. It passed high potential and ground megger tests and was reinstalled in the motor cooling jacket.

While repairs were being made to the stator, an examination of other rotary assembly components by the field engineer representative from MTI revealed that some damage had occurred to the interior surface of the impeller end ring, as shown in Figs. 3.9 and 3.10. There was no apparent damage to the impeller or the impeller back plate, and only moderate polishing had occurred on the load surfaces of the diffuser ring. The end ring, back plate, and diffuser ring are stationary surfaces that effectively surround the impeller.

The remaining two rotary assemblies were removed from their pressure vessels, and inspection revealed that similar damage had occurred to both impeller end rings. The cause of the damage and possible remedial

ORNL-PHOTO 7474-83

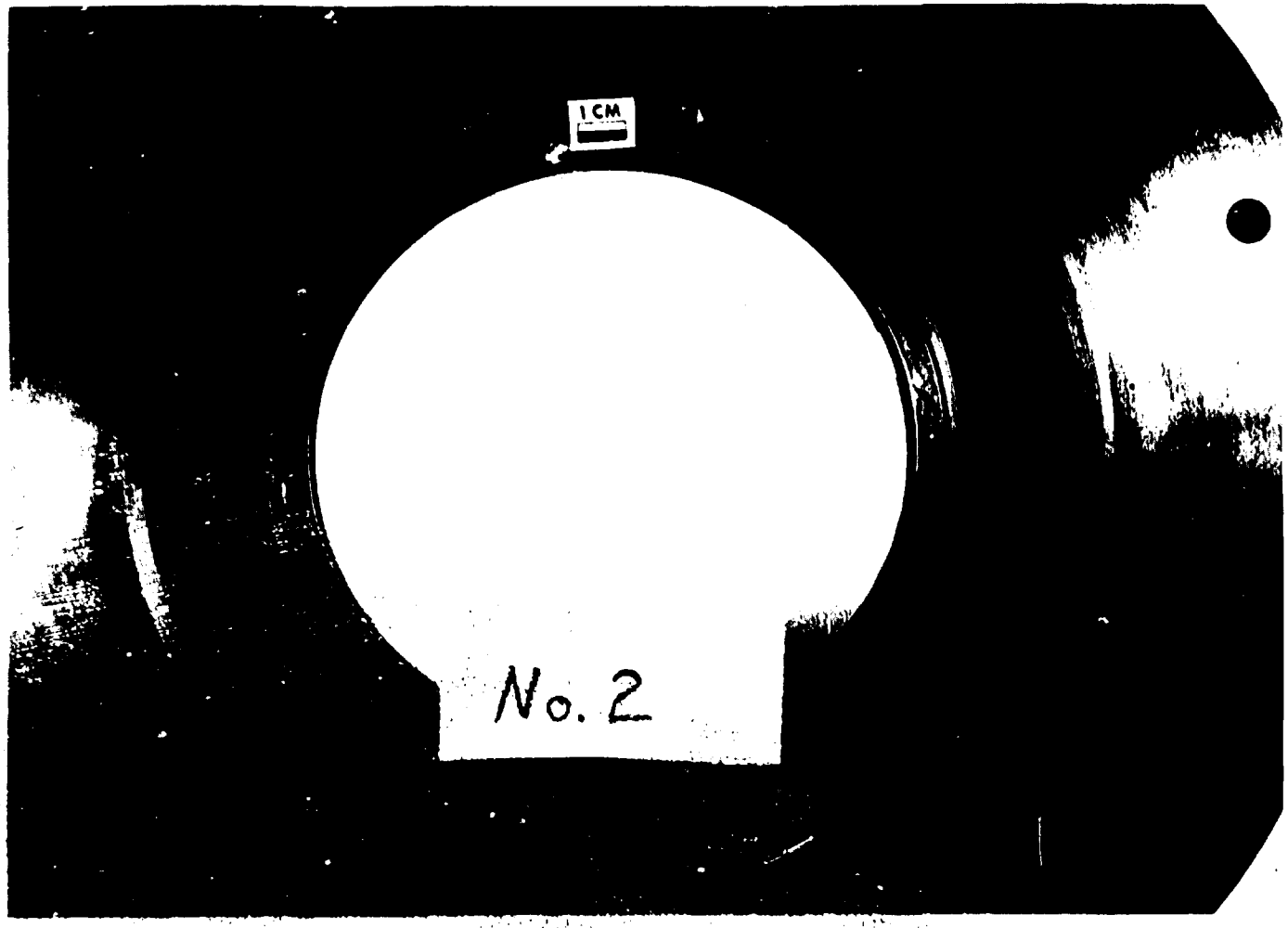

Fig. 3.9. Core Flow Test Loop helium circulator. Corrosion-erosion damage to impeller end ring in rotary assembly prototype.

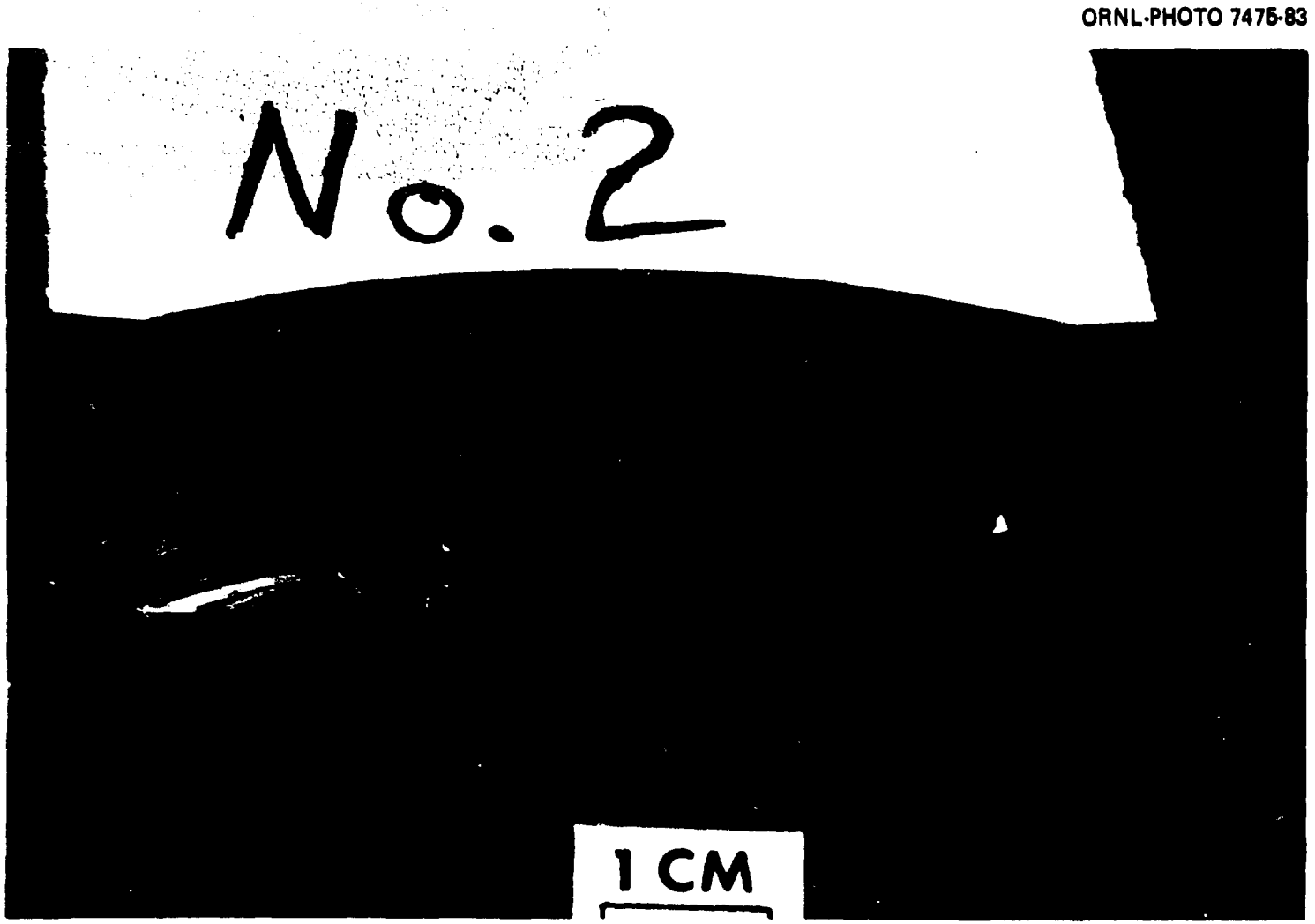

Fig. 3.10. Core Flow Test Loop helium circulator. Closeup of corrosion-erosion damage to impeller end ring.

measures were discussed with MTI and with the Gas Turbine Division of the General Electric Company of Cincinnati, who had experienced erosion of some stationary surfaces in jet aircraft engines.

It was postulated that the impeller motion (tip speed of about 180 m/s (600 fps) produced high-velocity gas in the housing. This gas flow removed weakly adherent oxide particles from the surface of the type 410 stainless steel ring. The freshly exposed metal surface was then corroded by the low concentration of oxygen-containing impurities in the circulating gas to form an oxide surface that was susceptible to subsequent erosion. This developed the marked grooves shown in the photographs.

A twofold approach to eliminating the damage process was adopted. A filler ring made of type 410 stainless steel was installed in the damaged ring of each of the three rotary assemblies. The rings were heat treated to produce an adherent oxide coating. In addition, reservoirs were machined into the reverse side of the rings to provide collection places for remaining particles that may circulate during loop operation. Figure 3.11 shows a filler ring. The curved surface on the filler ring matches the contour of the inlet shroud on the rotating impeller, and there is an axial clearance of about 4.6 mm (0.184 in.) between the ring and the shroud.

Circulator 2 was reassembled with the assistance of a field representative from the circulator manufacturer, MTI. It was operated in air with and without the ring installed. Vibration and acoustic measurements were recorded. The pockets in the ring may have increased the acoustic band somewhat, but the circulator noise was affected little by the ring. All three circulators were operated in air and then installed in their respective pressure vessels.

TEST ZERO was restarted in mid-October, and three runs of 120, 150, and 430 h were experienced from then to the first week in December. Near the end of October, VFPS 1 failed, was repaired, and resumed operation within 4 d. After an additional operation of 150 h, the circulators were shut down manually to accommodate a scheduled 2-d inspection of the three VFPSs by a representative of Servo-Optic Systems, the manufacturer of the power supplies. Six hours after operation was resumed, following 2 d of

ORNL-PHOTO 7513-83

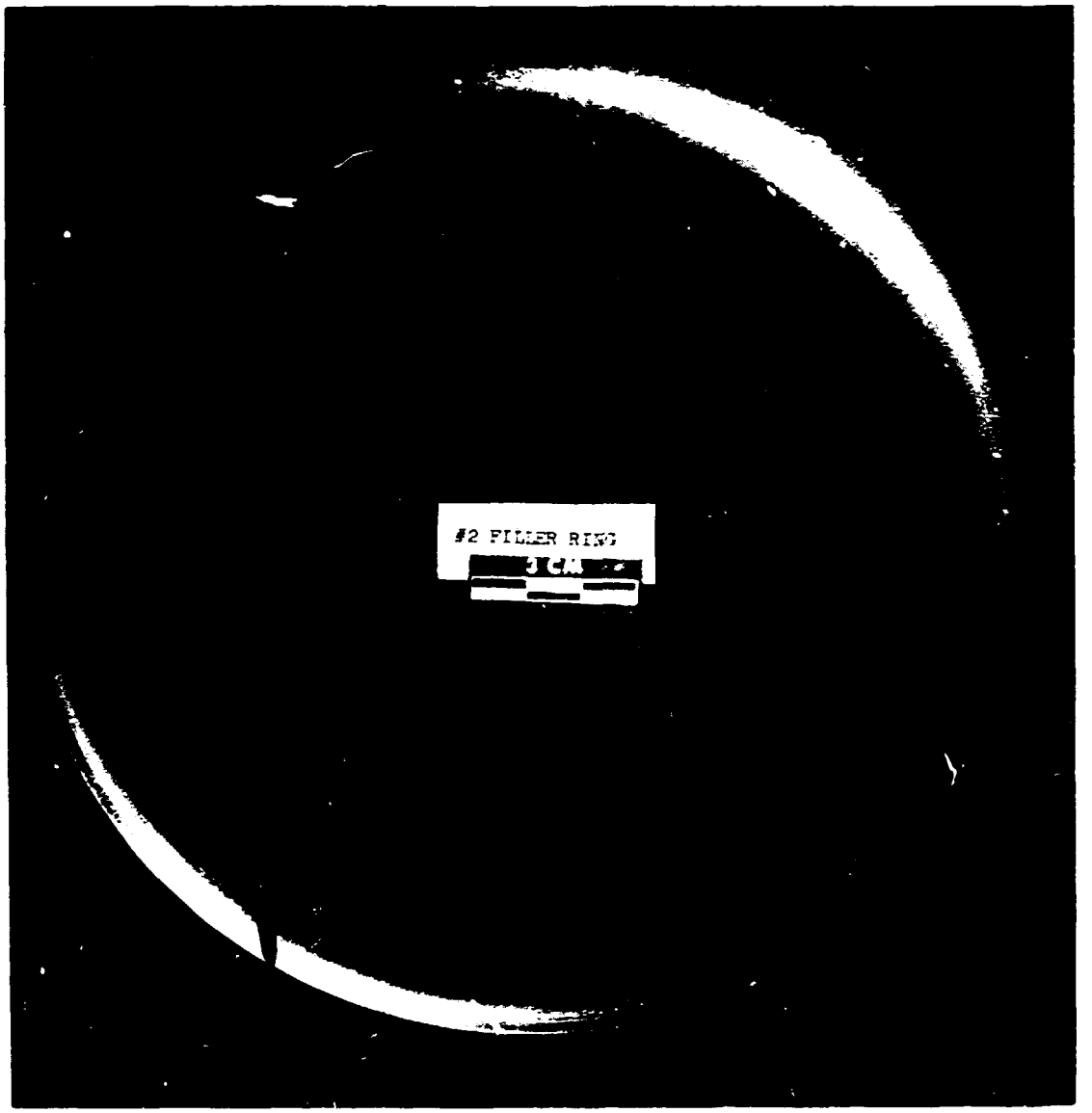

Fig. 3.11. Core Flow Test Loop helium circulator. The filler ring is bolted into impeller end ring to cover existing corrosion-erosion damage and to avoid further damage.

downtime, a fault occurred in VFPS 3; it was repaired, and operation was resumed 3 h later. The circulators were then operated continuously for about 430 h, and the helium heater was operated the last 330 h, when the run was halted by failure of several capacitors in VFPS 3. TEST ZERO operation was resumed on November 30, only to be halted on December 1 by a signal of low helium flow in the path through the helium heater and the graphite test structure.

Initial operation of the helium heater indicated that the calculated heater input power, based on helium flow and temperature rise across the heater, was one and one-half times the measured electrical power to the heater. Two reasons were proposed to explain the anomaly. One was that the temperature measurements provided by the thermocouples at the heater outlet were indicating higher than the actual gas temperature because of thermal radiation from the molybdenum heating element to the thermocouples. The other reason was that part of the helium flow was bypassing the heater and mixing with the heated helium downstream of the heater. Rather than open the CFTL helium system and disassemble the heater to determine the exact cause of the difficulty, the helium heater power was increased from 70 to 115 kW per assembly to provide the required helium temperature to the graphite test structure. The measured helium flow and heater power were then very close to their operating conditions, as determined during TEST P-1, even though the average indicated helium temperature at heater outlet was about 850°C versus 700°C for TEST P-1. The helium heater performed satisfactorily for about 360 h.

The test specification for TEST ZERO requires operation of the helium circulation system (the loop) with controlled concentrations of moisture and hydrogen of 20 and 200 ppm, respectively. The design of the ICS that provides the gaseous concentration control contains a moisture generator (MG) and flow-control valves having a very small flow coefficient C_v. The MG operates at a nominal temperature of 540°C and reacts hydrogen with a copper oxide bed to produce moisture.

Before the ICS is brought into operation, the adsorbed moisture in the loop must be reduced to less than 10 ppm. This was accomplished during near isothermal operation of the loop at about 540°C by a series of venting and filling operations. The loop helium pressure is vented to about half the specified test value and then refilled to the specified value several times with purified helium.

The initial operation of the MG did not produce an increase in the concentration of loop moisture. The MG was then operated in an open cycle mode, isolated from the loop. The hydrogen flow control valve, which has a very small orifice, was found to be partially plugged. Sonic velocity

of helium flow achieved during valve recalibration dislodged the plug. However, shortly after ICS operation was resumed, the capacitors in VFPS 3 failed, halting operation.

After the loop operation was resumed subsequent to replacement of the capacitors in VFPS 3, the flow of helium to the graphite structure began to decrease slowly. The decrease occurred even though constant helium pressure and temperature were maintained and the settings of the two helium flow control valves in the loop remained unchanged. Within a short time, the helium heater was scrammed on a signal of low helium flow. Circulator operation was continued briefly to measure the differential pressure across the full-flow helium filter. The measurement indicated that the pressure drop across the filter was significantly higher than that for the clean filter. The loop was depressurized and cooled to room temperature, and the filter was removed for inspection. A small quantity of black powder, less than 10 cm^3, was removed from the filter. Analysis indicated that it consisted of some iron, iron oxide, iron carbide, and about 33% carbon.

The full-flow helium filter consists of seven filter tubes that operate in parallel flow, each tube 38 mm in diameter (1.5 in.) and 1.1 m long (42 in.) (Fig. 3.12). The filter medium is 200 × 1400 stainless steel mesh that has a particle removal rating of 5 μm mean and 13 μm absolute. The particle removal requirement was recommended earlier by MTI, the circulator manufacturer, to protect the circulator gas-bearing surfaces from damage by small particles from the loop. The pressure drop was measured with air flow for each of the seven tubes, and substantial plugging in all tubes was indicated. Unsuccessful attempts were made to clean the filter, first with steam and subsequently by backflushing with water. A replacement filter was made by joining available filter tubes to a newly fabricated filter tube sheet. The replacement filter was installed into the filter pressure vessel in the CFTL.

Concurrent with the activities associated with the filter, the rotary assembly was removed from pressure vessel 3, and the helium heater was removed from the lower end of the CSPT test vessel.

ORNL-PHOTO 5131-80

Fig. 3.12. Core Flow Test Loop helium filter. Filter cartridge for full-flow helium filter consists of seven tubes that operate in parallel flow configuration.

The filler ring made of AISI type 410 stainless steel, which was installed earlier in rotary assembly 3 to protect the impeller end ring from erosion damage, was inspected. There was no evidence of damage to the filler ring or to the adjacent stationary surfaces that enclose the impeller after about 860 h of operation.

Inspection of the helium heater revealed that the alumina shroud tube around the molybdenum heating element in the heater assembly 2 was broken into many pieces (Fig. 3.13). Some of the alumina mandrel that supports the molybdenum heating element had melted and run out between the molybdenum coils and solidified in the annulus between the heating element and the alumina shroud (Figs. 3.14 and 3.15). The shroud tube on assembly 1 showed faint crack marks. The heating elements for assemblies 1 and 2 appeared to be in good condition. Although there was some discussion about installing new shroud tubes and reusing the existing molybdenum heating elements, the melted and cracked condition of the alumina mandrels made further use of these components undesirable.

Three modified helium heater assemblies that we had planned to use for TEST ONE were delivered in mid-December. Two of these assemblies were diverted to TEST ZERO use to replace the original assemblies. The heating elements in the original assemblies were made of HT grade molybdenum wire having a constant cross-sectional area. Because the electrical resistance of the molybdenum wire increases very significantly with temperature, the hot exit end of the original element generated considerably more heat than did the cooler inlet end. To adjust this situation, the cross section of the wire along the length of the modified element was reduced linearly to increase the heat generation in the inlet region.

Other heater assembly modifications included changing the pitch of the ten coils of the heating element at the outlet end to accommodate differential thermal expansion between molybdenum and alumina. A separate alumina spool to support these ten coils was mounted concentrically on the alumina mandrel that supports the heating element. Adjustable radial tabs were provided at the outlet end to assist in obtaining a more nearly concentric annulus for the helium flow along the heating element.

ORNL-PHOTO 6518-84

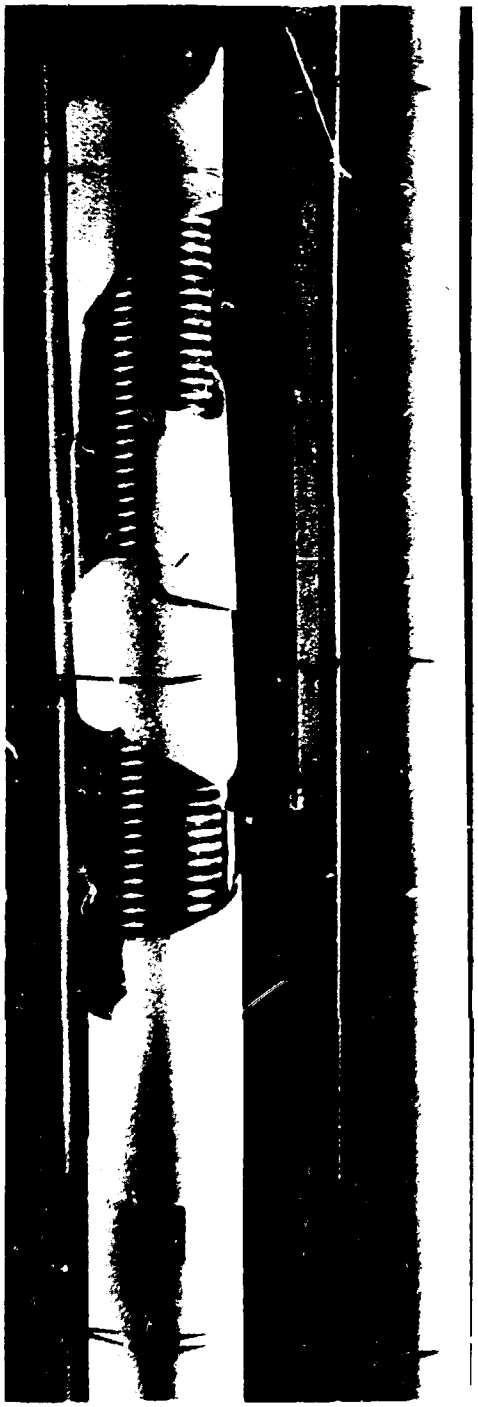

Fig. 3.13. Core Support Performance Test helium heater. Cracked and broken shroud tube in heater assembly 2 after 330-h run in TEST ZERO.

ORNL-PHOTO 6521-84

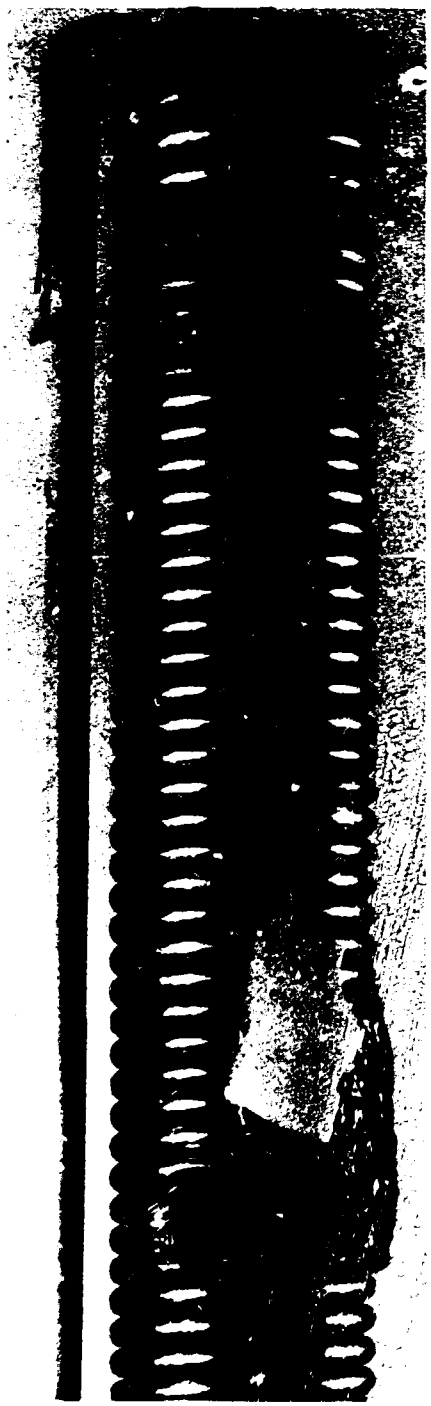

Fig. 3.14. Core Support Performance Test helium heater. Heater assembly 2 with shroud tube removed to reveal heating element. Note large scab of solidified material from alumina mandrel that supports the heating element.

ORNL-PHOTC 5520-84

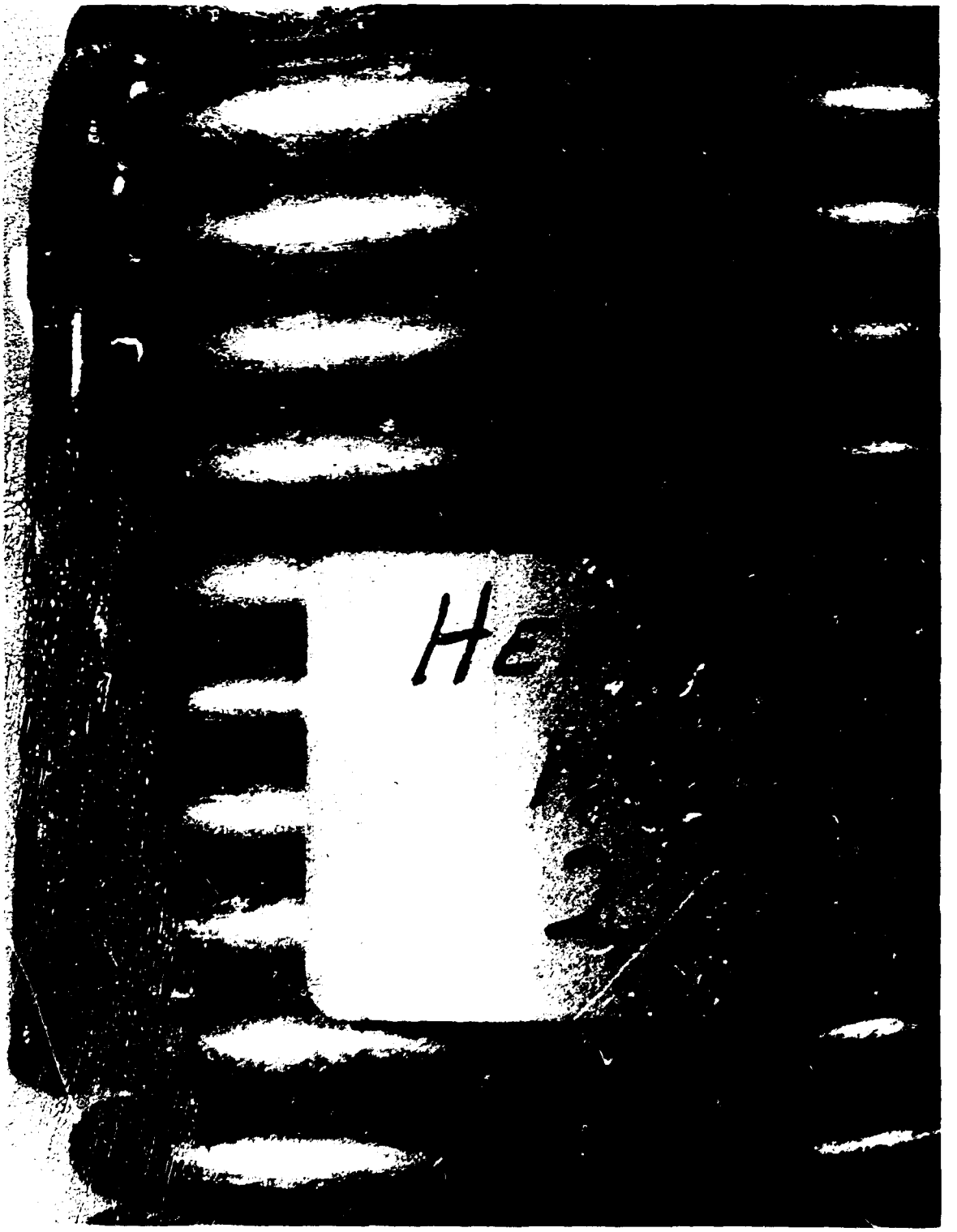

Fig. 3.15. Core Support Performance Test helium heater. Closeup of portion of heating element for heater assembly 2 at end of 330-h run in TEST ZERO. Note scab of solidified material, shiny molybdenum wire, and normal separation between turns in the element.

New alumina shroud tubes were installed, and a layer of stainless steel shim stock was wrapped around the outer surface of each tube. The shim stock should help support the shroud structure in the event the alumina cracks during heater operation and should also help to minimize helium flow bypassing the heating element.

At year's end, the assembly of the helium heater was nearing completion.

3.3 CSPT CHEMISTRY, TEST METHODS, AND SPECIFICATIONS — R. A. Strehlow

TEST P-1 of the CSPT series was conducted in the CFTL from March through June 1983. This section summarizes the operation of the chemical control and analysis equipment and the chemical behavior of the loop, which was of interest in conducting the remainder of the test series.

3.3.1 Objectives of TEST P-1

Of the two objectives of TEST P-1, one was operational, to test the various subsystems of the loop and to design and make any necessary changes that might be needed for subsequent phases of the test series. The other was to determine the chemical behavior of the principal impurities that were to be added or were expected to form during operation of the loop.

Two principal chemical questions were addressed in TEST P-1. One was to determine if the analytical system would permit a satisfactory measurement of the oxidation rate of the graphite test pieces in later tests. The other was to assure that the ICS functioned with adequate dependability.

The oxidation of graphite by water vapor is represented by the equation

$$C_s + H_2O = CO + H_2 \ .$$

Because the water vapor and the hydrogen partial pressures are to be controlled, both the loss of weight and the production of carbon monoxide must be measured in subsequent tests. To measure the carbon monoxide

production, it was necessary to develop methods for measuring leakage and venting flows and the concentrations of critical species. These methods were developed and tested in TEST P-1.

3.3.2 Modification of the Impurity Control System

The original design for the impurity admission system was based on pulsed additions of a fixed volume of gas at a relatively small pressure increment above loop pressure. Because of mechanical problems with the pulsed valves, a design change was made, which substituted manual control valves that had operated successfully in the moisture generation and addition system. The design change also included the addition of high-precision pressure gages to measure the driving pressure so that a range of acceptable operating conditions could be specified.

3.3.3 Tests of the Impurity Measurement System

The impurity measurement system (IMS) as installed for gas analysis consisted of several instruments, including a gas chromatograph, oxygen analyzers, and both electrolytic and capacitance trace moisture analyzers. Calibration methods were tested during TEST P-1. For moisture, a dilute mixture of hydrogen in helium when passed through a heated bed of copper oxide yielded satisfactory results at moisture levels less than 100 ppm (~20 Pa, partial pressure). Analyzed gas mixtures used for the gas chromatograph calibration were useful to assess both the reproducibility of the chromatographic results and their accuracy.

3.3.4 Moisture Generation and Measurement

Controlled moisture addition to the loop was to be accomplished by metering a low flow rate of a helium hydrogen mixture into a stream of helium flowing continuously through a heated copper oxide bed and then to the loop. The flow rates of the helium and the mixture containing hydrogen were intended to be a part of the normal makeup addition of helium.

3.3.5 Leak Rate Measurement and Significance

It is necessary to have two independent measures of the graphite oxidation rate. One is to determine the total amount of carbon monoxide

produced; the other is to weigh the specimens before and after the exposure. Because the amount of carbon monoxide produced is the product of its concentration and the total of leak and venting flows, the total flow from the system must be measured. By adding a quantity of argon and measuring its change of concentration with time while operating the loop with makeup of helium to maintain a constant total pressure, a good measurement of the total leak and venting flows could be achieved. This method was satisfactory.

3.3.6 Chemical Behavior of Loop

The chemical uncertainties of the loop operation during TEST P-1 were those associated with the measurement of the oxidation rate in later tests and with the compatibility of loop components relative to the gaseous impurities.

Among these questions, the chemistry of carbon monoxide is related to the carbon monoxide shift reaction and the disproportionation to carbon and carbon dioxide. We assumed that the disproportionation reaction would occur at a low rate compared with other reactions because the reaction is favored only at low temperatures, at which the reaction rate is low.

Consequently, the main chemical concern was directed to determining the possible role of the carbon monoxide shift reaction, that is, the reaction of water vapor with carbon monoxide to form hydrogen and carbon dioxide

$$H_2O + CO = H_2 + CO_2 \ .$$

The reaction is temperature dependent, being more favored in the forward direction at lower temperatures. The extent of reaction may be described in terms of the equilibrium constant $K(p)$

$$K(p) = p[H_2] \times p[CO] / \left| p[H_2O] \times p[CO_2] \right| \ .$$

This constant has a value of about unity at the temperatures designed for the test series and about 30 at the lowest temperatures of a gas volume

element in the loop. This could have made conduct of the test difficult, because it might have been necessary to use a higher loop venting rate than desired for maximum data quality or economy of operation. Experiments conducted showed that the steady-state position for this reaction agreed with the expected value for the temperature of the graphite specimens planned for the tests.

A second chemical uncertainty existed with regard to the chemical compatibility of the oxidizing gas mixture with the hot molybdenum heater wire in the gaseous mixture. Preliminary calculations showed that, at the design hydrogen-to-water ratio of more than 10, molybdenum should not corrode at an apprecible rate. Observation of the heaters following the test indicated that no significant corrosion of the molybdenum had occurred.

3.3.7 Specifications for Subsequent Tests

Draft specifications were prepared and developed in cooperation with A. G. Grindell, Engineering Technology Division, for both of the subsequent phases of the test series, TEST ZERO and TEST ONE.

3.4 CSPT ELECTRICAL DESIGN AND INSTALLATION — T. L. Hudson and E. M. Lees

The controlled power supply for the helium heater was operated satisfactorily, and the associated protective circuitry was calibrated. The circulator power measurement was improved. Operation of the three VFPSs for the helium circulator motors was initiated. Substantial effort was devoted to obtaining reliable operation of the VFPSs, and it appears that additional effort will be needed. Installation design for two additional 500-kW power supplies for the helium heater was completed.

The 500-kW power supply and control system for the helium heater was operated satisfactorily at about 50% of design capacity with a water-cooled resistive load. The system was then connected to the helium heater and operated satisfactorily.

The power measurement systems for the VFPS that provided electricity to the circulator motors were changed from a voltage loop to a current loop to reduce electromagnetic interference (emi) noise on the indicators.

After this and some other minor changes were made, there was an improvement in the power measurements at the circulator control cabinet.

More than a dozen failures of the VFPSs occurred during the year, and a number of approaches were used to achieve reliable operation. The method of stopping the circulators was revised to obtain a powered deceleration by use of logic circuitry internal to the VFPS rather than by the previous unpowered, free coastdown of the circulator during a scram. The unpowered stop subjected the VFPS components to undesirable electrical stresses. Preventive maintenance and a variety of tests were performed on the VFPSs by a field engineer from Servo-Optic Systems of Dallas, the VFPS manufacturer. Tubular heaters were installed inside each VFPS cabinet; when the VFPSs are not in operation, the heaters are energized to retard the condensation of moisture, which can have deleterious effects on VFPS components.

After each maintenance or repair effort, the VFPS is subjected to a proof test before being reconnected to its circulator motor. In the proof test, the VFPS is operated near design load for at least 8 h connected to a water-cooled resistive device.

Despite these efforts, the extended period of continuous operation required by the CSPT test specifications has not been achieved. Assistance is being requested locally and from Servo-Optic Systems.

The installation and control drawings were issued for two additional 500-kW heater power supplies, which would make available three 500-kW controlled circuits. The three units could provide up to 1.5 MW of controlled power for heating helium in the CFTL. As many as six 250-kW heater assemblies, the maximum number the present helium heater design can accommodate, could be supplied. All the required equipment is on hand; the installation activity has been delayed until funding is available.

3.5 CSPT MECHANICAL DESIGN — C. J. Claffey, W. R. Clark, P. L. Goranson, and W. A. Hartman

3.5.1 TEST ZERO Graphite Test Structure

The graphite test structure for TEST ZERO consists of four right-circular cylinders with flat ends. Each cylinder is 195.7 mm (7.704 in.)

in diameter and 457 mm (18 in.) in length. These cylindrical specimens are stacked end-to-end in the test section as shown in Fig. 3.16. Threaded graphite alignment buttons are screwed radially into the outer surface of the cylinders to assure a uniform annular flow passage for helium between the outside of the graphite cylinders and the inside of the test section liner. The stacked graphite cylindrical test specimens are doweled together and are provided with matched longitudinal holes for insertion of thermocouples.

The discovery of significant amounts of powder containing iron in the loop at the shutdown following TEST P-1 made it essential that iron-free graphite samples be installed for TEST ZERO so that the effect of this powder on the test results could be determined. A drawing was prepared to modify the upstream test piece by machining a slot along its length for the installation of 36 nuclear-grade Stackpole 2020 graphite inserts.

3.5.2 TEST ZERO Load Post

A thermocouple guide and specimen hold-down load post was installed on top of the stack of graphite test specimens as shown in Fig. 3.16. The load post serves to apply sufficient weight loading to assure positive contact between the cylindrical specimens. The load post also serves as a guide for thermocouples that enter the test vessel through the top head and pass downward into the graphite specimens.

3.5.3 TEST ZERO Graphite Handling Tool

A special handling tool was designed and built for manipulating the graphite specimens in the shop during their fabrication. This tool was later modified and adapted for use in installing and removing the graphite specimens in TEST ZERO. The tool includes provision for precise control of axial position and azimuthal orientation of graphite specimens.

3.5.4 TEST ZERO Load Post Handling Tool

A special tool was designed and built for installing and removing the thermocouple guide and specimen hold-down load post for TEST ZERO.

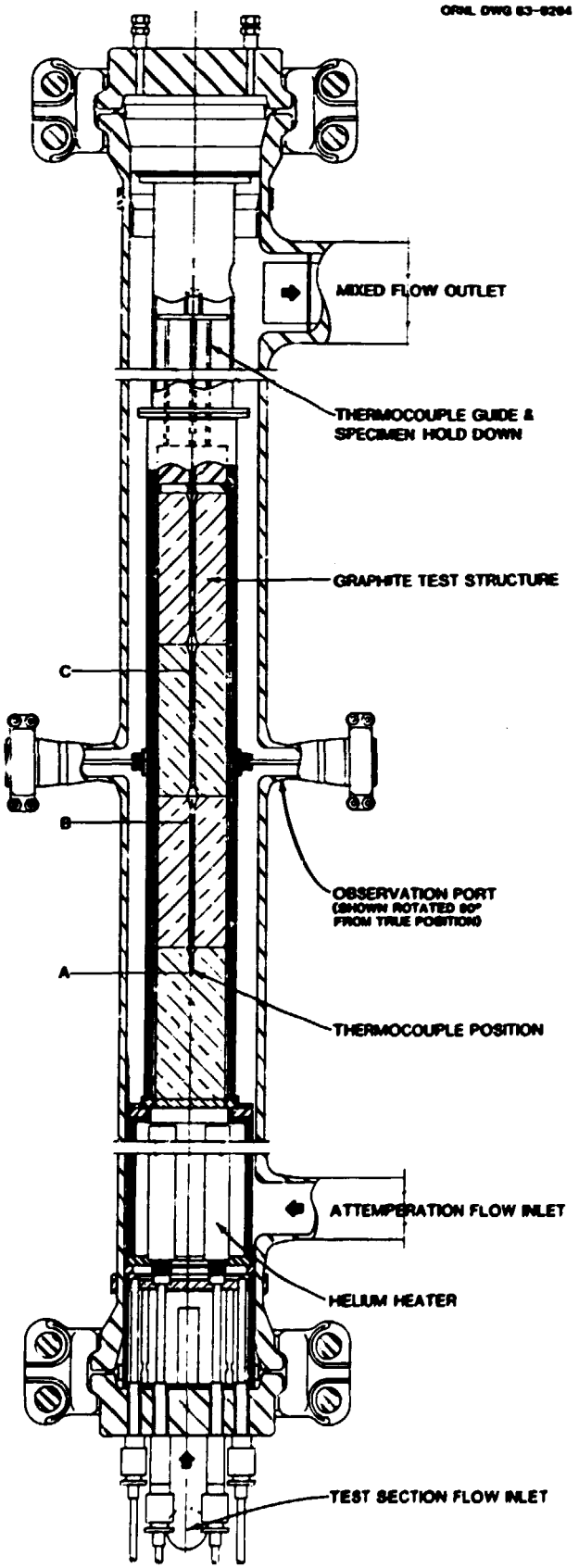

Fig. 3.16. Core Support Performance Test TEST ZERO test vessel and internals.

3.5.5 TEST ONE Graphite Test Structure

The graphite test structure for TEST ONE consists of five test pieces arranged as shown in Fig. 3.17. Four of these test pieces are 483 mm (19 in.) long, and the piece located at the bottom of the test section is 127 mm (5 in.) long.

The four upper test pieces have spherical end surfaces. The concave upper surfaces have a 160.3-mm (6.311-in.) radius. The radii of the lower convex surfaces range from 140.2 mm (5.520 in.) to 152.0 mm (5.984 in.). The bottom piece has a concave upper surface of 160.3 mm (6.311 in.) and a flat bottom surface.

Each of the four upper pieces has sections of two different outside diameters. The upper section of each is 200.7 mm (7.900 in.) in diameter, and the lower section of each is 193.0 mm (7.600 in.) in diameter. The short bottom test piece is 200.7 mm (7.900 in.) in diameter for its full length.

Each of the four upper test pieces has six alignment buttons for maintaining concentricity between the test pieces and the surrounding test section liner. This assures uniform annular flow of helium over the external surfaces of the test pieces. These spacing buttons are threaded radially into the outer surface of the cylindrical test pieces and are arranged with three buttons in each of two horizontal planes. The short bottom test piece has three spacing buttons in a single horizontal plane.

Each of the four upper test pieces has two additional buttons at about the midplane location. These buttons straddle a longitudinal rail attached to the inside of the test section liner. This rail prevents azimuthal rotation of the test pieces during insertion and dummy operation. The short flat bottom test piece at the bottom of the test section is prevented from rotating by doweling into the bottom support plate. One of the four upper test pieces is a composite of V-483-T2 graphite from Kernforschungsanlage in Jülich, Federal Republic of Germany, and the nuclear-grade Stackpole 2020 graphite. The two parts are held together with a threaded graphite stud.

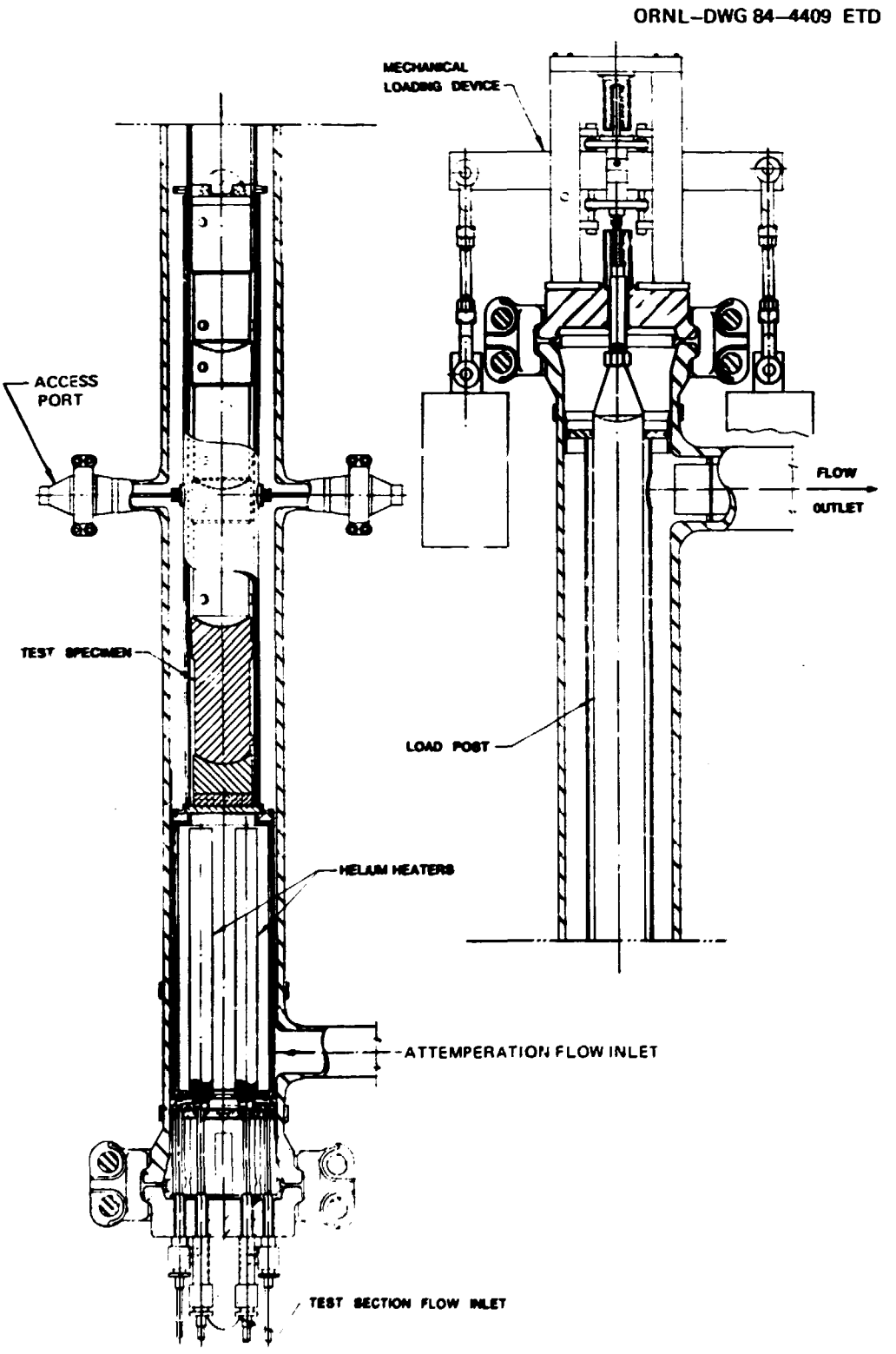

Fig. 3.17. Core Support Performance Test TEST ONE assembly.

3.5.6 TEST ONE Structural Loading Device

In the original conceptual design for TEST ONE, a bellows was to be used to supply pneumatically the 70-kN (15,000-lb) loading force on the test structure. The cooler inlet gas flow was to be introduced around this bellows, which limited its design temperature to 425°C (800°F). This gas was then to be heated in a recuperative heat exchanger by the hot gas leaving the test section.

The limitation of funds plus the lowered maximum temperature for TEST ONE resulted in the decision to delay the installation of the recuperative heat exchanger and its associated complex liner. For TEST ONE, the flow configuration for TEST ZERO will be maintained. This decision resulted in difficulties in designing the flow baffles to limit the temperature of the bellows. These difficulties were further complicated when modifications were made to accommodate the "soak-back" situation following a loss of helium flow.

A final decision was made to incorporate a deadweight loading system that eliminates the need for an elaborate pressure control system required to maintain a constant load during pressure changes in the loop. The deadweight loading system is shown in Fig. 3.18. The weight is external to the test vessel, and the force is transmitted through a bellows seal that is similar to a valve stem seal. A counteracting bellows at loop pressure compensates for variations in system pressure.

A trip was made to the EG&G Sealol Plant in Providence, Rhode Island, to witness and approve the leak testing and pressure testing of the bellows assemblies for the TEST ONE loading device. Leak testing was performed on each of the four bellows, both before and after pressure testing. Each bellows was subjected to a static pressure test in both free length and compressed conditions. Each bellows was additionally subjected to a cyclic test under external pressure for 100 cycles from free length to full compression. The test pressure (external) was 8.62 MPa gage (1250 psig), and the compression stroke length was 30.2 mm (1 3/16 in.). The leak test criterion was no evidence of helium leakage at a sensitivity of 1×10^{-9} std cm^3/s. All tests were satisfactorily completed.

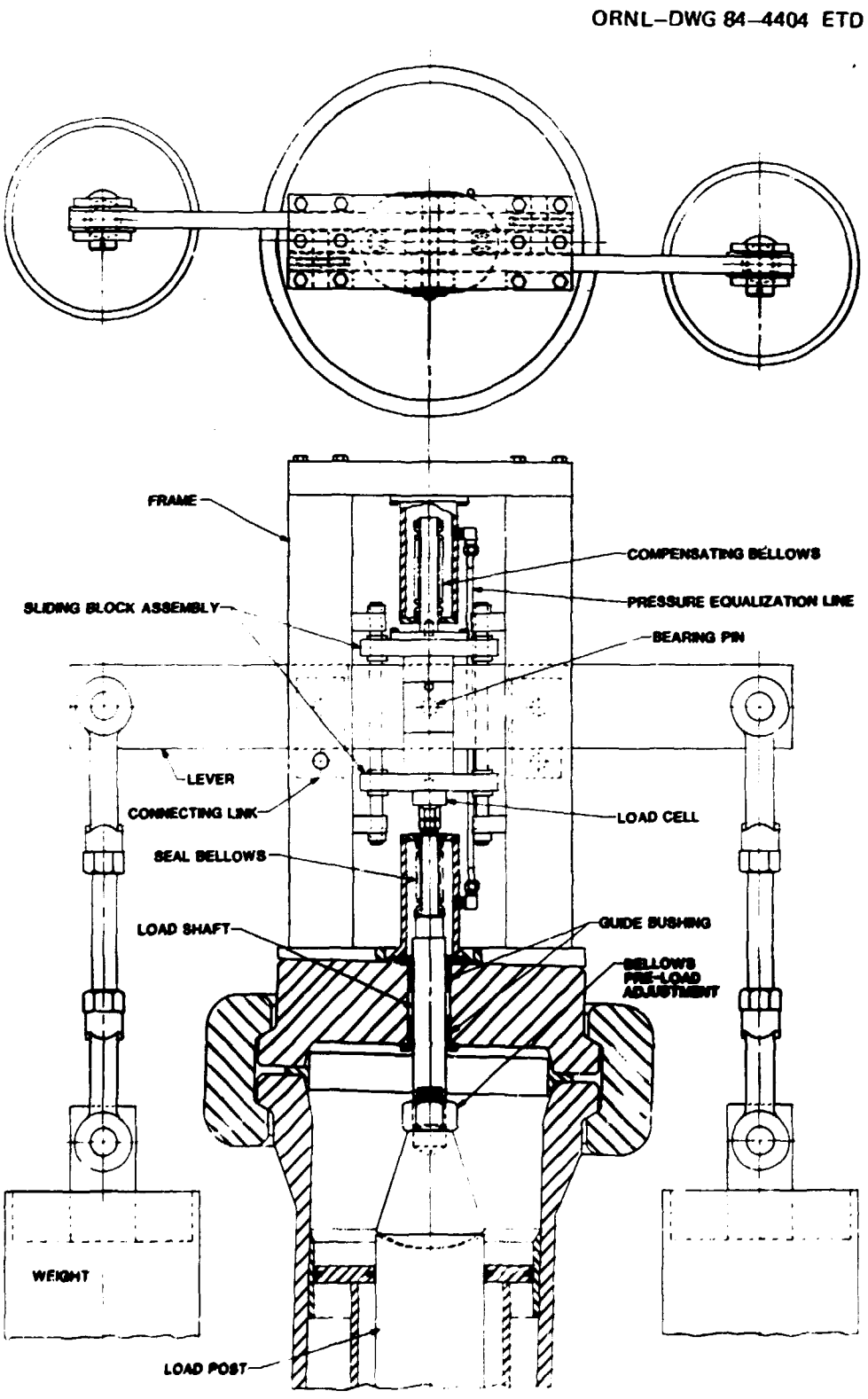

Fig. 3.18. Core Support Performance Test TEST ONE mechanical loading device.

3.5.7 TEST ONE Graphite Handling Tool

A special handling tool was designed and constructed for installing and removing the graphite specimens in TEST ONE. In principle, this handling tool performs the same function as the handling tool that was used for TEST ZERO. The only significant differences are those required to adapt for the special geometry of the TEST ONE specimens.

3.5.8 TEST ONE Test Section Liner Modification

After consulting with shop personnel, a drawing was prepared to show the necessary machining operations to be performed on the test section liner after completion of TEST ZERO and before initiation of TEST ONE. This modification to the liner is required to assure true cylindricity of the inside bore of the liner. This higher degree of dimensional quality is required in TEST ONE to minimize the adverse effect of misalignment of the articulated graphite specimens under a substantial compressive load.

A new feature to be added to the liner for TEST ONE is the longitudinal rail that will engage buttons on the graphite test pieces and thus prevent azimuthal rotation of the test pieces.

3.5.9 TEST ONE Pressure Vessel Modification

Some modification of the test vessel pressure boundary is required for TEST ONE. The type and quality of new materials used in this modification must be certified under the rules of the *ASME Boiler and Pressure Vessel Code*. Because of long lead times often encountered in procuring such materials, an advance bill of material was issued before drawings were issued for construction.

3.5.10 TEST ONE Stress Calculations

Calculations were completed for the bending moment and the resulting stress in the TEST ONE test section liner. The bending moment is the result of the inherent misalignment of the articulated stack of graphite specimens under a compressive load. For conservatism, the worst (loosest) combination of dimensions was used for the graphite parts. The adverse

effect of differential thermal expansion between the stainless steel liner and graphite specimens was also included in the results. The bending stress was found to be well below the accepted *ASME Pressure Vessel Code* (Sect. VIII, Div. 1) allowable stress for type 304 stainless steel at 760°C (1400°F).

Stress calculations were also performed for the stainless steel support plate at the bottom of the graphite test structure in TEST ONE. It was shown that the plate would safely sustain the combination of weight loading plus the load applied by the external loading device.

3.5.11 Helium Heater Design

A study was made to determine how many heater rods could practically be incorporated into the current test vessel with the helium heater flow inlet nozzle located in the lower Grayloc blind hub. Ideally, the six heaters originally planned when the flow inlet was at the upper end of the vessel would be retained. Layouts of six-heater, four-heater, and three-heater bundles were prepared, and the fabrication, assembly, and cost considerations were studied. The three-heater bundle with an installed helium heating capacity of 0.75 MW was selected because of (1) anticipated fabrication problems with six or four heaters and the flow inlet through the same hub, (2) the adaptability of the currently used Grayloc hub to the three-heater design, and (3) the availability of alumina and molybdenum materials needed for the three-heater bundle.

The disassembly of the helium heater after the completion of TEST P-1 revealed some broken alumina components and also evidence of arcing between adjacent turns of the heater element. The arcing was confined to a part of the coil near the hot end of the heater, where the grooves in the alumina core had been machined away to permit the coil to compress and accommodate differential thermal expansion. A high priority was assigned to developing a design change for TEST ONE heaters to eliminate this arcing. A concept was used in which a portion of the heater element is wrapped on a greater than normal pitch but is restrained from contacting adjacent turns by an alumina core piece having larger grooves on a larger pitch.

An additional feature of the new heater design is a tapering of the molybdenum wire to compensate for the lower electrical resistivity of the molybdenum at the inlet (colder) end of the heater. This tapering is obtained by grinding a conical surface on the outside of the coil after it is wound on the alumina mandrel.

A visit was made to Thermo Electron Company (TECO) in Wilmington, Massachusetts, to discuss the fabrication of these modified heaters. The TECO representative agreed that fabrication was feasible. Subsequently, an order to perform the work was initiated and sent to TECO with approved drawings of the modified design.

3.5.12 Helium Circulator Heat Shield

A special heat shield was designed and built for insertion into any one of the pressure vessels of the three helium circulators when its rotary assembly is removed and operation is continued with the other two circulators. This heat shield is required to protect the closure flange seals from excessive temperatures developed by thermal convection from the circulating helium.

3.5.13 Mobile Work Platform

A mobile work platform was designed primarily for providing access to the test section at the level of the observation ports.

3.6 CSPT INSTRUMENTATION AND CONTROLS — S. C. Rogers

Engineering assistance has been provided by Instrumentation and Controls Division (I&C) personnel for operations support and instrument maintenance during the past year. Concurrent with loop operation but mostly during intermittent periods of loop downtime, efforts were made to upgrade the capabilities and performance of the loop instrumentation and to solve problems associated with the vortex shedding flowmeters, electromagnetic noise, data acquisition system, impurity measurement system, and the impurity control system. All improvements to the loop instrumentation scheduled to be completed before initiation of CSPT TEST ZERO were accomplished, and the CFTL instrumentation is, with little

exception, fully operational and reliable. Additionally, the I&C supplement to the CFTL-CSPT Quality Assurance Plan was completed, and preparation of the CFTL I&C Operations and Maintenance manuals was begun.

3.6.1 Loop Instrumentation Modifications

Many measurement and control system design changes and maintenance actions were implemented to improve the performance and reliability of the CFTL operations. These changes include:

1. Addition of a diagnostic program (scram-catcher) to monitor the protective interlock logic in the programmable logic controller (PLC) and to identify the out-of-limit conditions causing system scrams.

2. Design and implementation of PLC interlock logic that scrams the circulator when the VFPSs fail because of blown fuses in the conductors supplying motor current. This interlock initiates a scram if the total differential pressure measurement across all three circulators falls below a predetermined value.

3. Revisions to the scram interlock logic of the PLC so that, upon an out-of-limits signal associated with the heater power supply, a heater Scram B is initiated. Scram B is a partial scram that allows the helium circulators to continue to operate while actions are taken to shut down the helium heaters and preserve, to the extent possible, thermal conditions in the loop. This is in contrast to a Scram A, which shuts down the entire loop.

4. Reprogramming of the PLC so that the scram-catcher display is activated on a Scram B (helium heater) in addition to being activated by Scram A (heating, cooling, and circulation).

5. Installation of jumper switches, which allow certain interlocks to be bypassed without making software changes that require shutting down the loop. The circulators, circulator power supplies, heater power supply, Scram A, and Scram B interlocks may be bypassed during loop operation by simply closing the appropriate switch on the control panel. Any bypass condition is indicated plainly on the CFTL main control boards.

6. Revisions to the electrical interlock circuits controlling each of the three circulator VFPSs. These revisions, which altered the method

of executing the circulators START/STOP commands, were made on the advice of the Servo-Optic Systems, Inc., engineering representative in an effort to prevent power supply malfunctions.

7. Recalibration of the VSFMs to extend the measurement ranges required by revised operating conditions.

8. Continuous recalibration of temperature and flow limit switch actuation setpoints to accommodate the ever-changing operating flow rates and temperatures.

9. Upgrade of the loop resistance temperature devices (RTDs) that measure circulator exit helium temperatures, test section exit helium temperatures, and heat exchanger exit helium temperature, from 0 to 400°C to 0 to 600°C.

10. Design and implementation of a means to control loop helium temperature automatically within the desired operating limits. This is accomplished by restricting cooling air flow to the heat exchanger and automatically controlling the fan speed, based on the measured circulator inlet helium temperature.

11. Design and implementation of a scheme whereby a pressure limit switch is used to control the carrier helium gas supply valve to maintain loop pressure within desired limits. This method automatically compensates for the leakage by adding helium when the pressure drops below the specified operating condition.

12. Procurement and installation of five precision bourdon-tube pressure gages at strategic locations in the loop.

13. Installation of a digital temperature indicator to indicate inlet and outlet helium temperature of each helium heater and the heat exchanger helium outlet temperature.

14. Modification of the Metrascope graphic, multichannel temperature indicator grounding circuits, which eliminated the noise problems previously experienced by the displays.

15. Correction of the circulator power supply measurements. After wiring errors were resolved, these indications function properly.

16. Fabrication and installation of thermocouple assemblies to measure test piece graphite temperature.

3.6.2 Vortex Shedding Flowmeters

Specially developed VSFMs are used to measure the total loop helium flow (FE-11), the test section heater helium flow (FE-4), and the attemperation flow (FE-7). Flowmeters FE-11 and FE-4 have experienced random periods of unacceptable noise on the output, and FE-7 has had even greater continuous noise to the extent that it is useless. Much effort was spent investigating these problems, and several corrective actions were taken.

All field wiring and interconnections were inspected, and the individual electronic signal conditioning circuits were verified in the laboratory. Sensor excitation levels were elevated to increase sensitivity, and spare sensing elements were installed, but none of these actions improved performance.

After consulting with the manufacturer, Neptune-Eastech, attention was focused on the susceptibility of the VSFM to disturbance by temperature variation and emi. Water-cooled chill blocks were designed, fabricated, and installed on the VSFMs to stabilize their temperature within the manufacturer's recommended range of operation. To reduce emi effects, ferrous conduit was installed in addition to other shielding and grounding modifications, and transformers were inserted in the VSFM power lines. These actions stabilized the outputs of FE-11 and FE-4 during normal steady-state operation, but they had no apparent effect on the sporadic output of FE-7.

The improvements made to the VSFM systems were comprehensive, and further improvements would require consideration of a redesign effort to provide more reliable tracking and processing of the small (a few millivolts peak-to-peak) vortex shedding signal. A redesign effort could be considered in three areas:

1. Review and possible improvement of the circuitry that tracks and processes the vortex shedding signal and transmits a 6-V (peak-to-peak) square wave signal from the process to the frequency-to-voltage converter circuit in the control room.

2. A decrease in the lengths of the two tubes that transmit the vortex pressure variations from the process pipe to the sensor. These tubing lengths are now about 76 mm (3 in.), and a shorter length would be expected to provide a stronger and therefore more reliable vortex shedding signal to the sensor. Shorter tubing lengths would, of course, move the sensor and electronics closer to the elevated temperature of the process piping, but, with the water cooling now installed on the sensor blocks, a shorter tubing length might be acceptable.

3. The use of a new bluff body configuration. One of the latest developments in the VSFM field addresses the problem of reliably detecting small vortex shedding signals.

3.6.3 Electromagnetic Noise

Large-amplitude (0.4- to 0.6-V, peak-to-peak), high-frequency (1-MHz) noise characteristic of phase-fired silicon controlled rectifier power controllers were found on thermocouple and other higher level signals throughout the CFTL. This noise was reduced but not completely eliminated by liberal application of capacitor filtering. Fortunately, the residual noise is beyond the response capabilities of most of the measurement and control instruments used in CFTL and thus causes no significant problems.

Thermocouples located near the helium heaters are subjected to high levels of 60-Hz noise that increases with the helium heater power. Those signals read at the data acquisition system (DAS) are partially filtered by large capacitors at the thermocouple patch panel, and the noise is further reduced by internal multiplexer passive filters. Finally, the effects of 60-Hz noise is virtually eliminated by sampling the signals over an integral number of cycles. Real temperature fluctuations induced by the turbulence of the gas flow remain. This was verified when a system scram activated a fast scan routine that provided useful information concerning divergence and fluctuations of the thermocouples that indicate the outlet gas temperatures at the heater helium. The divergence and fluctuations remained after loss of heater power. As the flow decreased (valve closing) and heater temperature was lowered, the "noise" was reduced, and thermocouple indications uniformly converged. On startup, the indications again

diverged to the previous levels. Thus, the discrepancies existing in this set of thermocouples then appeared to be caused by thermal flow effects and not by emi.

When the test structure for the CSPT TEST ZERO was installed, it was hoped that its support plate would produce better mixing at the heater exit and resolve discrepancies in the multiple-temperature measurements at that location. This was not the case, however, and thermocouple expert R. L. Anderson was asked to discuss the cause of the problems and to formulate possible solutions. The existing thermocouples were taken to the laboratory for examination. Replacements utilizing Inconel sheaths (instead of stainless steel) were received and installed. These thermocouples were arranged at the heater outlet to optimize their ability to measure mean helium temperature as it flows at high velocities out of the heater sections. Unfortunately, this action did not produce an indication of a single heater exit temperature.

Instrumentation and Controls personnel believe that flow phenomena and radiation effects make it impossible to obtain multiple-point temperature measurements that are in agreement at the heater exits. A means, such as an averaging block in which the thermocouples are embedded, must be used to force consistency in this case.

3.6.4 Data Aquisition System

The CFTL DAS is used to collect and process all information made available to it from the loop and test section instrumentation. The DAS consists of a DEC PDP-11/34 central processing unit (CPU), two RK07 disk units, two TE-16 magnetic tape units, an NEFF 640 high-speed analog input multiplexer, a VARIAN printer-plotter, and several terminals.

Computer systems such as these require routine preventative maintenance if they are to operate reliably over extended periods of time. Because of the lack of such maintenance in previous years, many maintenance actions were required by the CFTL DAS during this reporting period. The following is a summary of the problems encountered with the DAS and the corrective actions that were taken.

1. The scan task, which gathers data available at the input channels for use by the DAS, was omitting data during the scanning process. This problem was caused by a faulty component in the address generation area of the input controller hardware. The component was replaced, and the problem was eliminated.

2. The timing signals on the logic control board in the DAS analog input multiplexer were examined and adjusted, where appropriate, to allow the proper channels to be selected for sampling.

3. A failed cooling fan in the magnetic tape units power supply caused the power supply to overheat, turn itself off, and disable the tape unit itself. The fan was replaced and the problem corrected.

4. Another cooling fan in the CPU extension chassis failed, and it was promptly replaced.

5. The precision digital multimeter and programmable dc voltage standard, which are used to calibrate the input data channels automatically, were out of calibration and were sent to the ORNL Standards Laboratory for recalibration.

6. The Varian printer-plotter, which failed to function properly, was sent to an ORNL shop for repair. Replacement parts were ordered and installed; the printer-plotter was then returned and restored to the DAS. A filter to clean the liquid toner was ordered and will be installed when delivered.

7. After consecutive head crashes on RK07 Disk-1 damaged two disk packs, the Y-12 Plant Electrical Maintenance Group was called to service the unit. The group determined that spent rubber motor mounts were causing the crashes, and efforts were initiated to procure replacement mounts. Because the Digital Equipment Corporation (DEC) no longer stocks motor mounts as individual items but stocks the entire motor and bracket assembly in its local DEC service department, a DEC serviceman was called to service the failed disk units. Motor and bracket assemblies for each unit were replaced because of faulty shock mounts. However, this did not resolve the problem of the heads crashing. The heads were replaced and realigned; diagnostics were subsequently run to verify proper operation.

8. Diagnostics were performed on some of the other DAS components that had revealed memory parity errors, a problem not isolated and corrected during this report period. Additional diagnostics should be performed to complete this exercise.

9. The entire DAS was inspected and found to need cleaning, which was promptly done.

10. A failure of the CPU real-time clock prompted its batteries to be replaced. This did not correct the problem, but loss of the clock is not critical.

3.6.5 Impurity Measurement System

The installation of the Beckman IMS, an assembled gaseous impurity measurement and analysis system that automatically measures the impurity components in the circulating helium gas, was completed by the end of January. Beckman's service representative was subsequently available to conduct on-site performance tests. After modifications to bring certain instruments within accuracy specifications, these tests were successful in proving that the system functioned properly.

The IMS consists of several subsystems, including a sample-conditioning and stream selection system, an automated process gas chromatograph, an electrolytic trace moisture analyzer, a six-channel capacitance trace moisture analyzer, and an electrochemical trace oxygen analyzer.

The sampling system draws samples from three points in the helium system. The sample streams are the test structure environment, the impurity injection line, and the calibration gas line. Each stream is filtered and reduced in pressure and temperature to 350 kPa (50 psig) and 27°C (80°F) or less before being delivered to the analysis measurement instruments.

The gas chromatograph, which is automated for continuous unattended operation, sequentially samples the three streams on a cycle time of about 20 min.

The results of the analysis and system status information are printed and simultaneously transmitted to the DAS for logging. Data can also be

logged on a magnetic tape cassette. Chromatograms are presented on a strip chart recorder, and a six-pen recorder displays the results of the chromatographic analysis as concentration trend data.

Except for a few minor component failures, which were quickly remedied either by in-house personnel or by the Beckman service representative, the IMS has performed exeptionally well.

A service agreement proposal for the Beckman impurity measurement system was received from Beckman. To provide adequate preventative maintenance for the IMS, a memorandum requesting acceptance of the prepaid contract was delivered to the Purchasing Division, the contract was delivered to the Purchasing Division, and the contract was accepted.

3.6.6 Impurity Control System

For test periods of six months, the HTR core support test structure must be continuously subjected to a controlled environment. This environment is created by the addition of appropriate impurities to the helium gas circulating in the loop. To maintain the impurities at the desired levels, each one must be positively identified and controlled over various ranges of concentrations.

For this purpose, an ICS consisting of an oxygen-free helium supply and vent flow-regulating system, a gaseous impurity supply and injection control system, and a moisture generation and injection control system was provided. The system functions to maintain the desired impurity concentrations by adding and removing impurities from the circulating helium at a controlled rate.

The impurity cylinder manifold stations, the moisture generator pressure vessels, and the injection control valves are located in the loop area very close to the point of injection. These are remotely controlled from two instrument panels located in the auxiliary control room.

The method used to control the impurity concentrations is determined primarily by the need to vent the loop inventory continuously to maintain the desired concentration of hydrogen and carbon monoxide produced in the system by the reaction of water vapor with the graphite test structure. Clean helium makeup gas is added continuously to maintain the system pressure constant at the required operating pressure.

All impurities except moisture are supplied from three separate high-pressure cylinder manifolds containing the impurities CO, CO_2, and H_2 diluted in helium. These impurities are injected into the loop as a 1% mixture in helium. The moisture impurity is generated by the reaction of hydrogen with a matrix of copper oxide and is injected as a mixture of helium containing moisture.

The technique for producing moisture relies on the reduction of a hot (540°C) copper oxide bed by a hydrogen-bearing stream of helium. This technique is one of the few that does not depend strongly on temperature for control. Control of moisture injection is effected by varying the inlet hydrogen concentration and the ratio of bypass helium diluent flow to that of the water-bearing effluent from the copper oxide matrix. The reduced oxide can be regenerated in place by passing a stream of air over the hot bed to reoxidize the copper.

All impurities are delivered to the loop through the same line that carries the clean makeup helium so that the impurity mixture is injected rapidly into the loop at a point immediately upstream of the circulators. This same mixture can also be piped to the IMS for analysis.

The design, fabrication, and installation of the ICS was developmental in nature and required several modifications and redesigns to be fully operational.

The original design utilized electrical solenoid valves to meter small quantities of H_2, CO, and CO_2 going into the loop. These valves were stressed beyond their limitations, because all six eventually failed. A major redesign required pneumatically actuated flow control valves and pneumatic manual loading stations to be installed in place of the solenoid valves and electronic controllers.

Other modifications included the fabrication of a second moisture calibrator that used copper oxide pellets because the first calibration unit simply did not work; installation of various filters, check valves, and bypass valves; and adjustments in the various flow, temperature, and pressure settings to obtain the desired injection rates. To ensure continuous operational capability, spare parts were identified and procured.

Desired nominal concentrations of moisture, hydrogen, carbon monoxide, and argon were obtained when each of these impurities was successfully injected into the loop. The concentrations were then allowed to decay to obtain the average leak rate of the loop.

3.7 CORE AUXILIARY HEAT EXCHANGER TEST IN THE CFTL — J. P. Sanders

A conceptual design report of the CAHE test was coordinated by M. L. Sollenberger of the Project Engineering Section of the Engineering Division of Union Carbide Corporation, Nuclear Division (UCC-ND). This report is a comprehensive technical and programmatic document resulting from extensive efforts by C. J. Claffey and W. A. Hartman of Mechanical Design; R. D. Stulting of Electrical Engineering; S. C. Rogers of I&C Division; H. F. Wentworth of Civil and Architectual Design; R. M. Walker, A. E. Gilmore, and C. L. Garren of Engineering Mechanics; J. S. Kennedy of Engineering Estimating; and J. P. Sanders and A. G. Grindell of Engineering Technology Division (ETD). This report addresses the technical scope, administrative approach, evaluation of alternatives, uncertainties, schedule, and cost of modifying the existing CFTL facility to accommodate the CAHE test.

The following sections summarize the major design efforts.

3.7.1 CAHE Test Mechanical Design — C. J. Claffey and W. A. Hartman

3.7.1.1 Criteria

Criteria for performance of the CAHE test were furnished by GA. The test heat exchanger bundle is to be designed by GA; the pressure vessel that contains the test heat exchanger is to be designed by Martin Marietta Energy Systems, Inc.

3.7.1.2 Flow Diagram

A flow diagram (Fig. 3.19) giving flow parameters under each of the four proposed operating modes was prepared.

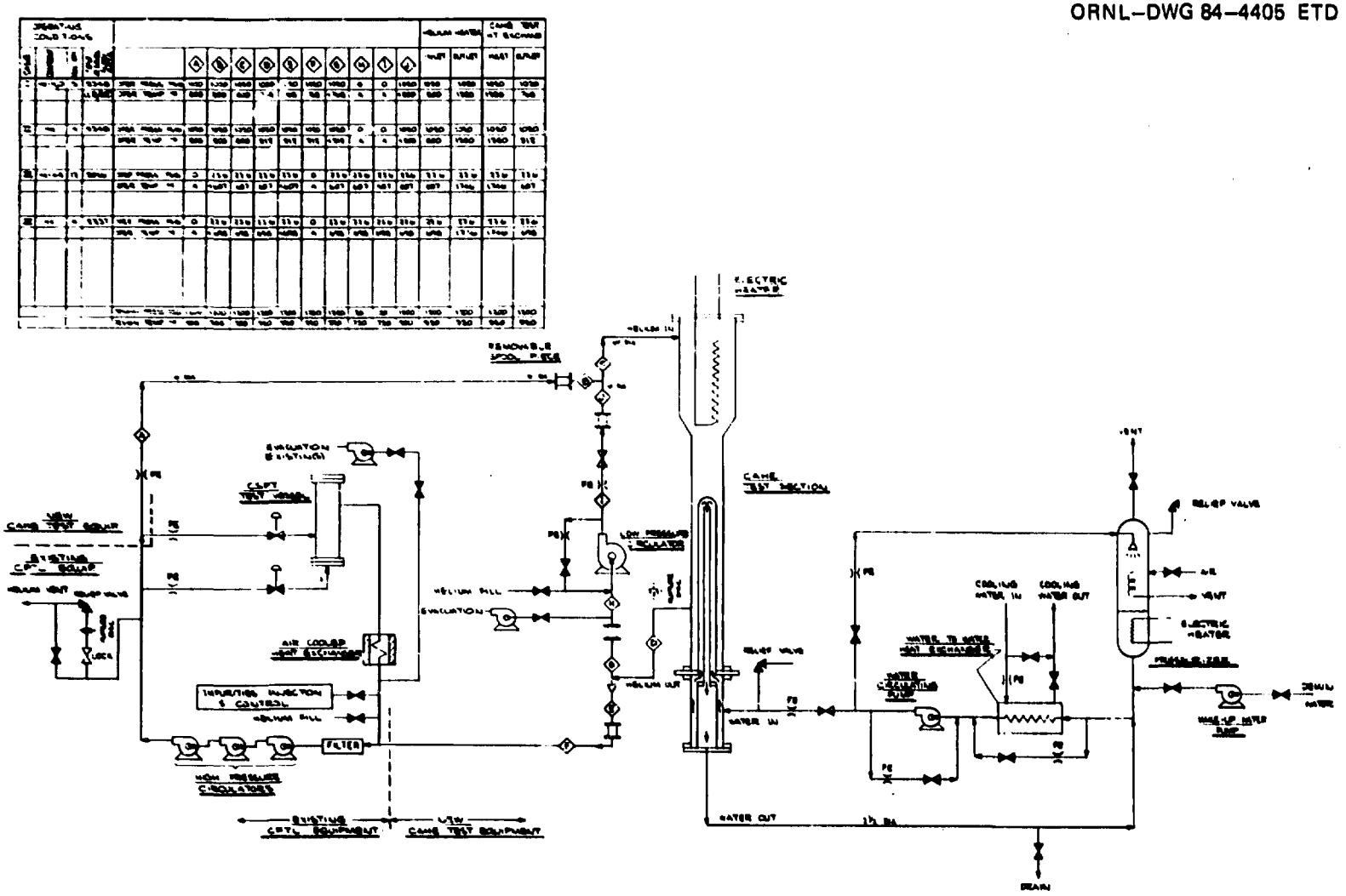

Fig. 3.19. Core Auxiliary Heat Exchanger test flow diagram.

3.7.1.3 CAHE Operating Modes

Four different operating modes are planned for CAHE operations. These are

1. high pressure with pure helium,
2. high pressure with a mixture of helium and moisture,
3. low pressure with pure helium, and
4. low pressure with a mixture of helium and air.

3.7.1.4 Existing CFTL System

The new CAHE facility will take advantage of much of the existing CFTL facility. As shown in the flow diagram (Fig. 3.19), operation during the high-pressure pure helium mode requires that the existing air-cooled helium heat exchanger be used to attemperate the test section exit flow to prevent overheating the existing helium circulators. These existing circulators are to be used during all high-pressure CAHE operations.

It is our intent to preserve all features of the present CFTL for use during CAHE operations as well as for future use.

3.7.1.5 Equipment Layout

An equipment layout was prepared (Fig. 3.20) to determine the necessary size of the addition to the east side of Building 9201-3 and to show the proposed location of that equipment to be installed inside existing Building 9201-3 at the CFTL site.

3.7.1.6 Building Addition

It is required that an extension be added to the east side of Building 9201-3 to contain the new CAHE test section and the pressurizer, which is a part of the high-pressure cooling water system.

A conceptual design of the building addition was prepared by the Civil and Architectural Engineering Department of UCC-ND.

3.7.1.7 Component Specifications

Criteria were assembled and brief specifications were prepared for obtaining vendor quotations for the required components in the CAHE

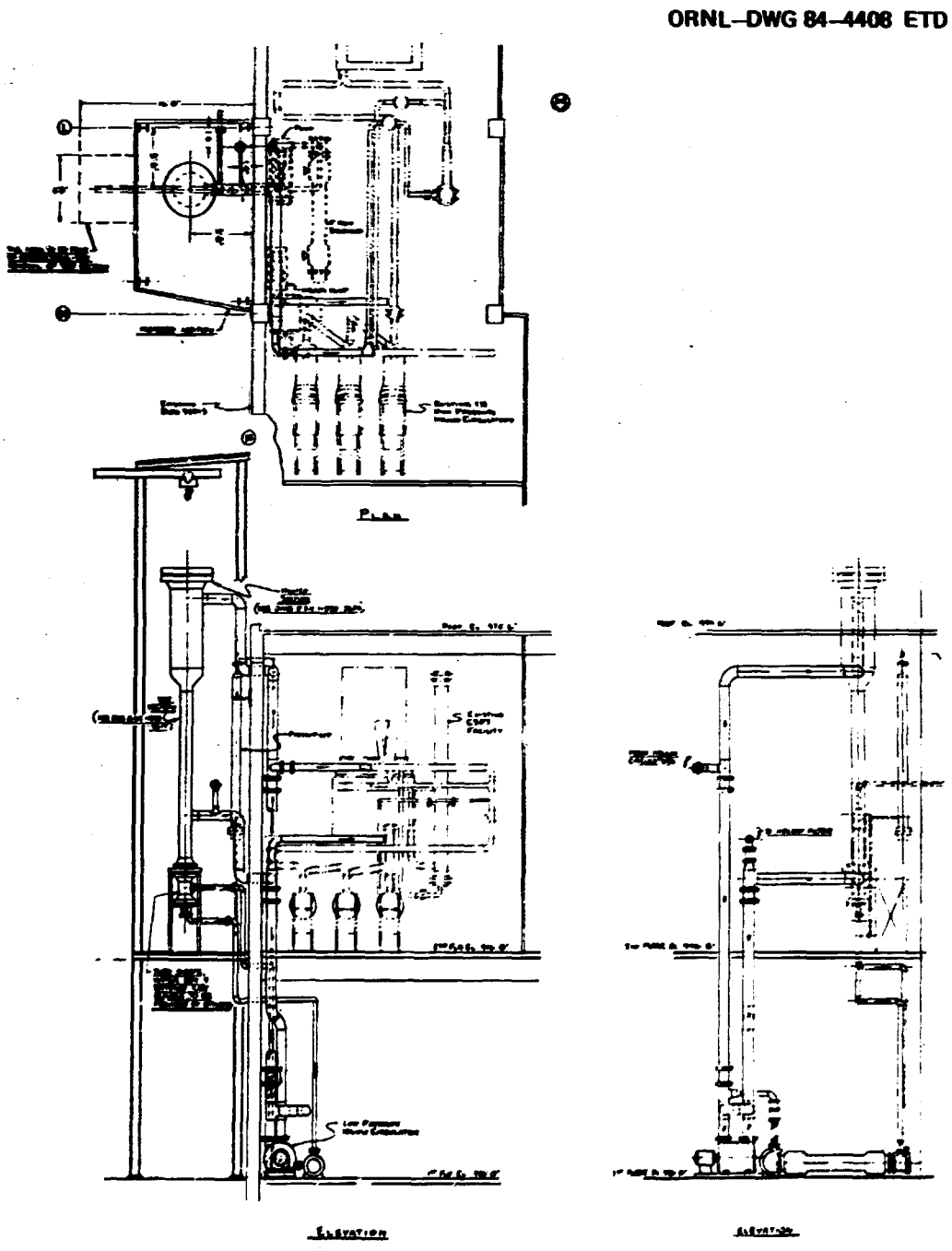

Fig. 3.20. Core Auxiliary Heat Exchanger test equipment arrangement.

systems. The quotations were used for preliminary design and for cost estimating. Components for which quotations were received are the low-pressure helium circulator, high-pressure water pump, water-to-water heat exchanger, and the electric immersion heater for the pressurizer.

Criteria were also prepared for the helium heater; the high-pressure water system pressurizer; the test section pressure vessel; and for piping in the helium system, the high-pressure water system, and the low-pressure water system. The helium heater, pressurizer, test vessel, and piping systems are to be designed by Martin Marietta Energy Systems.

3.7.1.8 Test Section

The test section is a 19-tube bayonet-type heat exchanger, which replicates a section of the 547-tube bundle in an actual CAHE. The test section will be designed and constructed under the direction of GA.

3.7.1.9 Test Vessel

The CAHE test vessel will be designed to contain the bayonet-type bundle, which is the test element. The basic size and vessel shape are defined in GA Dwg. 026948, sheet 1 of 2, except that the test vessel shall be integrated with the heater-containment vessel. The test vessel will be designed, fabricated, and stamped in accordance with the *ASME Boiler and Pressure Vessel Code*, Sect. VIII, Div. 1. The ORNL will provide for design and fabrication of the test vessel, and GA will provide the tube-sheets, water header, box, and bayonet tube bundle.

3.7.1.10 Helium Circulators

The three existing series-connected helium circulators will be used during testing under high-pressure helium conditions. A new low-pressure helium circulator will be purchased for low-pressure testing.

3.7.1.11 Helium Heater

The CAHE helium heater (Fig. 3.21) is similar in concept to the existing helium heater in the currently operating CFTL-CSPT. The new CAHE heater, however, will have a substantially greater capacity than the present heater. Additionally, the new CAHE heater must function under widely

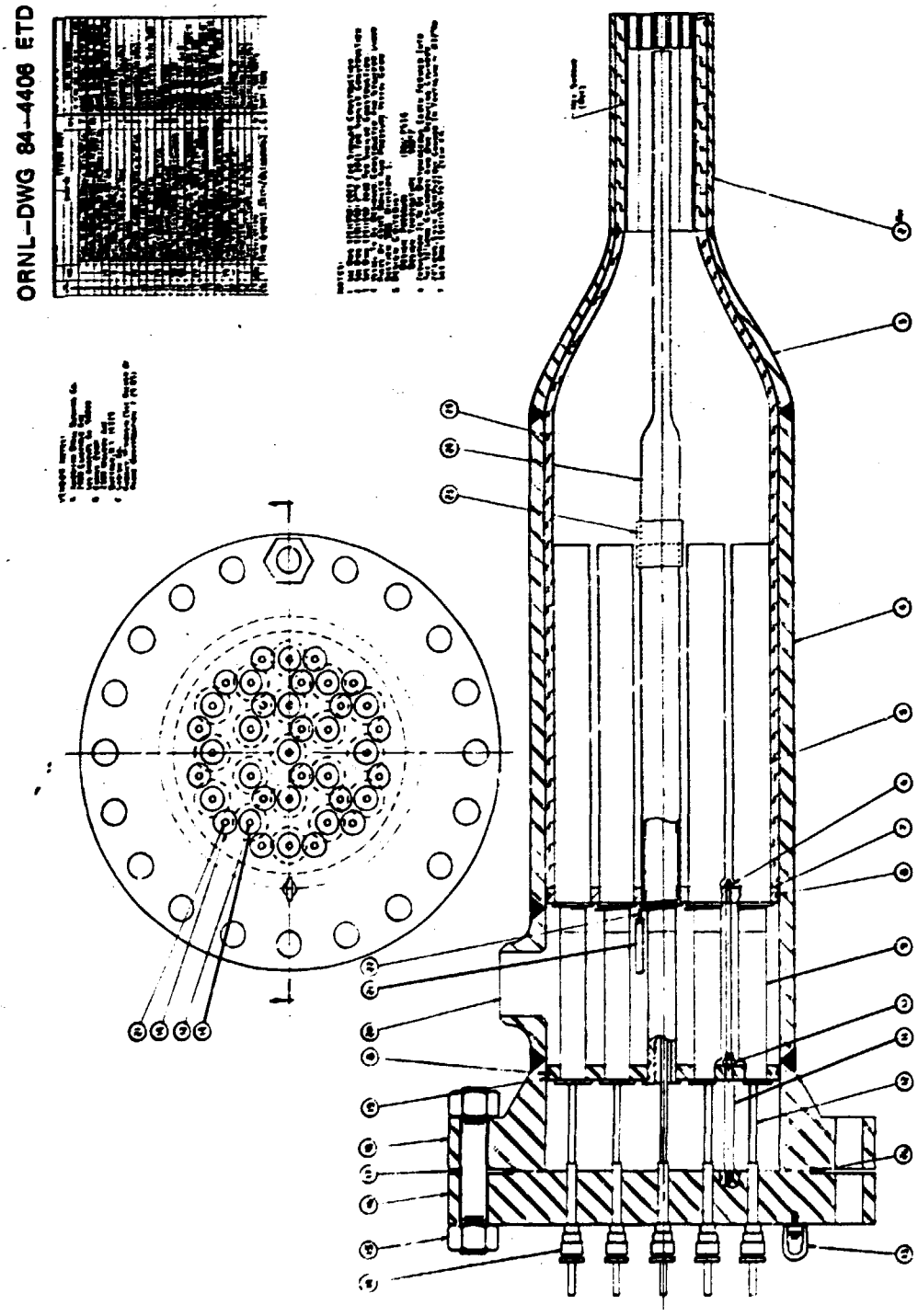

Fig. 3.21. Core Auxiliary Heat Exchanger test helium heater.

different pressure and flow conditions. An existing computer program, used for design of the original CFTL heaters, was used in optimizing electrical power, heater element wire size, number and spacing of coils, helium flow rate, and flow annulus parameters to arrive at an acceptable heater concept for CAHE.

The final concept uses ten 250-kW heater elements, except that one of the ten elements must operate 13% above 250 kW to provide the desired localized hot-streak effect. The heater layout requires an 18-in. iron pipe size (IPS) pipe section to enclose the heater elements.

The pressure-containing shell for the helium heater will be essentially an extension of the test section pressure vessel.

3.7.1.12 Pressurizer

The pressurizer (Fig. 3.22) for the high-pressure water loop will be designed and built by Martin Marietta Energy Systems. It is conceived as being electrically heated, with a flanged immersion heater of 20-kW capacity installed in the bottom of the pressurizer vessel. The pressurizer serves the following multiple functions.

- It initially heats the contained water to saturation temperature at the desired system pressure.
- It is instrumented and controlled to maintain this desired pressure during steady-state operation.
- It provides a means of degassifying the pressurized water by spraying a small stream into the vapor region at the top of the pressurizer. The evolved gases are then vented to the atmosphere.
- It serves as a surge tank, being sized so that, as it increases from ambient to operating temperature, it can accommodate the substantial change in the volume of the water.

The pressurizer will be designed, fabricated, and stamped under the provisions of the *ASME Boiler and Pressure Vessel Code*, Sect. VIII, Div. 1.

3.7.1.13 Heat Dump

Up to a maximum of 2.68 MW electrical power is used to heat the helium before it enters the test section. In the test section, this heat

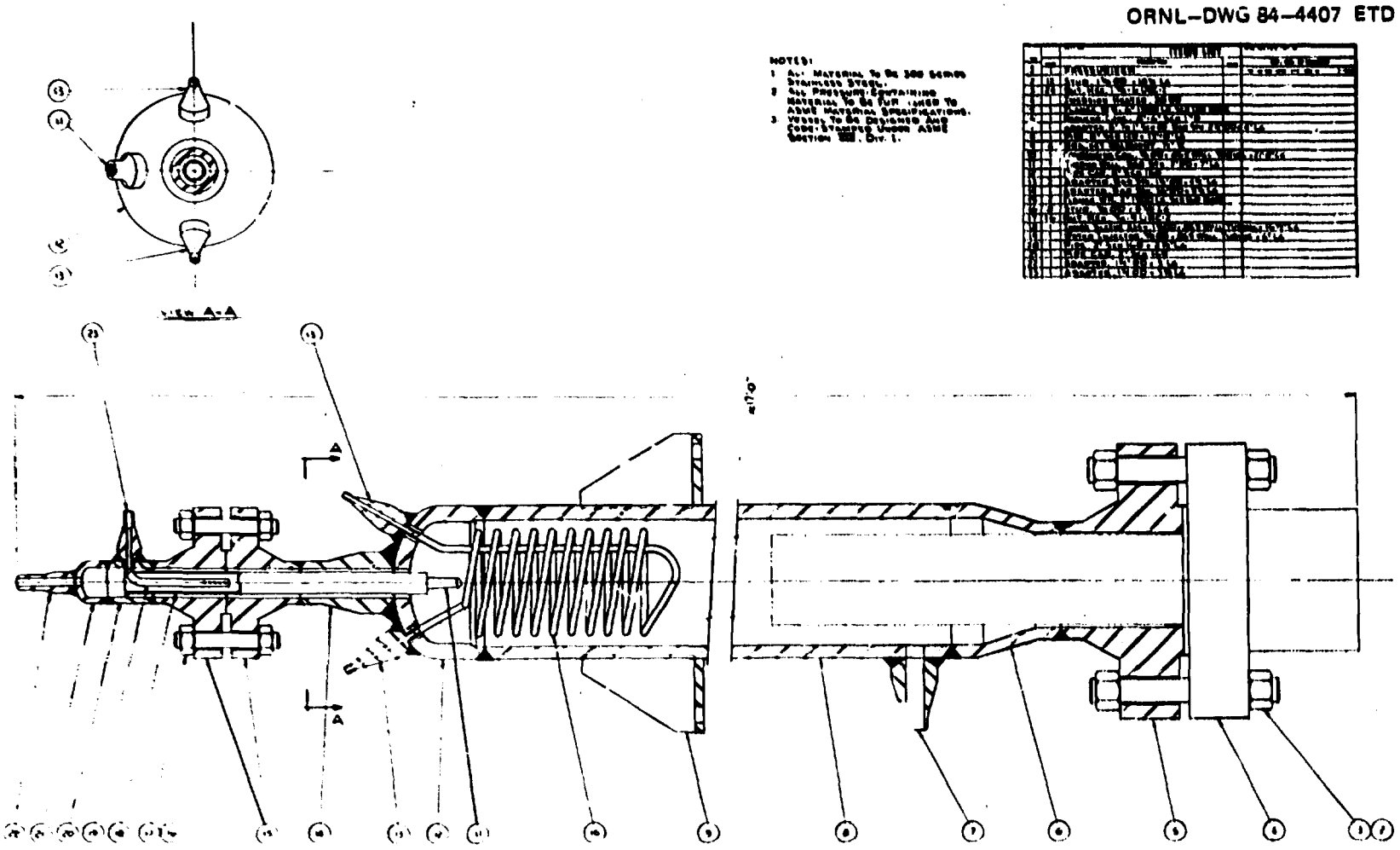

Fig. 3.22. Core Auxiliary Heat Exchanger test pressurizer.

is transferred from the helium to the high-pressure recirculating water system. In the water-to-water heat exchanger, the heat is transferred to the low-pressure cooling-water system. This low-pressure water is discharged to the industrial ditch on the south side of Building 9201-3. The ditch empties into New Hope Pond at the east end of the Y-12 Plant. After dissipating its heat while in the pond, the water is discharged into Poplar Creek.

3.7.1.14 Bills of Material

Bills of material were prepared for all CAHE systems and construction. These bills of material were used as the basis for the cost estimates.

3.7.1.15 Technical Presentation

On February 22, 1983, a presentation was made for the benefit of representatives from GA and DOE (Washington). The concept of the proposed design, a preliminary cost estimate, and a projected schedule were presented.

3.7.1.16 Conceptual Design Report

A conceptual design report was prepared for the CAHE. Significant subsections within the report are

- Physical description of project
- Purpose and justification
- System definition and baseline requirements
- Concepts and alternatives
- Uncertainties
- Preliminary assessment
- Method of accomplishment
- Schedule
- Cost estimate
- Outline specifications
- Reference data

3.7.2 CAHE Test Instrumentation and Controls — S. R. Rogers

Preliminary design and cost estimates were completed for the design modifications of the CFTL to evaluate the performance characteristics of the CAHE. The I&C portion of the CAHE test is estimated to be $800,000, $300,000 to be spent the first year and $500,000 the next year.

Test specifications generated by GA were reviewed, and several meetings were held among ORNL instrumentation experts and experts from Combustion Engineering, who had been reviewing the design of the test bundle. During these consultations, several difficult measurements required by the specifications were discussed, and alternative solutions were defined.

Instrument application flowsheets were designed and issued (see Figs. 3.23 and 3.24), and a narrative description of the instrumentation needs for the CAHE test was provided.

3.7.2.1 Recirculating Water System

The water system includes three major components: pressurizer, heat dump, and high-pressure pump.

The primary function of the pressurizer is to maintain water system pressure during steady-state operation. A pressure element senses this pressure and transmits it electrically to an automatic pressure controller. The pressure controller compares the actual pressure to the desired pressure (setpoint) and outputs a signal to adjust heater power and thereby adjust the pressure so that the error is reduced to zero. The pressure is constrained by limit switches, indicated, and input to the DAS. Water level in the pressurizer is sensed by a differential pressure transducer, whose output is transmitted to limit switches and indicated. Should the water rise to the full level, the system may become hard and endanger the pressure boundary; also, the heaters may overheat if the level should fall to the point where the heaters become uncovered.

The heat dump (water-to-water heat exchanger) removes excess heat from the water exiting the CAHE test section so that the water reenters the CAHE at the desired temperature. The temperature of the CAHE inlet water is sensed by a thermocouple and transmitted to an automatic temperature controller. The output of this controller actuates a flow

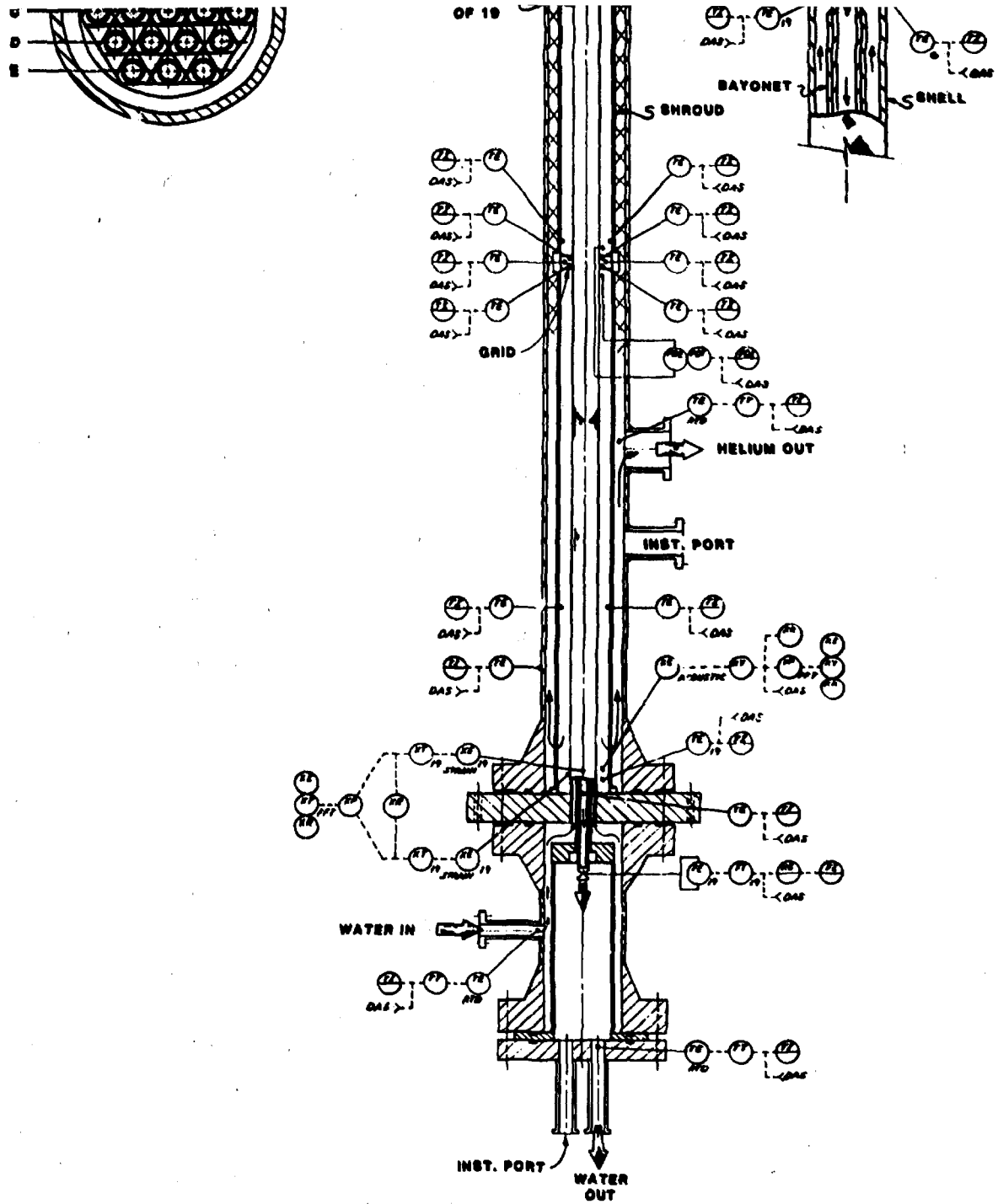

Fig. 3.23. Instrumentation diagram for core auxiliary heat exchanger test bundle.

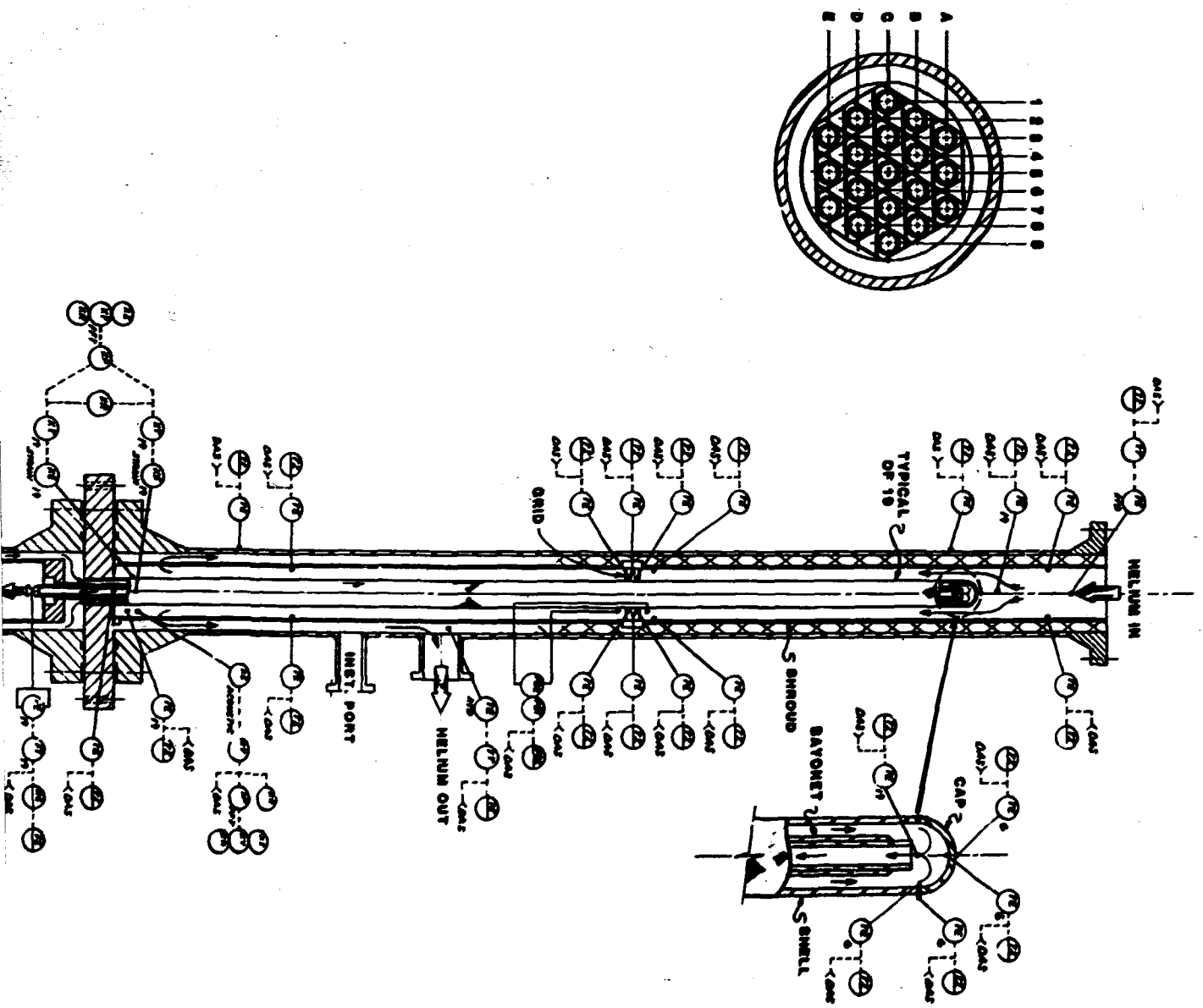
E
D
C
B
A
1
2
3
4
5
6
7
8
9
10
TYPICAL OF 10
GRID
HELIUM IN
HELIUM OUT
INLET PORT
SHROUD
BAYONET
CAP
SHELL

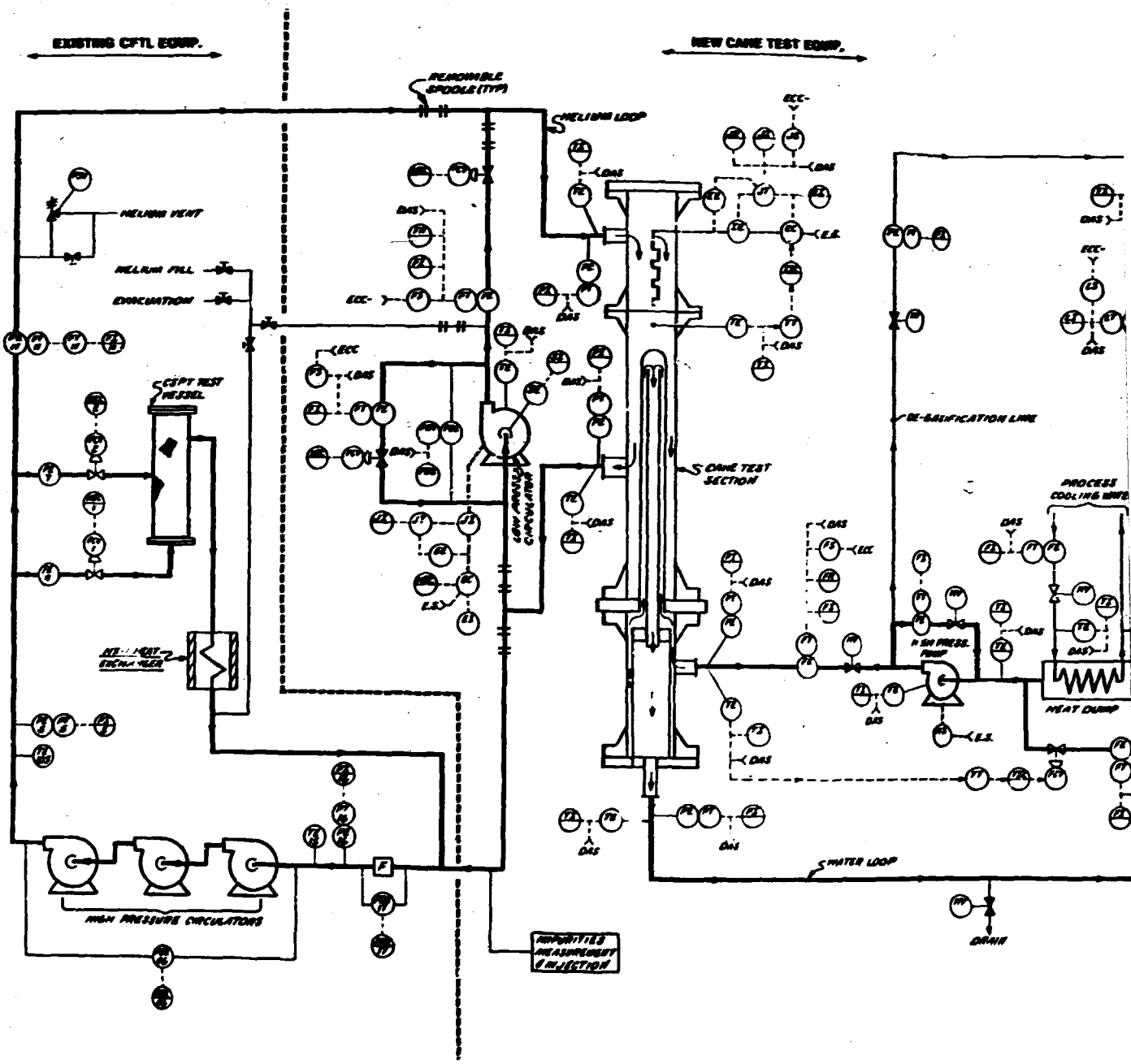

Fig. 3.24. Instrumentation diagram for the modification of the component flow test the 19-tube core auxiliary heat exchanger bundle.

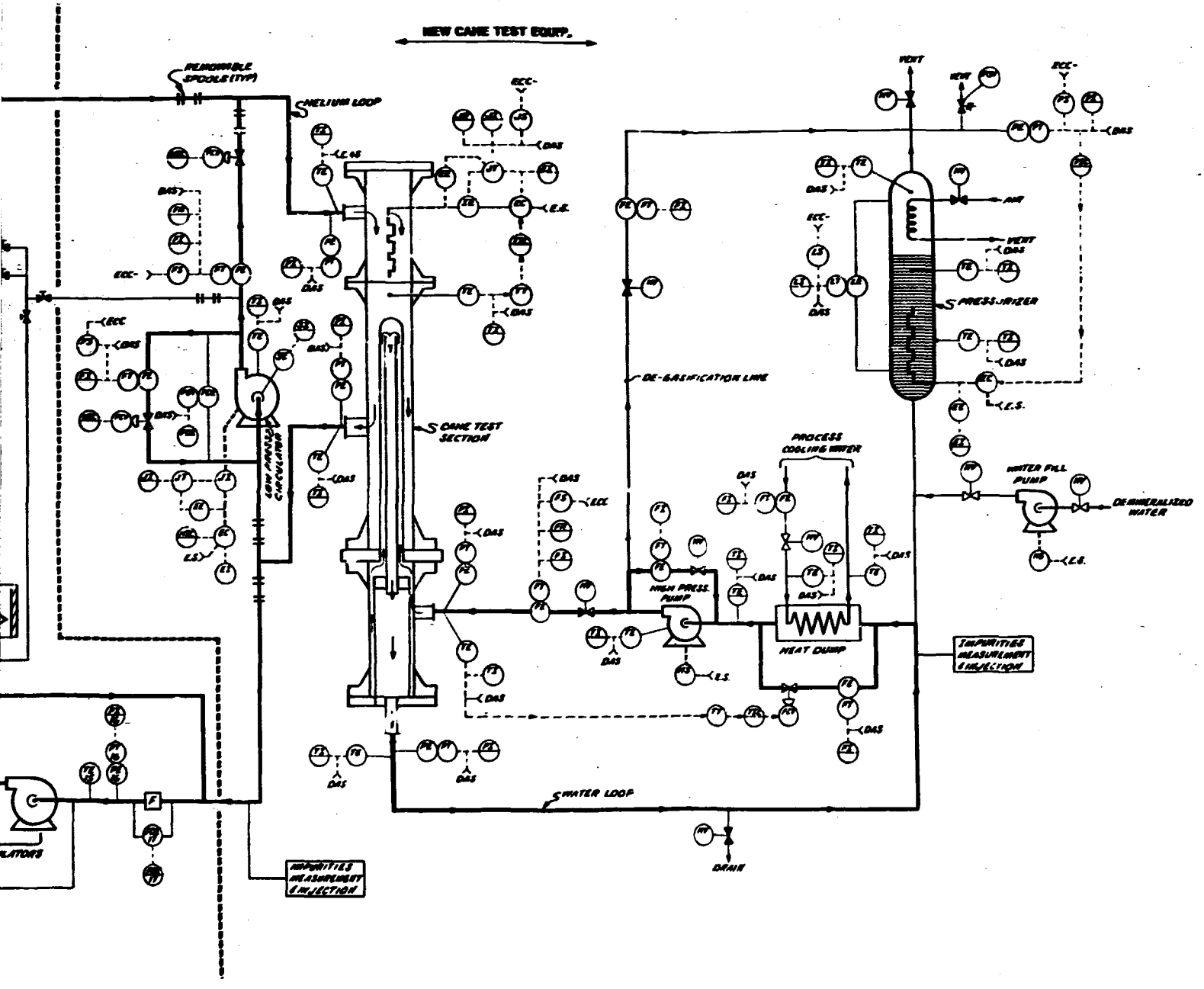

. Instrumentation diagram for the modification of the component flow test loop to test re auxiliary heat exchanger bundle.

control valve in the heat dump bypass line to adjust the duty cycle of the heat dump, thereby varying the amount of heat removed to maintain the desired temperature (setpoint). Flow and temperature indications in the bypass section aid in evaluating the heat dump performance. Control of the flow rate of process cooling water in the secondary side may serve as a course adjustment of the heat dump duty cycle.

A constant-speed, on-off, high-pressure pump circulates water around the water system. To maintain the desired flow rate, a flow control valve is provided in a bypass section around the pump and in the CAHE inlet line. The bypass section relieves the head created by the main flow control valve in the CAHE inlet line. Flow rate and temperature indications in the bypass section provide performance evaluation and protection for the pump. Sensing elements and transmitters are provided at the CAHE water system inlet and outlet for measuring and processing the key parameters of flow, temperature, and pressure.

3.7.2.2 Low-Pressure Helium System

A low-pressure helium circulator will be used during depressurized operation. Although not finally determined at this writing, it will probably have a constant-speed drive. Adequate power control and measurement is provided. A helium bypass line around the low-pressure circulator assists in flow control and protects the circulator from surge conditions. Helium flow rate and temperature in the bypass section, as well as temperature of and differential pressure across the low-pressure circulator, provide indications of the circulator performance for operation and protection. A remotely actuated flow control valve is required in the main low-pressure helium line to maintain desired flow in the steady-state condition and to ramp the flow during the flow-induced vibration tests.

3.7.2.3 High-Pressure Helium System

A modification of the existing CFTL loop is required for operation in the pressurized condition. The system will be introduced to the CAHE test section by means of removable spool pieces. The only significant instrumentation modification in the existing system is the relocation of total

helium VSPM FE-11 from its present position at the circulator outlet to a location downstream of the point where helium is diverted to the CSPT test vessel. This effectively moves FE-11 out of the high-pressure circulator bypass loop formed by the CSPT test section and HX-1 and into the main high-pressure helium loop so that it can directly measure total high-pressure helium flow.

Sensing elements and transmitters are provided at the CAHE helium inlet and outlet for measuring and processing the key temperature and pressure parameters.

3.7.2.4 Helium Heater

A 19-element 7.0-MW helium heater is required to provide the desired elevated temperature of the helium at the input to the CAHE tube bundle. Induction regulator-type devices not shown in Fig. 3.24 are used to control power to the helium heater. The voltage controller shown (EC) interfaces the automatic temperature controller output signal to the induction regulators. The temperature of the helium at the heater exit is transmitted to the input of the temperature controller and compared with the setpoint to determine the output control signal. Alternate control sequences may use power feedback instead of temperature feedback or perhaps straightforward manual control of heater power. Adequate instrumentation to measure and process heater voltage and power is provided. The heater power measurements and control described in this section assume ganged control of all 19 heating elements. In the case of individual control of heater elements (such as with hot streaks), additional instrumentation will be required.

3.7.2.5 CAHE Test Section Internal Instrumentation

Requirements for CAHE internal instrumentation have been documented by GA (ref. 6).

A rake of thermocouples, one over each of the 19 tubes, shall be provided to measure the helium inlet temperature. The rake should be placed where the gas is well mixed and should be designed to include radiation shielding and provide gas straightening. A long, averaging RTD located

upstream of the thermocouple rake may provide good cross-reference temperature. To complete the measurement of the helium side temperature difference for calculating the heat transfer coefficient, about 24 thermocouples will be located in the downflow region just above the exit screen in the spaces between the tubes. Averaging RTDs in the helium exit port and thermocouples in the helium upflow region to measure heat losses are also required, as well as a number of thermocouples in various locations along the shroud and grid.

A differential pressure transducer and transmitter and a high-temperature microphone and amplifier shall be provided to measure helium pressure drop across the support grid and acoustic phenomena occurring in the helium, respectively.

Thirty-eight strain gage measurements (two located 90° apart at the base of each of the 19 tubes) are necessary to measure vibration that may occur on each tube sheath. However, only a limited number of these measurements need to be recorded simultaneously if the flow-irduced vibration tests are repeated. Therefore, only six strain gage conditioners shall be provided, and a different set of strain gages shall be conditioned and recorded each time the flow is ramped. The fact that only the dynamic response (vibration) is of interest allows use of a single conditioner for multiple-strain gages without the need for recalibration. The recorded signals shall be played back into a fast Fourier transform device for analysis and hard copy, and an oscilloscope will be available for on-line observation. The recorder fast Fourier signal analyzer and oscilloscope shall be used on a temporary loan basis. Experimental calibration of the strain gages at operating temperature must be performed for meaningful interpretation of this measurement. This may be as simple as deflecting a tube a known distance and noting the resulting strain signal. The elastic properties of the tube at temperature must be considered, as well as the different modes of vibration that may occur.

Thermocouples will measure temperature of the water at the top and bottom of each bayonet tube; lead wires shall be routed through the inside of the bayonet tubes. Two end caps shall be instrumented with four thermocouples each to measure thermal gradients. Routing of these lead wires

has not been resolved because of the requirement for removal of the bayonet tubes. The flow of water in each of the individual tubes is adjusted by the CAHE vendor by installing individual flow restrictors. The flow balance that is obtained is not likely to change during the test.

Precision transducers and transmitters shall be provided to measure inlet and outlet helium and water pressures.

Instrumentation leads shall penetrate the CAHE test section through horizontal flanged lids at top and bottom and through a proposed "instrument ring" as suggested by Combustion Engineering representatives.

3.7.2.6 Data Acquisition System

An extensive PDP-11/34-based DAS exists in the CFTL. For the CAHE test, an additional 200 or so channels must be interfaced and entered into the instrument data base, and specialized software must be generated to process data as required but not yet determined by GA. Additionally, both preventative and unexpected maintenance is a continuing liability of such a large and complicated computer system. Additional funding is required to maintain the DAS for CAHE.

3.7.2.7 Impurity Injection and Analysis

Extensive facilities exist in the CFTL for trace impurity level control and analysis. The CAHE test requires that gross (20%) quantities of air and moisture be injected into the helium system and that pH and dissolved oxygen be analyzed in the water system. The air and moisture concentrations in the helium system partially exceed present IMS and ICS ranges, and no hardware now exists in the CFTL to measure pH and dissolved oxygen in the water system. Additional instrumentation is therefore required to expand IMS and ICS capabilities.

A list of uncertainties accompanied the narrative description of instrumentation needs for the CAHE, which follows.

1. Existing high-pressure helium VSFMs may have to be recalibrated or replaced. Recalibration may be necessary if required accuracy cannot be properly verified and traced as required by the Nuclear Regulatory

Commission licensing criteria. In this event, it may be more cost-effective simply to replace these flowmeters with relatively inexpensive (about $10,000–$20,000 each) flowmeters suitable for the less demanding CAHE requirements.

2. The I&C cost estimate for CAHE test bundle instrumentation assumes ORNL funding for all materials and design labor but excludes CAHE vendor labor costs for installation of sensors inside the CAHE test section. Should ORNL be billed for these costs by the CAHE vendor, ORNL costs would increase significantly.

3. Any changes in the GA CAHE test specification will affect costs.

4. The I&C cost estimates assume 100% capital funding for all loop-related instrumentation. Expense funding in lieu of capital funding would increase these estimates.

S. C. Rogers accompanied J. P. Sanders to GA to discuss instrumentation needs for the proposed CAHE test and possible areas for cost reduction. The results of the meeting are more clearly defined test objectives and overall reduction of measurement requirements, resulting in significant cost reductions. During the meeting, GA representatives made significant modifications in the CAHE test specifications in the area of measurement requirements. Among these were deletion of the individual water flow measurements in each tube, reduction in the number of end caps to be instrumented with thermocouples from six to two, and reduction in the number of strain gages to be simultaneously recorded from 38 to 6. This last modification eliminated 32 signal conditioners.

A bill of materials was formed from the final I&C portion of the CAHE conceptual design. Informal requests for bid on key items were submitted to the Purchasing Division. The subsequent bids were received and reviewed, and the I&C CAHE cost estimates were then completed.

3.8 REFERENCES

1. J. P. Sanders, "Introduction," pp. 145–52 in *High-Temperature Gas-Cooled Reactor Technology Development Program Annual Progress Report for Period Ending December 31, 1982*, ORNL-5960, June 1983.

2. H. C. Young and A. G. Grindell, "Piping Modifications," pp. 178–80 in *High-Temperature Gas-Cooled Reactor Technology Development Program Annual Progress Report for Period Ending December 31, 1982*, ORNL-5960, June 1983.

3. H. C. Young and A. G. Grindell, "Helium Heater Construction and Installation," pp. 186–89 in *High-Temperature Gas-Cooled Reactor Technology Development Program Annual Progress Report for Period Ending December 31, 1982*, ORNL-5960, June 1983.

4. H. C. Young and A. G. Grindell, "Vessel Manufacture and Installation," pp. 180–86 in *High-Temperature Gas-Cooled Reactor Technology Development Program Annual Progress Report for Period Ending December 31, 1982*, ORNL-5960, June 1983.

5. A. G. Grindell, *Test Specifications, TEST ZERO for the Core Support Performance Test*, Q-11590-ET-006-S-0, Oak Ridge National Laboratory, Oak Ridge, Tenn., Aug. 4, 1983.

6. J. Kaufman, *Test Specification — Core Auxiliary Heat Exchanger Heat Transfer Test*, Document 906593/2, GA Technologies, San Diego, Calif., Feb. 18, 1983.

4. HTR PHYSICS (WBS 3610.04)

D. E. Bartine and D. L. Moses

4.1 INTRODUCTION — D. L. Moses

The analysis of high-temperature reactors (HTRs) requires numerical methods capable of modeling the neutronic and thermal-hydraulic characteristics of a large thermal reactor core. The analysis methods must also be capable of simulating various stages in the burnup history of a large core. If options in core burnup or control strategies are to be explored in detail, the analysis must be repeated to determine the effects of changes.

During the past year the major efforts in HTR physics were in developing and demonstrating methods to simplify the complex analysis requirements for HTR cores. The ability to perform steady-state thermal-hydraulic analyses for prismatic HTRs was added to the VENTURE code system. These methods were applied to study the effects of reducing the power density in a large core. The impact on temperature distributions and core pressure drops was calculated. This information will be used in an assessment of core performance and operating costs as a function of power density. A report covering the prismatic thermal-hydraulics work is forthcoming.

The utility of depletion perturbation theory (DPT) methods was demonstrated in a problem for designing a core loading pattern to obtain a desired power-temperature distribution throughout core life. Least-squares fitting was used with DPT sensitivity coefficients to effect a search for an optimum loading pattern without requiring multiple burnup studies. Finally, the use of reflector albedos was studied to simplify the reflector geometry required for large core neutronic simulations. Preliminary results indicate that the number of mesh points in large three-dimensional problems may be cut almost in half with little or no error in core flux calculations.

4.2 CORE PHYSICS ANALYSIS

4.2.1 Power Density Study — D. R. Vondy

Core calculations were performed to assess the effect of variations in core power density on core performance for a stack height of eight fuel elements. The core plan view of seven-fuel-element refueling patches for quarter-core refueling is shown in Fig. 4.1. Two-dimensional core history calculations were performed for this arrangement through several refuelings to bring the core into equilibrium cycle evaluations. A burnable poison scheme was used for axial power adjustment, but radial power density flattening was not done. Note that the core history has cyclic variations due to differences in refueling batches. These differences are 106, 106, 106, and 121 fuel elements involved in each of four successive reloads. A three-dimensional model treating only four patches with a full core axial traverse was also used. Summary data from representative core history calculations are shown in Table 4.1.

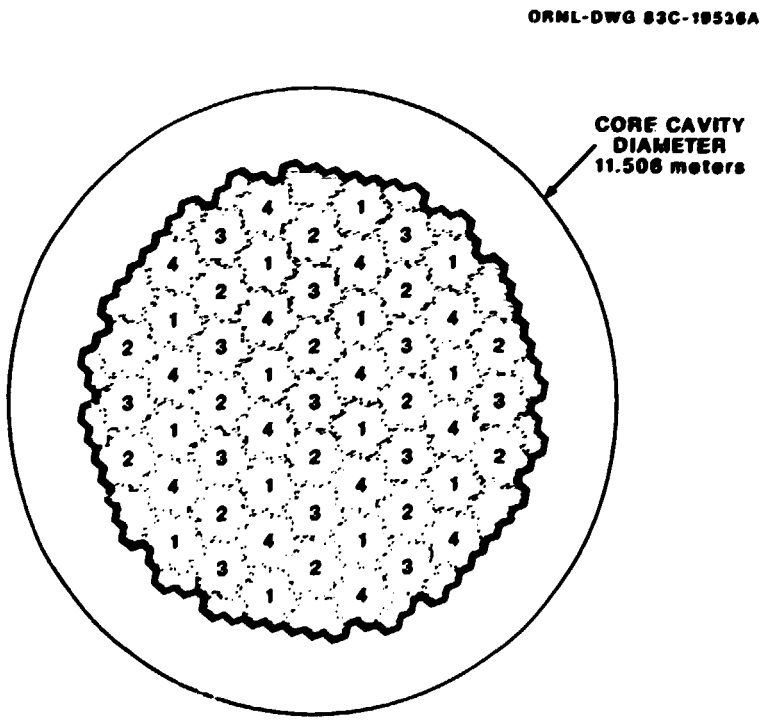

Fig. 4.1. Seven-fuel-element patch layout for the 2240-MW(t) core at 7.16-W/cm^3 power density.

Table 4.1. Core data for HTR history calculations

Model	Four-patch		Two-dimensional core traverse
Power density, W/cm^3	5.75	7.16	7.16
Refueling period, full-power days	410.7	416.0	416.0
Peak power density, W/cm^3	9.26	11.30	11.52
Fissile data, kg			
Loading	2246	2072	1989
Batch refueling	742	734	723
Discharge	344	290	257
Fissile feed, kg/full-power day	1.81	1.76	1.74
Exposure, MW(t)d/kg of heavy metal	81.7	101.5	101.3

Thermal hydraulic calculations were also performed for the core with the power distribution data from the core histories. Full core thermal hydraulic calculations were performed with the two-dimensional traverse and the axial power distribution from the four-patch model. Representative results are shown in Table 4.2 for conditions after refueling and with a coolant inlet temperature of 320°C and an outlet temperature of 700°C. These calculations were performed with fixed-fuel-element design and orificing by patch to effect equal patch-average outlet coolant temperatures.

The data in Table 4.3 were generated to show the fraction of fuel hotter than reference temperatures for a fixed fuel element design and power density. The rise in temperature of the fuel associated with a significant increase in the power density is judged to be rather modest.

The calculated pressure drop data exclude flow losses through the reflectors, the open orifice, and the rest of the system. A condensation of results is

Power density (W/cm^3)	Partial coolant pressure drop	
	(kPa)	(atm)
5	28.4	0.28
6	37.5	0.37
7	49.6	0.49

Table 4.2. HTR core thermal hydraulics results

Model	Four-patch		Full core
Power density, W/cm^3	5.75	7.16	7.16
Fuel temperature, °C			
Average	682	671	675
Power-weighted	673	665	668
Peak	928	942	935
Fraction fuel hotter, °C			
>800	0.137	0.109	0.089
>850	0.054	0.032	0.011
>900	0.018	0.003	0.001
Core pressure drop,			
kPa	26.8	41.7	46.9
atm	0.264	0.412	0.463

Table 4.3. Power density effect on fuel temperature distributions

Power density (W/cm^3)	Fraction of fuel above				
	950°C	900°C	850°C	800°C	750°C
5.75	0.0005	0.004	0.034	0.11	0.23
7.10	0.0018	0.0219	0.0573	0.139	0.263

These data allow the evaluation of pumping costs and the performance of economics analysis for determining plant operating cost.

4.2.2 Design Optimization by Depletion Perturbation Theory — B. A. Worley

Analysis of the fuel cycle performance of a reactor requires knowledge of the entire fuel burnup history. The optimal design depends on the desired performance parameter or combination of parameters to be minimized (or maximized). The emphasis to date has been on the use of some combination of iterations involving a number of direct calculations, static perturbation theory, binary exchange methods, and empirical relationships.[1-3] The object of this study is to demonstrate an approach to optimization based on DPT (ref. 4).

The DPT equations directly couple the nuclide burnup equations and the neutron balance equations. The equations require the calculation of forward and adjoint solutions for the neutron flux and nuclide transmutations. Any number of flux calculations can be performed during the burnup period; the DPT method accounts for flux renormalization to maintain the desired reactor power. The calculated sensitivities are generally used for (1) determining the effects of design changes on parameters evaluated at various times during the fuel cycle and (2) assessing the importance of parameters and performing uncertainty analysis. This work, however, uses the sensitivity data for design optimization.

The application is for analysis of a modular HTR. The reactor has axially dependent fuel loadings to achieve an axial power shape that keeps fuel temperatures below a specified maximum. For this reason the axial power shape must remain stable over the fuel burnup period of five years. Boron is used as a burnable poison.

The design optimization involves minimizing, in a least-squares sense, the change in region-averaged power densities over the five-year irradiation period. Specifically, we seek to minimize the function

$$y = \sum_{i=1}^{I} \sum_{j=1}^{J} \left(P_{ij} - \frac{1}{J} \sum_{k=1}^{J} P_{ik}\right)^2 , \qquad (1)$$

where P_{ij} is the region-averaged power density in region i and j in the burnup period, I is the number of regions, and J is the number of time points to be examined during burnup period.

Restricting the free parameters to nuclide loadings, the calculated power density sensitivity data are b_{ijk}, defined by

$$b_{ijk} \equiv \partial P_{ij}/(\partial n_{ik}) \ , \tag{2}$$

where n_{ik} is nuclide density for the nuclide k.

The change in P_{ij} is estimated to first order by the sum $\sum_k b_{ijk}\,\Delta n_{ik}$, so Eq. (1) can be rewritten as

$$y = a\Delta n^T + \Delta n\ \mathbf{B}\ \Delta n^T \ , \tag{3}$$

where a is the row vector consisting of combinations of the b_{ijk}, B is the square matrix consisting of combinations of the b_{ijk}, and Δn is the row vector of the changes in the nuclide loadings.

To test the optimization procedure, three axial loading regions were chosen and three nuclides were varied: ^{235}U, ^{232}Th, and ^{10}B for nine independent variables. Eleven flux and ten burnup calculations were performed over the five-year cycle, but the time points to be considered were limited to beginning- and end-of-cycle.

The nuclide loading changes were constrained, and the function y was minimized to give a set of Δn. The direct calculations were performed with the "optimized" loadings; the results are listed in Table 4.4 under case 1. Use of the new loadings reduced the objective function by a factor of 0.03. The maximum change in region-averaged power density was 0.06 W/cm^3 compared with 0.34 W/cm^3 for the reference case. The peak region-averaged power density increased slightly.

To determine if the peak region-averaged power density could be decreased while also decreasing the objective function, an additional constraint of 5.80 W/cm^3 on the peak region-averaged power density was imposed. As shown in the table, the objective function y increased only slightly from case 1 and was still much smaller than the reference case.

In summary, this work demonstrates an application of DPT that is unique because of its use in design optimization over the entire fuel

Table 4.4. Region-averaged power densities for a modular HTR

Reactor design, 250 MW(t); core height, 6.34 m; core diameter, 3.5 m; average power density, 4.1 W/cm^3; high-enriched uranium-thorium fuel cycle; five-year refueling period

Axial loading region[a]	Region-averaged power density (W/cm^3)		
	Reference	Case 1	Case 2
	Beginning-of-cycle		
1	5.82	5.95	5.76
2	3.41	3.12	3.31
3	1.35	1.36	1.57
	End-of-cycle		
1	5.95	5.98	5.80
2	3.07	3.06	3.27
3	1.42	1.38	1.52
	$\sum_i^3 [P_i(\text{BOC}) - P_i(\text{EOC})]^2$		
	0.144	0.005	0.007

[a]Region 1 is top half of core, region 2 is next quarter of the core; and region 3 is bottom quarter of the core.

cycle. A single flux adjoint calculation for each flux calculation is sufficient to obtain *all* sensitivities over the cycle, and the use of a large number of parameters can be dealt with efficiently.

4.2.3. HTR Reflector Albedo Analysis — B. A. Worley and J. O. Johnson

Design and performance analysis of a new reactor system requires calculations involving cross-sectional processing, neutronics, thermal hydraulics, fuel management, and combinations of any or all of these analyses. The analysis is made more efficient by the development of methods

that reduce the cost of the analysis without any appreciable change in the calculated result. Toward this end, an investigation was performed into replacing the detailed simulation model for the HTR graphite reflector with a set of energy-dependent albedos.

The albedo boundary condition is imposed by replacing the reflector simulation with a core surface boundary condition relating the *net* neutron current at the core surface to the core surface flux. The net surface current for the broad energy group g is defined by

$$J_{sg} = \sum_{g'=1}^{G} \alpha_{gg'} \phi_{sg'} ,$$

where the albedo $\alpha_{gg'}$, defined by $\alpha_{gg'} = J_{sg}/(\phi_{sg'})$, is the ratio of the net surface current in group g to the surface flux in group g'. To apply albedos in place of a reflector model, the $\alpha_{gg'}$ can be calculated as a function of the *reflector* properties only. The $\alpha_{gg'}$ are determined by performing an independent calculation on the reflector. This is done by imposing a source $\phi_{sg'}$ at the reflector surface and calculating the J_{sg} in each group g. The albedos can be determined by diffusion theory, transport theory, and so forth or can be measured experimentally.

The use of albedos to replace the core reflector model has not seen much practice in reactor design computations, primarily because there is little motivation to do so. The commercial light water reactors in industry today use water for the core reflectors. Because water has a small diffusion length, only the first several inches of the reflector need to be modeled. Therefore, simulating the water reflector in a core calculation with albedos will not result in significant savings in computational time or effort. However, the HTR utilizes a graphite reflector, which requires modeling up to 1 m of material. As many as 60 to 70% of the mesh points in a finite-difference calculation can be required in the reflector for some three-dimensional models. The incentive to model the reflector by use of albedos is obvious.

To investigate the reflector albedo problem, an HTR core was analyzed with the multigroup, multidimensional, finite-difference, diffusion theory

code VENTURE. The preliminary analysis was carried out in cartesian geometry (x-y) with a two-group cross-sectional library, which had been processed for HTR core analysis before this work. A series of calculations was performed in two dimensions and two energy groups.

Table 4.5 presents the relevant information from the reflector fixed-source calculations used to determine the albedos. With respect to the overall results, the computing time and input-output requirements are of interest. The calculational results are presented in Tables 4.6 and 4.7 and in Figs. 4.2 through 4.5. The analysis was performed for a homogeneous core and an asymmetric heterogeneous core. The implication of these results is that space-independent group-dependent albedos may be useful for HTR core analysis. As shown in Tables 4.6 and 4.7, the central processing unit time was decreased by almost a factor of 3, the calculated value for k_{eff} agrees within 0.1%, and the flux values at the core reflector interface agree closely, except at the corner of the core as shown in the flux traverses presented in Figs. 4.2 through 4.5.

Table 4.5. Albedos[a]

α_{11}	0.07436
α_{21}	−0.05730
α_{12}	0.0
α_{22}	0.01263
Central processing unit time, s	7.10
Input-output calls	785

[a]The albedos were calculated with a one-dimensional model of the reflector, diffusion theory, and the same mesh spacing as the reference two-dimensional model. The net neutron current is defined to be positioned in the outward direction from the core.

Although the results in the last section are encouraging, the entire procedure should be performed in hexagonal geometry by use of the four-group cross-sectional set normally used in the HTR core physics. If the

Table 4.6. Homogeneous core

Case	K_{eff}	ϕ_{Core}	ϕ_{Ref}	Time (s)	Input-output calls
Flux on centerline at core reflector interface					
Core-reflector	1.02669	1.350E+08[a]	1.310E+08	527.44	1406
		1.190E+08	1.228E+08		
Core plus albedo	1.02624	1.31786E+08		164.52	868
		1.14879E+08			
Flux at corner of core					
Core-reflector		4.341E+07	4.183E+07		
		7.627E+07	7.728E+07		
Core plus albedo		5.14528E+07			
		8.20911E+07			

[a]Group 1 flux; group 2 flux.

Table 4.7. Heterogeneous core

Case	K_{eff}	ϕ_{Core}	ϕ_{Ref}	Time (s)	Input-output calls
Flux on centerline x					
Core-reflector	0.99676	1.321E+08[a]	1.282E+08	768.63	1559
		1.318E+08	1.354E+08		
Core plus albedo	0.99651	1.286E+08		168.91	844
		1.264E+08			
Flux on centerline y					
Core-reflector		1.077E+08	1.045E+08		
		1.101E+08	1.131E+08		
Core plus albedo		1.035E+08			
		1.033E+08			
Flux at corner of core					
Core-reflector		3.552E+07	3.424E+07		
		7.135E+07	7.212E+07		
Core plus Albedo		3.964E+07			
		7.179E+07			

[a]Group 1 flux; group 2 flux.

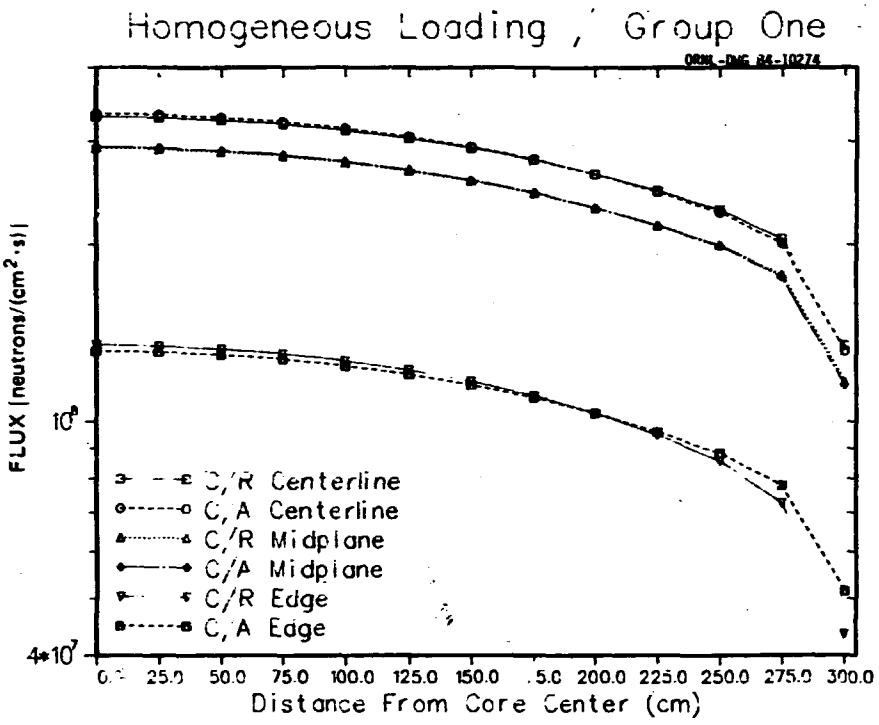

Fig. 4.2. Comparison of core/reflector (C/R) and core/albedo (C/A) group 1 flux traverses for the homogeneous core.

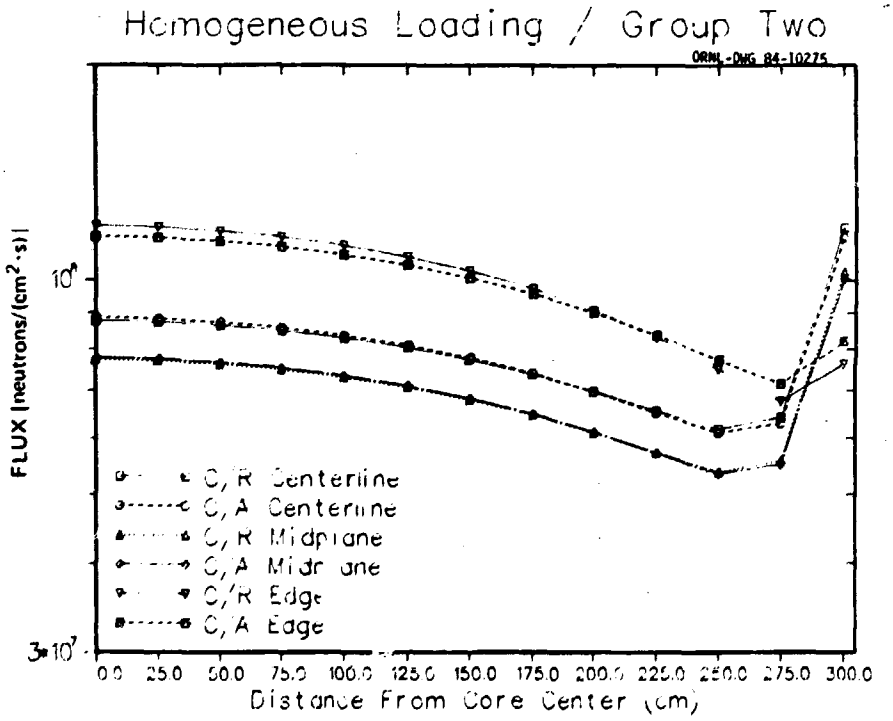

Fig. 4.3. Comparison of core/reflector (C/R) and core/albedo (C/A) group 2 flux traverses for the homogeneous core.

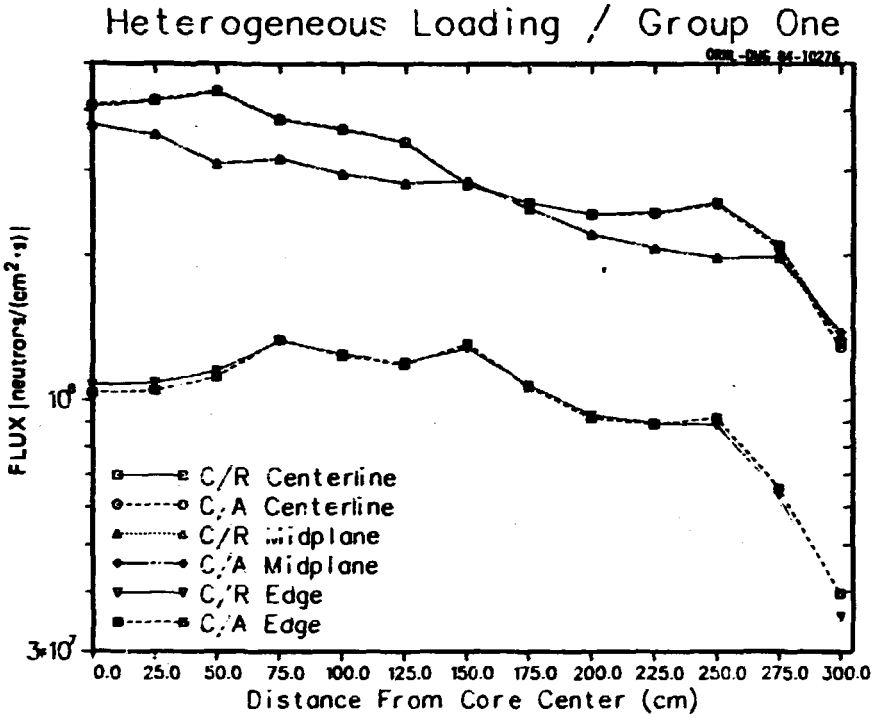

Fig. 4.4. Comparison of core/reflector (C/R) and core/albedo (C/A) group 1 flux traverses for the heterogeneous core.

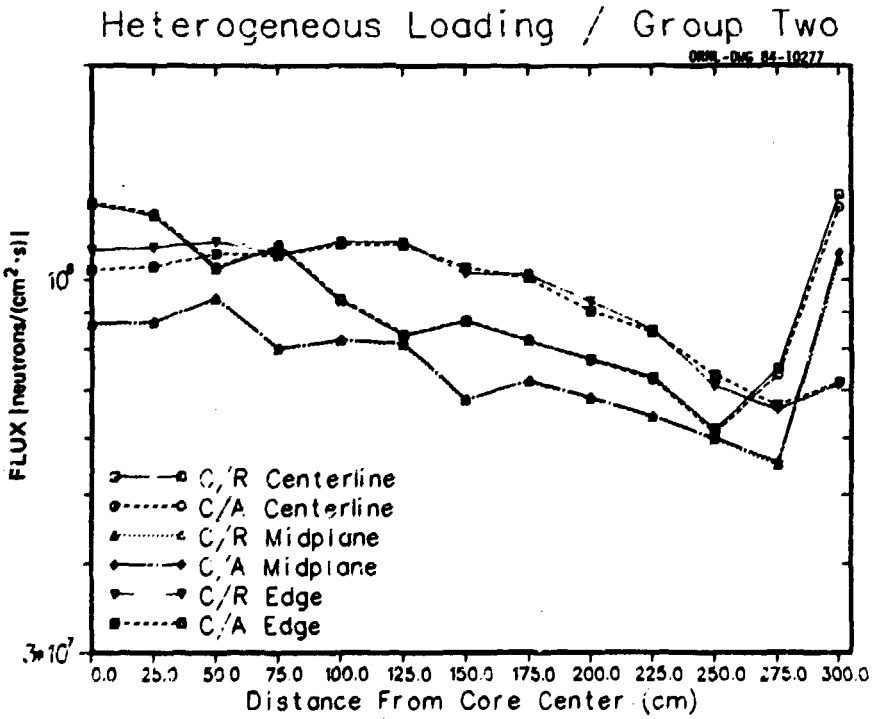

Fig. 4.5. Comparison of core/reflector (C/R) and core/albedo (C/A) group 2 flux traverses for the heterogeneous core.

results again depict excellent agreement with the standard core-reflector eigenvalue calculation, then the four-group albedos can be applied to HTR calculation with minor adjustments in the core cross section at the core-reflector interface. It should be noted that the reflector density strongly influences the albedos. Albedos must be determined as a function of the reflector density. If the comparison between the reference core-reflector eigenvalue calculation and space-independent-group-dependent albedo eigenvalue calculation is poor, space-energy-dependent albedos should be developed.

4.3 THERMAL HYDRAULICS — D. R. Vondy

The effort in this program was directed to implementing the capability for performing thermal hydraulics calculations for the HTR core. The results discussed in Sect. 4.2.1 were produced with this capability. Geometric data and point power densities are used directly in our core analysis calculational system. Temperature feedback capability is included but without considering local resonance shielding effects at this time. The hydraulics problem is solved for one-dimensional coolant flow in a three-dimensional problem, ignoring cross and bypass flows. Blocking into patches is considered, and the required orificing is calculated to effect some specified condition such as equal patch-average coolant exit temperatures. Full core calculations have been performed for 2634 coolant channels and 36,708 power density values. Core pressure drop and coolant channel surface temperatures are determined.

Local thermal cell calculations are then executed over the geometry for treating the flow of heat from the fuel to the coolant channel, typically at 5400 locations for the whole core. Fuel temperature distributions are thus generated and extremes are determined.

A thermal hydraulics calculation is executed at preselected points in the reactor history. Extensive capability is provided to perform auxiliary analysis; for example, results can be generated at reference conditions, and the calculation can be repeated for changes in power level, coolant inlet, and outlet temperature. Certain perturbation

results were coded to be performed automatically, but this has been changed to limit this extended analysis to small problems to hold down computation costs.

The core analysis computation system is modular, permitting quite flexible use of the available capability. For example, given a set of power density data as a best source, the thermal hydraulics code could be executed as many times as desired to explore the effect of changes in one or more of the many variables.

4.4 REFERENCES

1. L. H. Rohach and A. F. Rohach, "Perturbation Theory in Nuclear Fuel Management Optimization," *Nucl. Sci. Eng.* 82, 151–61 (1982).

2. H. J. Fenech et al., *Advanced In-Core Fuel Management Optimization Methodology for PWRs*, EPRI Research Project RP 1251-1, Electric Power Research Institute, Palo Alto, Calif., 1980.

3. G. V. Neill and D. P. Johnson, *COROPT: A Computer Program for Finding Optimal LMFBR Mixed-Oxide Fuel Cores*, General Electric Co., Sunnyvale, Calif., 1977.

4. M. L. Williams, "Development of Depletion Perturbation Theory for Coupled Neutron/Nuclide Fields," *Nucl. Sci. Eng.* 70, 20–36 (1979).

5. PCRV CONCRETE DEVELOPMENT (WBS 3611.01)

D. J. Naus

The concrete development task consists of generic studies designed to provide technical support for ongoing activities related to the prestressed concrete reactor vessel (PCRV), to contribute to the technological data base, and to provide independent review and evaluation of the relevant technology. During this reporting period activities were conducted in three subtask areas: (1) analysis methods development, (2) concrete properties, and (3) model testing technique development.

5.1 ANALYSIS METHODS DEVELOPMENT

The set of computer subroutines developed for finite-element computations of creep effects in reinforced concrete structures was validated.[1] The program, designated as CREEP80, considers the creep law to be linear, uses a rate-type creep law based on expanding the relaxation function of concrete into a series of real exponentials (Dirichlet series), incorporates material properties either as empirical creep data or as the double-power law for creep, utilizes a step-by-step stable iteration procedure in combination with iterations in each time step, incorporates temperature variations ($\leq$80°C) into creep behavior, and defines shrinkage either by using formulas or by specifying a set of experimentally observed values. This program was validated against results from seven multiaxially loaded concrete cylinders that underwent creep tests,[2] and the results were collected.[3]

5.2 CONCRETE PROPERTIES

Objectives of the concrete properties subtask are to develop a bank of highly reliable data and to support development of improved analysis

methods. Current activities are related to the review of concrete behavior under uniaxial and multiaxial states of stress and the development of high-strength concrete mix designs in support of the High-Temperature Reactor (HTR) PCRV design for a steam cycle-cogeneration (SC-C) plant.

5.2.1 Concrete Behavior Under Uniaxial and Multiaxial States of Stress

The behavior of concrete material systems with respect to fracture, analytical treatment, and behavior under uniaxial and multiaxial stresses was investigated. Specified items addressed include (1) concrete modeling, crack propagation, and fracture; (2) analytical treatment of time-dependent behavior; (3) deformation and fracture under various stresses; (4) historical review of studies to determine concrete behavior under multiaxial stresses; (5) commentary on test methods used to study concrete behavior under multiaxial stresses; and (6) current practice for multiaxial loading considerations in PCRV design.[4]

5.2.2 Development of High-Strength Concrete Mix Designs in Support of HTR-SC-C PCRV Design

Recent design optimization studies at GA Technologies indicated that a significant PCRV size reduction can be effected with 55-MPa (8000-psi) concrete in conjunction with large-capacity [13.3-MN (1500-ton)] prestressing tendons.[5] This can lead to substantial cost savings in both the PCRV and secondary containment. However, the use of 55-MPa (8000-psi) concrete for the PCRV design will involve incremental material and developmental costs because previous PCRV designs for the HTGR-SC plants (Fulton and Summit) were based on 45-MPa (6500-psi) concrete mixes. Results of a cost trade-off study at GA Technologies indicate that, despite the incremental costs of development of high-strength concrete mix designs, there will still be a cost savings of several million dollars from a reduced PCRV size.[5]

In conformance with requirements outlined by GA Technologies,[6] a testing program was defined to develop high-strength concrete mix designs with aggregate materials from four sources, which are in close proximity to areas representing potential sites for an HTR-SC-C plant.[7] These sites

have been identified as Florida City–Turkey Point, Florida; Port Arthur, Texas; Pennsylvania–Delaware border area; and Blythe, California. The program will be conducted in three phases. Phase 1 involves an evaluation of the suitability of admixtures, one cement, and aggregate materials from each of the areas; development of high-strength concrete mix designs; and determination of strength and elastic properties at various ages and under different curing conditions. Phase II is an evaluation of the effect of elevated temperatures up to 316°C (600°F) on both sealed and unsealed specimens. Phase III involves a determination of the creep characteristics of the concretes developed under Phase I when subjected to loadings representing 30, 45, and 60% of their ultimate strength at temperatures up to 71°C (160°F). Thermal properties and the effects of thermal cycling on strength and elastic properties will also be evaluated under this phase of testing. More details on each phase of the high-strength concrete testing program have been accumulated.[7]

5.3 MODEL TESTING TECHNIQUE DEVELOPMENT

Section III, Div. 2 of the ASME "Code for Concrete Reactor Vessels and Containments" requires a model test whenever a model of a prototype with characteristics similar to those of current design has not been constructed and tested in accordance with code provisions or if analytical procedures to predict ultimate strength and behavior in the range approaching failure have not been established.[8] Because the newer generation PCRV design includes an asymmetric cavity arrangement and offset core, existing model test data developed for single-cavity and symmetric multicavity PCRV designs may not meet the intent of the above requirements. In addition, the complexity of the new design may require further development and verification of the three-dimensional finite-element analytical codes, especially for determination of long-term time-dependent behavior and for the prediction of ultimate strength in the load range approaching failure conditions. Contingency plans are therefore being developed so that a PCRV model test can be conducted in a timely manner should it be established as a requirement for licensing.

Using results of a review of PCRV-related model tests,[9] we established that two model testing areas require additional development: circumferential prestressing and leaktight liner systems. A test program has therefore been under way to establish satisfactory methods for circumferentially prestressing PCRV models ranging in size from 1:30- to 1:10-scale and for lining the models so that they do not leak prematurely to terminate a test. Also included in this activity was an evaluation of the performance of fibrous concrete.

Activities related to prestressing the models circumferentially were merely to identify a prestressed concrete pipe manufacturer who could apply prestress at a prescribed force level to models ranging in size from about 1 to 4 m in diameter. Relative to the liner system, a design was developed to incorporate the use of a 12-gage AISI 1008 drawing-quality steel in conjunction with a flanged head. (The flanged head eliminates the corner joint, which has been a weak point in previous liner designs.)

To demonstrate the validity of the above concepts, a 1:30-scale single-cavity PCRV model was fabricated with a representative high-strength concrete [79.42 MPa (11,520 psi)]. The model, designated PV34, was tested by hydraulically pressurizing it to failure. Model failure occurred in the head region at 24 MPa (3475 psi) (Fig. 5.1). During the test both the liner and circumferential prestressing systems functioned as designed. Techniques have therefore been demonstrated for solving two of the problem areas for successful testing of a PCRV model.

As noted earlier, a second 1:30-scale single-cavity PCRV model was also fabricated with comparable strength [69.29-MPa (10,050-psi)] fibrous concrete to provide an indication of the relative merits of this material for PCRV construction. The fibrous concrete model, designated PV35, was also tested by hydraulically pressurizing it to failure. Model failure occurred by rupturing 23 wraps of the circumferential prestress wire at 27.72 MPa (4020 psi). Even though the circumferential prestressing had failed, the liner remained leaktight and continued to contain pressure. As noted in Fig. 5.2, the head of model PV35 remained intact, and the few cracks that occurred were relatively small and closed on depressurization. Test results indicated that the shear strength of fibrous concrete is at

ORNL-PHOTO 7467-83

Fig. 5.1. The PV34 head after failure testing. Diameter of head, approximately 1 m.

ORNL-PHOTO 7468-83

Fig. 5.2. The PV35 head after failure testing. Diameter of head, approximately 1 m.

least 15% greater than that of plain concrete at comparable compressive strength levels and that fibrous concrete exhibits potential as a PCRV construction material.

Details on the model testing techniques developed, testing procedures, and test results have been accumulated.[10]

5.4 REFERENCES

1. Z. P. Bazant and E. C. Rossow, unpublished data, August 1981.

2. J. E. McDonald, *Time-Dependent Deformation of Concrete Under Multiaxial Stress Conditions*, ORNL/TM-5052, October 1975.

3. J. R. Dougan, unpublished data, October 1983.

4. D. J. Naus, unpublished data, May 1983.

5. K. C. Cheung, GA Technologies, San Diego, Calif., unpublished data, Dec. 17, 1982.

6. K. C. Cheung, GA Technologies, San Diego, Calif., unpublished data, Dec. 24, 1982.

7. D. J. Naus, unpublished data, May 1983.

8. "Code for Concrete Reactor Vessels and Containments," *ASME Boiler and Pressure Vessel Code*, Nuclear Power Plant Components, Sect. III, Div. 2, American Society for Mechanical Engineers, New York, 1975.

9. D. J. Naus, unpublished data, June 1980.

10. C. B. Oland, unpublished data, September 1983.

6. STRUCTURAL CERAMICS TESTING (WBS 3611.02)

D. J. Naus and P. L. Rittenhouse

6.1 THERMAL BARRIER HARD CERAMIC MATERIALS — D. J. Naus

In the bottom head region of the core outlet plenum, pads fabricated from hard ceramic materials and separated by interface materials are used to support the graphite posts that support the core. We are evaluating candidate ceramic pad materials for their ability to withstand representative thermal gradient and mechanical loading conditions.

During the past year three candidate ceramic pad materials were investigated: grade 85 alumina, grade 995 alumina, and fused silica. Test articles fabricated from these materials were in the form of right circular disks having a centrally located cylindrical hole extending vertically through each disk. By using a specially designed test fixture that incorporated either flat or conical platen sets, we subjected these pads to mechanical loading conditions to provide a parametric representation of what would be induced into the ceramic pads because of thermal gradients. This phase of testing, which is part of an overall series of tests,[1] was conducted only at room temperature.

We conducted 34 tests in which the candidate ceramic pads were mechanically loaded with the test fixture presented in Fig. 6.1. The pads were initially loaded with flat platens to a load of 890 kN (200 kip). At the conclusion of the flat platen loading, the flat platens were replaced by conical platen sets having the required taper as specified in our plan,[2] and the loading was repeated until either the pad failed (cracked) or a load of 890 kN (200 kip) was achieved. Platen offsets used in the investigation ranged from 0 mm (flat) to 0.36 mm (0.014 in.). During each loading cycle strain, displacement and acoustic emission data were obtained as a function of load.

ORNL-PHOTO 8289-82

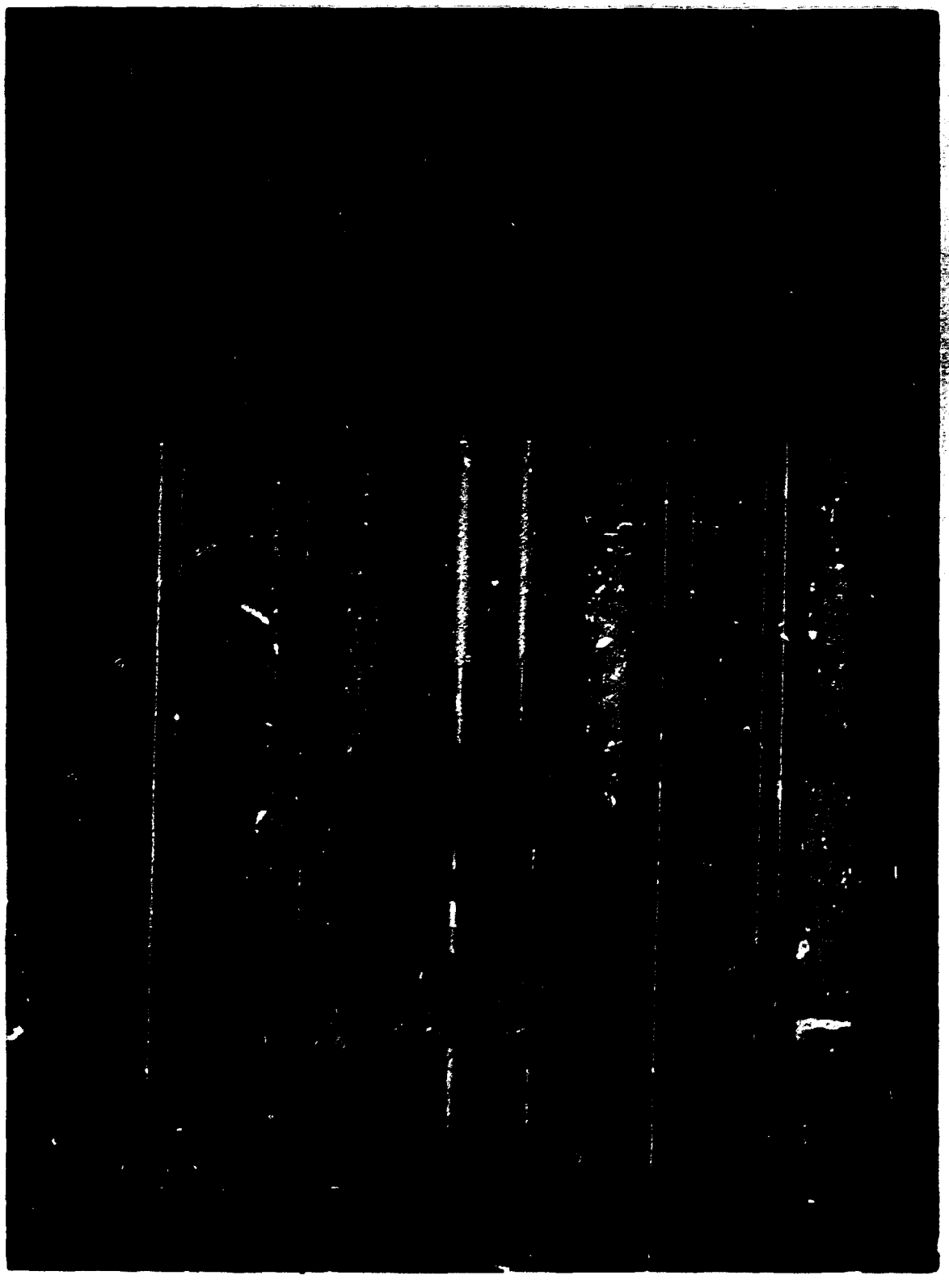

Fig. 6.1. Test fixture used to load thermal barrier hard ceramic pads mechanically.

Although a detailed analysis of the results was not our responsibility, a few general conclusions can be derived from the investigation: (1) flat platens (no induced pad rotation) did not produce specimen failures for either alumina or fused silica materials at the load level examined [890 kN (200 kip)]; (2) specimens that failed exhibited only one apparent mode of failure (failure in three or less cracked sections with the cracks not extending completely through the specimen thickness over its entire diameter so the specimen remained intact); (3) the fused silica pad material was significantly more active from an acoustic emission standpoint than were the alumina pad materials; (4) acoustic emission activity tended to decrease as the number of interface layers between the platens and pad increased; (5) specimen-to-specimen acoustic emission activity with respect to total counts for pads fabricated from the same material and tested under the same conditions was very good; and (6) although based on a very limited amount of data, it appears that acoustic emission exhibits a possibility as a nondestructive evaluation screening technique for identifying defective pads.[3]

6.2 CREEP OF CERAMICS — H. E. McCoy

Compressive creep tests are in progress on SiO_2, grade TM 11982. The tests are operating at 649°C and 69 and 35 MPa. They have been in test about 14,500 h, and each has strained about 1.6%. The creep behavior is characterized by a period of primary creep decelerating to a very low steady-state creep rate. One test each of two types of Al_2O_3 (AD-998 and AD-85) has run 3000 h at 750°C and 69 MPa. Very little strain has occurred in the Al_2O_3 materials under these test conditions.

6.3 CHARACTERIZATION OF CORE SUPPORT CERAMICS — R. J. Lauf and H. E. McCoy

Three candidate materials for the High-Temperature Reactor (HTR) core support pad have been examined in the as-received condition and after creep testing in simulated HTR-He. The long-term goal of this program is to develop a reliable data base and to relate observed creep behavior to specific microstructural mechanisms. Only in this way can we make reasonable estimates of the long-term stability of the core support pads under steady-state as well as accident conditions.

It is important to note that, to identify the dominant creep mechanism with certainty, it is necessary to measure the creep rate at several temperatures and thereby to determine the activation energy of the dominant deformation process. Until that is done for our materials, any conclusions must be regarded as tentative.

The materials examined are Thermo Materials fine-grained fused silica and Coors AD-85 and AD-995 aluminas. Creep data are summarized in Table 6.1 for the materials examined thus far. Additional creep tests are in progress.

Table 6.1. Creep test results on core support ceramics

Test	Material	σ_{Max} (MPa)	σ_{Max} (psi)	T (°C)	Time (h)	Steady-state creep rate (h^{-1})
23344	TM SiO_2	20.7	3,000[a]	538	7,000	3.29×10^{-7}
23078	AD-85	69.0	10,000[b]	750	11,085	1.17×10^{-7}
23093	AD-995	69.0	10,000[b]	750	9,501	1.05×10^{-7}

[a]Four-point bending.

[b]Compression.

6.3.1 Fused Silica

Thermo Materials fine-grained fused silica was tested in four-point bending at 538°C and a maximum stress of 20.7 MPa (3000 psi). A period of relatively rapid primary creep lasted about 1500 h, during which approximately 3.25% creep strain occurred. From 1500 to 7000 h, the steady-state creep rate was approximately 3.29×10^{-7} h^{-1}.

No microstructural changes were observed other than some darkening of the larger SiO_2 grains. This is attributed to partial reduction of the SiO_2 by the highly carburizing atmosphere. The effect of this reduction on the fracture toughness and thermal conductivity of the fused silica has not yet been determined.

X-ray diffraction showed no devitrification of the glassy silica after an earlier creep test. Two very small diffraction peaks were in both the creep-tested and the as-received material, but the bulk of the fused silica was amorphous before and after creep testing.

6.3.2 AD-85 Alumina

Coors AD-85 alumina was tested in compression at 750°C and a stress of 69.0 MPa (10,000 psi). Primary creep lasted about 200 h and accounted for about 0.55% total strain. The steady-state creep rate up to 11,000 h was about 1.17×10^{-7} h^{-1}, accounting for an additional 0.1% creep strain.

No microstructural changes were observed optically. Transmission electron microscopy showed the development of dislocation arrays in the Al_2O_3 grains (Fig. 6.2). Some intergranular material was shown to be amorphous by electron diffraction, but based on x-ray results the total amount of glassy material is quite small. Some spinel ($MgAl_2O_4$) was identified by x-ray diffraction (XRD) before and after creep testing. The

E-46572

Fig. 6.2. Dislocation array in Al_2O_3 grains in AD-85 alumina, suggesting that strain hardening is taking place.

presence of spinal in AD-85 is expected on the basis of its composition. Because of the observed dislocation arrays and limited amount of glass, it appears that the transition from primary to secondary (steady-state) creep is related to work hardening within the Al_2O_3 grains.

6.3.3 AD-995 Alumina

Coors AD-995 alumina was tested in compression at 750°C and a stress of 69.0 MPa (10,000 psi). The total creep strain after 9500 h was only 0.12%. Because of the scatter in the data resulting from temperature fluctuations as well as the small amount of total strain, it is difficult to determine the steady-state creep rate. It appears to be about $1.05 \times 10^{-7}\ h^{-1}$, but this number is not highly reliable.

Optical microscopy showed no microstructural changes after creep testing. Transmission electron microscopy showed the development of dislocation arrays, often leading to subgrain formation (Fig. 6.3). The dislocation density was less than that in the AD-85 sample, consistent

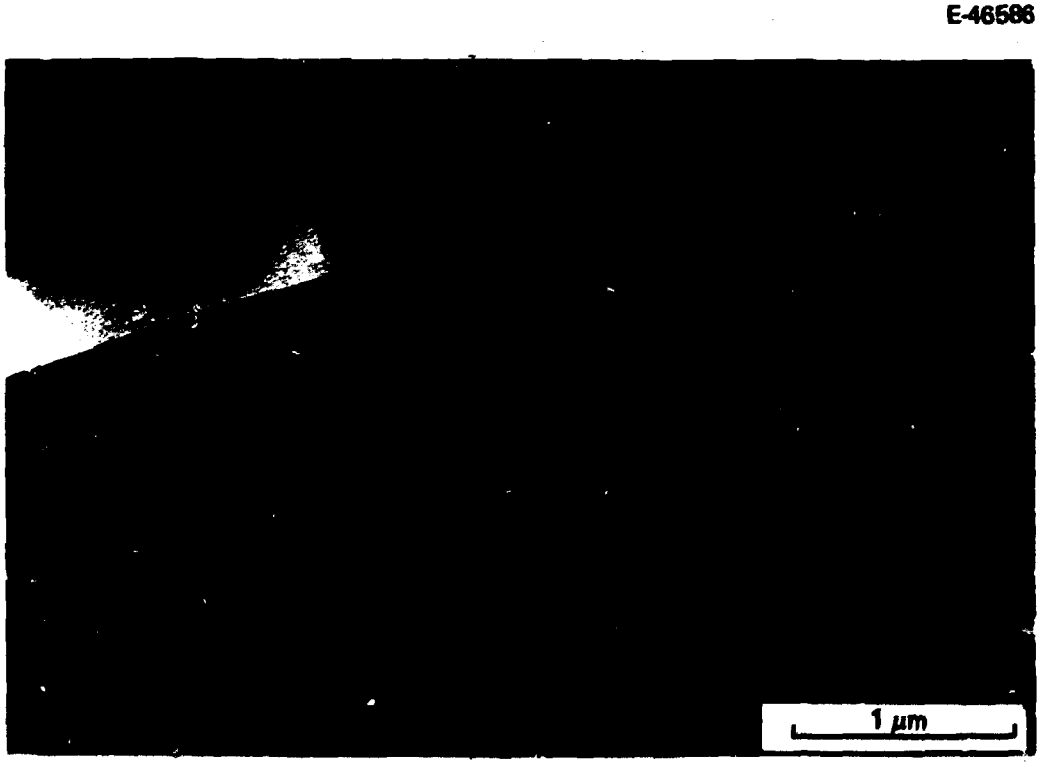

Fig. 6.3. Creep tested AD-995 alumina. Note dislocation array forming a subgrain boundary.

with the lower total strain experienced by the AD-995. No glass was found, although pockets of intergranular material (probably spinel) were observed. No phases other than Al_2O_3 were detected by XRD before or after creep testing.

As in the case of AD-85 alumina, the buildup of dislocation arrays in AD-995 is consistent with the model of work hardening as the mechanism responsible for the transition from primary to secondary creep.

6.4 REFERENCES

1. R. K. Luci, GA Technologies, San Diego, Calif., unpublished data, Dec. 23, 1982.

2. D. J. Naus, unpublished data, March 1983.

3. C. B. Oland and D. J. Naus, unpublished data, August 1983.

7. HTR FUEL MATERIALS QUALIFICATION (WBS 3650.02)

M. J. Kania and F. J. Homan

7.1 INTRODUCTION

The High-Temperature Reactor (HTR) Fuel Materials Qualification Program at Oak Ridge National Laboratory (ORNL) continues as part of the national fuel development effort being conducted in cooperation with GA Technologies (GA). The ORNL portion of the program includes irradiation testing of fuel fabricated by GA in irradiation capsules assembled by ORNL and operated in ORNL reactors. We also conduct postirradiation examinations (PIEs) on the irradiated fuel in special equipment developed for this purpose. The GA responsibilities include interface with core designers and with licensing activities and development of fuel performance models with data developed from the irradiation tests conducted at ORNL. GA Technologies also has responsibility for fuel manufacturing, including design, process development, and quality control.

In addition to the cooperation with GA, the ORNL program includes specific cooperative tasks with the German Nuclear Research Center at Jülich [Kernforschungsanlage (KFA) Jülich]. The cooperation with KFA is part of the formal agreement between the U.S. and German governments for gas-cooled reactor development. Several cooperative projects were completed during the past several years. The two active areas of cooperation during this reporting period are described here.

At the end of 1983 the Fuel Materials Qualification Program was organized around four subtasks: (1) Irradiation Testing, (2) PIE, (3) U.S.–Federal Republic of Germany (FRG) Cooperative Work, and (4) PIE Equipment Development and Maintenance.

7.1.1 Irradiation Testing

Irradiation of capsules HRB-17 and -18, which make up the hydrolysis experiment, has been postponed until late FY 1984. This experiment is designed to determine the behavior of Triso-coated UCO (UO_2 and UC_2 mixture) fissile particles that fail in the presence of moisture. Progress during 1983 includes the completion of various subassemblies necessary for capsule construction and the assembly and testing of the moisture generation system and the reactive gas analysis system necessary for capsule operation. Design modifications to the in-core portion of capsules were also completed. Bonded fuel specimens, encapsulated unbonded particle samples, and encapsulated graphite diffusion samples for inclusion in the HRB-17 and -18 capsules were received from GA.

Documentation of the HRBTAN computer code in the form of a user's manual was completed. This code provides the necessary analytic tool for HRB-series capsule thermal analysis at the design, operation, and PIE states of the experiment.

7.1.2 Postirradiation Examination

Capsule HT-35 was discharged from the High Flux Isotope Reactor (HFIR) in November 1980 and has remained in the PIE schedule with a relatively low priority since that time. Nearly all the PIE work has been completed on the fissile and fertile fuel from this capsule during 1983, with the exception of the postirradiation gas analysis (PGA) of the unbonded fertile fuels. Details of the completed PIE work are presented in Sect. 7.3.1.

1. Transmission electron microscopy (TEM) of silicon carbide (SiC) coatings removed from irradiated UCO fissile particles indicated a significant difference in their microstructure when compared with similar coatings examined from irradiated carbon (inert) particles. These differences are attributed to differences in operating temperature between the inert and fissile particles and were more dramatic in the higher temperature portion of the capsule. Fission products were found in the SiC coating of

one specimen in a similar location and configuration to those observed in previous out-of-reactor annealing studies. No uranium was detected in the coating, but evidence of plutonium was found.

2. Irradiated microsphere gamma analyzer (IMGA) examinations were completed on all the fissile and fertile particle batches from this capsule. One fissile particle batch exhibited a large number of failed particles in both the high- and low-temperature portions of the capsule. Silver retention for all the fissile batches was on the 50 to 60% level and is attributed to uncertainties in our ability to calculate accurate inventories for ^{110m}Ag. Large particle-to-particle variation in silver retention was observed and was most variable in the high-fluence high-temperature region. The IMGA examinations were also completed on selected fertile fuels scheduled for PGA examination.

Analyses of IMGA examinations conducted on irradiated fuel from capsules HRB-11 and -12 and not previously published were completed. The examinations were performed on selected fissile fuels fabricated with SiC and zirconium carbide (ZrC) Triso coatings as part of an assessment of ZrC irradiation performance in comparison with SiC performance. The ZrC Triso-coated fuel indicated failure rates 2 to more than 100 times greater than the SiC Triso-coated fuel. This large difference is attributed to the relatively low level of fabrication development of the ZrC design rather than to any inherent problems with the ZrC in an irradiation environment.

Metallographic examinations on the UCO fissile particle batch 6157-11-020 irradiated in capsule HRB-15a indicated severe corrosion of the SiC layer, which in some cases nearly penetrated the layer. The fission product palladium was identified through electron microprobe examinations as present in those areas of corrosion. Analysis of the SiC coating performance in capsule HRB-15a fuels has raised a number of unanswered questions about fabrication and performance. These include the role that SiC microstructure plays, the causes for batch-to-batch variations in resistance to palladium attack, and the observed particle-to-particle variation in silver retention.

Reevaluation of the silver release data generated through IMGA examination and analysis on GA fuel irradiated in capsule HRB-15b supports the conclusion that all the low-enriched uranium (LEU) fissile particle types retained cesium and silver. These data, the HRB-15a data, and German data lend support to a strongly temperature-dependent silver release model for irradiation temperatures above 1050°C.

Preliminary observations on the metallography of the HRB-16 fuel rods indicate that some fissile fuel batches experienced severe SiC corrosion but that other batches in nearby irradiation positions experienced none. The particle batch experiencing the most severe corrosion was the UCO fissile batch 6157-11-010. This is a sister batch to 6157-11-020, which also experienced severe corrosion but in irradiation capsule HRB-15a.

Analysis of the long-term acid-leach measurements on GA fuels from experiment R2-K13 revealed a low number of particles with total coating failures: 0.3 to 1.4% for fissile fuel and 0.1 to 0.4% for fertile fuel. Both fuel types were Triso coated. The electrolytic deconsolidation and preliminary IMGA results revealed a much higher number of failed fissile particles in fuel rod 2B2, which was irradiated at a mean operating temperature of 1170°C for more than 516 full-power days.

7.1.3 U.S.-FRG Cooperative Program

The ORNL and KFA-Jülich have agreed to extend PWS FD-1 to include all performance data for all fuel cycles. The ORNL contribution (report) to this effort was completed. This report concentrates on design and fabrication influences on coated-particle fuel performance.

The IMGA examinations were completed on irradiated German fuels from set 2 under PWS FD-20. These included unbonded particles from experiments FRJ2-P23, FRJ2-P25, and DR-S6. Detailed analyses of the IMGA data are under way and will be completed in early 1984.

7.1.4 Equipment Development and Maintenance

The availability of the IMGA system was much improved in 1983 compared with the previous year (80% availability versus 30%). This is attributed to much improved maintenance and the installation of an additional

data storage device. A new pulse height analyzer (PHA) system to replace the original PHA was purchased and delivered. An ND-6700 system with attendant operating system and data analysis software was selected.

The upgraded PGA system is near full operation. The IQ-200 mass spectrometer system has been fully interfaced to a DEC LSI-11/23 computer, and data acquisition software has been written and implemented. The system is configured so that small orifices control the inlet of gas to the spectrometer. With correctly sized orifices, the gas pulse from a single particle can be extended to 30 min compared with less than 1 s during previous PGA operation. This will improve the accuracy and sensitivity of our gas inventory measurements.

7.2 IRRADIATION CAPSULE ASSEMBLY AND OPERATION — J. A. Conlin

7.2.1 Hydrolysis Experiments HRB-17 and HRB-18 — R. L. Senn

Irradiation of the two capsules that make up the hydrolysis experiment has been postponed to late FY 1984. This experiment, which was previously described,[1] is designed to determine the behavior of Triso-coated dense UCO fissile particles that fail in a moist environment. Progress during 1983 included completion of various subassemblies necessary for construction of the capsules and for assembly and testing of the moisture generation and gas analysis systems necessary for capsule operation. Certain design modifications to the in-core portion of the capsules were also completed.

7.2.1.1 Capsule Design and Construction — R. L. Senn

Several months were consumed in attempting to achieve an acceptable braze of the thermocouples and gas lines to the two bulkheads located at the top of the in-core portion of the capsules. Acceptable leak-tight brazes were finally achieved, and construction of the capsules was moving forward at the end of this reporting period.

The following materials were received from GA for installation in capsules HRB-17 and -18:

1. twelve fuel rods (six for each of the two capsules), each packed and labeled for its intended position within the desired capsule,
2. two Incoloy-clad unbonded particle-tray sample containers (one for each capsule), each about 2 cm (0.75 in.) long by about 1 cm (0.5 in.) in diameter, and
3. two niobium-clad graphite-diffusion sample containers (one for each capsule), each about 13 cm (5 in.) long by 1 cm (0.5 in.) in diameter.

Note that the inclusion of a single niobium-clad diffusion experiment in each capsule represents a modification of the previous design, which included stainless steel cylinders in the lower part of the capsule assembly instead of the long diffusion experiment. Stainless steel cylinders are still being used for heat generation (from nuclear heating) in the area above the six fuel rods in each capsule.

A thermal analysis was completed to determine the effects of replacement of the previously used stainless steel cylinders with the sealed Incoloy-clad unbonded particle-tray experiment and the sealed niobium-clad graphite-diffusion sample container described above. Temperatures were calculated at various levels and for various times during the experiment. These values were compared with I. I. Siman-Tov's previous calculations for similar time periods for the fuel rod just above the unbonded particle experiment. The analysis showed that the particle tray assembly will provide somewhat more heat during most of the irradiation period than will the previously planned stainless steel cylinder. Similarly, the graphite diffusion container temperatures are satisfactory for experiment control, although the temperatures drop off toward the bottom of the capsule.

Analysis of the various temperatures in the experiment during various days and cycles of the experiment shows that achieving the design nominal fuel inside-radius temperature of 800°C continues to be possible throughout the life of the experiment, except for the first days of operation in cycle one, when the temperatures will be high until the initial ^{235}U

loading is burned out. Therefore, the new design appears to be satisfactory for the unbonded particle experiment to serve as a guard heater for the lower fuel rod.

A further minor change in capsule design included the placement of three piggyback samples in holes drilled from the bottom of the graphite specimen holder to about the midplane of the HRB-18 capsule. Each piggyback will contain eight samples encapsulated in a 0.22-cm (0.087-in.) OD by 0.17-cm (0.067-in.) ID Nb-1% Zr tube sealed at both ends with brazed niobium spheres in a helium-argon atmosphere under a slight vacuum. Of the 24 samples, 22 contain a single Triso-coated fissile particle, and two contain a short length of pure silver wire. POCO graphite pieces prevent the particles and wires from contacting the niobium containers.

Three similar but unfueled piggyback assemblies will be installed in the HRB-17 capsule to keep each of the capsules identical with each other in heat-transfer characteristics. The difference of a few fissile particles should be insignificant.

7.2.1.2 Moisture Generation and Gas Analysis Systems — D. R. McNeilly and R. L. Senn

The moisture generation system was assembled and tested. We experienced some difficulty with ice forming over the surface of the refrigerant as a result of moisture in the ambient air that circulated above the refrigerant. This problem was resolved by sealing the area to prevent ambient air from entering and by using dry instrument air as a cover gas. A level probe was also developed to detect the refrigerant level and to provide an alarm when the level deviates from a preset point. A spare moisture generator and an ice bath system were procured to serve as backups in the event of equipment failure.

A glove box was procured and modified to contain the gas chromatograph and other gas analysis equipment. The gas chromatograph was tested successfully except for the measurement of hydrogen. We installed a new column that successfully measured hydrogen, but the presence of neon (which will be part of the capsule mixed control gas) masks the hydrogen results. Further consultation with experts in gas chromatography indicated that an

even longer column [1.18-m (25-ft) versus the 0.57-m (12-ft) column already installed] should provide adequate separation of the hydrogen from neon. The longer column has been ordered.

Automatic control of the six-way valves (used to switch various gas streams to the gas chromatograph) by the Spectro Physics integrator was achieved. The Spectro Physics integrator controls the gas chromatograph, analyzes and prints out the results, and provides an automatic report. These features are all working satisfactorily. The integrator was also interfaced to ORRDACS, our central data acquisition and control computer.

The standard instrument diagrams and drawings were modified as required for this experiment and issued. Actual modification and calibration of the standard instrumentation could not be accomplished during this work period because of the extended shutdown of the HFIR and construction work occurring in the experiment control area.

7.2.2 HRB Thermal Design Code, HRBTAN — I. I. Siman-Tov

The HRBTAN code was developed specifically for the thermal analysis of HTR-HRB capsule fuel irradiation experiments in the HFIR. A draft of a user's manual for this code was written.

The HRBTAN code provides the necessary analytical tool for an HTR-HRB capsule thermal analysis at the design, operation, and postirradiation stages of the experiment. The code allows for time and spatial variation of fission and gamma heat within the capsule. It also takes into account the variation in fuel composition with time and position caused by burnup, by ^{233}U and ^{239}Pu generation, and by neutron flux variation. The code simplifies previous procedures but is limited to a specific geometry of seven radial regions. This user's manual provides guidelines for input preparation for the HRBTAN code and describes the output generated. The manual has a brief description of the thermal analysis problem to be solved and the mathematical model used. A sample problem is included with the HRBTAN code listing.

7.3 POSTIRRADIATION EXAMINATION OF IRRADIATION EXPERIMENTS

During this reporting period PIE efforts were concentrated on ORNL fuels irradiated in capsule HT-35 and GA-fabricated fuels irradiated in capsules HRB-15a, -16, and R2-K13. Detailed analyses of previously acquired IMGA data were conducted on ORNL and Los Alamos National Laboratory fuels irradiated in capsules HRB-11 and -12 and on GA fuels irradiated in capsules HRB-15a and -15b. At the end of the reporting period, irradiated fuels from experiments HT-35, HRB-16, and R2-K13 remain in PIE at the High-Radiation Level Examination Laboratory. Fission and activation-product inventory calculations also continue as part of a low-level effort to establish an accurate data base for predicting ^{110m}Ag in LEU fuels.

7.3.1 Capsule HT-35 — M. J. Kania, F. J. Homan, and R. J. Lauf

Irradiation experiment HT-35 was the last HFIR target capsule irradiated in a test series that dates back to 1968. The experiment was designed to answer a number of fuel performance-related questions that arose during the examination of fuel from previous irradiation capsules. It was a cooperative test with GA, and the capsule was irradiated for 2140.5 h of full reactor power (100 MW) and discharged from HFIR in November 1980. The capsule received a relatively low priority during the postirradiation phase, and all the planned examinations have not yet been completed. A detailed description of the capsule design and irradiation operating history has been published.[2] Capsule disassembly and metrology performed on the graphite and fuel components were reported previously.[3] Examinations of the SiC coatings from inert (carbon) kernels by TEM before and after irradiation were also reported.[4]

Examinations completed on the irradiated SiC coatings from fuel particles by TEM are reported here. In addition, the fission-product retention examinations by IMGA of ORNL fissile and fertile batches have been completed[5] and are also reported here. The only remaining task to be completed is the fission gas retention examinations by the PGA system.[6] This system is just now becoming fully operational, and these measurements are

expected to be completed in the first quarter of FY 1984. Upon completion of this work, a final report will be prepared on the irradiation experiment HT-35.

7.3.1.1 TEM Examination of Irradiated SiC Coatings

The purpose of this work is to determine the effect of microstructural features (and hence deposition process variables) on the irradiation performance of the SiC coatings. A great deal of out-of-reactor work has been done to determine the kinetics of fission product–SiC interactions.[7] The examination of SiC irradiated in capsule HT-35 involves SiC specimens deposited on inert (carbon) particles and SiC specimens deposited on fissile particles. Together with out-of-reactor work, these experiments allow us to study irradiation damage and fission product interactions separately as well as together.

Silicon carbide coatings with systematically varied microstructures were deposited on inert particles and irradiated to fast neutron fluences up to 8.8×10^{25} neutrons/m^2 ($E > 29$ fJ) in the magazine end plugs of HT-35. The results of this study were reported elsewhere;[4] important findings are

1. Irradiation at 1050°C and below produces small 5-nm (~50-Å) defect clusters (Fig. 7.1), which frequently lie along the remains of stacking faults. A defect-free region about 10 nm (100 Å) wide exists along grain boundaries. Irradiation at higher temperatures (1150°C) produces voids (Fig. 7.2) that are typically 5 nm (50 Å) in diameter. The voids lie parallel to remnant stacking faults in some grains but are distributed randomly in others. The foregoing observations are in substantial agreement with the work of Price, who used pyrolytic SiC disks rather than actual coated particles.[8]
2. The influence of process variables on irradiation behavior is summarized as follows: (a) A relatively high initial stacking fault density tends to inhibit void formation, suggesting that stacking faults, like grain boundaries, form a sink for point defects. (b) Any cavities initially present in SiC are not "healed" during irradiation, so a low-density coating remains inferior to a high-density coating.

E-38089

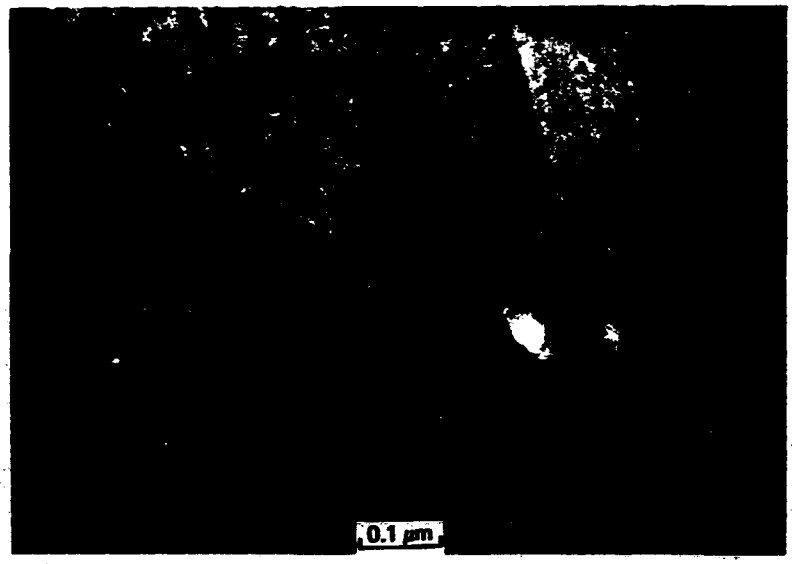

Fig. 7.1. Damage clusters (dark spots) in silicon carbide from an inert particle irradiated in magazine 1 bottom end cap of HT-35 (fluence = 7.3×10^{25} neutrons/m^2).

E-44594

Fig. 7.2. Voids in SiC from an inert particle irradiated in HT-35 magazine 3 bottom end cap at approximately 1050°C to a fast neutron fluence of 7.5×10^{25} neutrons/m^2.

Because of the difficulty in preparing coatings from fissile particles for TEM (notably their high activity), this somewhat more limited phase of the work sought to address the following questions: Is the mechanism of fission product attack or transport influenced by neutron irradiation? Do irradiation-induced voids take part in fission product redistribution? Is irradiation damage modified or aggravated by the presence of fuel or fission product elements?

Silicon carbide coatings from UCO particles (~7% ^{235}U) irradiated in capsule positions 1, 3, 14, and 16 were examined by TEM. Specimens from position 1 (4.1×10^{25} neutrons/m^2) and position 3 (4.7×10^{25} neutrons/m^2) contain defect clusters (Fig. 7.3) indicative of the relatively low irradiation temperature. Note the similarity to Fig. 7.1; comparison of the

E-45474

Fig. 7.3. Defect clusters in silicon carbide from a UCO particle irradiated in position 1 of HT-35 (fluence = 4.1×10^{25} neutrons/m^2).

size of the damage clusters shows that the actual irradiation temperature of the fuel particle itself appears to be somewhat higher than that of the inert particles in higher flux positions. This is a result of the heat generated within the fissile particles.

The temperature difference between fissile and inert particles becomes more dramatic in the higher temperature positions. Specimens from position 14 (7.5×10^{25} neutrons/m^2) and position 16 (7.9×10^{25} neutrons/m^2) contain large tetrahedral voids (Fig. 7.4), suggesting a particle surface temperature several hundred degrees greater than that of inert particles in nearby end caps.

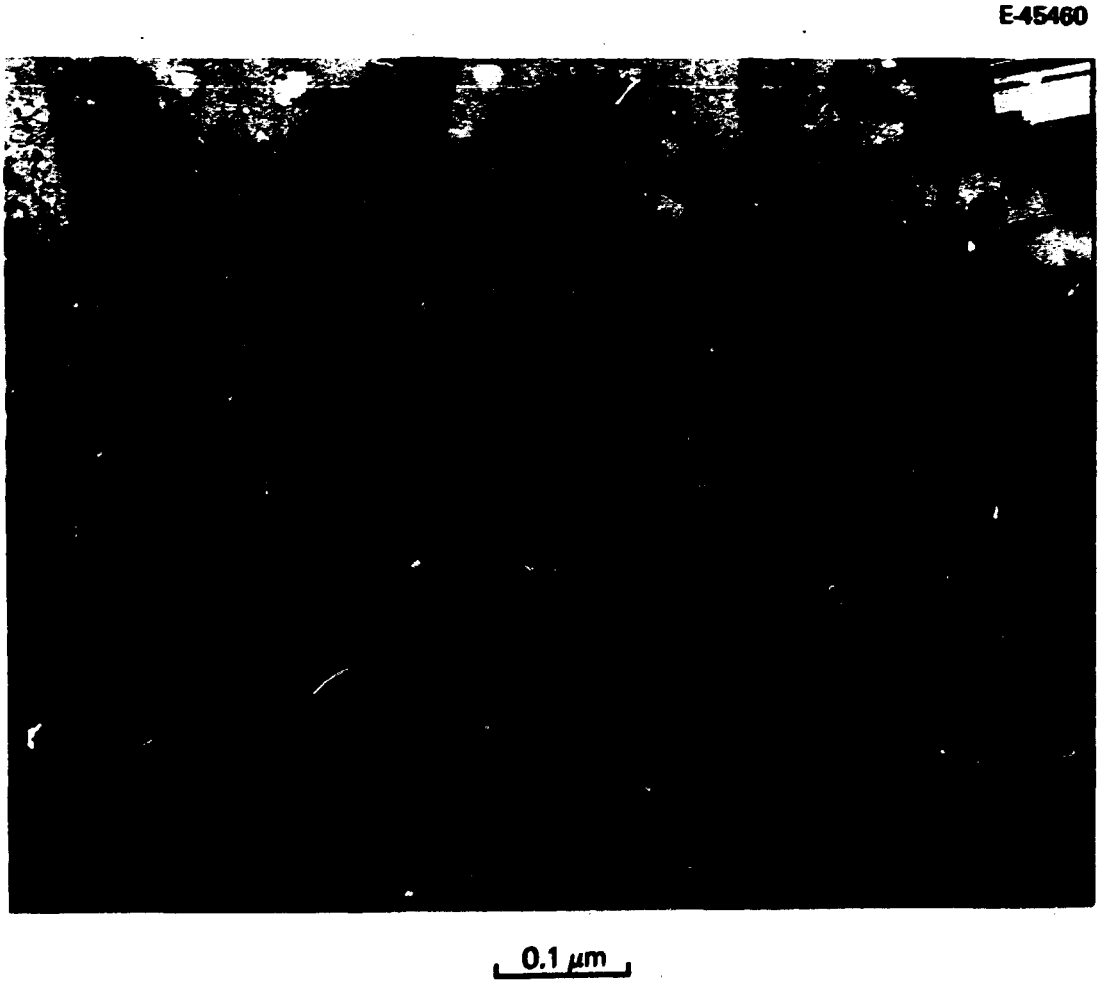

Fig. 7.4. Tetrahedral voids in silicon carbide from a UCO particle irradiated in HT-35 position 16 (fluence = 7.9×10^{25} neutrons/m^2).

Fission products were found in one specimen from position 16. A metallic fission product nodule [Fig. 7.5(*a*)] was observed along a grain boundary near the inside surface of the SiC layer (penetration was estimated to be perhaps 5 μm). Note the similarity to fission product nodules observed in out-of-reactor work [Fig. 7.5(*b*)]. Because the appearance and location of the fission product nodules are identical to those of the metal phase observed in out-of-reactor experiments, we have greater confidence in the validity of simulated fission product studies. Energy-dispersive x-ray analysis of the dark phase in Fig. 7.5(*a*) showed it to be mainly palladium (with possibly a small amount of ruthenium). Silicon and carbon are no doubt present as well but cannot be conclusively identified because of interference from the adjacent silicon carbide grains. No uranium was detected in the nodule, in contrast to out-of-reactor samples. We attribute this to the fact that the out-of-reactor specimen had a carbide kernel; the irradiated kernel was an oxycarbide, and this seems to have decreased the uranium mobility. Surprisingly, there was some indication of plutonium in the energy-dispersive x-ray spectrum from the nodule. To confirm the presence of plutonium, the gamma energy spectrum of the entire TEM sample (a 3-mm-diam aluminum disk containing several thinned SiC fragments) was measured for 2 h. The gamma energy spectrum suggests that several plutonium isotopes are present; however, because of matrix absorption effects, the spectrum peaks are not sharp enough to be identified conclusively. The potential importance of this question suggests that further work should be directed to getting a definitive identification.

No fission products were detected in association with the voids, providing further evidence that grain-boundary diffusion is the dominant means of fission product transport. Because irradiation damage and fission product interactions appear to be independent processes, conclusions drawn from studies in which the effects were treated individually should be useful in predicting HTR fuel performance.

7.3.1.2 Postirradiation Examination of Irradiated Fuels

Gamma spectrometry measurements were performed on the unbonded fissile particles deconsolidated from driver fuel rods 1, 3, 6, 9, 14, 16, 19, 22,

(a) 0.1 μm

E-35146

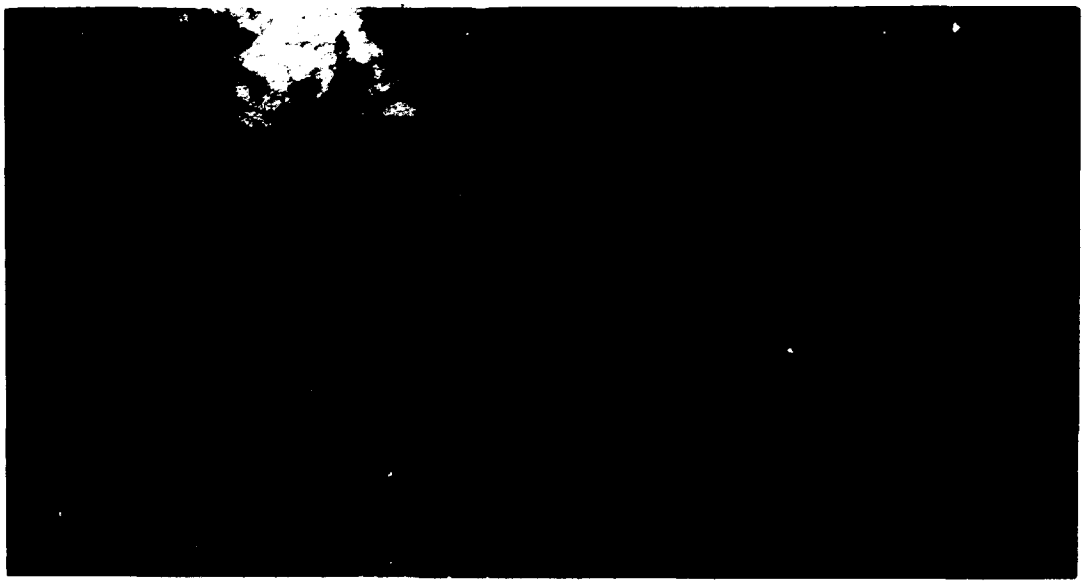

(b) 0.5 μm

Fig. 7.5. (*a*) Fission product nodule in silicon carbide from UCO particle irradiated in HT-35, position 16 (fluence = 7.9×10^{25} neutrons/m^2). (*b*) Nodules of simulated fission products in silicon carbide of UC_2 particles from out-of-reactor annealing studies.

and 25. These measurements were made with the IMGA system for assessing SiC microstructural influences on fission product retention. The IMGA data for each of the fissile particle populations from the above irradiation positions are shown in Table 7.1, which also shows the number of failed particles and the as-fabricated SiC characterization data. One particle batch, OR-2884H, irradiated in positions 1 and 14, exhibited the largest number of failed particles. Batch OR-2886H also exhibited a small number of failures in position 25. Failure was based on ^{137}Cs retention; deficiencies greater than 10% of the mean inventory of each batch were indicative of a failed particle. No failures were recorded in the examination of the other batches in the remaining six rods.

Table 7.1. Irradiated microsphere gamma analysis and as-fabricated characterization data for fissile particle batches irradiated in capsule HT-35

Rod	Batch	Particles[a]		SiC characterization	
		Examined	Failed	Deposition rate (μm/min)	Thickness (μm)
1	OR-2884 H	219	24	0.94	32.8
3	OR-2888 H	255	0	0.24	42.5
6	OR-2885 H	451	0	0.72	35.9
9	OR-2887 H	430	0	0.48	53.0
14	OR-2884 H	101	21	0.94	32.8
16	OR-2888 H	455	0	0.24	42.5
19	OR-2885 H	278	0	0.72	35.9
22	OR-2887 H	211	0	0.48	53.0
25	OR-2886 H	155	2	0.45	31.6

[a]SiC coating deposited at 1550°C with a laboratory-scale 35-mm-diam (1.38-in.) coating furnace.

Figure 7.6 describes the ^{137}Cs retention for each fissile batch as a function of burnup [% FIMA (fissions per initial heavy metal atoms)] achieved in capsule HT-35. The lowest burnup position corresponds to fuel rod 1 and increases with position number to the highest burnup, corresponding to rod 25. These data were derived by comparing the measured ^{137}Cs:^{106}Ru activity ratio to the calculated ^{137}Cs:^{106}Ru activity ratio. The fact that cesium retention is only at the 90 to 100% level (those batches where no failures were recorded) can be attributed to uncertainties in the input neutronics data for the HFIR target facility inventory calculations. Figure 7.7 describes the ^{110m}Ag retention for the same particle populations described in Fig. 7.6. Silver retention is also plotted as a function of fissile particle burnup. Retention was determined by comparing the ^{110m}Ag:^{106}Ru activity ratio measured with IMGA with the same ratio calculated from HFIR neutronics data. Mean values ranging from 50 to 60% represent the level of the existing neutronics input data for ^{110m}Ag inventory calculations. We believe that retention at this level is representative for a nonfailed particle.

From the fission product retention (Figs. 7.6 and 7.7), particle batch OR-2884H exhibited consistently large variation for both cesium and silver. This is illustrated by the large error bars representing the range in retention values in both the high- and low-temperature irradiation positions, rods 1 and 14. As shown in Table 7.1, this fissile batch contained the largest number of failed particles. Fissile batch OR-2886H, which also indicated some failed fuel, had large variations in its cesium and silver retention values. The silver data (Fig. 7.7) indicates that all five of the fissile batches had relatively large particle-to-particle variations in silver retention in the high-temperature irradiation positions (1200–1300°C), whereas the particle-to-particle variation was somewhat reduced in the low-temperature positions (850–950°C). The exception to this was the fuel from position 1, which contained failed fuel as described above.

Figures 7.8 and 7.9 show the ^{137}Cs retention of fertile particles examined with IMGA before examination with the PGA system. The data shown in Fig. 7.8 are for the fertile particle test set, which was fabricated

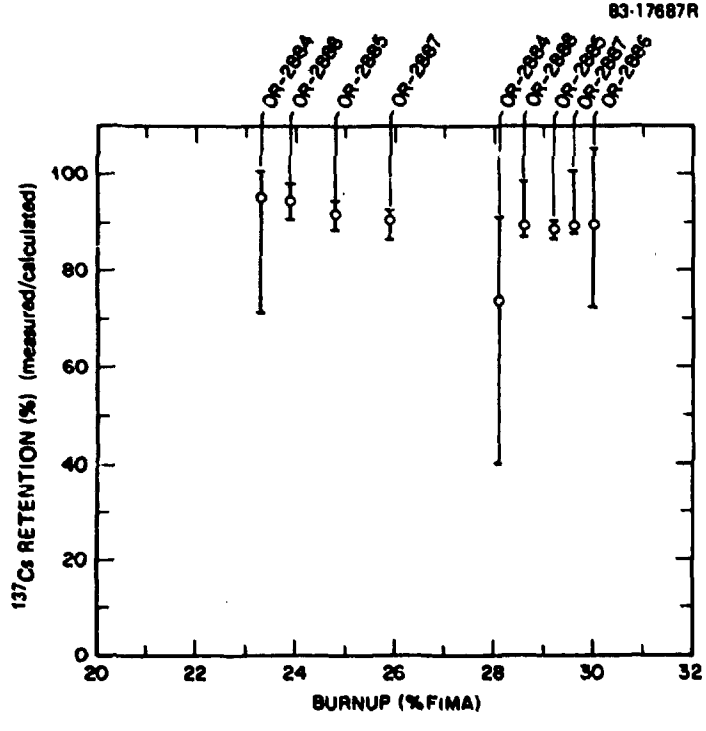

Fig. 7.6. Cesium retention as a function of particle burnup for fissile particle batches irradiated in capsule HT-35. These particles were irradiated to assess the influence of SiC microstructure on fission product retention. Brackets indicate range in cesium retention.

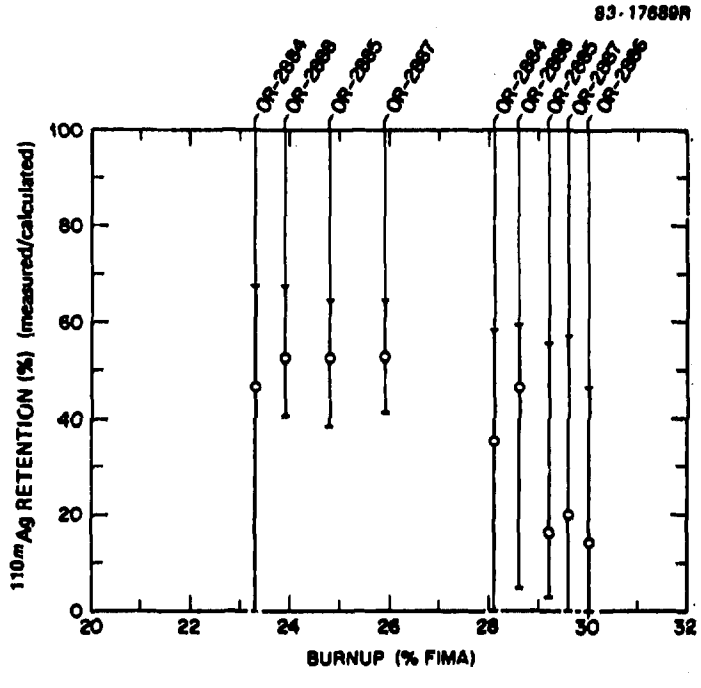

Fig. 7.7. Silver retention as a function of particle burnup for fissile particle batches irradiated in capsule HT-35. These particles were irradiated to assess the influence of SiC microstructure on fission product retention. Data points represent mean retention values for each batch, and the brackets indicate ranges in values observed.

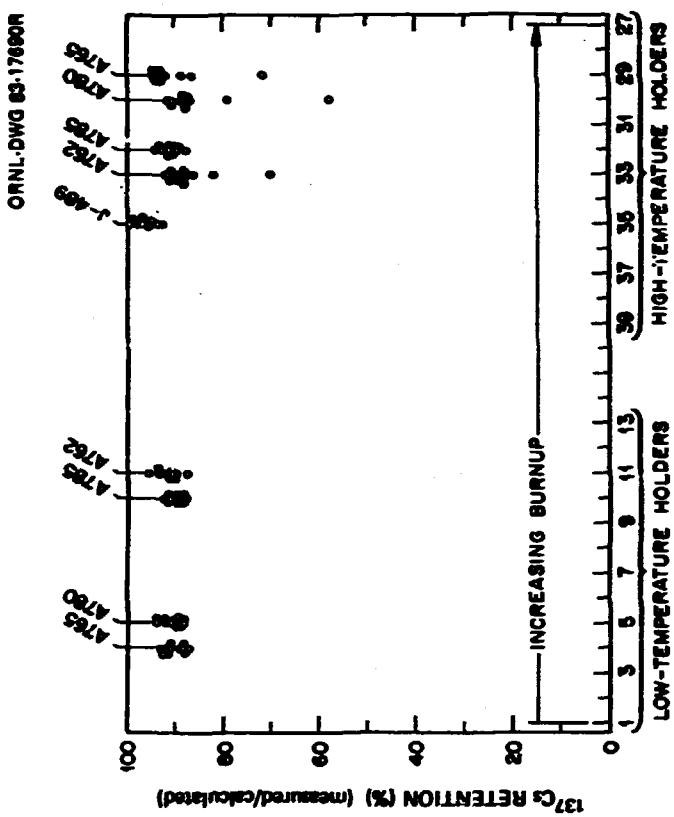

Fig. 7.9. Cesium retention in Biso-coated fertile particles irradiated to assess influence of fabrication process variables on irradiation performance.

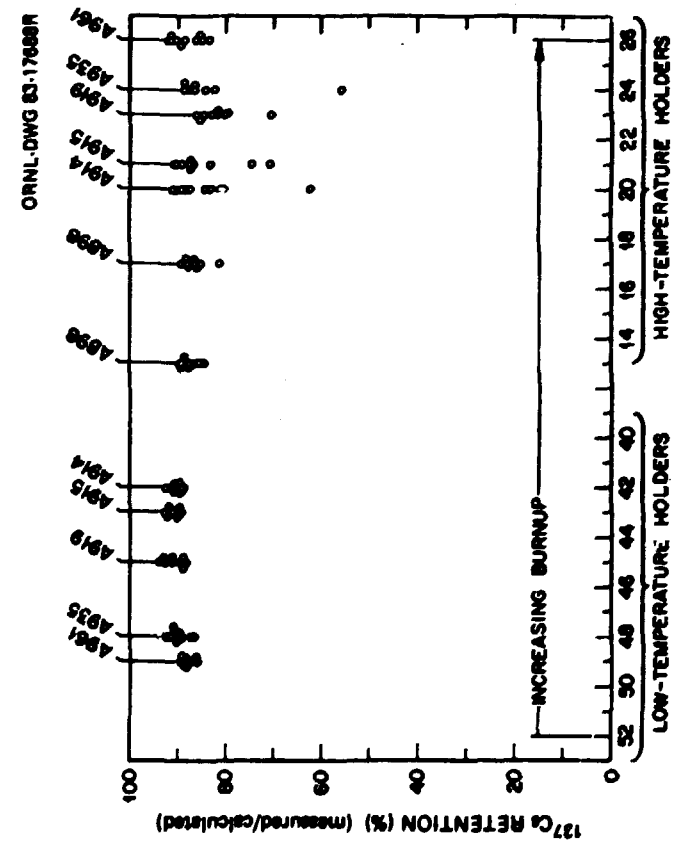

Fig. 7.8. Cesium retention in Biso-coated fertile particles fabricated with CO_2 as a diluent in the hydrocarbon coating gases.

with CO_2 as a diluent in the standard coating gases. The data shown in Fig. 7.9 are for the fertile particle test set designed to assess fabrication process variable influence on Biso-coated irradiated performance.[9] These same particle batches (Fig. 7.9) were irradiated in the HRB-14 (ref. 10) and HT-34 (ref. 11) capsules. In both fertile particle test sets, the cesium retention is good except at the irradiation positions having the highest burnups [located closest to the reactor horizontal midplane (HMP)]. These are positions 20 through 33 in Figs. 7.8 and 7.9. At each of these positions one or more of the ten particles selected had deficient cesium inventories. The identity of these particles has been maintained to compare their fission gas retention properties with their cesium behavior. The unbonded particles analyzed with IMGA before PGA examination are being stored until the PGA measurements can begin.

A small number of unbonded fissile particles (1 to 15 from deconsolidated fuel rods for IMGA examinations) were mounted for metallographic examination. (These are the batch numbers shown in Table 7.1). A small number of fissile particles, batch A-976 irradiated to assess the performance of the UC_xO_y kernels in comparison with the weak-acid-resin (WAR)-derived kernels, were also mounted for metallographic examination. A full analysis of these examinations has not yet been completed.

7.3.2 Capsules HRB-11 and -12 — M. J. Kania and V. S. Inouye*

Fuel from nine irradiation positions in both capsules HRB-11 and -12 were electrolytically deconsolidated to obtain unbonded particles for gamma spectrometry measurements. The examinations were conducted with the IMGA system from April through June 1979. These data were not published in the final report on capsules HRB-11 and -12 (ref. 12). Table 7.2 lists the fuel rods examined and the fissile particle batch number, coating type, and objectives for each experiment.

The IMGA data on fuel rods 4 and 9 from capsule HRB-11 were not valuable enough to make a performance estimate; therefore, they were not

*Student, Washington University, St. Louis.

Table 7.2. Weak-acid-resin fissile particle batches irradiated in fuel rods in capsules HRB-11 and -12

Fuel rod	Fissile batch	Coating type	Objective[a]	Comment
		Capsule HRB-11		
4	A-615	SiC-Triso	1	IMGA data analysis incomplete
5	A-601	SiC-Triso	1,2	
8	OR-2460 H	SiC-Triso	3	
9	OR-2459	SiC-Triso	3	IMGA data analysis incomplete
10	OR-2463 H	SiC-Triso	2,4	
11	OR-2456 H	SiC-Triso	2,4	
17	OR-2471 H	SiC-Triso	2,4	
18	OR-2466 H	SiC-Triso	2,4	
20	OR-2458 H	SiC-Biso	2,4	
		Capsule HRB-12		
6	OR-2480 H	Biso	5,6	
7	8-HT	ZrC-Triso[b]	5	
8	10-HT	ZrC-Triso[b]	5	
9	9-HT	ZrC-Triso[b]	5	
10	OR-2493 H	SiC-Triso	6	
11	OR-2497 H	SiC-Triso	6	
16	OR-2494 H	SiC-Triso	6	
17	OR-2486 H	SiC-Triso	6	
19	OR-2320 H	SiC-Triso	6	

[a]Objectives:

1. Compare particles fabricated in coating furnace by use of a fritted gas distribution system with those fabricated by use of a conical gas distribution system.
2. Investigate the effects of initial kernel oxygen-to-uranium ratio (O:U) on the irradiation performance.
3. Determine if minimum buffer layer thickness in reference fissile particle design is optimal.
4. Qualify a second manufacturing source for resin material.
5. Compare weak-acid-resin (WAR)-derived fissile kernels having an SiC-Triso coating design with similar kernels having a ZrC-Triso coating design.
6. Investigate the influence of SiC coating deposition rate on fission product retention.

[b]ZrC coatings deposited on WAR kernels by Los Alamos Scientific Laboratory.

considered in the analysis. Calculated ^{137}Cs and ^{106}Ru fission product inventories were derived from irradiation data provided in ref. 12 and neutronics data for the HFIR Permanent Beryllium (PB) Facility and Removable Beryllium (RB) Facility described in refs. 13 and 14, respectively. The general uncertainty of the measured-to-calculated activity ratio for ^{137}Cs:^{106}Ru was about 25%. This value represents the 90% confidence interval for an approximate 15% uncertainty in the neutronics data, combined with a 4 to 5% uncertainty in the IMGA counting data. The latter is attributed to the counting statistics for ^{106}Ru, as in most cases the ^{137}Cs value was less than 1% of the mean value.

Irradiation performance was based on the measured-to-calculated ^{137}Cs:^{106}Ru activity ratios for the seven fissile particle batches analyzed from HRB-11. Performance estimates based on low ^{137}Cs retention as indicative of failed particles are presented in Table 7.3.

Table 7.3. Failure fraction estimates for selected fissile batches irradiated in capsules HRB-11 and -12

Fuel rod	Batch	Particles		Mean failure fraction (%)
		Examined	Failed	
		HRB-11		
5	A-601	226	0	0.0
5	A-602	226	0	0.0
8	OR-2460 H	242	8	3 3
10	OR-2463 H	169	24	14.2
11	OR-2456 H	147	53	3>.1
17	OR-2471 H	155	0	).0
18	OR-2466 H	192	1	0.5
20	OR-2458 H	279	>21	>7.5
		HRB-12		
6	OR-2480 H	98	87	88.8
7	8-HT	186	43	23.1
8	10-HT	96	30	31.3
9	9-HT	100	56	56.0
10	OR-2493 H	341	46	13.5
11	OR-2497 H	158	4	2.5
16	OR-2494 H	171	18	10.5
17	OR-2486 H	92	1	1.1
19	OR-2320 H	172	14	8.1

Fissile particle batches A-601 (rod 5) and OR-2471 H (rod 17) exhibited the best irradiation performance, with no detectable failed particles. Each of the other particle batches in the remaining rods exhibited some particle failure, with mean failure fractions ranging from 0.5 to 36.1%. Particle batches OR-2463 H (rod 10) and OR-2456 H (rod 11), having had the highest failure fractions of 14.2 and 36.1%, respectively, were irradiated under the most severe environment near the center of the capsule.

In a manner similar to that for HRB-11, irradiation performance for the nine fissile particle batches analyzed from HRB-12 was based on the measured-to-calculated ^{137}Cs:^{106}Ru activity ratios. Table 7.3 also lists their respective performance estimates. Particle batch OR-2486 (rod 17) exhibited the best performance, with a 1.1% mean failure fraction. The Biso-coated particle batch OR-2480 H, which exhibited a mean failure fraction of 88.8%, was clearly the worst performing batch based on ^{137}Cs retention. The remaining fissile particle batches had failure fractions that ranged from 2.5% in rod 11 to 56% in fuel rod 9.

The objectives listed in Table 7.2, with the exception of 1 and 5, were fully addressed in the final report on these capsules.[12] The IMGA analyses of rods 4 and 5 of HRB-11 were initiated to achieve objective 1, which was to compare the irradiation performance of fuels fabricated by use of a frit with those fabricated by use of a cone gas distribution system in a coating furnace. Unfortunately, we were unable to use the IMGA data generated for fuel rod 4 because the original data analysis was not detailed enough that good activity ratio distributions were generated. To complete objective 5, which was to compare the irradiation performance of ZrC-Triso-coated fuels with SiC-Triso-coated fuels, the data illustrated in Figs. 7.10, 7.11, and 7.12 and those described in Table 7.3 were used.

The data shown in Fig. 7.11 illustrate the results for the three ZrC-Triso-coated particle batches irradiated in fuel rods 7, 8, and 9 of capsule HRB-12. Mean failure fractions derived from low ^{137}Cs inventories on these particle types were 23.1, 31.3, and 56.0%, respectively. The irradiation environment of the ZrC-Triso fuels compares well with irradiation positions 17 through 20 in both HRB-11 and -12. Figure 7.10 shows the results of SiC-Triso-coated fuels irradiated in rods 17, 18, and 20 of

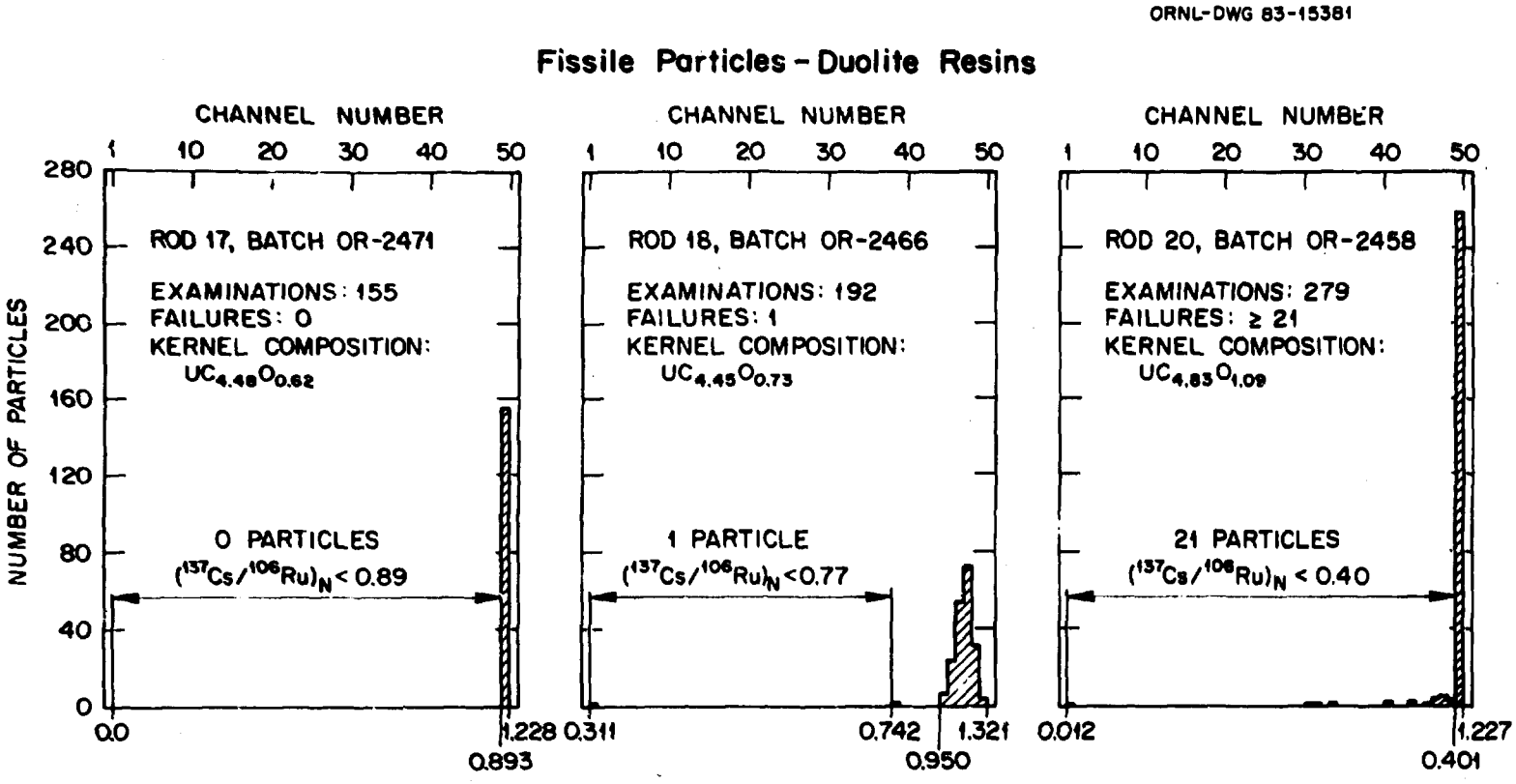

Fig. 7.10. Measured-to-calculated ^{137}Cs:^{106}Ru activity ratio for fuel rods 17, 18, and 20 in capsule HRB-11.

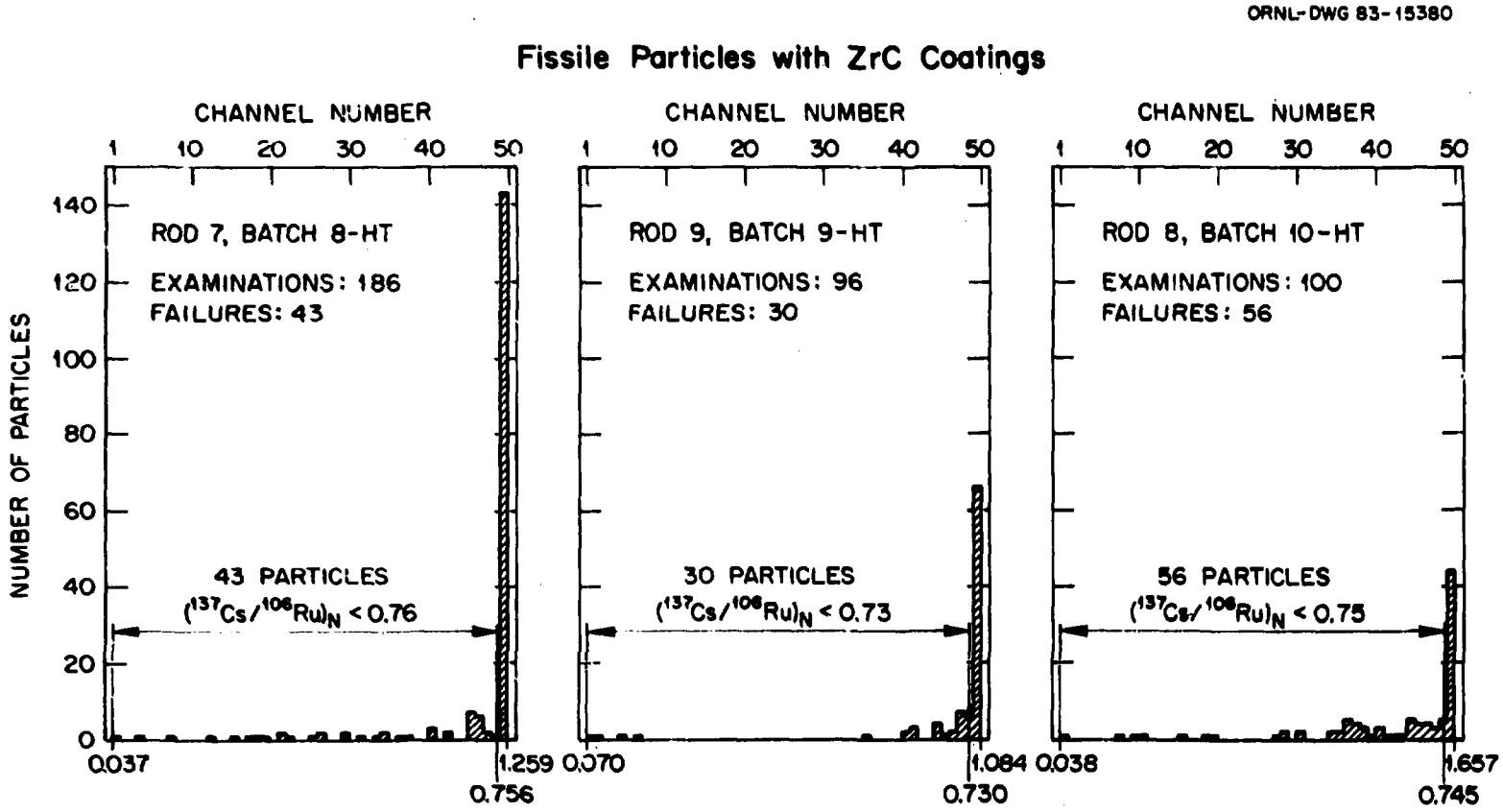

Fig. 7.11. Measured-to-calculated ^{137}Cs:^{106}Ru activity ratio for fuel rods 7, 8, and 9 in capsule HRB-12.

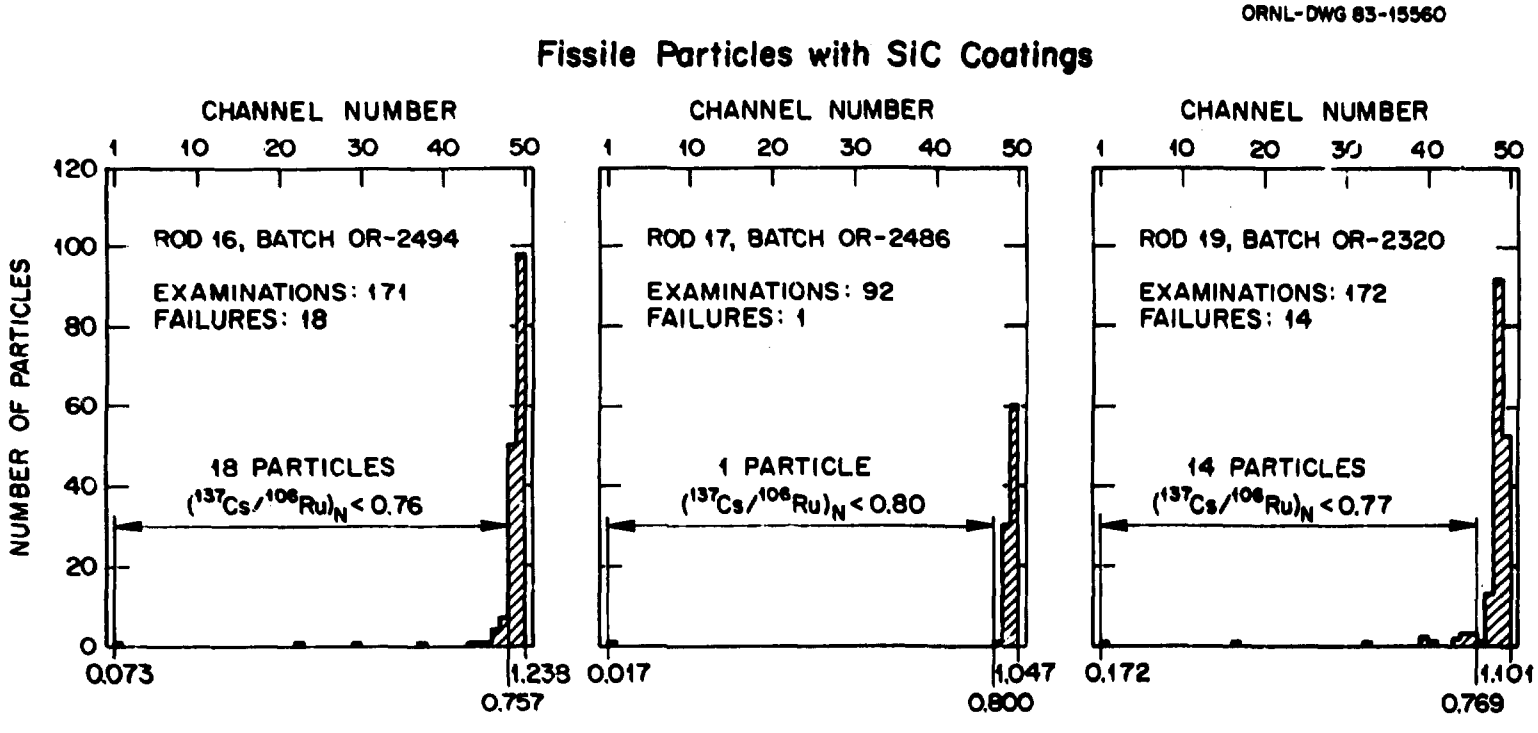

Fig. 7.12. Measured-to-calculated ^{137}Cs:^{106}Ru activity ratio for fuel rods 16, 17, and 19 in capsule HRB-12.

HRB-11 by use of a similar failure criterion for failed particle detection. Mean failure fractions for these three particle batches were 0.0, 0.5, and about 7.5%, respectively. Figure 7.12 provides similar data on SiC-Triso-coated batches irradiated in fuel rods 16, 17, and 19 of HRB-12. The mean failure fractions of these three particle batches were 10.5, 1.1, and 8.1%, respectively. Comparison of the ZrC-Triso-coated fuel with the SiC-Triso-coated fuel indicates that the SiC coating had a better irradiation performance than did the ZrC coating as determined by ^{137}Cs retention. The ZrC-Triso fuel experienced failure fractions in similar irradiation environments at rates 2 to more than 100 times that for SiC-Triso coated fuel.

Observations recorded during the metallographic examination of the ZrC-Triso fuel of rods 1 and 2 (same fuel as that in rods 7 and 9) in HRB-11 revealed several failed particles caused by pressure vessel rupture. This indicates that the as-fabricated ZrC coatings in HRB-12 were underdesigned or exhibited low strength. In addition, we observed large numbers of outer pyrocarbon coating failures caused by fast-neutron-induced damage. This also contributes to reduced strength for the ZrC-Triso design during irradiation. Thus, the higher failure rates of the ZrC-Triso-coating design are attributed to the relatively low level of development that exists in the fabrication of ZrC coatings for HTR fuels. This contrasts with any inherent problem associated with the ZrC coating in an intense irradiation environment.

A report documenting the results of the IMGA examination and analysis of the selected fuels from capsules HRB-11 and -12 is now in preparation.

7.3.3 Capsule HRB-15b — M. J. Kania

A reevaluation of the IMGA data generated to determine ^{110m}Ag retention for the HRB-15b fuels was completed. Corrections were made to the original IMGA data accounting for source-to-detector geometry errors and incorrect notations on initial examination data sheets. The corrected IMGA data were then compared with calculated fission product inventories based on HFIR-RB neutronics data. The results for fission products ^{106}Ru and ^{137}Cs and the activation product ^{110m}Ag are shown in Table 7.4 for particle batches containing only uranium fuels. Figure 7.13

Table 7.4. Comparison of measured and calculated activities for ^{106}Ru, ^{137}Cs, and ^{110m}Ag in selected fuels irradiated in capsule HRB-15b

Position	Measured activity[a] (μCi)			Calculated activity[a] (μCi)			Ratio of measured ratio to calculated ratio	
	^{106}Ru	^{137}Cs	^{110m}Ag	^{106}Ru	^{137}Cs	^{110m}Ag	^{137}Cs:^{106}Ru	^{137m}Ag:^{106}Ru
12	7.901E+2	1.297E+2	3.571	7.656E+2	1.259E+2	4.810	9.982E−1	7.194E−1
18	1.065E+3	1.703E+2	5.045	1.085E+3	1.694E+2	7.186	1.024	7.152E−1
80	1.588E+3	1.844E+2	1.264E+1	1.457E+3	1.696E+3	1.192E+1	1.010	9.849E−1
84	1.702E+3	1.953E+2	1.296E+1	1.728E+3	1.979E+2	1.397E+1	1.002	9.228E−1
90				1.611E+3	1.838E+2	1.304E+1		
98	1.114E+3	1.256E+2	8.474	1.116E+3	1.271E+2	9.036	9.900E−1	9.395E−1
104	1.601E+3	1.683E+2	1.74E+1	1.491E+3	1.705E+2	1.206E+1	9.193E−1	9.066E−1
116[b]	1.522E+3	1.782E+2	1.177E+1	1.514E+3	1.758E+2	1.222E+1	1.008	9.581E−1
118[b]	9.778E+2	1.128E+2	7.465	9.495E+2	1.121E+2	7.646	9.771E−1	9.481E−1
124				1.082E+3	1.278E+2	8.709		
138	9.527E+2	1.125E+2	6.757	1.004E+3	1.234E+2	7.974	9.608E−1	8.930E−1
148	7.810E+2	1.003E+2	4.905	7.503E+2	9.931E+1	5.769	9.703E−1	8.168E−1
150	1.522E+3	1.984E+2	9.750	1.473E+3	1.945E+2	1.127E+1	9.872E−1	8.373E−1
156[b]	8.129E+2	1.058E+2	4.554	8.343E+2	1.142E+2	6.237	9.508E−1	7.494E−1
168	1.072E+3	1.580E+2	6.006	1.068E+3	1.591E+2	7.457	9.894E−1	8.024E−1

[a]To convert to becquerels, multiply by 3.7×10^4.

[b]SiBiso coatings.

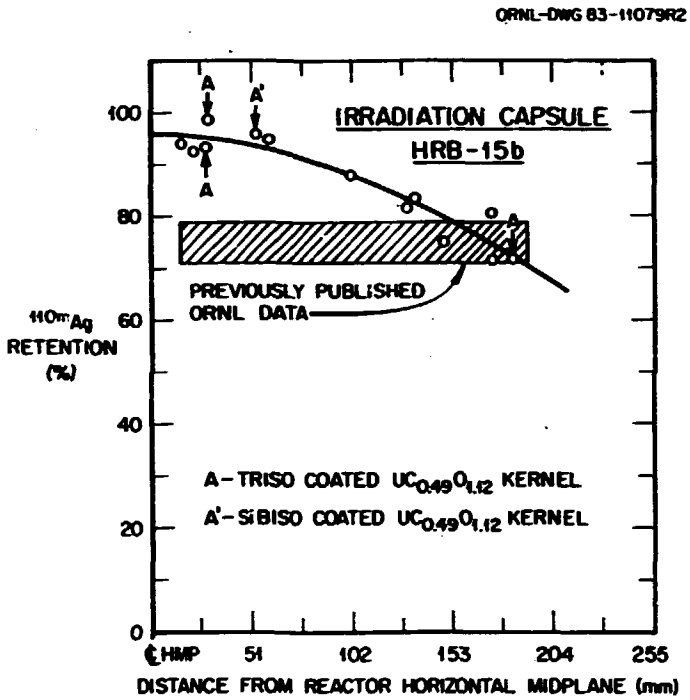

Fig. 7.13. Silver retention in capsule HRB-15b fuels as a function of irradiation position (HMP = HFIR horizontal midplane).

is a plot of the measured-to-calculated ^{110m}Ag:^{106}Ru activity ratios for these selected fuels as a function of irradiation position from the HFIR HMP. Quite noticeable is the gradual decrease in ^{110m}Ag retention as the distance between irradiation position and HFIR-HMP increases. This same decrease is not apparent in the ^{137}Cs retention data shown in column 8 of Table 7.4. A parabolic fit to the silver retention data was calculated and is also shown in Fig. 7.13.

The irradiation temperature of the HRB-15b fissile fuels ranged from about 840 to 915°C, with the lower temperature occurring near the ends of the capsule. The fuel burnups, also position dependent, ranged from 19.4% FIMA at the ends of the capsule to 26.7% FIMA near the HFIR-HMP (mixed-oxide fissile fuels not included). The accumulated fast fluence range, again position dependent, ranged from about 4.0 to 6.6 × 10^{25} neutrons/m^2 (E > 29 fJ) for the fuel positions of interest. These operating parameters

indicate that the most severe irradiation conditions in HRB-15b occurred in the fuels located near the HMP rather than at the ends of the capsule. This impression is just opposite the ^{110m}Ag retention results that Fig. 7.13 presents.

Four of the irradiation positions, 12, 80, 104, and 116, contained the same kernel type, a dense $UC_{0.49}O_{1.12}$ kernel, and are noted by "A" and "A′" in Fig. 7.13. The A indicates Triso coatings, whereas the A′ indicates an SiBiso coating. Of these positions, the particles irradiated in position 12 exhibited the poorest ^{110m}Ag retention, about 72%, despite the fact that this position experienced the lowest operating conditions for temperature, fluence, and burnup. There is no apparent reason for the fuel in position 12 to have a 25% lower ^{110m}Ag retention than the same fuel irradiated in positions nearer the HFIR-HMP. The counting statistics associated with the 884-keV energy peak of ^{110m}Ag for the fuel in position 12 ranged from about 12 to about 17% (1 σ error). These values compare with ranges of about 7 to about 9% at positions nearer the HMP.

It is not now possible to make a definitive statement regarding the ^{110m}Ag retention in the HRB-15b fuels. Other PIE examinations conducted at GA support the conclusion that most of these fuels retained their silver.[15] If one adopts this position, Fig. 7.13 supports the hypothesis that there is a position-dependent flux effect that strongly influences the ^{110m}Ag inventory at irradiation positions nearest the ends of the capsules. Correcting the data for measured-to-calculated ^{110m}Ag:^{106}Ru activity ratios in Table 7.4 and using the normalized fitted curve of Fig. 7.13 results in ^{110m}Ag retention values as shown in Fig. 7.14. Therefore, the measured-to-calculated ratio lies between 90 and 105% for all capsule HRB-15b positions indicated in Table 7.4.

The ^{110m}Ag retention data from capsules HRB-15b and HRB-15a and that for the German irradiation capsule FRJ2-P23 (ref. 16) are shown in Fig. 7.15 as a function of irradiation temperature from 850 to 1470°C. Error bars are shown on the German data only, but a similar range would be applicable to the U.S. data. These data show a definite temperature

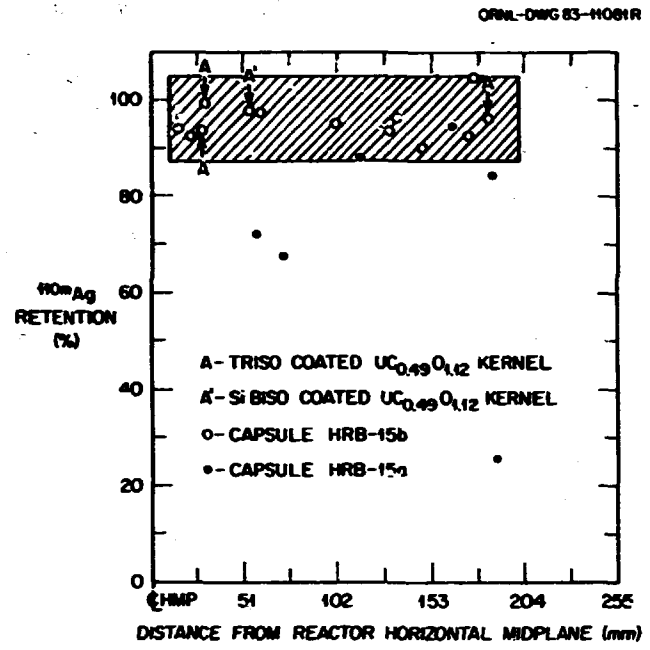

Fig. 7.14. Silver retention in irradiated low-enriched uranium fuels from capsules HRB-15a and -15b. Data have been corrected for end effects described in Fig. 7.13.

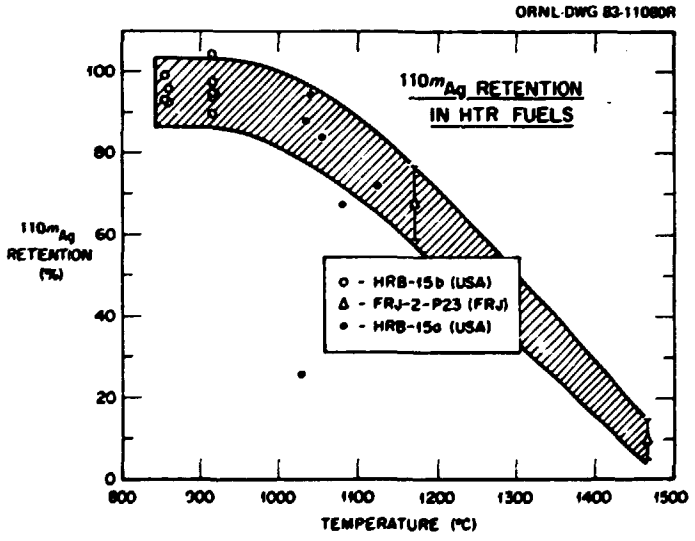

Fig. 7.15. Silver retention in High-Temperature Reactor Triso-coated fuels as a function of temperature. Beyond operating temperatures of 1050°C, ^{110m}Ag retention rapidly decreases to 10% at 1470°C.

effect, with retention being near 100% from about 900 to about 1050°C and then rapidly decreasing to about 10% at approximately 1470°C. The data in Fig. 7.15 show apparently good agreement between the U.S.- and German-derived ^{110m}Ag retention in Triso-coated HTR fuels.

The U.S. data in Fig. 7.15 must be considered preliminary; they require further examination to characterize the apparent flux effect at the irradiation positions near the top and bottom of the HFIR core. Silver retention data from capsule HRB-14 as well as the GA data from encapsulated piggyback samples from HRB-15a and -16 are being reevaluated following similar procedures outlined here. The ORNL and KFA-Jülich have also agreed to exchange fission product retention data to solve uncertainties about silver retention in HTR fuels.

7.3.4 Capsule HRB-15a — M. J. Kania, F. J. Homan, and L. G. Shrader

7.3.4.1 Metallographic and Electron Microprobe Examinations

Metallographic and electron microprobe examinations on the new mount containing $UC_{0.4}O_{1.6}$ particles from batch 6157-11-020 irradiated in fuel rod 17 were completed. Particles from this rod were identified as having severe SiC corrosion that in some cases nearly penetrated the SiC layer.[14] Electron microprobe examination of the new mount clearly identified the fission product palladium present in those areas of corrosion. No chlorine above background levels was detected in the kernel or coatings, indicating that the corrosion was due to the palladium-SiC interaction. This fuel rod was irradiated at one of the low-fluence-low-burnup positions in HRB-15a, achieving a burnup of 21.6% FIMA and accumulating a fluence of 3.94×10^{25} neutrons/m^2 ($E > 29$ fJ) at a mean operating temperature of about 1040°C.

Metallography was also completed on the repolished metallographic mounts containing loose-particle trays 7, 8, and 9. Each of these trays contained Triso-coated ThO_2 particles, tray 7, batch 6252-21-010; tray 8, batch 6252-24-010; and tray 9, batch 6252-25-010. A close examination of the particle coatings in trays 8 and 9 revealed numerous areas in which the buffer and inner pyrocarbon (iLTi) coatings were missing, leaving a

clear path from the kernel to the SiC coating. Our initial thoughts were that the buffer and pyrocarbon materials from these regions were removed during polishing. Closer examination indicated that the gaps were caused by cracking and subsequent shrinkage of the buffer and pyrocarbon coatings. In those areas in which the inner pyrocarbon was completely removed from the SiC interface, corrosion of the SiC coating was evident (Fig. 7.16, tray 8; Fig. 7.17, tray 9). This corrosion was present in each area where an open path from the kernel to the SiC developed during irradiation. Extent of the corrosion was a maximum of 5 to 10 μm in the 35-μm SiC coating.

Examination of the particles in tray 7 revealed no corrosion of the SiC layer as was the case in trays 8 and 9. The reason is that the iLTI coating remained intact and that there was no direct path from the kernel to the SiC layer. The examination of tray 7 did reveal one failed particle.

7.3.4.2 ^{110m}Ag Release Calculations

Fission and activation product inventory calculations were completed for the fissile particle batches irradiated in rods 1, 2, 7, 13, 15, and 17 of capsule HRB-15a. The activities presented in Table 7.5 are an update of previous calculations.[14] The range in ^{110m}Ag activity given represents two sets of calculations, one using a silver removal cross section, ^{110m}Ag(n,γ), equal to 2.54×10^{-27} m^2 (25.4 b) and the other equal to 3.98×10^{-27} m^2 (39.8 b). These two values represent the uncertainty limits on this parameter in the environment of the HFIR RB Facility. Only a small difference was noted in the ratio of measured-to-calculated mean ^{110m}Ag:^{106}Ru activity ratios by use of these two cross section values.

7.3.4.3 Analysis of SiC Coating Performance on Fissile Particles

The examination and analysis of SiC coatings on fissile fuel particles irradiated in capsule HRB-15a has raised a number of questions about the fabrication and performance of the SiC coatings:

Microstructure

Essentially all the work to date to correlate SiC microstructure with deposition conditions concludes that low deposition temperatures

R-77794

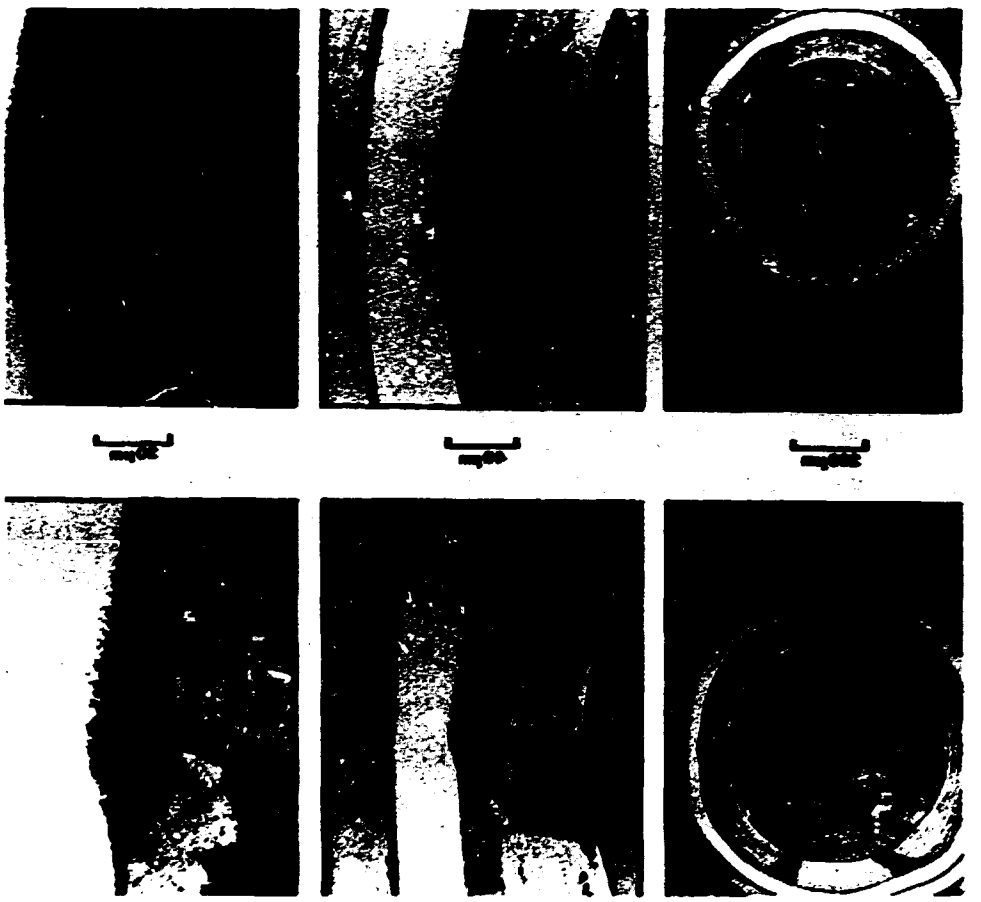

Fig. 7.16. Fertile particle batch 6252-24-010 with an SiC-Triso coating irradiated in capsule HRB-15a, tray 8. Particles achieved a fluence of 6.1×10^{25} neutrons/m^2 ($E > 29$ fJ), a burnup of 6.4% fissions per initial heavy metal atom, and a mean operating temperature of 1125°C. Silicon carbide corrosion observed at all points where a cracked buffer and inner pyrocarbon exist, leaving an open path from the kernel to the SiC coating. Maximum corrosion depth observed, less than 10 μm of the 35-μm-thick SiC layer.

R-77795

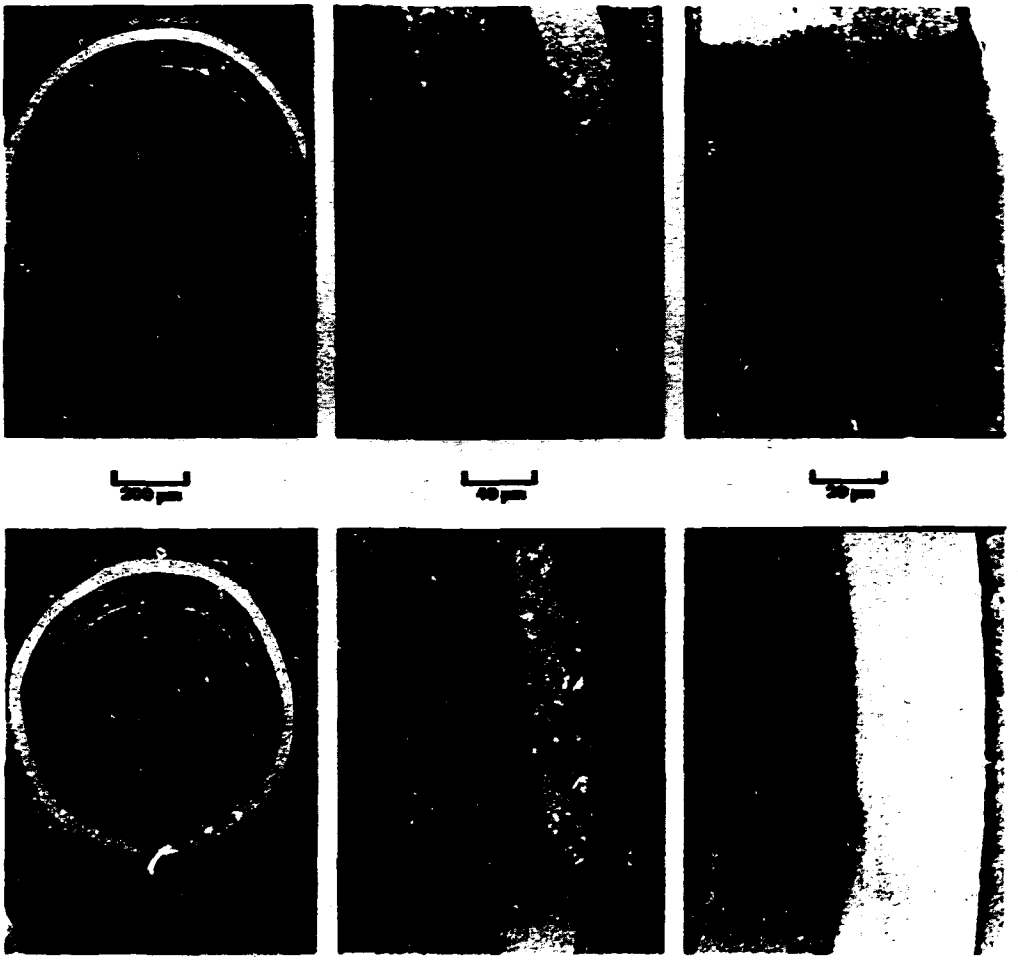

Fig. 7.17. Fertile particle batch 6252-25-010 with an SiC-Triso coating irradiated in HRB-15a, tray 9. Particles achieved a fluence of 6×10^{25} neutrons/m^2 ($E > 29$ fJ), a burnup of 6.3% fissions per initial heavy metal atom at a mean operation temperature of 1120°C. Silicon carbide corrosion observed at points where buffer and inner pyrocarbon failed, with a penetration of about 5 μm into the SiC layer.

Table 7.5. Comparison of irradiated microsphere gamma analyzer (IMGA)-derived activity and calculated ratios for fissile particle batches irradiated in fuel rods 1, 2, 7, 13, 15, and 17 of capsule HRB-15a

Ratio	Gamma spectrometry data (IMGA)				Calculated ratio	Measured-to-calculated ratio	
	Minimum	Mean	Maximum	s^a (%)		Mean	Range
				Rod 1			
$^{95}Zr:^{106}Ru$	6.623	7.190	7.774	4.79	8.457	0.850	0.783–0.919
$^{110m}Ag:^{106}Ru$	2.261E–3	4.042E–3	5.737E–3	11.87	8.061E–3–8.660E–3	0.467–0.501	0.261–0.712
$^{137}Cs:^{106}Ru$	1.446E–1	1.533E–1	1.612E–1	3.16	1.629E–1	0.941	0.899–0.989
$^{144}Ce:^{106}Ru$	3.020	3.223	3.440	3.38			
				Rod 2			
$^{95}Zr:^{106}Ru$	5.845	6.362	7.184	4.89	7.377	0.862	0.792–0.974
$^{110m}Ag:^{106}Ru$	3.468E–3	5.333E–3	7.302E–3	12.63	9.085E–3–9.887E–3	0.539–0.587	0.351–0.804
$^{137}Cs:^{106}Ru$	1.020E–1	1.421E–1	1.554E–1	3.30	1.483E–1	0.958	0.688–1.048
$^{144}Ce:^{106}Ru$	2.608	2.786	3.141	3.21			
				Rod 7			
$^{95}Zr:^{106}Ru$	4.378	4.533	4.882	1.22	5.346	0.848	0.819–0.913
$^{110m}Ag:^{106}Ru$	9.955E–6	5.700E–3	7.562E–3	21.26	1.148E–2–1.309E–2	0.435–0.497	7.605E–4–0.659
$^{137}Cs:^{106}Ru$	7.909E–3	1.054E–1	1.137E–1	13.69	1.176E–1	0.896	6.723E–2–0.967
				Rod 13			
$^{95}Zr:^{106}Ru$	4.048	4.238	4.433	1.81	5.437	0.779	0.745–0.815
$^{110m}Ag:^{106}Ru$	1.122E–3	5.266E–3	7.878E–3	31.77	1.135E–2–1.290E–2	0.408–0.464	8.698E–2–0.694
$^{137}Cs:^{106}Ru$	8.890E–2	1.086E–1	1.129E–1	1.95	1.190E–1	0.912	0.747–0.948
$^{144}Ce:^{106}Ru$	2.106	2.192	2.289	1.62			
				Rod 15			
$^{95}Zr:^{106}Ru$	4.544	4.767	5.056	2.11	5.982	0.797	0.760–0.845
$^{110m}Ag:^{106}Ru$	4.716E–3	6.246E–3	7.759E–3	8.09	1.067E–2–1.192E–2	0.523–0.585	0.396–0.726
$^{137}Cs:^{106}Ru$	1.132E–1	1.176E–1	1.225E–1	1.62	1.278E–1	0.920	0.886–0.958
$^{144}Ce:^{106}Ru$	2.160	2.571	2.788	4.93			
				Rod 17			
$^{95}Zr:^{106}Ru$	5.457	5.860	6.326	3.25	7.767	0.754	0.703–0.815
$^{110m}Ag:^{106}Ru$	–9.637E–4	1.375E–3	6.301E–3	125.66	8.717E–3–9.441E–3	0.146–0.157	0.000–0.723
$^{137}Cs:^{106}Ru$	3.748E–2	1.406E–1	1.500E–1	6.57	1.538E–1	0.914	0.244–0.975
$^{144}Ce:^{106}Ru$	2.637	2.878	3.114	3.87			

[a]s, Sample standard deviation.

(below 1500°C) result in a banded or striated structure. Silicon carbide deposited at high temperatures (above 1650°C) has long columnar grains oriented in the direction of deposition. Silicon carbide deposited under "optimum" temperature conditions (around 1550°C) has fine grain structure. In Table 7.6 the deposition conditions for five batches of SiC coatings are summarized. The first two batches listed were irradiated in capsule HRB-15a (also in capsule R2-K13); the last three batches were irradiated in capsule HRB-15b. From the deposition temperatures listed, all batches would be expected to have long columnar grains. But only two of the batches had this structure, while one batch had fine grains, and two batches had a striated appearance. All these batches were fabricated at GA, and the coating conditions are now being reviewed there.

Variation in resistance to palladium attack

All the fissile particles examined at ORNL from the HRB-15a capsule had SiC coatings deposited under nearly identical coating conditions. The only major difference between these coatings is that one batch (6157-11-020, included in rod 17) was produced in the GA production coater and that the other batches were produced in a research size coater at GA. Despite the nearly identical coating conditions, there was significant variation in performance of these SiC coatings, including resistance to palladium attack (Table 7.7). The possibility was explored that this variation in resistance to palladium attack might be linked to differences in quality of the inner pyrocarbon coating, but this does not seem to be a valid explanation. A permeable inner pyrocarbon coating does not protect the kernel from chlorine intrusion during the deposition of the SiC coating (chlorine is produced by decomposition of the SiC coating gas). Higher rates of fission product attack of the SiC coating have been observed in particles that have chlorine in the kernel. For the particles compared here, the highest rates of SiC attack by palladium were observed in batches in which the inner pyrocarbon coating rate was the lowest. Low pyrocarbon coating rate has been correlated in the past to high levels of impermeability to chlorine.

Table 7.6. Summary of deposition conditions, microstructures, and fission-product retention data for several batches of Triso-coated fissile particles irradiated in HRB-15a and 15b

(At coating temperatures above 1650°C all SiC coatings should have had large columnar grains. Also, the fine grain structure is thought to be most retentive of fission products. These data show no definitive correlations between coating conditions and microstructure or between microstructure and fission product retention)

Batch	Coating conditions			Density (Mg/m^3)	Microstructure[b]	Irradiation conditions			Fission product release (%)	
	Temperature (°C)	H_2/MTS[a]	(μm/min)			Temperature (°C)	Burnup (% FIMA[c])	Fluence[d]	^{137}Cs	^{110m}Ag
6151-11-010	1650	149	0.257	3.22	LCG	1250	26	5.5	3	90
6157-11-G20	1650	149	0.250	3.22	FG	1150	26	5.3	3[e] 8[f]	30[e] 80[f]
6152-01-0111	1700	110	0.136	3.21	LCG	900	22	3.5	1[g]	65[g]
6157-09-0120	1700	100	0.328	3.16	S	900	22	3.5	1[g]	3[g]
6151-21-0111	1700	110	0.331	3.16	S	900	22	3.5	10[g]	65[g]

[a]MTS, methyltrichlorosilane.

[b]LCC, large columnar grains (high deposition temperature); S, striated (low deposition temperature; and FG, fine grains (considered optimum).

[c]FIMA, fissions per initial heavy metal atom.

[d]Units of 10^{25} neutrons/m^2 ($E > 29$ fJ).

[e]*Unpublished data of* J. W. Ketterer, GA Technologies, San Diego, Calif.

[f]Unpublished data of M. J. Kania, Oak Ridge National Laboratory, Oak Ridge, Tenn.

[g]Release during 1500°C anneal for 10,000 h following irradiation. Measurements made on ten particles.

Source of data: GA Technologies, San Diego, Calif.

Table 7.7. Summary of coating conditions and palladium attack observations for several Triso-coated fissile particle batches irradiated in capsule HRB-15a

(A wide range of palladium attack observations were made on particles with very similar coating conditions)

Batch	Coating temperature (°C)	H_2/MTS[a]	Coating rate (μm/min)	Density (Mg/m^3)	Attack depth observed[b] (μm)	Particles attacked (%)
6151-23-010	1700	120	0.23	>3.197	3	50
6152-04-010	1700	110	0.18	>3.217	3	40
6152-05-010	1700	110	0.29	>3.217	15	65
6157-11-010	1650	149	0.26	>3.223	30	70

[a]MTS, methyltrichlorosilane.

[b]Predicted attack: 4 μm.

Source of data: GA Technologies, San Diego, Calif.

Although the inner pyrocarbon coating rates are batch averages and considerable variation about the batch average has been shown in other studies for pyrocarbon coatings, this does not seem like a promising explanation of the variability in resistance to palladium attack shown in Table 7.7.

Variation in silver retention

Comparisons between calculated and measured silver-to-ruthenium and cesium-to-ruthenium activity ratios for Triso-coated fissile particles from two of the six fuel rods irradiated in capsule HRB-15a and subsequently examined with IMGA were presented in Table 7.5. Comparing the silver-to-ruthenium data for rods 1 and 17 shows a substantial variation in performance between the particles from rod 17. The mean retention from the rod 1 particles was 50% compared with about 15% for the particles from rod 17 (some of which lost 100% of their silver). There is no information about the fabrication or irradiation conditions for these particles to explain the performance differences. There may be a correlation between palladium attack and silver loss, and this will be checked experimentally.

7.3.5 Capsule HRB-16 — M. J. Kania and G. C. Marsh

Seven irradiated fuel rods from capsule HRB-16 were sectioned and mounted for metallographic examinations. The rods were fabricated by GA and occupied irradiation positions 2, 6, 7, 8, 9, 13, and 14. Preliminary examinations have been completed and general observations recorded. In fuel rod 7, which contained the Triso-coated UCO fissile particle batch 6157-11-010 fabricated in production-scale facilities, significant SiC corrosion was observed. This behavior is similar to the behavior observed with a similar UCO particle batch 6157-11-020 irradiated in rod 17 of capsule HRB-15a (Sect. 7.3.4.1). To a much lesser degree, SiC corrosion was noted in fuel rods 2 and 13, which contained three different types of fissile particle batches. The exact particle batch or batches exhibiting the corrosion have not been determined. Some kernel migration was also noted in fuel rods 13 and 14, each of which contained Triso-coated UO_2 fissile particle batches.

The extended metallographic examinations will be completed in FY 1984. At that time detailed inventories of all particles observed in each metallographic section will be performed. A total of three cross sections will be made for each rod to improve the statistics supporting general observations.

7.3.6. Capsule R2-K13 — M. J. Kania

Two fuel rods containing GA fuel and irradiated in capsule R2-K13 were subjected to a 25-h acid leach, and the total amount of thorium and uranium removed was quantitatively measured. The amounts recovered are

Rod	Thorium (μg)	Uranium (μg)
2B2	1120 ± 10	3200 ± 20
3A1	300 ± 10	730 ± 20

The above measurements and the initial fissile and fertile fuel loadings, irradiation history, and environment were used to determine the numbers of particles that had exposed fuel kernels after irradiation. The exposed fissile and fertile fuel kernels result from total coating failure during irradiation.

Both rods contained the same Triso-coated UCO fissile particle, but the Triso-coated fertile particle batches in each were different. Rod 2B2 contained a composite batch, 6252-12 COMP, and rod 3A1 contained batch 6252-12T 04 B2 (the latter was one of the fertile batches making up 6252-12 COMP). Calculated actinide burnups for ^{233}U, ^{235}U, ^{239}Pu, and ^{241}Pu were provided by KFA-Jülich.[17]

The fissile and fertile fuel inventories remaining in each fuel rod at the end of the R2-K13 irradiation were estimated from the neutronics data for the R2-Studsvik reactor and initial fuel inventories. Fissile and fertile fuel inventories, beginning of life (BOL) and end of life (EOL), are

	^{232}Th (g)		^{235}U (g)		^{238}U (g)	
Rod	BOL	EOL	BOL	EOL	BOL	EOL
2B2	0.301	0.268	0.05917	0.00026	0.24217	0.20812
3A1	0.301	0.271	0.05917	0.00037	0.24217	0.20922

The acid leach investigations were conducted more than 15 months after reactor discharge of the R2-K13 experiment; thus, for practical purposes, all ^{233}Pa was considered to have decayed to ^{233}U. The number of uranium atoms generated from ^{232}Th is just the difference between BOL and EOL inventory. Uranium inventory generated during irradiation is presented in Table 7.8. However, a significant quantity of this uranium inventory was lost from fission of ^{233}U — burnups of 3.73% FIMA in rod 2B2 and 3.50% FIMA in rod 3A1. Each fuel rod had the same initial fuel loading, which represents a total of 1.546×10^{21} heavy metal atoms. Thus, the ^{233}U burnup values represent a loss of 67 and 69% of the uranium inventory in rods 2B2 and 3A1, respectively (Table 7.8). The uranium inventory consists primarily of ^{233}U and ^{234}U isotopes with the ^{233}U most dominant.

Based on these calculations and the initial fuel loadings, ^{232}Th and ^{233}U concentrations on a per-particle basis were also determined. Results of the calculations are summarized in Table 7.8 for each of the fertile particle batches in rods 2B2 and 3A1.

For the fissile particle batch, 6157-11-020, similar calculations were performed to determine the uranium inventory at EOL. End-of-life ^{235}U and ^{238}U inventories were determined for the entire fuel rod. The

Table 7.8. Fissile and fertile fuel inventories remaining in fertile particles from rods 2B2 and 3A1 of experiment R2-K13

Rod	Inventory at end of life					
	Per fuel rod (atoms)				Per particle (μg)	
	^{232}Th	^{232}Th to ^{233}U	^{233}U fissions	^{233}U	^{232}Th	^{233}U
2B2[a]	6.96E+19	8.57E+19	5.77E+19	2.80E+19	374.3	15.1
3A1[b]	7.03E+19	7.79E+19	5.41E+19	2.38E+19	383.9	13.0

[a]Particle batch 6252-12 COMP had 420.7 μg ^{232}Th per particle; therefore, rod 2B2 contained approximately 716 fertile particles.

[b]Particle batch 6252-12T 04 B2 had 426.3 μg ^{232}Th per particle; therefore, rod 3A1 contained approximately 706 fertile particles.

decrease in the ^{238}U inventory results in the buildup of plutonium isotopes and does not contribute to the EOL uranium inventory. The decrease in the ^{235}U inventory results from fission and from neutron capture reactions creating higher mass uranium isotopes, that is, ^{236}U and eventually ^{237}U. Following procedures used earlier for the fertile particle batches, uranium concentrations for the total fuel rod and on a per-particle basis were calculated (Table 7.9).

The number of particles with total coating failure was obtained from the EOL thorium and uranium concentrations measured in the 25-h acid-leach investigations. For rod 2B2, a total of 1120 ± 10 μg Th was recovered. Data from Table 7.8 indicate that a mean particle from this fuel rod would be expected to contain 374.3 μg Th at the time of the leach investigation. Thus, the leached thorium inventory represents the equivalent of 3.0 ThO_2 fuel kernels from particle batch 6252-12 COMP. The amount of uranium (^{233}U) represented by these three fertile kernels is 45.3 μg. For rod 3A1, a total of 300 ± 10 μg Th was recovered from the acid-leach investigation. Using the data in Table 7.8, a mean ThO_2 kernel from this rod would contain 383.9 μg Th. This represents an equivalent of 0.8 ThO_2 kernels from particle batch 6252-12T 04 B2. The corresponding amount of uranium (^{233}U) this represents is about 10.9 μg.

Table 7.9. Fissile and fertile fuel inventories remaining in fissile particles from rods 2B2 and 3A1 of experiment R2-K13

Rod	Inventory at end of life					
	Per fuel rod (atoms)				Per particle[a] (μg)	
	^{238}U	^{235}U	^{235}U fissions	^{236}U and ^{237}U	^{238}U	^{236}U[b]
2B2	5.27E+20	6.66E+17	1.26E+20	2.50E+19	152.6	7.4
3A1	5.29E+20	9.48E+17	1.26E+20	2.50E+19	153.4	7.5

[a]Particle batch 6157-11-020 had a total of 221.0 μg U per particle; therefore, rods 2B2 and 3A1 each contained approximately 1364 fissile particles.

[b]Actual concentration makes up about 5% of the total uranium inventory of the fissile particle and includes the isotopes ^{235}U, ^{236}U, and ^{237}U.

To determine the number of equivalent fissile fuel kernels represented in the acid-leach data, a similar analysis was performed. In this analysis it was necessary to subtract the ^{233}U inventories for each of the fuel rods of interest. For rod 2B2, 45.3 μg was deleted for the total uranium content of 3200 ± 20 μg, resulting in 3155 ± 20 μg attributed to fissile kernels. By use of data from Table 7.9, a mean UCO kernel at time of leach would contain 160 μg U. This translates into an equivalent of 19.7 UCO fissile fuel particles in rod 2B2 having total coating failure. In rod 3A1, 10.9 μg ^{233}U was removed from the leached uranium inventory, leaving about 720 ± 20 μg U. A mean UCO kernel for the rod would contain about 160.9 μg U at time of leach (Table 7.9). This represents an equivalent of 4.5 fissile fuel particles in rod 3A1 having total coating failure.

Table 7.10 summarizes the results of the calculations described above. Included are the initial number of particles used in the fabrication of fuel rods 2B2 and 3A1 as well as the equivalent number of failed particles represented by the recovered actinide inventory from the 25-h

Table 7.10. Summary of particle performance in fuels rods 2B2 and 3A1 irradiated in experiment R2-K13

Rod	Batch	Number of particles		Fraction with total coating failure (%)
		Total	Failed	
		Fertile particles		
2B2	6252-12-COMP	716	3.0	0.42
3A1	6252-12T 04 B2	706	0.8	0.11
		Fissile particles		
2B2	6157-11-020	1363	19.7	1.44
3A1	6157-11-020	1364	4.5	0.33

acid leach. In fuel rod 2B2, which maintained a mean operating temperature of 1190°C for 516 full-power days, the number of particles having total coating failure at EOL represents about 1.4% of the fissile batch and 0.42% of the fertile batch. In rod 3A1, which maintained a mean operating temperature of 985°C, the number of particles having total coating failure at EOL represented 0.33% of the fissile batch and 0.11% of the fertile batch.

Rods 2B2 and 3A1 were then subjected to an electrolytic deconsolidation to obtain unbonded particles for subsequent IMGA examination. Samples of the electrolyte solutions from each rod were analyzed for total thorium and uranium content. The results of these analyses are

Rod	Concentration in electrolyte from deconsolidation (μg/mL)	
	Thorium	Uranium
2B2	4 ± 1	94 ± 10
3A1	<1	<10

In rod 3A1, the heavy metal content was only at the detection level. However, for rod 2B2, much higher levels of heavy metal were detected. The total amount of electrolyte used in the deconsolidation was 400 mL. For rod 2B2, this amounts to 1.6 mg Th and 37.6 mg U. The the data presented in the long-term leach analysis (274.3 μg ^{232}Th per fertile particle and 160 μg U per fissile particle) indicate that the heavy metal

contents in the electrolyte solutions represent the total heavy metal inventory in 4.3 ± 1.1 fertile particles and 235 ± 25 fissile particles.

We are not certain how to deal with this large amount of uranium as represented by the electrolyte analysis. The electrolyte data together with the long-term acid-leach data represent an EOL uranium inventory of 19% for the fissile UCO fuel and about 1% of the thorium inventory for rod 2B2.

The unbonded particles from both rods are now being examined with IMGA; however, the detailed analyses of the data from that examination are not completed. Preliminary data analyses indicate only a small number of failures in the fuel from rod 3A1 but a much larger number of failures in rod 2B2. A detailed analysis of the examination data is scheduled in FY 1984.

7.4 U.S.-FRG COOPERATIVE PROGRAM

This work is being performed under the Fuel, Graphite, and Fission Product Subprogram, which is one of several programs included under the Umbrella Agreement between the United States and the FRG. The fuel development work covered in this subprogram is being performed by ORNL, GA, and KFA-Jülich. During this reporting period, a draft report was prepared by ORNL under project work statement (PWS) FD-1, which deals with fuel performance of fuel cycles other than the low-enriched fuel cycle. An abstract of this report is provided in Sect. 7.4.1. Only PWS FD-20 remains as an active project work statement in the fuel development area. All ORNL PIE activities associated with German-irradiated fuels are reported in Sect. 7.4.2.

7.4.1 PWS FD-1 (Extended) — F. J. Homan and M. J. Kania

The PWS FD-1 was the first undertaking of the U.S.-FRG cooperation in HTR fuel development. The goal of this project was to review all the performance data on LEU HTR fuel particles and to document the highlights of this work in a final report. This task was completed successfully, and the report has been a very useful source of information.[18]

At the February 1983 subprogram management meeting, the KFA-Jülich representative suggested that the scope of PWS FD-1 be extended to include

all the performance data for all fuel cycles. GA Technologies indicated a disinclination to be involved in the extension of PWS FD-1 because of resource (personnel) limitations, but ORNL and KFA agreed that the project would be worthwhile.

The ORNL contribution to this report was completed and sent to KFA for review and comment. This report has also been prepared for publication.[19] The report concentrates on the design and fabrication influences on coated-particle fuel performance. An abstract of this report follows.

> A quarter century of development and testing of candidate coated-particle fuel designs has led to the current reference fuel for the U.S. HTGR. The reference fuel system for the low-enriched uranium (LEU) fuel cycle is a Triso-coated "UCO" fissile particle and a Triso-coated ThO_2 fertile particle. The performance trends established through the irradiation testing program are reviewed in this report, and the impact of these trends on the evolving design are discussed. The problem areas remaining for the reference fuel particle system are stated, and recommendations are made for experimental work to resolve these problems.

7.4.2 PWS FD-20 — M. J. Kania and G. A. Moore

Through PWS FD-20 irradiated HTR fuel specimens from the German fuel development program are shipped to ORNL for detailed postirradiation examination. Examinations of interest to the German program include IMGA, PGA, x-radiography, and electron microprobe.

The second set of irradiated fuels to be examined under this project work statement were received at ORNL in August 1982, and their examination with the IMGA system began in October 1983. Unbonded coated particles from experiments FRJ2-P23/compact 14, FRJ2-P25/compacts 32, 27, 21, and 13; and DR-S6/compacts 19 and 22 were included in set 2. The unbonded particles, 1500 to 2000 from each compact, were obtained from the irradiated compacts through a chemical deconsolidation performed at KFA-Jülich before shipment.

The IMGA examinations have been completed on a representative number of particles from each of the seven fuel sources listed above. A complete analysis of the IMGA data has not yet been completed; however, we expect to complete this work by the end of March 1984. The gamma spectrometry measurements performed on each particle during the IMGA examination concentrated on the fission and activation products ^{106}Ru, ^{134}Cs, ^{137}Cs,

^{144}Ce, and ^{154}Eu. The gamma energy peaks of interest in determining the inventories of each of these isotopes were the same gamma peaks that were monitored during gamma spectrometry measurements performed at KFA-Jülich. For the single compact from experiment FRJ2-P23 and the four compacts from experiment FRJ2-P25, some preliminary IMGA examination data analysis has been completed. A comparison between the IMGA-derived mean fission product inventories and those measured at KFA are shown in Table 7.11.

Table 7.11. Comparison of IMGA- and KFA-Jülich-derived fission and activation product inventories for set 2 fuels examined under PWS FD-20

Experiment/ compact	Number of particles examined	IMGA data (GBq/g U)			KFA data (GBq/g U)		
		^{134}Cs	^{137}Cs	^{106}Ru	^{134}Cs	^{137}Cs	^{106}Ru
FRJ2-P23/14	1567	13.48	11.96	17.22	11.8	14.0	19.5
FRJ2-P25/32	1607	9.86	10.90	14.93	9.66	11.8	16.3
/27	1606	13.31	12.46	17.00	13.4	14.2	17.3
/21	1660	12.43	12.45	16.24	12.8	13.6	16.6
/13	1629	10.48	12.75	16.75	10.8	14.1	14.7
DR-S6/19	300[a]	*b*	*b*	*b*	*b*	*b*	*b*
/22	300[a]	*b*	*b*	*b*	*b*	*b*	*b*

[a]Only 300 particles were examined because of the long time delay between IMGA examination and reactor discharge (from September 1975 to November 1983).

[b]Preliminary analysis not completed.

In general the agreement between ^{134}Cs inventory for the ORNL and KFA data is very good. The agreement between the ^{137}Cs and ^{106}Ru inventory data is relatively poor. At this time we are not in a position to determine the measurements that are in error or if other considerations should be taken into account. Details about the gamma spectrometry measurements performed at KFA with regard to number of particles examined and counting statistics have not been factored into this preliminary inventory analysis. As these data become available, they will be properly considered.

Selected particle sets, 10 to 12 particles each, are now being gamma counted from each of the compacts. These particles will then be broken in the PGA system to measure the inventory of stable krypton and xenon isotopes present in each particle. This work will also be completed by the end of March 1984.

7.5 EQUIPMENT DEVELOPMENT AND MAINTENANCE — M. J. Kania

The IMGA, the PGA, and the x-radiography facility are three important pieces of equipment in use in the PIE of HTR fuels. Although they are used in routine PIE, we continue to maintain and upgrade their capabilities for better quality information.

7.5.1 Irradiated Microsphere Gamma Analyzer — M. J. Kania and G. A. Moore

During the reporting period the availability of the IMGA system was nearly 80%, a major improvement over the previous year. Equipment failures associated with the TP-5000 pulse height analyzer and the data storage devices were responsible for most of the downtime. A problem with the automated particle handler, which caused a 5 to 10% loss of particles examined during transfer to the collector storage bins, was isolated and eliminated without requiring a major decontamination of the IMGA cubicle and without radiation exposure to operating personnel.

Detailed fuel examinations were completed for capsule HT-35, which included the fissile and fertile particles from deconsolidated driver fuel rods and unbonded fertile particles contained in graphite holders. Set 2 fuels under PWS FD-20, which included irradiated fuel from experiments FRJ2-P23/compact 14, FRJ2-P25/compacts 32, 27, 21, and 13, and DR-S6/compacts 19 and 22, were subjected to IMGA examinations. Two fuel rods irradiated in the R2-K13 experiment were also examined with the IMGA system. These fuels were fabricated by GA and irradiated in the U.S.-FRG cooperative experiment R2-K13. In addition, a comparative study by GA and ORNL was undertaken to determine if any real differences existed in fission product inventory determinations at the two facilities.

The significant results of this comparison were that, for gamma-active isotopes such as ^{106}Ru, ^{134}Ce, ^{137}Cs, and ^{144}Ce, the agreement was good within ±2%. However, for the isotopes ^{110m}Ag and ^{154}Eu the values were lower by 11 and 4%, respectively, than corresponding GA-derived inventories. No solutions to resolve these differences were apparent, although it was felt that agreement to within even 11% for ^{110m}Ag was sufficient.

A major equipment upgrading occurred this year with the acquisition of a new pulse height analyzer system to replace the TP-5000 system initally purchased for IMGA. A Nuclear Data, Inc., ND-6700 system was selected. Initial deliveries began in March 1983, and the final delivery and installation of the automated particle-handler interface occurred in July 1983. Complete operation of the particle handler under software control with the ND-6700 system was demonstrated in compliance with our specifications. Software development to connect the present IMGA operating system, now in FOCAL-11 program language, to FORTRAN IV is well under way. Once the software transfer is complete, the new system will take over completely. The two systems are located in close proximity to each other, so the transfer will be minor and should involve no shifts in our PIE schedule. Personnel orientation with the new analyzer system has been completed, and the ND-6700 system is being used to perform IMGA system calibration calculations and fission product inventory calculations.

7.5.2 Postirradiation Gas Analyzer — M. J. Kania

During this reporting period the PGA system was not available for use. Modifications to the system in FY 1982 were not made fully operational. The reasons for this were lack of technical support and the inability to interface the quadrupole mass spectrometer to the PDP-8A minicomputer.

Progress on the PGA system is now to the point that full operation is within our grasp. The new IQ-200 mass spectrometer system has been interfaced to a DEC LSI-11/23 computer, and the FORTRAN IV software, written and implemented. Some minor problems exist in data transfer, but these are now being isolated and corrected. The mechanical components of the system remained in a good state of operation, with the exception of the turbomolecular vacuum pump. A new pump was ordered and installed.

The system is now configured so that small orifices are used for the inlet of gas to the quadrupole mass spectrometer. By correctly sizing these orifices, we have been able to extend the gas pulse, generated by breaking a particle, from 1 to 2 s to over 30 min. This permits only a very small increase in pressure for the spectrometer and will not change its sensitivity as a result of a large pressure increase. This will improve our accuracy and sensitivity for gas inventory measurements.

Irradiated fissile and fertile fuels from capsules HT-34, -35, and HRB-15a have been examined and analyzed and are waiting for PGA examination. This work will begin as soon as full PGA operation has been demonstrated.

7.5.3 X-Radiography Facility — M. J. Kania

A new high-voltage power supply and console were purchased in FY 1982 for this facility, and delivery of this system was made in late October 1982. Installation of the system began in February 1983 by representatives from Seifert X-Ray Corporation. Unfortunately, not all the modifications requested with the unit were accomplished, and some portions of the equipment were returned to Seifert for additional modifications. The new console with the necessary modifications has not yet been delivered.

The system is currently operating with the original 5- to 50-keV power supply. This is adequate for the interim period until detailed fuel particle examinations are needed for capsule HRB-16 fuel.

7.6 REFERENCES

1. R. L. Senn, "Hydrolysis Experiments HRB-17 and HRB-18," pp. 8–9 in *High-Temperature Gas-Cooled Reactor Technology Development Program Annual Progress Report for Period Ending December 31, 1982*, ORNL-5960, June 1983.

2. T. N. Tiegs, I. I. Siman-Tov, and M. J. Kania, "Capsule HT-35," pp. 23–27 in *High-Temperature Gas-Cooled Reactor Technology Development Program Annual Progress Report for Period Ending December 31, 1980*, ORNL-5753, August 1981.

3. M. J. Kania and T. N. Tiegs, "Capsule HT-35," pp. 16–21 in *High-Temperature Gas-Cooled Reactor Technology Development Program Annual Progress Report for Period Ending December 31, 1981*, ORNL-5871, June 1982.

4. R. J. Lauf, "Irradiation Behavior of Pyrolytic Silicon Carbide," pp. 72–73 in *Proceedings of 41st Annual Meeting of Electron Microscopic Society of America* held in Phoenix, Ariz., on Aug. 8–12, 1983, ed. G. W. Bailey, San Francisco Press, San Francisco, 1983.

5. M. J. Kania and K. H. Valentine, *The Irradiated-Microsphere Gamma Analyzer (IMGA) — An Integrated System for HTGR Fuel Performance Assessment*, ORNL-5606, November 1980.

6. J M Robbins et al., "A System for Measuring Fission-Gas Inventories of HTGR Fuel Particles," pp. 241–45 in *Proc. 27th Conf. Remote Systems Technology*, 1979, American Nuclear Society, LaGrange Park, Ill., 1981.

7. R. J. Lauf, T. B. Lindemer, and R. L. Pearson, "Out-of-Reactor Studies of Fission Product-Silicon Carbide Interactions in HTGR Fuel Particles," *J. Nucl. Mater.* 120(1), 6–30 (February 1984).

8. R. J. Price, "Neutron Irradiation-Induced Voids in the β-Silicon Carbide," *J. Nucl. Mater.* 48(1), 47–57 (1973).

9. M. J. Kania, B. A. Thiele, and F. J. Homan, *Irradiation-Induced Permeability in Pyrocarbon Coatings: Final Report of Work Conducted Under PWS FD-12*, ORNL/TM-8341, October 1982.

10. F. J. Homan and M. J. Kania, *Irradiation Performance of Triso-Coated Fissile and Biso-Coated Fertile HTGR Fuel Particles in Irradiation Capsule HRB-14*, to be published at Oak Ridge National Laboratory.

11. E. L. Long, Jr., et al., *Performance of HTGR Biso- and Triso-Coated Fertile Particles in Capsule HT-34*, ORNL-7674, August 1981.

12. F. J. Homan et al., *Irradiation Performance of HTGR Fuel Rods in HFIR Experiments HRB-11 and -12*, ORNL-5584, June 1980.

13. E. J. Allen, *CACA-2: Revised Version of CACA — A Heavy Isotope and Fission-Product Concentration Calculational Code for Experimental Irradiation Capsules*, ORNL/TM-5266, February 1976.

14. M. J. Kania et al; unpublished data, April 1983.

15. J. W. Ketterer and R. E. Bullock, *Capsule HRB-15B, Postirradiation Examination Report*, GA-A15940, General Atomic Company, San Diego, Calif., June 1981.

16. R. Forthmann, Kernforschungsanlage-Jülich, Jülich, Federal Republic of Germany, unpublished data.

17. H. Nabielek, Kernforschungsanlage (KFA)-Jülich, Federal Republic of Germany, personal communication to M. J. Kania, ORNL, December 1981.

18. F. J. Homan, H. Nabielek, and L. Yang, *Low-Enriched Fuel Particle Performance Review*, GA-A14759, General Atomic Company, San Diego, Calif.; Jül-1502, Kernforschungsanlage-Jülich, Jülich, Federal Republic of Germany, August 1978.

19. F. J. Homan and M. J. Kania, *Effects of Design and Fabrication Variables on HTGR Coated-Particle Fuel Performance*, to be published at Oak Ridge National Laboratory.

8. FISSION PRODUCT STUDIES (WBS 3650.03)

O. K. Tallent and R. P. Wichner

8.1 INTRODUCTION — R. P. Wichner

The purpose of this study is to obtain data to calculate or estimate the rate of transport of important actinides and fission products throughout a High-Temperature Reactor (HTR) under both normal and accident conditions. The diffusion rates and vapor pressures of actinides present as oxides or carbides adsorbed on H451 graphite are being investigated. In addition, experiments are being performed to elucidate the chemical forms of fission product compounds vaporized from failed or defective fuel.

8.2 ACTINIDE DIFFUSION IN GRAPHITE — O. K. Tallent, T. T. Godsey, and R. L. Towns

Plutonium diffusion under conditions approximating those of the primary coolant loop in an HTR is being investigated. The experimental method being used is similar to that previously used to study uranium diffusion in graphite.[1] Results from a preliminary test are shown in Table 8.1. This test was conducted for 90 h at 1000°C. Plutonium (initially present as PuO_2) diffused to distances of 0.0012, 0.0037, 0.0062, and 0.0095 cm in the graphite at respective concentrations of 0.60, 0.75, 0.45, and 0.10 $\mu g/cm^3$. A preliminary diffusion coefficient for the plutonium of 1.5×10^{-11} cm^2/s was evaluated from the data. This value compares with previously determined values of 1.85×10^{-12} and 1.06×10^{-11} cm^2/s, respectively, for uranium initially present as UO_2 and UC_2 at 1000°C (ref. 1). We plan to continue this work with plutonium dioxide (PuO_2) and plutonium sesquicarbide (Pu_2C_3) at temperatures of 1000, 1200, and 1400°C.

Table 8.1. Penetration distance of plutonium, initially plutonium dioxide, in H451 graphite at 1000°C in 90 h

Penetration distance (cm)	Plutonium concentration ($\mu g/cm^3$)
0.0012	0.60
0.0037	0.75
0.0062	0.45
0.0095	0.10

8.3 PLUTONIUM VAPOR PRESSURE MEASUREMENT — O. K. Tallent, T. T. Godsey, and R. L. Towns

Determination of the rate or extent of transport of plutonium in an HTR requires knowledge of the vapor pressure of plutonium that has diffused or otherwise been transported to a gas passage surface in the reactor. To this end, the vapor pressure of plutonium (initially present as plutonium dioxide or sesquicarbide) adsorbed on the surface of H451 graphite was measured at 1000, 1200, and 1400°C with a transpiration vapor pressure measurement method. A schematic of the equipment is shown in Fig. 8.1. The total volume and the flow rate of the carrier helium gas passed through the system was carefully measured during each test. The gas was passed over a graphite pellet containing adsorbed plutonium in a furnace at temperatures of 1000, 1200, and 1400°C. The pellet was contained in either a ceramic or a quartz tube, depending on the temperature. Plutonium vaporized from the pellet was recrystallized on colder sections of the tube or on a quartz tube cold trap. All measurements were made at gas flow rates in which the plutonium gas densities were independent of the gas flow rate.

At the end of each test, the quartz tube trap and sections of the gas flow apparatus downstream from the pellet were leached in 250 mL of 12 *M* HNO_3–0.08 *M* HF solution at about 100°C for 8 h to dissolve the recrystallized plutonium. The amount of plutonium in the leach solution was determined from gross alpha and alpha pulse height analyses. The plutonium vapor pressure was calculated from the amount of plutonium dissolved and the total volume of helium carrier gas passed through the system.

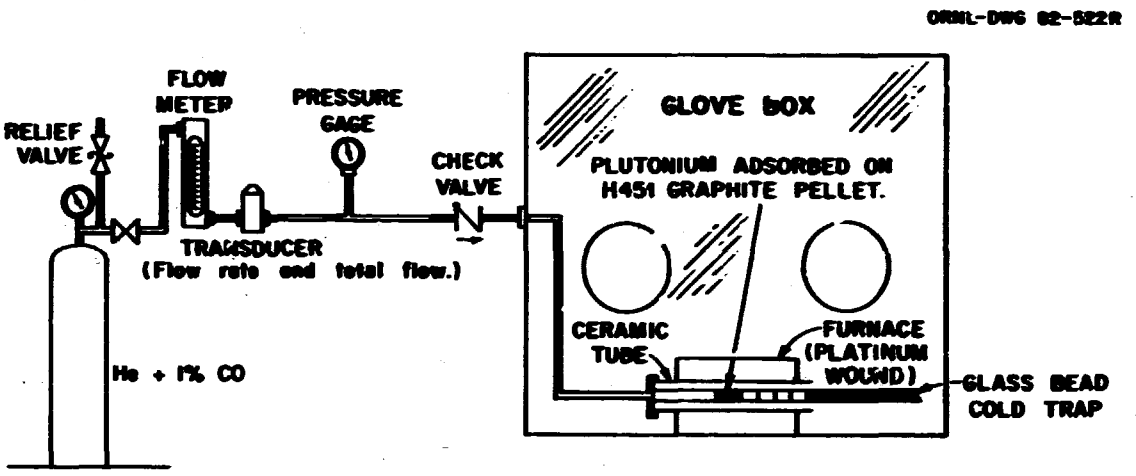

Fig. 8.1. Apparatus for measuring vapor pressure of plutonium adsorbed on H451 graphite.

The investigation showed that the vapor pressure of plutonium present in an adsorbed state on the surface of H451 graphite can be defined in terms of an adsorption isotherm and that the effective vapor pressures are lower than those of pure Pu_2C_3. Figure 8.2 shows adsorption isotherms for 1000, 1200, and 1400°C. The isotherms are defined by the following equations, where P is in megapascals and C is in micromoles of Pu_2C_3 per square meter of graphite surface area, m^2.

Equation	Temperature (°C)	Correlation coefficient	
$\log P = -10.57 + 0.59C$	1400	0.94	(1)
$\log P = -12.04 + 0.97C$	1200	0.99	(2)
$\log P = -14.95 + 0.79C$	1000	0.70	(3)

The correlation coefficients indicate that the equations for the 1400 and 1200°C isotherms represent the data very well. The low correlation coefficient for the 1000°C isotherm probably results from experimental error in recovering and analyzing the plutonium, which was vaporized in much smaller amounts in the 1000°C tests. At low plutonium surface concentration (<0.2 $\mu mol/m^2$ of surface area), the plutonium vapor pressures are about three orders of magnitude less than that of pure Pu_2C_3 (ref. 2). The heat of plutonium (as Pu_2C_3) adsorption increases with decreasing Pu_2C_3 surface coverage, with the measured value at 0.05 μmol Pu_2C_3/m^2 being

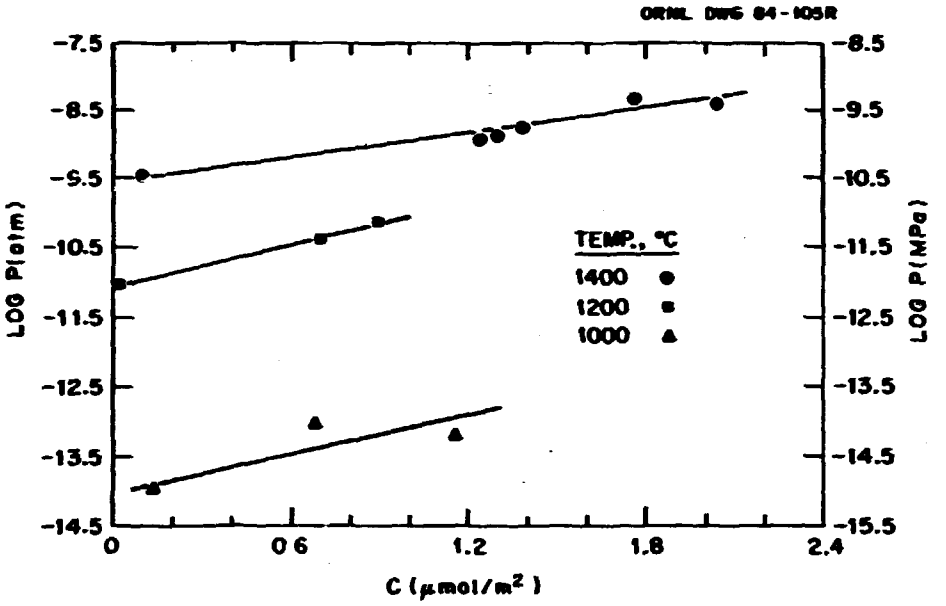

Fig. 8.2. Plutonium sesquicarbide adsorption isotherms on H451 graphite.

431 kJ/mol. The Pu_2C_3 concentration required for monolayer surface coverage on the graphite was 3.27 $\mu mol/m^2$, and the effective Pu_2C_3 molecular area was about 0.5 mm^2.

The plutonium on the surface of the graphite is normally present as Pu_2C_3; however, at low carbon monoxide concentrations in the helium cover gas, the plutonium may be present as an oxide.[3] Vapor pressures at 1000 and 1400°C for plutonium adsorbed as oxides (PuO_2 and Pu_2O_3) were respectively measured to be 3.16×10^{-9} and 1.58×10^{-7} kPa (3.16×10^{-11} and 1.58×10^{-9} atm). A semilog plot of vapor pressure versus reciprocal temperature, including data of Paprocki et al.,[4] is shown in Fig. 8.3. The curve drawn to represent the data is nonlinear, as can be seen. The two data points from our work and nine data points from Paprocki et al. are represented with a 0.98 correlation coefficient by the following expression

$$\log P = -7.57 - 4396(10^4/T) + 0.002T \ , \qquad (4)$$

where P denotes plutonium vapor pressure in kilopascals and T denotes temperature in kelvins. The graphite surface coverage by the adsorbed

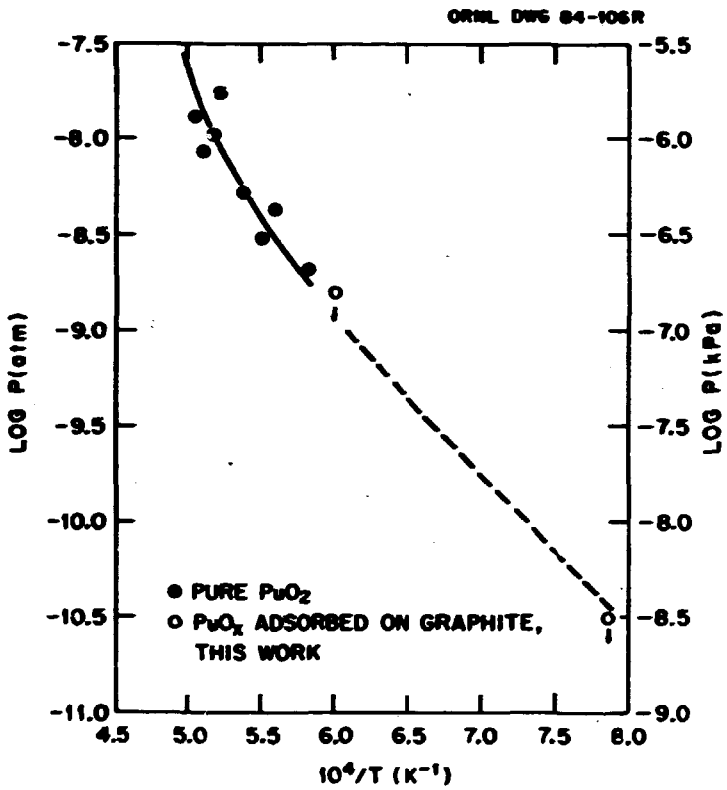

Fig. 8.3. Plutonium oxide(s) vapor pressure as a function of reciprocal temperature. *Source of pure PuO_2 data*: S. J. Paprocki et al., pp. 1–14 in *The Volatility of PuO_2 in Nonreducing Atmospheres*, BMI-1591, Battelle Memorial Institute, Columbus, Ohio, 1962.

plutonium oxides was about 42% in each test. In view of this fractional surface coverage, it is somewhat surprising that the adsorbed plutonium data correlate well with the pure PuO_2 data. The quantities of plutonium vaporized in the adsorbed plutonium tests were very small, being about 0.2 to 8 μg, such that error due to plutonium cross contamination could have been introduced. The real vapor pressures may be less than the measured values indicated in the figure.

The principal purpose of this investigation was to obtain information for estimating realistic plutonium concentrations in the primary cooling system of HTRs. Quantifications required for the actual estimates, including plutonium birth location and rate and plutonium diffusion direction and rate, will be reported later. Our general observation, based on

the results of this study, is that the release of plutonium to the coolant gas will be several orders of magnitude less than will estimates based on no plutonium holdup in the graphite.

8.4 FISSION PRODUCT RELEASE FROM FAILED FUEL AND DETERMINATION OF CHEMICAL FORMS — O. K. Tallent, T. T. Godsey, and R. L. Towns

This investigation involves determination of the chemical forms of fission products released from failed or defective fuel. These determinations are being made partly by inference from location and test temperature of fission product deposits. Equipment and experimental method for the investigation were tested this year by use of cesium and iodine as the initial testing materials. The iodine in the tests was initially added as cesium iodide (CsI), with additional cesium added as cesium carbonate (Cs_2CO_3). These initial source compounds were either adsorbed on the surface of H451 graphite pellets or sealed in holes 0.15 cm from the surface of the pellets. The pellets were heated at 425, 1000, or 1400°C for periods ranging from 10 min to 5 d under a flow of helium gas containing 0.01, 0.1, or 1% carbon monoxide. The vaporized cesium and iodine were condensed or adsorbed on graphite thermal gradient tubes at temperatures from 1000 to 30°C. At the end of each test, the thermal gradient tube was divided into segments, and each segment was analyzed for cesium and iodine by neutron activation analysis. A few of the segments were subjected to electron surface chemical analysis as an additional method for determining the chemical form of the adsorbed cesium and iodine.

The compositions of cesium and iodine species deposited on the thermal gradient varied significantly with temperature. The data in Table 8.2 are typical in that a large fraction of vaporized material was deposited as CsI (Cs:I mole ratio, ~1.0) at an intermediate temperature (~430°C) on the thermal gradient. At higher temperatures (>500°C), cesium-rich compounds were deposited; at lower temperatures (<400°C), iodine-rich compounds. Electron surface chemical analysis indicated the cesium-rich compounds to be oxygen-bearing, possibly cesium hydroxide (CsOH). This method indicated the presence of iodide ion (I^-) in the intermediate temperature deposits, consistent with these deposits being mainly adsorbed as CsI.

Table 8.2. Vaporized cesium and iodine deposited on graphite thermal gradient

(Initial graphite pellet contained 3.91 μmol CsI sealed into a center hole. Pellet temperature, 1000°C. Time for deposit, 15 min; carrier gas composition, 0.1% CO in helium)

Temperature (°C)	Cesium (μg)	Iodine (μg)	Mole ratio (Cs:I)
620	676.0	340.0	2.07
527	16.8	4.0	4.37
430	107.1	100.6	1.11
360	0.9	1.5	0.62
170	0.1	1.2	0.09
130	0.0	5.4	<0.02

Tests of the lower temperature (iodine-rich) deposits showed that the iodine in the deposits could be relatively easily volatilized or desorbed at temperatures not exceeding 100°C, consistent with these deposits being molecular iodine (I_2). The amount of iodine in the lower temperature deposits (apparently I_2) was decreased by decreasing the carrier gas carbon monoxide (CO) composition and increasing the Cs:I mole ratio in the source pellet. About 0.2% of the deposited iodine was found in the lower temperature deposits by use of 0.01 vol % CO and an initial Cs:I mole ratio of 10. This average iodine vapor density was from 5 to 10 times less in each test than was the vapor density of pure CsI at the same temperature.[5] This was true even though a large fraction of the vaporized iodine appeared to be either CsI or I_2. The lowered vapor pressures apparently resulted from bonding between the adsorbates (CsI and I_2) and the adsorption sites on the surface of the graphite.

8.5 REFERENCES

1. O. K. Tallent, R. P. Wichner, and R. L. Towns, *Diffusion of Uranium in H-451 Graphite at 900 to 1400°C*, ORNL/TM-8205, March 1983.

2. W. M. Olson and R. N. R. Mulford, "Thermodynamics of the Plutonium Carbides," pp. 467–78 in *Proceedings of a Symposium on the Thermodynamics of Nuclear Materials with Emphasis on Solution Systems Held by the International Atomic Energy Agency*, vol. 1, IAEA, Vienna, 1967.

3. T. M. Besmann and T. B. Lindemer, "Assessment of the Thermodynamic Values for ($PuO_{1.5}$) and High-Temperature Determination of the Values of ($PuO_{1.5}$)," *J. Am. Ceram Soc.* 66(11) 782–85 (1983).

4. S. J. Paprocki et al., pp. 1–14 in *The Volatility of PuO_2 in in Nonreducing Atmospheres*, BMI-1591, Battelle Memorial Institute, Columbus, Ohio, 1962.

5. I. Borin and O. Knacke, *Thermochemical Properties of Inorganic Substances*, Springer Publishing Co., New York, 1973, p. 254.

9. STRUCTURAL METALS STUDIES (WBS 3660)

P. L. Rittenhouse

9.1 INTRODUCTION

Our work on High-Temperature Reactor (HTR) structural metals is aimed at filling design needs for materials data and technology. The tasks in progress emphasize alloys selected as reference materials for critical components (e.g., thermal barriers, heat exchangers, and reactor internals) of HTR steam-cycle systems. Work on structural metals for HTR steam-cycle systems is also conducted by GA Technologies (GA). Coordination of the work at GA and at Oak Ridge National Laboratory (ORNL) is provided through an HTR Materials Working Group.

Experimental work in three areas,

- decarburization of 2 1/4 Cr-1 Mo steel,
- compatibility of type 316 stainless steel and alloy 800H with B_4C-graphite compacts, and
- fracture toughness characterization of prestressed concrete reactor vessel (PCRV) steels,

was completed in 1983, but some analysis and reporting efforts are continuing into 1984. A new study on the high-temperature fracture toughness of Inconel 718 was initiated. Continuing studies include stress-rupture and long-term creep, thermal stability, fatigue behavior, and welding-related fabrication technology for the HTR steam generator.

9.2 MECHANICAL PROPERTIES OF ALLOYS AND WELDMENTS (WBS 3660.01)

9.2.1 Creep Testing — H. E. McCoy and J. F. King

Testing in 1983 involved a large number of materials, including Hastelloy X weldments (two welding processes and two filler metals),

Inconel 617 (two heats), Inconel 617 gas tungsten arc (GTA) weldments, Inconel 618 base metal, Inconel 618 GTA weldments, HD556 base metal, HD556 GTA weldment, Hastelloy X-alloy 800H weldments (two welding processes), Incoloy 802 base metal, Incoloy 802 GTA weldment with Inconel 617 filler metal, Inconel 718, and 2 1/4 Cr-1 Mo steel (three heats). Creep test temperatures ranged from 482 to 871°C; test environments were air and HTR-He. The helium composition in the test chamber is [in pascals (microatmospheres)] 34.0 (337) H_2, 3.2 (32) CH_4, 1.0 (19) CO, 0.2 (2) H_2O, and <0.05 (<0.5) N_2. Oxygen in removed by reaction with H_2 as the gas passes through a furnace at 500°C.

Techniques were developed previously for making sound welds in Hastelloy X by both the GTA and shielded metal arc (SMA) welding processes; Hastelloy X and Hastelloy S were used as filler metals. The test data on Hastelloy X base metal and welds were complied in ref. 1; several conclusions were reached.

- Suitable welds were made in Hastelloy X with Hastelloy X filler metal and either the GTA or SMA welding process. Good welds were also obtained with Hastelloy S filler metal and the GTA welding process. Over the test range of 25 to 871°C, transverse specimens of all weldments had higher yields and ultimate tensile stresses than did the base metal and had fracture strains of 20 to 40%.
- Creep tests in excess of 40,000 h on two heats of Hastelloy X base metal showed no measurable differences in creep rate between the two heats or between test environments of air or HTR-He.
- The creep fracture strain was less for base metal samples tested in HTGR-He than for those tested in air.
- Carbon analyses of the entire cross sections of Hastelloy X creep samples showed that the kinetics of carburization increased markedly above 800°C.
- The creep curves for Hastelloy X are concave upward and do not have a long period of linear secondary or minimum creep. For example, only 6% of the time to rupture was required to reach 1% creep strain, and about 30% of the time to rupture was required to reach tertiary creep.

- Creep tests on weldments showed that the creep curves were not detectably different for transverse weldment and base metal samples. The main difference was the general failure of weldments at lower strains. Strains of 4 to 10% were commonly noted for SMA welds of Hastelloy X with Hastelloy X filler metal and of 10 to 20% for the other two weldments. Aged samples often exhibited higher fracture strains, indicating that better properties could likely be obtained with a postweld heat treatment.

The status of understanding of the creep behavior of Inconel 617 and 618 has not changed appreciably since last year.[2] Test durations have now reached 35,000 and 15,000 h for Inconel 617 and 618, respectively. Testing of both of these materials is in a phaseout period.

Incoloy 802 was welded satisfactorily with Inconel 617 filler metal and the GTA process. However, Inconel 617 is slightly stronger than Incoloy 802, and failure occurred in the base metal in test specimens with a transverse weld. The longest creep tests run on Incoloy 802 were about 12,000 h. The fracture strains of these test samples were 1 to 3%, illustrating the fact that low fracture strain is one of the weaknesses of this material. No further work is planned for this alloy.

HD556 is the strongest alloy evaluated. This alloy can be joined suitably with filler metal of the same composition, but the cast weld metal is weaker than the wrought base metal, and failure in a sample containing a transverse weld occurs in the weld metal. The longest creep test time was 21,000 h. Fracture strains under creep conditions were high, but the ductility at ambient temperature degraded rapidly with exposure at elevated temperatures. No further work is planned for this alloy.

Hastelloy X and alloy 800H were joined with both Inco weld A (SMA) process and ERNiCr-3 (GTA) process filler materials. Alloy 800H has lower creep strength than do the other materials involved, so failure consistently occurred in the alloy 800H. This work was reported in detail in ref. 3.

Testing is continuing on three heats of 2 1/4 Cr-1 Mo steel, and test times have reached 57,000 h. This alloy can be either carburized or

decarburized in the nominal helium composition being used as a test environment, depending on the test temperature and the concentration of residuals such as moisture. The creep strength appears to be influenced by the carburization and decarburization processes. The amount of creep testing of this material will be increased during the coming year.

Although some tests will be continued on materials being phased out, most of the testing during the coming year will be on Hastelloy X, 2 1/4 Cr-1 Mo steel, and Inconel 718.

9.2.2 Effects of Thermal Aging — H. E. McCoy

Most of the alloys being evaluated change properties as a result of exposure at elevated temperatures. A number of test samples are being exposed to determine the magnitude of these effects. Some of the changes are thermally induced, and some are the results of interactions with the HTR-He environment. Thus, aging tests are being run in both inert gas and HTR-He.

Samples of Inconel 617 and Hastelloy X base metal and weldments have been tested following a 32,500-h exposure to HTR-He. Some strength changes occurred, but the observation of primary interest was that the fracture strain at ambient temperature was reduced. Samples of Inconel 618 base metal and weldment have been aged to 20,000 h and exhibit only small changes in creep strength and in ductility at ambient temperatures. Inconel 718 has been aged 10,000 h in HTR-He, and the tensile properties at ambient and elevated temperatures were not changed appreciably. The impact energy of Inconel 718 was reduced at least 50% by aging at 590 to 650°C. Samples of 2 1/4 Cr-1 Mo steel have been aged about 6000 h in HTR-He, and some will be removed after 10,000 h for evaluation.

9.2.3 Fatigue Testing — J. P. Strizak

Investigations of the low-cycle and high-cycle fatigue properties of Hastelloy X were undertaken in 1983. Interim results of testing at 760°C in air and simulated HTR-He environments are discussed in detail in a report being published. Highlights of the report are given below.

9.2.3.1 Low-Cycle Fatigue Properties of Hastelloy X

Figure 9.1 shows results of continuous-cycling tests at 760°C on solution-annealed Hastelloy X. Comparing the data generated in HTR-He with those generated in air shows that the helium environment was not detrimental to fatigue life. Previously reported data at 538 and 871°C support this observation.[4]

Creep-fatigue tests were conducted at 760°C by use of a triangular waveform with hold periods of 0.1 to 1.0 h, introduced at either the peak tensile or compressive strain amplitude. Thus, creep-damage occurred during each cycle via stress relaxation. The effect of hold periods on the low-cycle fatigue life of Hastelloy X was substantial (Fig. 9.2). Life reduction was most pronounced at low strain ranges. For example, at a strain range of 0.5%, the life reduction regardless of hold mode (tension only, compression only, or tension and compression) was about 10:1; whereas, at a strain range of 2%, the life reduction was about 2:1. Figure 9.2 shows that compressive hold periods were somewhat more damaging to the fatigue life of Hastelloy X than were tension hold periods. This is thought to be true because of the high tensile mean stresses that developed in tests having compressive hold periods. Test results at a strain range of 0.5% showed that increasing the tensile or compressive hold period from 0.5 to 1.0 h did not further reduce fatigue life. Generally, the most damaging effect on the fatigue life of Hastelloy X occurred when hold periods were introduced at both the tensile and the compressive strain amplitudes of the cyclic waveform.

The prediction of long-term material behavior under combined creep and fatigue loading is an important and difficult aspect of elevated temperature design. Currently, the ASME Code recommends the use of the linear damage approach.[5] An alternative approach that has received considerable attention is strain range partitioning. The available creep-fatigue data on Hastelloy X were examined by these two procedures.

The linear damage summation approach separates the damage incurred in a material into time-dependent (creep) and time-independent (fatigue) components. At failure, the damage reaches some critical value D, given by

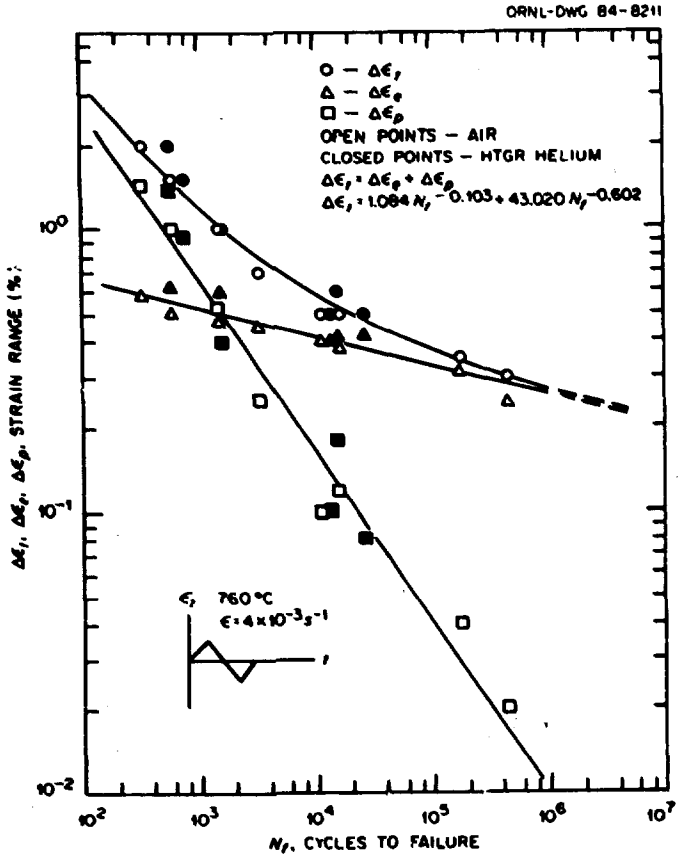

Fig. 9.1. Fully reversed strain-controlled fatigue tests conducted on Hastelloy X in air and HTR-He environments at 760°C.

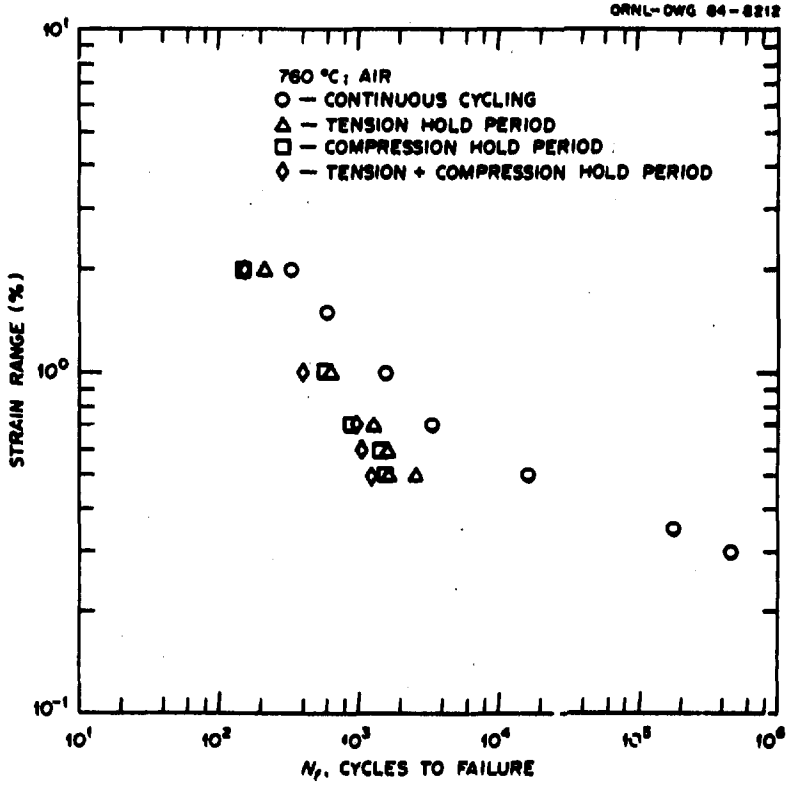

Fig. 9.2. Strain hold periods reduce the fatigue life of Hastelloy X. Compressive hold periods are generally more damaging than tension.

$$D = D_c + D_f \ , \qquad (1)$$

where D_c and D_f are the creep and fatigue damage fractions, respectively. The value of D is often assumed to be 1. However, a value less than unity may be appropriate to avoid overoptimistic prediction.

Creep damage and fatigue damage values determined for Hastelloy X are plotted in Fig. 9.3. A wide range of values was obtained. Because of very short creep-rupture times of the stress levels developed in the creep-fatigue tests, particularly at strain ranges above 0.5%, creep-damage values much greater than 1 were calculated. Figure 9.3 indicates a trend for decreasing fatigue and creep damage values with decreasing strain range. It seems that a bilinear damage diagram for Hastelloy X may be appropriate for tension or compression hold periods in either air or HTR-He environments. Should the damage values decrease to very small fractions, the utility of the linear damage summation approach for predicting long-term behavior for Hastelloy X may be questionable.

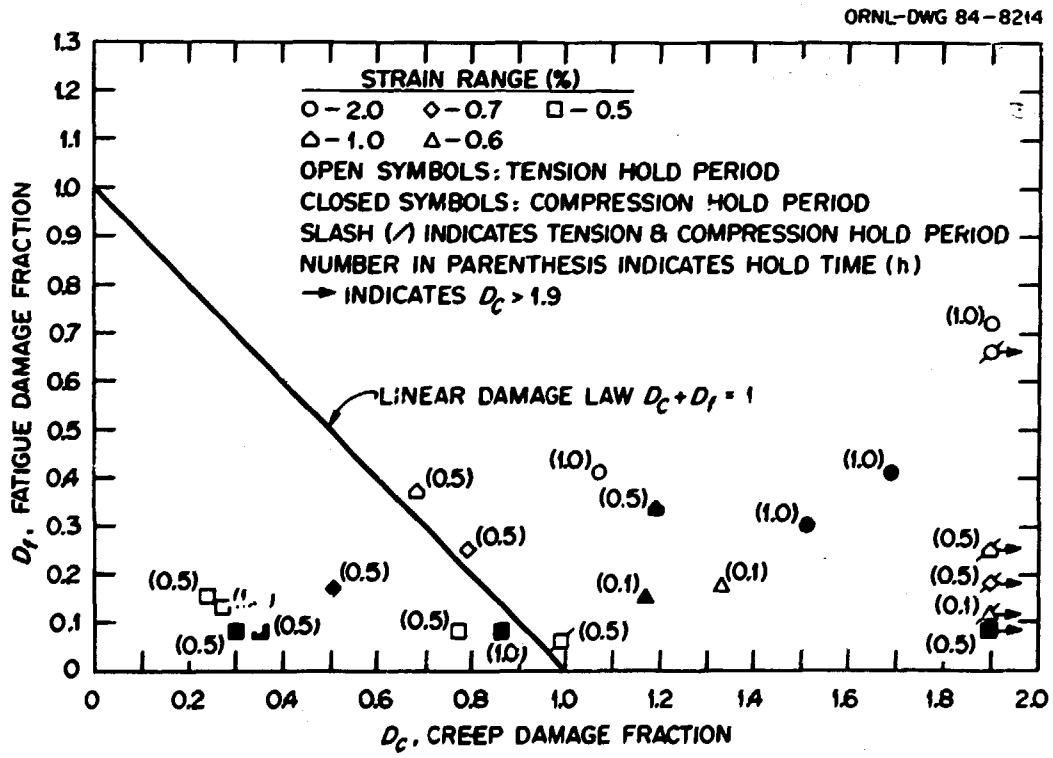

Fig. 9.3. Damage diagram for Hastelloy X at 760°C.

The strain range partitioning procedure partitions the inelastic strain range $\Delta\varepsilon_{in}$ traversed by a cycling specimen into four possible components:

$\Delta\varepsilon_{pp}$ = tensile plastic strain reversed by compressive plastic strain (here "plastic" strain is defined as time-independent inelastic strain),

$\Delta\varepsilon_{pc}$ = tensile plastic strain reversed by compressive creep strain (here "creep" strain is time-dependent inelastic strain),

$\Delta\varepsilon_{cp}$ = tensile creep strain reversed by compressive plastic strain,

$\Delta\varepsilon_{cc}$ = tensile creep strain reversed by compressive creep strain.

For a given set of loading conditions, the predicted cycle life is determined by the "interaction damage rule,"

$$1/N_{pred} = F_{pp}/N_{pp} + F_{pc}/N_{pc} + F_{cp}/N_{cp} + F_{cc}/N_{cc} , \qquad (2)$$

where $F_{pp} = \Delta\varepsilon_{pp}/\Delta\varepsilon_{in}$; $F_{pc} = \Delta\varepsilon_{pc}/\Delta\varepsilon_{in}$; $F_{cp} = \Delta\varepsilon_{cp}/\Delta\varepsilon_{in}$; $F_{cc} = \Delta\varepsilon_{cc}/\Delta\varepsilon_{in}$; and the quantities N_{pp}, N_{pc}, N_{cp}, and N_{cc} refer to the expected cycle life as if all the inelastic strain had been that component ($\Delta\varepsilon_{pp}$, $\Delta\varepsilon_{pc}$, $\Delta\varepsilon_{cp}$, $\Delta\varepsilon_{cc}$).

Generally, the life relationships $\Delta\varepsilon_{pp}$ versus N_{pp}, $\Delta\varepsilon_{pc}$ versus N_{pc}, and so on are power law functions of the form $y = ax^b$. Furthermore, the life relationships are proposed to be temperature independent.

The $\Delta\varepsilon_{pp}$-versus-N_{pp} data for solution-annealed Hastelloy X in Fig. 9.4 were obtained from continuous cycling tests from 22 to 871°C. The relationship appears to be temperature dependent up to 649°C; however, data from 649 to 871°C were adequately described by a single function.

The remaining three strain range partitioning (SRP) life relationships are shown in Figs. 9.5 through 9.7. The SRP data are considerably more consistent compared with the linear damage summation approach. It seems that the limited available data at both 760 and 871°C could be adequately described by power law functions when additional data are obtained, particularly at low strain ranges.

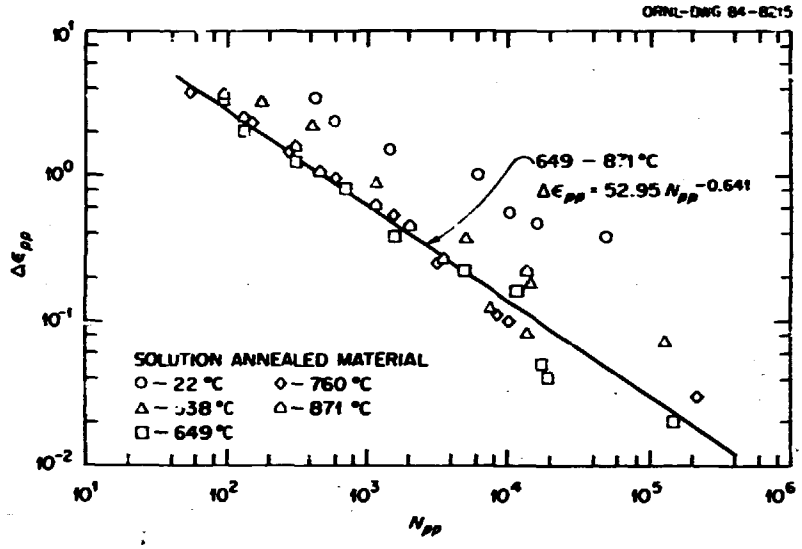

Fig. 9.4. Strain range partitioning life relationships for *pp* strain for Hastelloy X from 22 to 871°C.

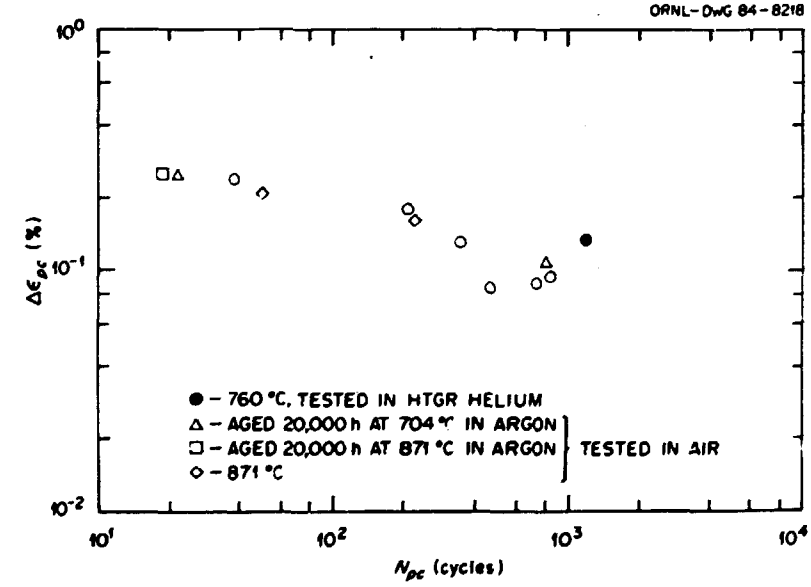

Fig. 9.5. Strain range partitioning life relationship for *pc* strain for Hastelloy X.

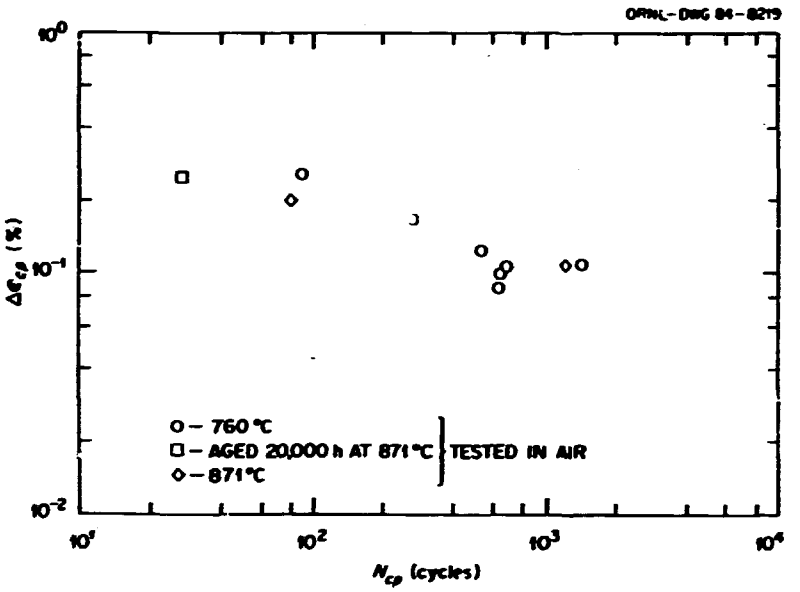

Fig. 9.6. Strain range partitioning life relationship for *cp* strain for Hastelloy X.

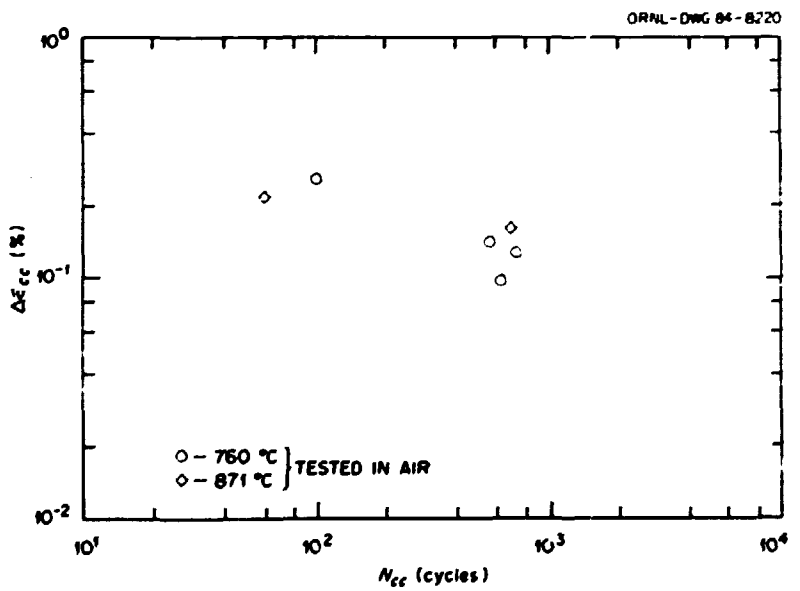

Fig. 9.7. Strain range partitioning life relationship for *cc* strain for Hastelloy X.

9.2.3.2 High-Cycle Fatigue Behavior of Hastelloy X

High-cycle fatigue tests were conducted on solution-annealed Hastelloy X at 760°C in air. The results are plotted in Fig. 9.8. The data, although obtained in air at a slightly higher temperature, were comparable to results generated by Roy Williams (General Electric, Schenectady, New York) at 750°C in a simulated HTR-He environment. High-cycle fatigue testing in air is now under way at 650°C.

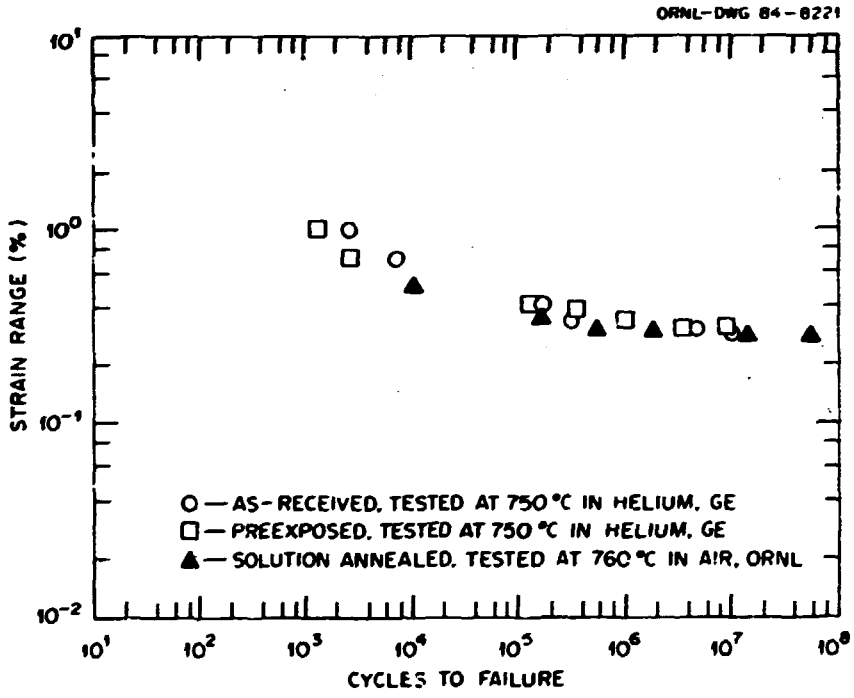

Fig. 9.8. High-cycle fatigue behavior of Hastelloy X at 760°C.

9.3 CORROSION AND COMPATIBILITY (WBS 3650.02)

9.3.1 Decarburization of 2 1/4 Cr-1 Mo Steel — H. Inouye

The aim of this study was to measure the decarburization of 2 1/4 Cr-1 Mo steel by HTR-He and to identify the variables controlling the kinetics so that a suitable relationship between these factors could be developed and used for predictive purposes. The test matrix, the steel microstructures, and the test gas details are listed in Table 9.1. The exposures were conducted in a closed-loop system with the test gas at

48.3 kPa (7 psig) and recirculated at 12 L/min. Analyses of the test gas showed less than 1% difference in the H_2, CH_4, CO, and CO_2 between the retort inlet and outlet; however, some H_2O was generated during the runs.

Table 9.1. Test matrix and test gas for decarburization runs

Test matrix
Temperatures, °C: 427, 510, 580, and 650
Exposure, h: 1000, 1500, 2000, 3500, 7000
Specimen microstructures (initial)
Annealed: Ferrite plus pearlite
Normalized: Bainite
Test gas
Helium: 48.3 kPa gage (7psig) at a flow rate of 12 L/m with 10.1 (100) H_2/1.0 (10) CH_4/5.1 (50) CO/1.5 (15) CO_2/1.5 (15) H_2O [Pa (μatm)]

The 6.35-mm-diam corrosion specimens were progressively decarburized with increasing exposure times in the manner shown in Fig. 9.9. Characteristically, the plots show very low decarburization rates at 427 and 510°C, amounting to a carbon loss of only about 50 ppm in 7000 h, starting with an initial concentration of 925 ppm. Larger carbon losses of about 225 and 800 ppm were measured for the same exposure time at 580 and 650°C, respectively. Comparison of the data in Fig. 9.9 with the analysis of 3.18-mm-diam specimens showed that the extent of decarburization also varied inversely with the specimen diameter. Thus, the variables controlling decarburization are time, temperature, and specimen geometry.

Sections of corrosion specimens showed the progressive transformation of the ferrite plus pearlite microstructure in the annealed steel to ferrite containing a fine dispersion of $M_{23}C_6$ and M_6C carbides. Likewise, the initial bainitic microstructure produced by the normalizing heat treatment also transformed during exposure to the same end products. Decarburized surface layers or other evidence of carbon gradients were not apparent in any of the metallographic specimens.

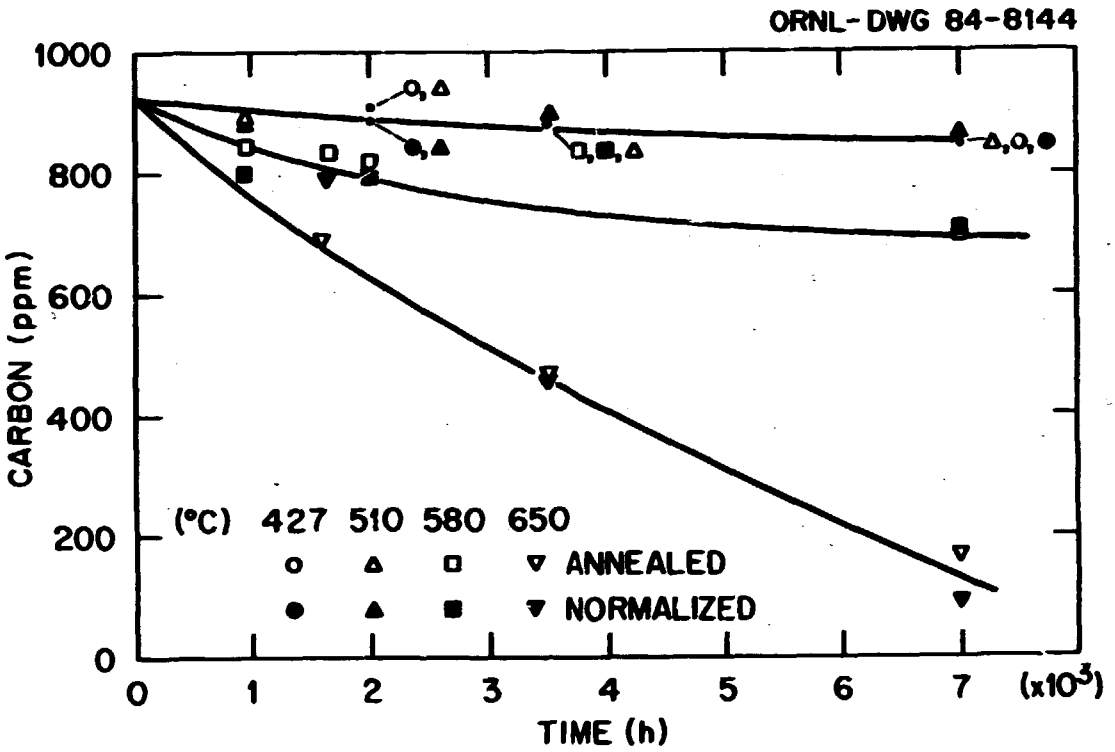

Fig. 9.9. Decarburization of 6.35-mm-diam 2 1/4 Cr-1 Mo steel by helium impurities: 10.1 (100) H_2/1.0 (10) CH_4/5.1 (50) CO/1.5 (15) CO_2/1.5 (15) H_2O [Pa (μatm)].

The carbon gradients in the decarburized specimens were calculated from the analyses of specimens machined to successively smaller diameters. Figure 9.10 shows the calculated carbon gradients for temperatures of 427 to 650°C and a 7000-h exposure. These particular plots suggest that steel specimens having an initial bainitic microstructure were more resistant to decarburization than were specimens having a ferrite plus pearlite microstructure at 427 and 570°C but not at 650°C. However, similar plots for specimens decarburized for shorter times showed no consistent trend one way or the other. Thus, the initial microstructure appeared to have little if any effect on the decarburization rates.

The diffusivity of carbon was calculated from plots like those of Fig. 9.10 for exposure times of 1000, 1500, 3500, and 7000 h. The D values that best fit the data of Fig. 9.9 are listed in Table 9.2, and its dependence on the test variables mentioned above[6] is

$$C_m - C_o/(C_s - C_o) = 2.256(Dt)^{1/2}/L \ , \qquad (3)$$

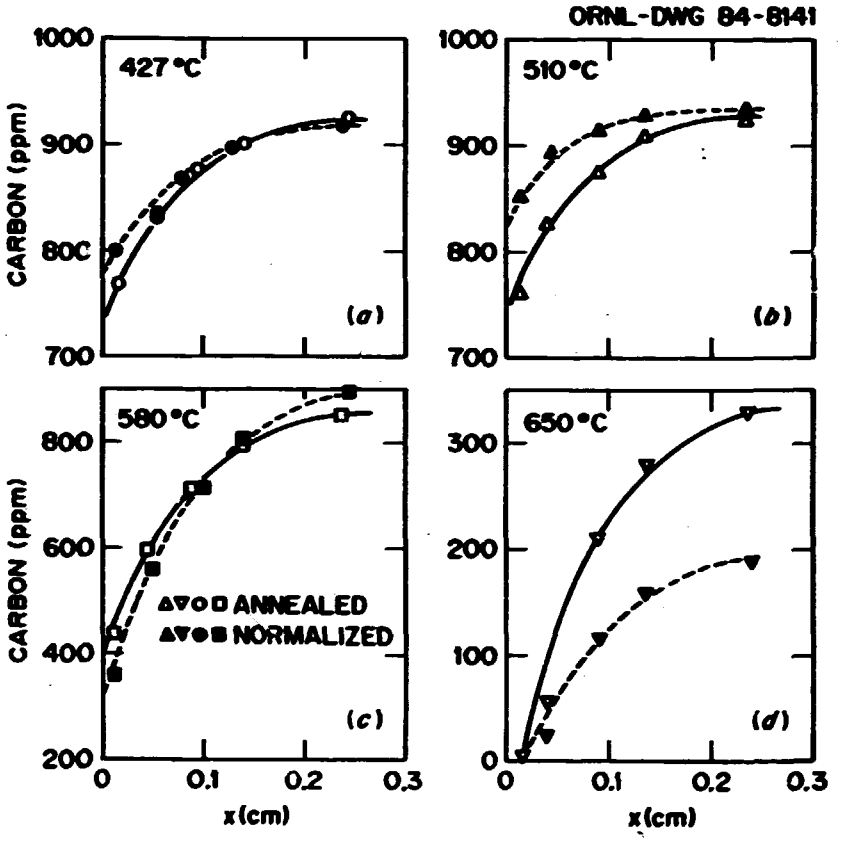

Fig. 9.10. Carbon gradients for 6.35-mm-diam 2 1/4 Cr-1 Mo steel decarburized 7000 h.

Table 9.2. Diffusivity of carbon in 2 1/4 Cr-1 Mo steel during decarburization by HTR-He

[10.1 (100) H_2/1.0 (10) CH_4/5.1 (50) CO/1.5 (15) CO_2/1.5 (15) H_2O Pa (μatm)]

Temperature (°C)	C_s[a] (ppm)	D (cm^2/s)
427	750	2×10^{-11}
510	780	5×10^{-11}
580	385	1.0×10^{-10}
650	0	5.3×10^{-10}

[a]Average carbon content for intersection of curves in Fig. 9.11 at $x = 0$.

where

C_m = mean carbon concentration (ppm),
C_o = initial carbon concentration (ppm),
C_s = surface carbon concentration (ppm),
D = carbon diffusivity (cm^2/s),
t = decarburizing time (s),
L = radius of specimen (cm).

For a slab-type specimen the constant in Eq. (3) becomes 1.128 and L is its half-thickness. For predictive purposes, Eq. (3) tends to give C_m values on the low side of that measured. At 427 to 580°C, the calculated C_m is within 1 to 2% of the measured values but increases to about 10% or more at 650°C and, as shown in the comparison curves in Fig. 9.11, was more pronounced for the intermediate exposure times of about 1 to 2000 h. This lack of agreement between the measured and calculated carbon results from an exponent in the quantity $(Dt)^{1/2}$ that was not exactly 1/2 as assumed by Eq. (3) but was actually 0.60 for the 1000-h exposure and 0.48 after 7000 h.

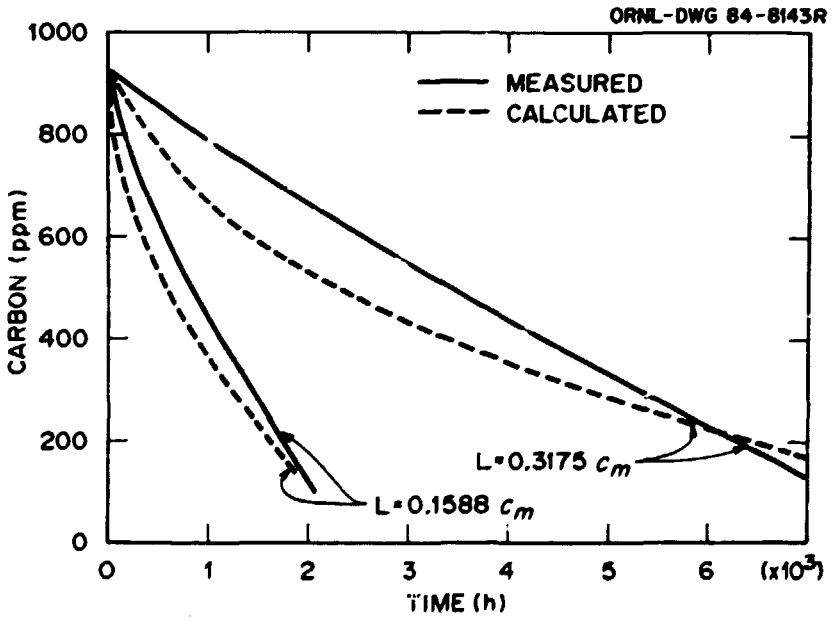

Fig. 9.11. Comparison of measured versus calculated C_m at 650°C

The variation of D with $1/T$ is plotted in Fig. 9.12 and is also compared with the D values estimated from decarburization data reported for other media.[7-9] These plots showed that D was strongly dependent on the environment at the lower temperatures but became more insensitive to the environment as the temperature increased. This trend suggests that the carbon activity of the decarburizing media controls the decarburization rates at lower temperatures and that the dissolution rates of carbides are rate controlling at high temperatures.

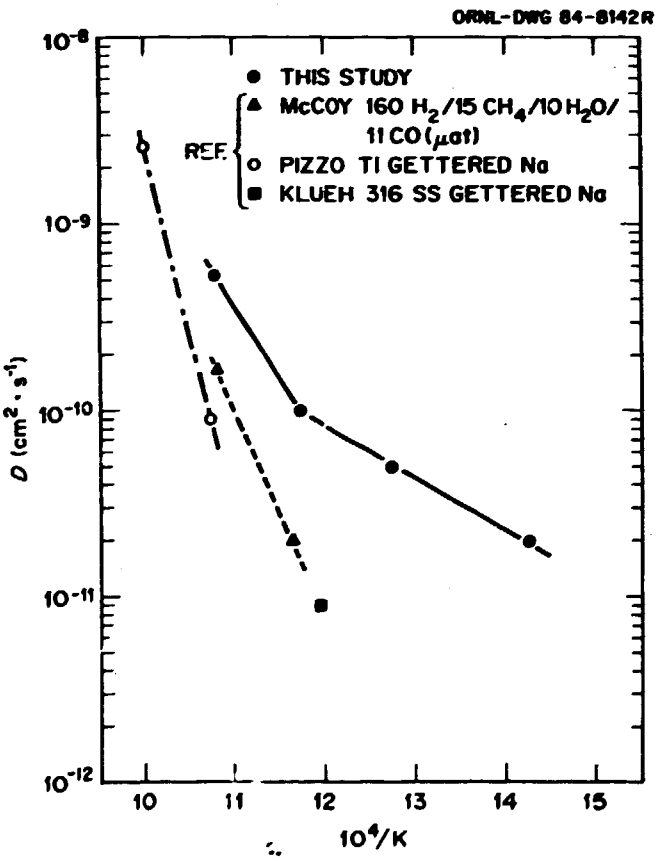

Fig. 9.12. Variation of D versus $1/T$ for several decarburizing media. *Sources of data:* H. E. McCoy, *Creep Behavior of 2 1/4 Cr-1 Mo Steel and Other Alloys in Simulated HTGR Helium*, ORNL/TM-6822, June 1979; R. L. Klueh, unpublished data, December 1983; and P. P. Pizzo and L. V. Hampton, unpublished data, December 1983.

9.3.2 Compatibility of Alloys with B_4C Compacts — P. F. Tortorelli

Experiments were initiated to characterize the solid-state reactions between boronated graphite compacts and both type 316 stainless steel and alloy 800H. The purpose was to assess directly the magnitude of these reactions between boronated graphite control rods and their cladding material in the absence of radiation. Stacks of alternating layers of mechanically polished B_4C-graphite, alloy 800H, and type 316 stainless steel were held under a compressive load at 700 and 810°C in flowing HTR-He (Fig. 9.13). The experiments were designed so that pieces of the stack could be removed at exposure intervals of 1000, 3000, 6000, and 10,000 h for metallographic evaluation of the extent of surface reactions.

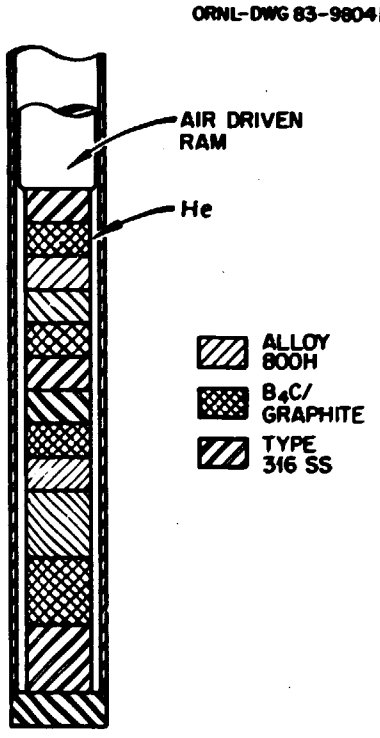

Fig. 9.13. Schematic of specimen stack used in boronated graphite compatibility study.

During 1983, 1000-h exposures of type 316 stainless steel and 3000- and 6000-h exposures of this stainless steel and alloy 800H were completed. The interface reactions between these alloys and the boronated graphite were characterized by visual examination and optical metallography of polished cross sections. In selected cases, cross sections were also analyzed by scanning electron microscopy, energy-dispensive x-ray analysis,

and electron probe microanalysis. The results from the analyses to date have indicated several general tendencies, described below. A more quantitative analysis of the exposed specimens is under way in an effort to understand the rather complex reaction process better.

At a given exposure time, the reaction at 810°C proceeded to a greater depth than did those at 700°C, and, for a given temperature, the reacted volume increased with time. Although measurable, the depths of the reaction layers were relatively shallow after 6000 h. For a fixed exposure time and temperature, type 316 stainless steel was more reactive than was alloy 800H. Although both alloys had about the same depth of carburization after 3000 h at 700°C, there appeared to be more B_4C particles attached to the exposed surface of the type 316 stainless steel. Furthermore, after 6000 h at 810°C, the type 316 stainless steel showed a greater depth of general surface reaction relative to the similarly exposed alloy 800H, although the alloy 800H exhibited a greater tendency for grain-boundary penetration (Figs. 9.14 and 9.15). Some grain-boundary reaction was also detected for the alloy 800H exposed for 6000 h at 700°C. It is conceivable that, with still longer exposures, the depths of localized grain-boundary penetration in the alloy 800H specimens could greatly exceed the depths of general surface reaction in the type 316 stainless steel. An assessment of this possibility must await the results of 10,000-h exposures, which will be completed in March 1984. Analyses of these specimens will also allow both a formulation of a model for the reactions of these alloys with boronated graphite and a qualitative determination of whether such reactions will compromise the integrity of the control rod cladding over the projected reaction operating period.

9.4 JOINING TECHNOLOGY (WBS 3660.03) — J. F. King

The HTR Joining Technology Program is continuing to study welding-related fabrication concerns with the steam generators. Previously, we evaluated the weldability of an alloy 800H forging that simulates a steam generator superheater tubesheet.[10] The tubesheet design calls for the surface to be weld clad with ERNiCr-3 weld metal, which provides sound material for the tube-to-tubesheet welds. We are developing procedures

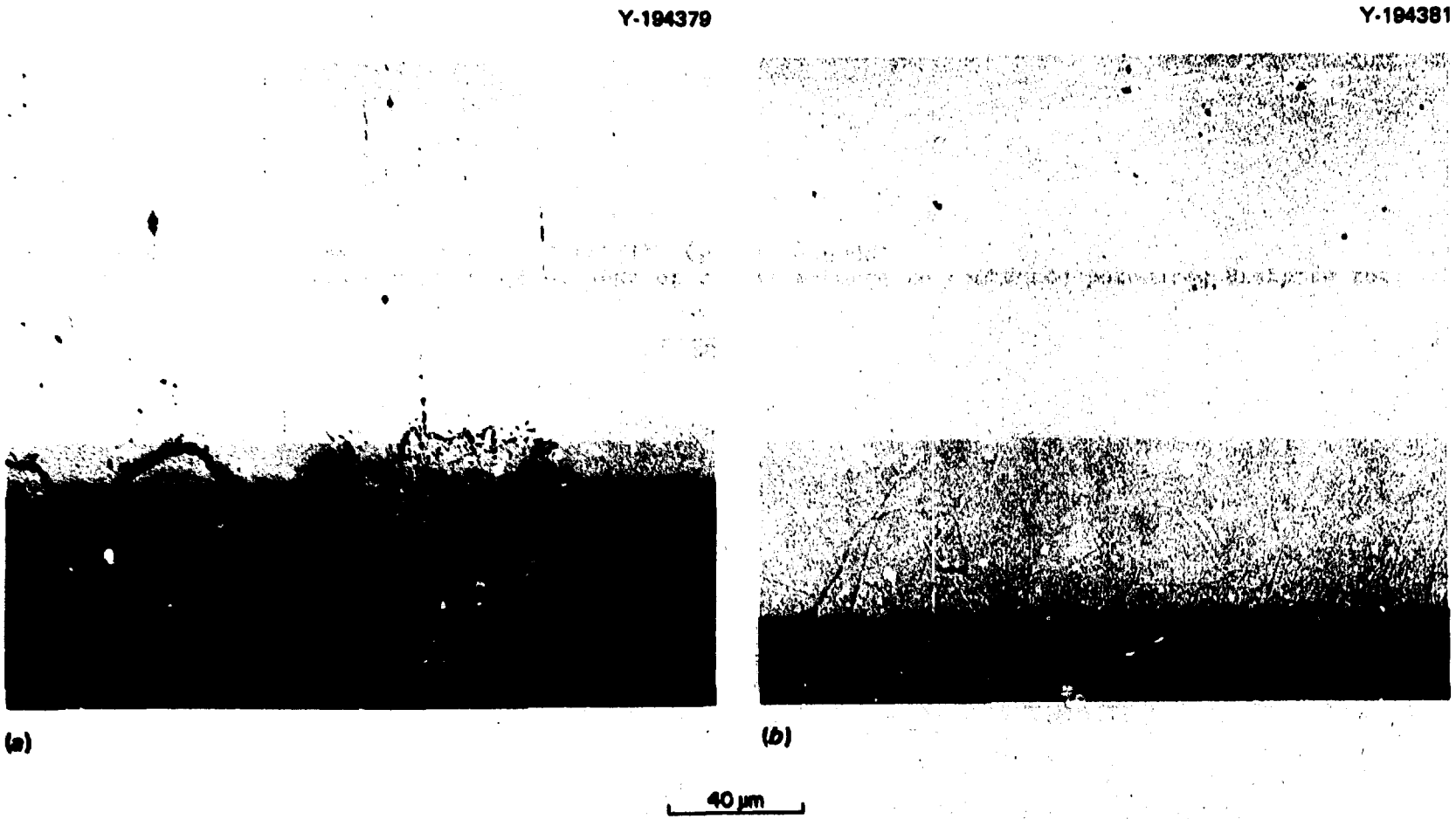

Fig. 9.14. Polished cross sections of alloys exposed to compacted boronated graphite for 6000 h at 810°C (*a*) Type 316 stainless steel. (*b*) Alloy 800H.

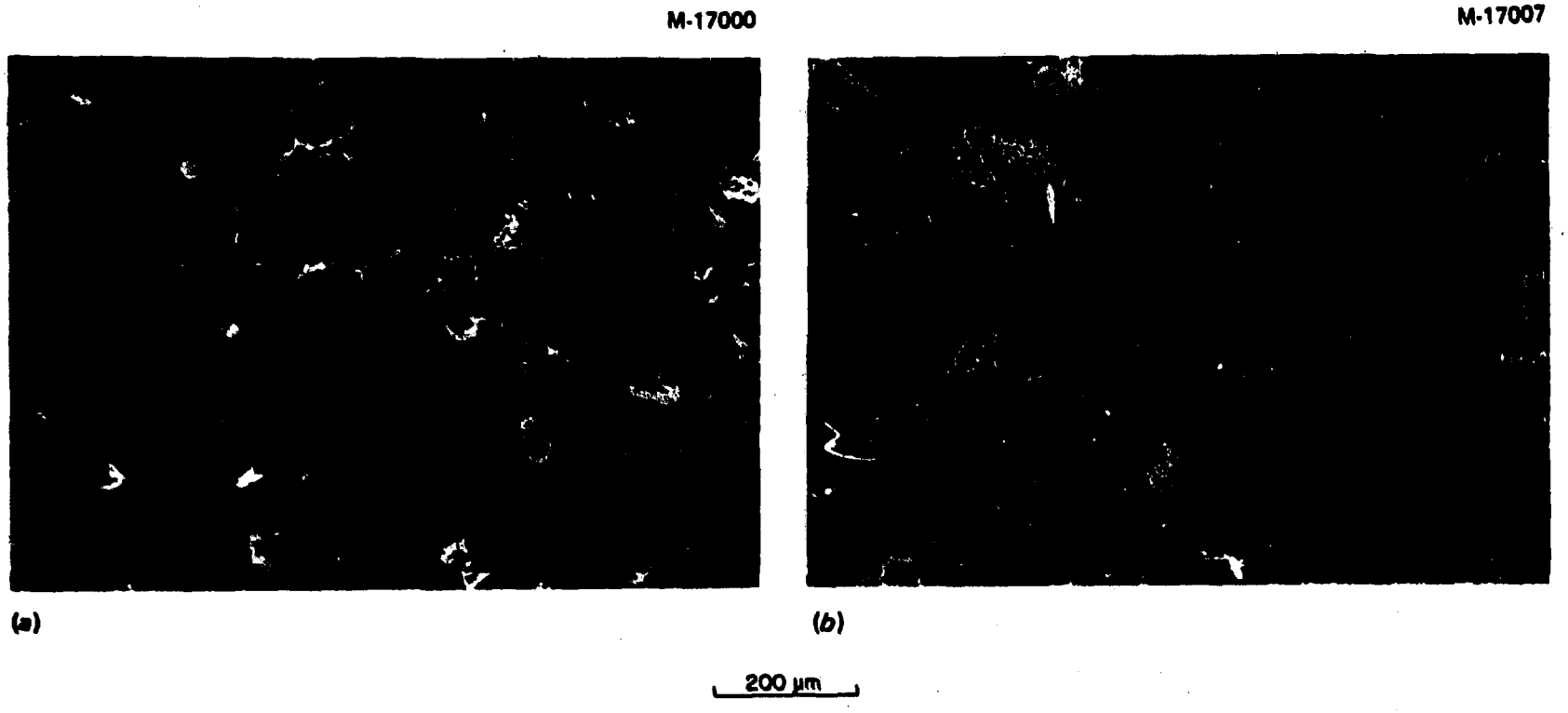

Fig. 9.15. Scanning electron micrographs of alloys exposed to compacted boronated graphite for 6000 h at 810°C. (*a*) Type 316 stainless steel. (*b*) Alloy 800H.

for joining the superheater tubing to the tubesheet by internal bore welding. During this reporting period, we purchased an internal bore GTA welding head, fabricated various holding fixtures and inert gas shielding chambers, and initiated the welding development work. The results of this work are summarized.

9.4.1 Superheater Tube-to-Tubesheet Joints

The steam generator superheater tube-to-tubesheet welds require the joining of alloy 800H tubing to a weld-clad alloy 800H tubesheet forging. We anticipate that the tubesheet forging will be about 1.5 m (60 in.) in diameter and 380 mm (15 in.) thick. After the surface is weld clad, it will be drilled and machined to produce a tubesheet to which 462 tubes will be welded. The general configuration of these tube-to-tubesheet joints is shown schematically in Fig. 9.16. Internal bore welds will be made from the inside surface (nominally 23.2 mm) of the tubing and tubesheet face by extending a welding torch through the 380-mm-thick (15-in.) tubesheet. The weld must be made through a tube wall thickness of 4.4 mm (0.173 in.), which may require a multipass weld with filler metal addition. The successful operation of any HTR steam generator requires that each of these welds be of high integrity.

9.4.2 Experimental Welding Equipment

An internal bore welding (IBW) head was obtained for use in the laboratory welding development program to study tube-to-tubesheet joining. The IBW head (Fig. 9.17) consists of the welding torch, automatic voltage control, wire feeder, and head rotating mechanism. This welding head is controlled by a programmable direct-current GTA power supply. The welding torch (Fig. 9.18) consists of an internal copper conductor with shielding gas channels, a tungsten electrode, and a boron nitride gas cup and insulators. The filler wire guide tube is not shown in this figure, but it mounts on the outside of the insulator and directs the wire toward the tungsten electrode.

Experimental welds are being made with the equipment shown in Fig. 9.19. The welding head is mounted on a lathe, as shown. The alloy 800H tubing is supported in an alignment fixture, which is bolted to the

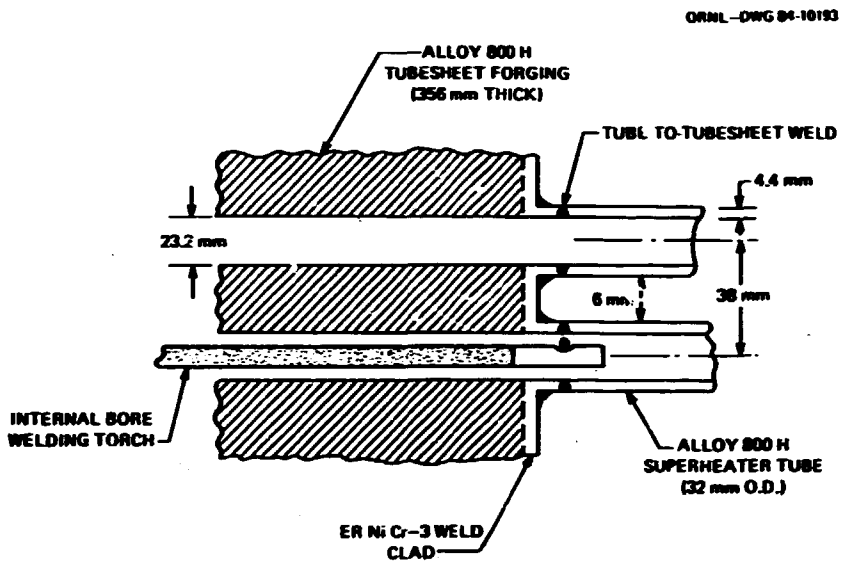

Fig. 9.16. Internal bore tube-to-tubesheet welds will be made between alloy 800H tubing and a weld-clad alloy 800H tubesheet forging.

Y-194739

Fig. 9.17. Internal bore welding head for the development program consists of a welding torch with automatic voltage control, a wire feeder, and a head rotating mechanism.

Y-194737

Fig. 9.18. Welding torch consists of a tungsten electrode held by an internal copper conductor surrounded by a boron nitride gas cup and insulator.

Y-104738

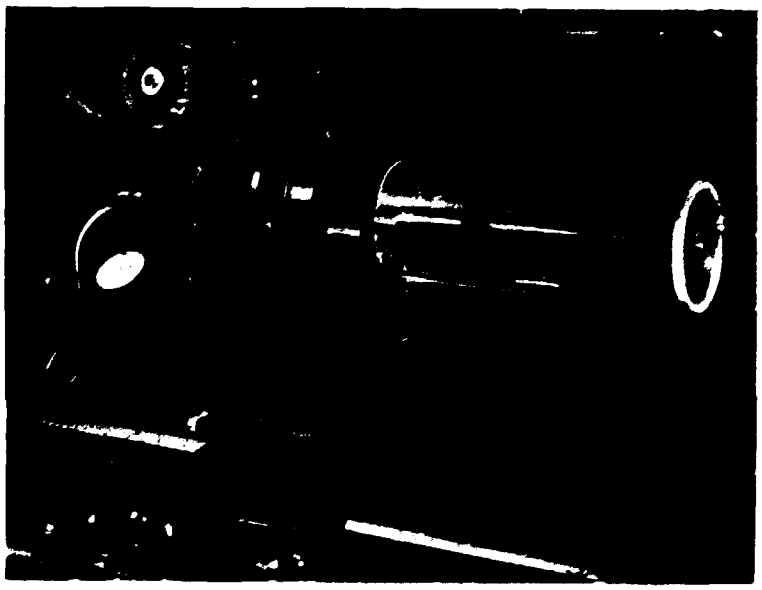

Fig. 9.19. Experimental welds being made in alloy 800H tubing supported in an alignment fixture surrounded by an inert gas purge chamber.

lathe bed. This arrangement allows easy insertion and withdrawal of the welding torch and accurate positioning of the electrode in relation to the weld joint. An inert gas purge chamber was fabricated to shield the weld puddle from the air and to allow viewing of the welds as they are being made. This purge chamber is mounted over the tubing, as shown in Fig. 9.19.

9.4.3 Welding Development

Welding development is being conducted on reference size alloy 800H tubing. Because this is not a standard tubing size, we have fabricated tubular sections by machining and boring solid rod stock. Our initial screening tests of the welding parameter variables and welding equipment familiarization is being performed by joining alloy 800H to alloy 800H. After this initial work, we will butter the specimens with ERNiCr-3 filler metal to simulate the clad tubesheet side of the joint.

The preliminary welding tests were directed at maximizing the penetration of the tube wall thickness while maintaining a controllable weld puddle around the circumference of the tube. These tests were conducted with the tube axis in the horizontal position. It does not appear from these preliminary tests that we will be able to fully penetrate autogeneously the relatively thick wall tubing (4.4-mm wall thickness). This indicates that a multipass weld with filler metal addition will be required. The autogeneous welding approach, if possible, is attractive because it would simplify the welding procedure of this relatively difficult weldment.

We are investigating joint geometries and shielding gas compositions suitable for a multipass weldment. This involves making an autogeneous root pass through a reasonable root face thickness, followed by fill passes to complete the weld. Reasonable success has been obtained in penetrating 3.3 mm for the root pass with a shielding gas mixture of 75% He and 25% Ar. Additional shielding gas compositions will be examined for use in this weldment. Concurrently, we are refining the welding parameters (amperage, voltage, and travel speed) to achieve consistent penetration around the joint. The weldment requires that we reduce the heat input to the weld as it progresses inside the tube to compensate for the

material temperature increase that results from the confined space in which we are working. When the many variables associated with producing consistent root pass welds are defined, work will proceed toward the fill passes.

9.5 FRACTURE TOUGHNESS STUDIES — D. O. Hobson and R. K. Nanstad

9.5.1 Steels for the PCRV

Studies of the fracture toughness of PCRV liner and penetration steels and their weldments are completed, and a final report has been drafted. The report assesses the applicability of the current ASME Code Appendix G guidelines[11] to the PCRV steels under consideration for HTR components. The objectives were, primarily, to

1. define a reference fracture toughness curve for ferritic components of the HTR pressure boundary similar to the K_{IR} curve in Appendix G, and
2. define for this curve a temperature-indexing procedure based on standard materials qualification tests (e.g., Charpy V-notch and drop-weight) similar to the RT_{NDT} procedures of Appendix G.

We recognized from the beginning that the multiplicity of materials and heat treatments in this study would complicate those objectives. Three different plate materials (SA-537, classes 1 and 2), one forging (SA-508, class 1), and three weldments and their heat-affected zones (various combinations of the base materials) were examined by several different test methods: hardness, metallography, drop-weight, tensile, Charpy V-notch impact, precracked Charpy V-notch [both static (slow bend) and impact], compact testing (both static and rapid load), and crack arrest.

We felt that, to justify a different K_{IR} curve, the test data should show substantial deviation from that curve — either above it to justify raising it or below it to justify lowering it.

Figure 9.20 is a summary of the various test results for the base and weld metal materials. The curves are the lower bounds of the several

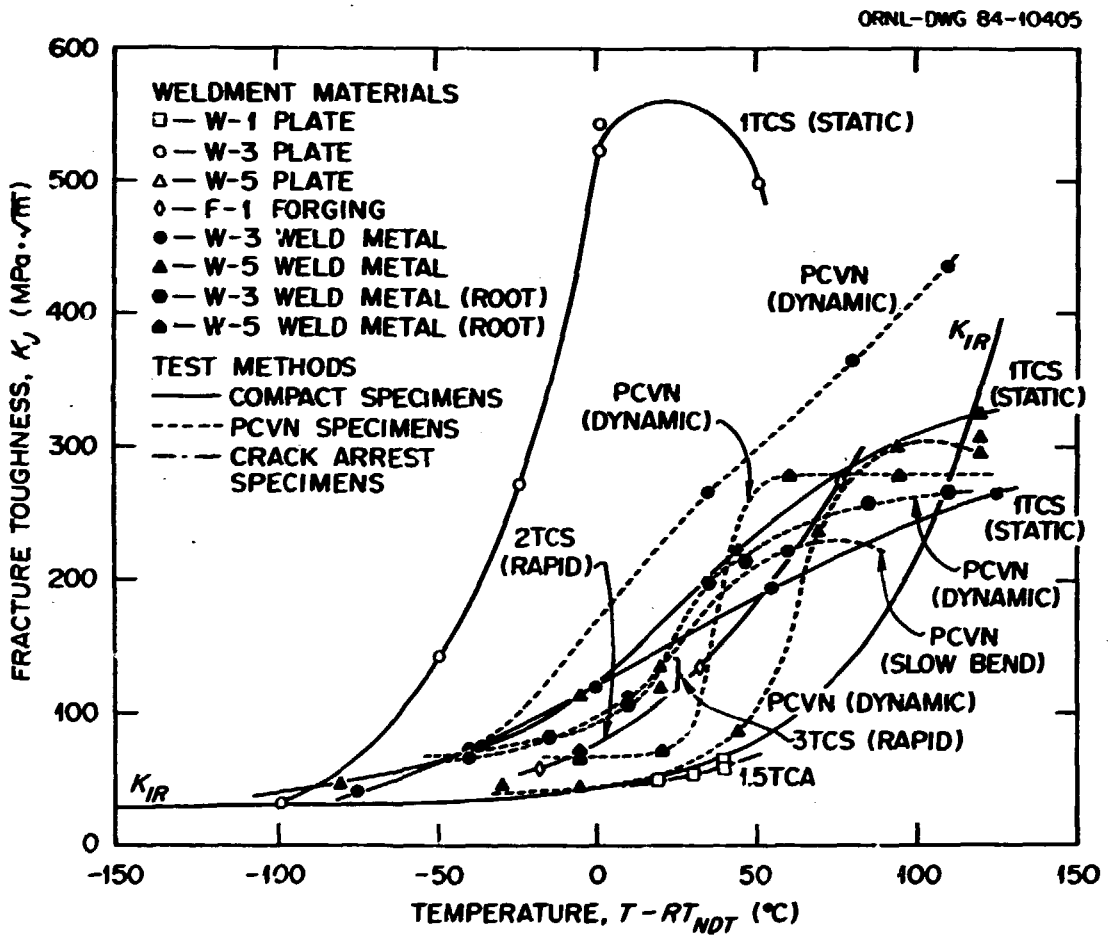

Fig. 9.20. Fracture toughness test results for base and weld metal materials.

sets of fracture toughness data, and the points are the test results that define those lower bounds. All data are plotted relative to RT_{NDT}. The K_{IR} curve from the Code Appendix G is shown underlying all the present test data except four of the crack arrest points.

The data in this study provided no strong incentive to change either of the two Appendix G guidelines. The unavailability of large specimen sizes (we used compact specimens up to 3-T size) precluded the kinds of tests used originally to define the K_{IR} curve. The most severe test type available, within our specimen size constraints, was the 1.5-T crack-arrest test. Four of those eight crack-arrest data points fell below the K_{IR} curve (the other four were invalid). The data were generated for the

P-1 (SA-537, class 1) plate material, which also had shown the lowest toughness with the precracked Charpy V-notch test and the lowest Charpy energy of any of the base materials.

Drop-weight tests were used to produce NDT values that were used in conjunction with Charpy data to ascertain if NDT was equal to RT_{NDT}, the reference nil-ductility temperature. The Code procedure specifies that the NDT temperature T_{NDT} be determined by drop-weight tests with a specified specimen size taken from the quarter-thickness location.[11] Then, at a temperature of T_{NDT} + 33°C (60°F), three Charpy tests are conducted with standard specimens from the quarter-thickness location. Two alternative procedures are available at this point. This study used the alternative that required not less than 0.889-mm (0.035-in.) lateral expansion and not less than 67.8-J (50-ft-lb) absorbed energy at T_{NDT} + 33°C. These criteria were met in all but one of the seven materials drop-weight tested in this study. For the W-3 weld metal, a T_{NDT} of −80°C (−112°F) was found by drop-weight testing, but the Charpy values at T_{NDT} + 33°C were below the indexing requirements. An RT_{NDT} of −60°C (−76°F) was subsequently calculated with the Charpy impact energy lower bound curve.

To reiterate, this study has shown no compelling reason to change either the K_{IR} reference curve or the indexing procedure defined by the Code Appendix G guidelines, both based on light-water reactor (LWR) pressure vessel steels. The fact that four of the crack-arrest test results fell below the K_{IR} curve is not, we believe, cause for concern. The maximum underfall is approximately 13% in fracture toughness or about a 10°C difference in $T - RT_{NDT}$. It is probable that, if further testing were performed on the LWR materials originally used to derive the K_{IR} curve, normal scatter would cause data to fall below the curve. It is also probable that the evolution of the crack arrest test procedure has minimized factors that tend to elevate fracture toughness levels. The ASTM crack-arrest procedure is still under development, as is the understanding of crack-arrest fracture toughness itself; thus, the significance of crack-arrest data falling slightly below the K_{IR} curve is probably minimal.

9.5.2 High-Temperature Fracture Toughness Studies

A new program was begun to study the fracture behavior of Inconel alloy 718 at elevated temperature (up to 565°C) in both the aged and unaged conditions.

Alloy 718 is a nickel-base superalloy for use in high-temperature HTR components. The nominal composition of the reference material is shown in Table 9.3 (vendor analyses).

Table 9.3. Typical chemical compositions of alloy 718 plate

Element	Content (wt %)	Element	Content (wt %)
Ni	52.43	Ta	<0.10
	52.11		<0.10
Cr	18.39	Mn	0.27
	18.01		0.30
Fe	19.28	Si	0.13
	19.03		0.13
Nb + Ta	5.16	C	0.05
	5.07		0.05
Ti	1.06	Cu	0.02
	0.98		0.03
Al	0.53	B	0.003
	0.60		0.004
Mo	3.06	P	<0.005
	3.02		<0.005
Co	<0.05	S	<0.002
	<0.05		<0.002

Scoping tests to determine K_J, cyclic crack growth rate da/dN, J_{IC}, and tearing modulus will be conducted on the alloy in the unaged condition. Such tests will determine the crack growth behavior of the alloy at elevated temperatures. In addition, specimens will be aged for 10,000, 20,000, and 30,000 h at 565°C and tested by a procedure similar to that used on the unaged material.

A 25.4-mm-thick plate of alloy 718 has been received from EG&G Idaho, Inc., and is part of a series of products from a Department of Energy

reference heat melted and fabricated by the Stellite Division of Cabot Corporation. This plate is being sawed into numerous blanks from which specimens will be machined.

9.6 REFERENCES

1. H. E. McCoy and J. F. King, *Evaluation of Hastelloy X for Gas-Cooled Reactor Applications*, ORNL/TM-8499, November 1982.

2. H. E. McCoy and J. F. King, "Creep and Tensile Properties of Alloys and Weldments," pp. 46–48 in *High-Temperature Gas-Cooled Reactor Technology Development Program Annual Progress Report for Period Ending December 31, 1982*, ORNL/5960, June 1983.

3. H. E. McCoy and J. F. King, *Creep and Tensile Properties of Alloy 800H–Hastelloy X Weldments*, ORNL/TM-8728, August 1983.

4. J. P. Strizak et al., *The Influence of Temperature, Environment, and Thermal Aging on the Continuous Cycle Fatigue Behavior of Hastelloy X and Inconel 617*, ORNL/TM-8130, April 1982.

5. *Interpretations of the ASME Boiler and Pressure Vessel Code, Case N-47*, American Society of Mechanical Engineers, New York, 1974.

6. L. S. Darken and R. W. Gurry, *Physical Chemistry of Metals*, McGraw-Hill, New York, 1953, p. 447.

7. H. E. McCoy, *Creep Behavior of 2 1/4 Cr-1 Mo Steel and Other Alloys in Simulated HTGR Helium*, ORNL/TM-6822, June 1979.

8. R. L. Klueh, unpublished data, December 1983.

9. P. P. Pizzo and L. V. Hampton, unpublished data, December 1983.

10. J. F. King and G. M. Goodwin, "Joining Technology," pp. 61–71 in *High-Temperature Gas-Cooled Reactor Technology Development Program Annual Progress Report for Period Ending December 31, 1982*, ORNL/5960, June 1983.

11. "Nuclear Power Plant Components," *ASME Boiler and Pressure Vessel Code*, Sect. III, Div. 1, 1977 ed., American Society of Mechanical Engineers, Philadelphia, 1977.

10. GRAPHITE MATERIALS QUALIFICATION (WBS 3670.01)

W. P. Eatherly

10.1 INTRODUCTION

The graphite program during 1983 was concentrated on three areas: irradiations of graphites in the High Flux Isotope Reactor (HFIR), studies on mechanical and statistical properties, and support of the Core Support Post Test (CSPT).

The irradiation program remained somewhat schizophrenic; the predominant interest for prismatic reactors is in a fluence of about 1×10^{26} neutrons/m^2 at about 900°C, whereas the pebble bed is more concerned with fluences of about 5×10^{26} near 600°C. In addition to screening experiments on German graphites, the major effort was fracture mechanics and verification that improved versions of H451 graphite will preserve the existing irradiation data base.

The existing American Society of Mechanical Engineers trial practice graphite code for nuclear reactors recommends the use of statistics without specifying their nature and implies the future use of fracture mechanics. Efforts continued this year in defining the characteristics of fracture mechanics in unirradiated graphites and in defining the statistical nature of H451 tensile strength. Both problems are complex, and we anticipate that these efforts will continue in the coming year.

The near full-scale study of oxidation for the core support posts, particularly in the Hertzian stress domain, demanded considerable effort of the graphite program. This included procuring and qualifying the graphites, setting up the necessary quality assurance program for licensing purposes, improving model calculations for penetrating oxidation, and preparing test methods for postoxidation examination. This work is not reported here but will be presented in context in the reports on the CSPT.

10.2 GRAPHITE IRRADIATIONS

10.2.1 Irradiation Experiments — R. L. Senn

Irradiation of HFIR target capsule HTK-5, containing 64 graphite specimens, was completed as scheduled. The HTK-5 was a Federal Republic of Germany (FRG) priority experiment containing five FRG experimental graphites for comparison with H451 and POCO AXF graphites. Capsule HTK-5 was installed December 24, 1981, and removed December 12, 1982, after 15 HFIR fuel cycles of irradiaion at 600°C. Irradiation of HFIR target capsule HTK-6, containing 64 graphite specimens, was also completed as scheduled after a seven-cycle irradiation in HFIR outer target position F-7. The HTK-6 was a High-Temperature Reactor (HTR) priority experiment containing grades of H451 from two lots, an improved H451 and TS-1621, for comparison with selected FRG grades. Capsule HTK-6 was installed July 18, 1982, and was removed January 5, 1983, after seven fuel cycles of irradiation at 900°C.

A new type of capsule design was introduced this year into the HFIR target (HT) series. These capsules, designated as the HTF series, are designed to irradiate graphite specimens for fracture mechanics testing. These capsules are identical externally to others of the HT type, but internally the graphite geometries are quite different; hence, new thermal design calculations had to be performed to provide for different gamma heating densities and, thus, altered gas gaps. Three capsules were constructed and irradiated during 1983. Capsules HTF-1 and -2 were prepared for a seven-cycle irradiation at 600 and 900°C, respectively. Capsule HTF-3 was originally planned as a 600°C 15-cycle experiment. Each capsule contained ten double-fracture mechanics specimens, each pair being separated after the irradiation into two compact-cylinder fracture specimens. Graphites selected for irradiation, in order of loading from top to bottom of the capsule were: four H451 pairs, one GraphNOL N3M, one ATR-2E, one H451, one N3M, one ATR-2E, and, finally, one N3M. Capsules HTF-1 and -2 were inserted into HFIR on May 4, 1983. Capsule HTF-3 was not inserted until May 28, 1983, because of difficulties in handling the

delicate specimens and their mounts. All three were removed on September 20, 1983, just before the extended shutdown of HFIR for replacement of the beryllium reflector.

Capsule HTF-1 was helium filled and designed to operate at 600°C specimen surface temperature. Postirradiation examination (PIE) showed the specimens to be extensively corroded and that carbon had been transported to form a cokelike material. The original gas gap and interior of the capsule were largely filled with this cokelike material. Because of the extensive damage to the specimens, further examination and testing was impossible, and the anticipated results from this capsule were lost.

Accordingly, an initial unusual occurrence report (UOR), ORNL-83-17-ET-83-1, was issued October 7, 1983. An investigating team met to evaluate the possible causes of the experiment failure. Clearly, there was some source of oxygen in the sealed capsule, and the investigation centered around a determination of how oxygen could have gotten into the experiment during assembly, inasmuch as no sufficient source of oxygen from the samples could be discerned.

Ultimately, we decided that it was unlikely that the gas used to fill the capsule in the welding chamber was contaminated and that the capsule fill gas might have been slightly contaminated during a final weld repair. During this procedure the capsule was removed from the welding chamber, the bad weld removed, and the capsule replaced in the chamber for rewelding. Although the proper pumpdown procedures were used again, two possibilities that might have caused the problem occurred. (1) A screw, which temporarily (and loosely) fills the gas passage before the final weld, was not removed during the second pumpdown and might have prevented thorough evacuation during following operations. (2) A gas line between an argon bottle used for the welding torch cover gas might have had some oxygen trapped inside during attachment of the bottle.

A final version of the UOR is in preparation. Revised procedures for gas-sampling techniques, welding chamber operation, and weld repair are being written to correct any deficiencies that might have contributed to the HTF-1 failure.

Capsule HTF-2, which also contained ten double graphite fracture mechanics specimens, was irradiated for six cycles at 900°C specimen surface temperature and filled with neon gas. During the initial PIE, the specimens were intact and appeared to have survived the irradiation satisfactorily. Further testing and evaluation of the specimens by Metals and Ceramics Division personnel is under way.

Because of the difficulties with HTF-1, we decided to open HTF-3 (a 600°C helium-filled duplicate of HTF-1 planned for the 15-HFIR-cycle irradiation). The HTF-3 was irradiated for five cycles. The procedures and personnel used with HTF-1 were used to build and fill this capsule, except that no final weld repair was necessary. Again, during the initial PIE, the specimens were intact and had survived the irradiation satisfactorily.

10.2.2 Results of Irradiation Testing: OC-5 Creep Capsule — C. R. Kennedy

The specimens from OC-5 creep experiment were measured and the results analyzed with respect to past OC-1, -2, -3, and -4 experiments. The one still missing set of data involves the coefficients of thermal expansion (CTE), which have not been measured because of the unavailability of the CTE apparatus. Flux monitors have not been read yet, but the reproducibility of the flux in OC-1, -2, -3, and -4 permits quantification of the data with a high degree of confidence.

Modulus of elasticity measurements showed slightly increased values for both stressed and control specimens. No difference could be distinguished between the controls and specimens with up to as high as 4% creep deformation. The electrical resistivity measurements also reflected only minor increases in resistivity, with no distinguishing differences between controls and stressed specimens.

The creep specimens in the west column of the capsule were overstressed in OC-1 and were strained from 0.75 to 1.50% greater than were the specimens in the east section. These specimens were also recycled in OC-3 and -5 under the design stresses of 13.8 and 20.7 MPa to determine the effect of this overstress on creep rates and physical properties. Table 10.1 compares the creep rates of the east specimens under steady

Table 10.1. Creep coefficients of specimens from OC-5

Graphite	Creep coefficient $[Pa^{-1} \cdot (neutrons/m^2)^{-1} \times 10^{35}]$	
	East column	West column
H451 with grain, 13.8 MPa	2.17	2.03
H451 with grain, 20.7 MPa	2.10	0.92
H451 against grain, 13.8 MPa	2.61	2.68
H451 high modulus with grain, 13.8 MPa	1.94	
H327 with grain, 13.8 MPa	1.60	1.85
H327 against grain, 13.8 MPa	2.60	2.38
AXF, 20.7 MPa	1.16	0.15

load conditions with the west specimens overstressed in OC-1. In most cases the creep coefficient for both the east and west specimens yielded essentially the same results for stress levels of 13.8 MPa. Both the overstressed specimens of AXF and H451 with 20.7 MPa demonstrated a significant reduction in the creep coefficient. This behavior would be expected if the strains from the initial overstress were relaxed. It appears that there may be a threshold for strain recovery from large rapid overstressing.

The creep-rate coefficients in Table 10.1 are slightly lower than the ones measured from OC-3 because of slightly decelerating creep. They are still linear with the preirradiated modulus of elasticity compared with the 600°C results, as shown in Fig. 10.1. Again, the differences between the rates at 600 and 900°C appear to be additive rather than multiplicative.

10.2.3 Results of Irradiation Testing: HFIR Survey Capsules — C. R. Kennedy

Although the results of HT-5 and -6 are preliminary, there are several relevant conclusions. We now have a reasonable number of various grades that have been irradiated past their maximum densification fluence from 600 to 900°C. We observed previously that the damage rates that result in dimensional changes do not vary appreciably over this temperature range; but, as the irradiation temperature increases, the life

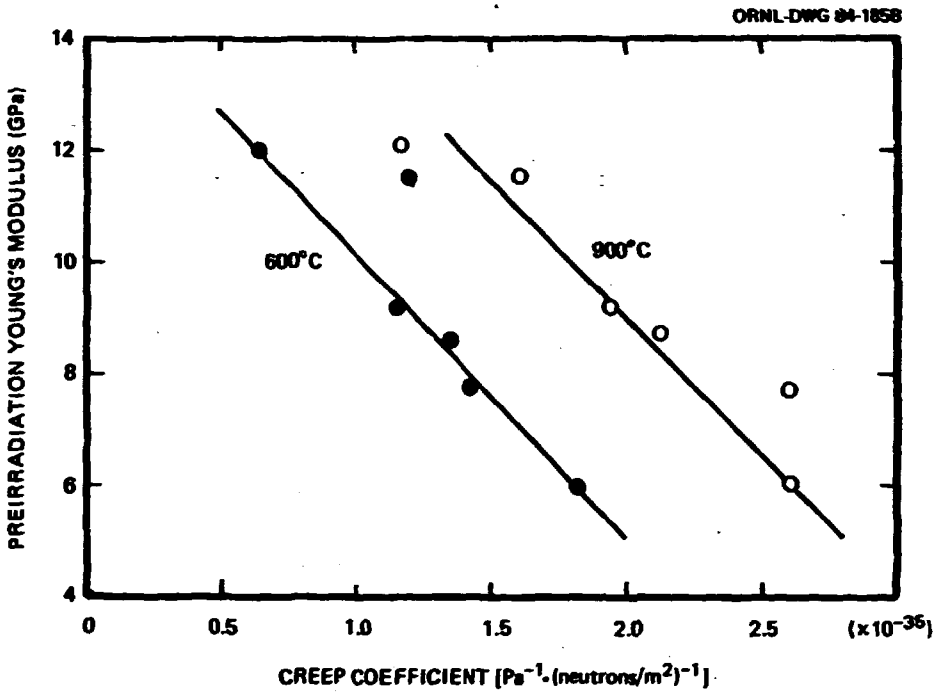

Fig. 10.1. Correlation of creep coefficient with initial Young's modulus for the 900°C experiments (OC-1, -3, and -5) and the 600°C experiments (OC-2 and -4).

expectancy from loss of density occurs much sooner at the elevated temperatures. The maximum densification that occurs with temperature is shown in Fig. 10.2. Clearly, all the graphites have essentially the same reduction in maximum densification with increasing temperature. This suggests that the structural accommodation of the anisotropic growth in the c-axis and a-axis shrinkage by irradiation is reduced by increasing the irradiation temperature. That is, the internal volume to accommodate the irradiation growth is reduced, thus causing the growth to increase the internal shear stresses actively at the interparticle boundaries and to initiate fracturing and structural degradation at lower fluences. The loss of the internal accommodating void volume can result from simply heating the graphite to the irradiation temperature as anisotropic crystallographic thermal expansion coefficients fill in the accommodating void volume.

The accommodating void volume is largely a result of cooling the graphite in the final stages of graphitization. The anisotropic c-axis

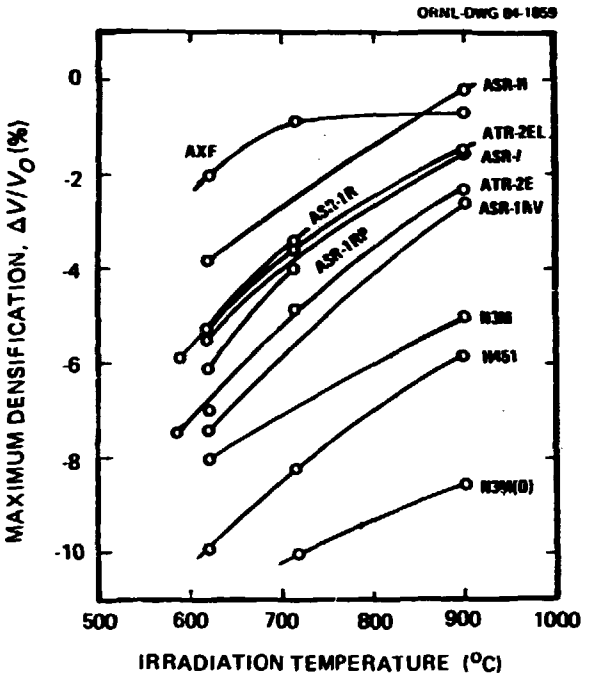

Fig. 10.2. Maximum densification of various graphite grades as a function of temperature for recent High Flux Isotope Reactor irradiations.

shrinkage and the relatively stable a-axis generate the necessary cracking between the layer planes to generate the void volume to accommodate the irradiation growth. The extent of this accommodation can be measured by comparing the volumetric coefficient of thermal expansion with the theoretical. The difference between the two is a measure of the void volume created by the final stages of fabrication; therefore, a graphite with a large volumetric coefficient of thermal expansion will densify very little under irradiation, and one with a small volumetric coefficient of thermal expansion will densify greatly. However, we also know that, if the graphite has higher initial density, it will also densify very little under irradiation. Therefore, the total densification under irradiation can be considered a function of the volume created by the anisotropic coefficients of thermal expansion and the overall porosity:

$$(\Delta v/V_0)_I = f[(\Delta v/V_0)_{CTE}, (\Delta v/V_0)_D] ,$$

where

$(\Delta v/V_0)_I$ = maximum densification under irradiation;

$(\Delta v/V_0)_{CTE}$ = 2000 $(27 \times 10^{-6} - CTE_v)$, the void volume created by cooling down from 2000°C;

$(\Delta v/V_0)_D$ = (2.05 − initial bulk density)/2.05 = the void volume within the structure accessible to helium, where 2.05 is the apparent helium density.

Now that we have irradiated a reasonable number of grades with a range of $(\Delta v/V_0)_I$, it is relevant to examine the data to determine the relative significance of $(\Delta v/V_0)_{CTE}$ to $(\Delta v/V_0)_D$. This should also allow the prediction of the maximum densification of future materials. As a first approximation and for simplicity, we assume a linearized function for a sensitivity calculation in the form

$$(\Delta v/V_0)_I = A + B\,(\Delta v/V_0)_{CTE} + C(\Delta v/V_0)_D .$$

A multiple linear regression analysis yields the coefficient values $A = -0.0825$, $B = 2.85$, and $C = 0.85$ at 620°C irradiation temperature. Considered as a type F1 functional fit, the standard deviation on $(\Delta v/V_0)_I$ is 0.0076. However, it is interesting to note that, as a type S1 statistical fit, the correlation coefficient is $r^2 = 0.90$. In other words, the linearized fit to the data is indeed quite a good representation. Measured and computed values are compared in Table 10.2.

Table 10.2. Comparison of measured and calculated maximum densification

(Irradiation temperature, 620°C)

Grade	$\Delta v/V_0$ (%)		Grade	$\Delta v/V_0$ (%)	
	Measured	Calculated		Measured	Calculated
V356	9.6	9.2	ASR-1RP	6.7	7.4
V483	9.1	8.1	ASR-1RS	7.1	7.3
ATR-2R	7.0	7.1	ASR-2R	8.5	8.4
ATR-2E	7.1	7.1	UKAEA-11	5.3	5.2
ATR-2EL	6.5	8.0	AXF	1.6	1.4
ASR-1R	5.3	5.9	H451	9.9	9.3

We conclude that at 620°C the thermal expansion voids are 3 times (B = 2.85) more effective than their intrinsic volume in controlling the irradiation-induced densification, whereas the helium-accessible voids are effective on a 1:1 ratio (C = 0.85). We also note that each of the three terms in the equation are of comparable magnitude $O(10^0)$ and hence that the densification is equally sensitive to both types of voids.

We also note from Fig. 10.2 that the quantity $(\Delta v/V_0)_I$ changes by 3 to 4 vol % at 900°C. This suggests that the coefficient B should be about 10 rather than the 2.85 we calculate at 620°C. Quite clearly, the linearized sensitivity equation we have fitted successfully at 620°C must at the very least have temperature-dependent coefficients. Unfortunately, we do not yet have sufficient reliable property data to perform a sensitivity calculation at 900°C.

In summary, virtually all the data consistently appear to imply that the decrease in life expectancy of graphite with increasing temperature is only mildly related to growth-rate changes. The major cause of the lifetime reduction is the loss of void volume by thermal expansion to accommodate the differential anisotropic growth of irradiation. The thermal expansion is between 3 and 10 times more effective than is the bulk porosity in reducing the potential densification by irradiation.

From the various HTK-series capsules, we now also have a fair number of graphites that have approached full life, defined as the point at which the material has expanded back to its original volume (Fig. 10.3). The green-coke aerospace graphite, GraphNOL N3M developed at Oak Ridge National Laboratory (ORNL), is the longest lived over the entire range of 600 to 900°C, and the standard material produced at Great Lakes Research Corporation (GLRC) is somewhat superior to the modified material made at ORNL (N3MO). The extruded FRG graphite ATR-2E is the best of the German graphites, with the vibratory-molded ASR-1R materials as a family varying from markedly inferior to nearly the same at 600°C. The improved H451I prototype graphite was essentially identical to H451, as expected.

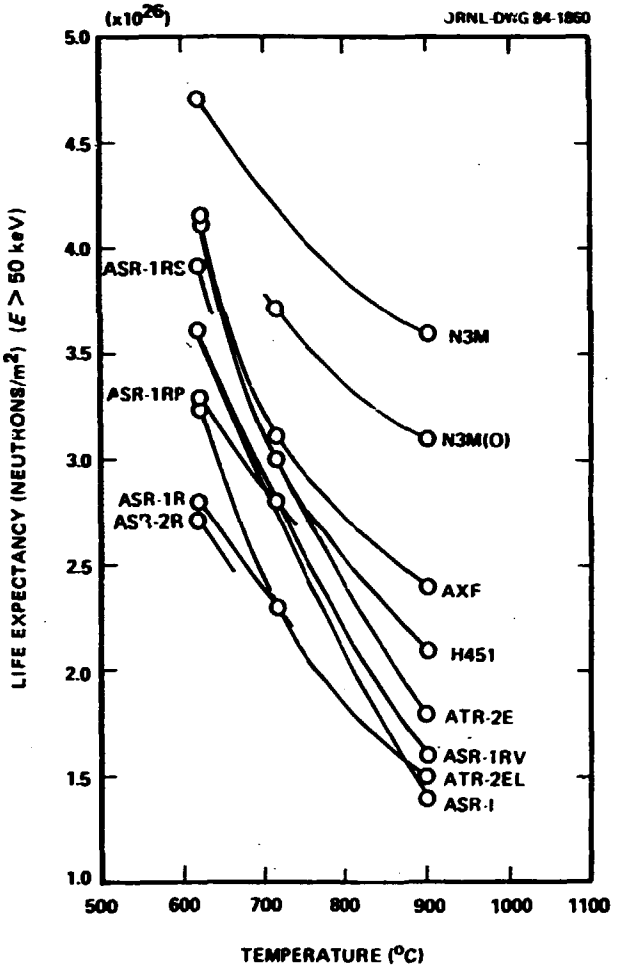

Fig. 10.3. Life expectancy of various graphite grades irradiated in High Flux Isotope Reactor survey experiments.

10.2.4 Results of Irradiation Testing: Fracture Mechanics Series — C. R. Kennedy

Fracture toughness specimens of graphite grades H451, GraphNOL N3M, and ASR-1RS were irradiated in HFIR experiments HTF-2 (900°C) and HTF-3 (600°C). The experimental design and the short-rod fracture specimen were described in the last annual report.[1] Each experiment included 20 fracture toughness specimens irradiated to different fluences up to 1.5×10^{26} neutrons/m^2, $E > 50$ keV. This fluence exceeds the HTR fuel block requirements but does not reach maximum densification for the U.S.

grades H451 and GraphNOL N3M. It is adequate at 900°C to exceed the maximum densification and initiate volume expansion for grade ASR-1RS. The dimensional changes agree well with past HTF-capsule experiments, as seen in Figs. 10.4 and 10.5 for grades H451 and GraphNOL N3M, respectively. The results for grade ASR-1RS are given in Chap. 11.

Fracture toughness K_{IC} results are given in Figs. 10.6 and 10.7 for grades H451 and GraphNOL N3M, respectively. In all cases, the fracture toughness increases initially with fluence; however, the 900°C irradiated specimens of grade ASR-1RS decrease in fracture toughness as specimens begin to expand in volume (shown in Chap. 11). The strain energy-release rate G_{IC} is calculated from the fracture toughness values and the sonic elastic modulus E:

$$G_{IC} = K_{IC}^2/E$$

(Figs. 10.8 and 10.9). Clearly, in all cases there is loss in G_{IC} with fluence, and the loss is faster at 900°C than at 600°C. These results are significant in that they conflict with previous concepts describing the fracture characteristics of graphite under irradiation. These concepts used the Griffith-Irwin equation for fracture,

$$\sigma_f = (G_{IC}E/2\pi a)^{1/2} ,$$

where σ_f is the ultimate strength and a is the radius of the critical defect size, and postulated that both G_{IC} and a remain unaffected by irradiation. Thus, the strength is simply related to the square root of the modulus, in fairly good agreement with all the studies comparing the fracture strength with Young's modulus. However, our results clearly show that G_{IC} does not remain constant but decreases with fluence. If G_{IC} decreases with fluence, the observed increase in strength can result from only a compensating decrease in the critical defect size. We have noted that sonic attenuation decreased with fluence, which does indeed imply that the flaw size is decreasing. These results strongly indicate that not only does the critical defect close but also heals itself, suggesting an irradiation-enhanced diffusion process. Numerical calculations suggest that the initial flaw size is comparable to the optical domain size, but

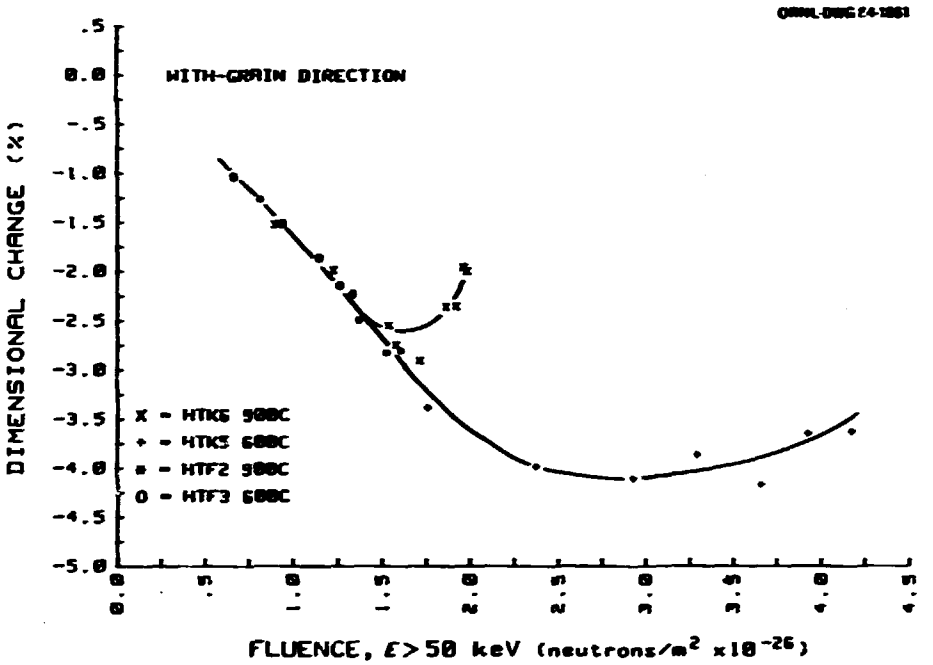

Fig. 10.4. Dimensional changes in H451 graphite comparing HTF-2 and -3 with HTK-5 and -6.

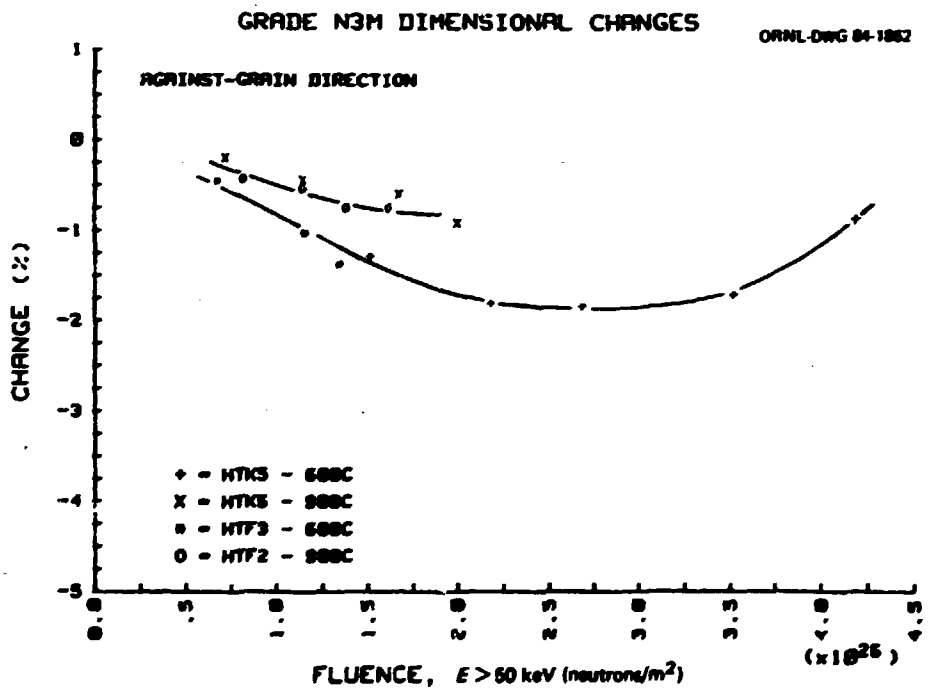

Fig. 10.5. Dimensional changes in GraphNOL N3M comparing HTF-2 and -3 with HTK-5 and -6.

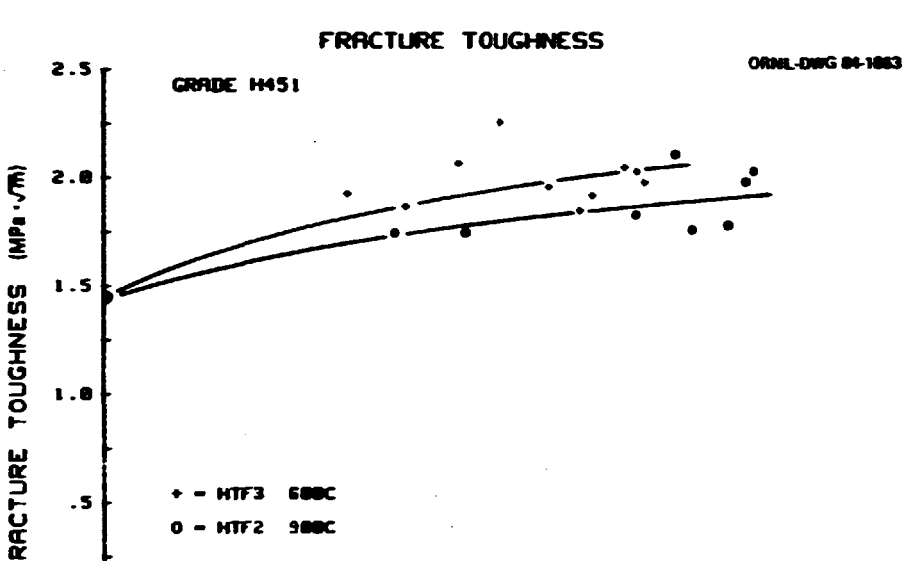

Fig. 10.6. Fracture toughness of grade H451 graphite as affected by irradiation.

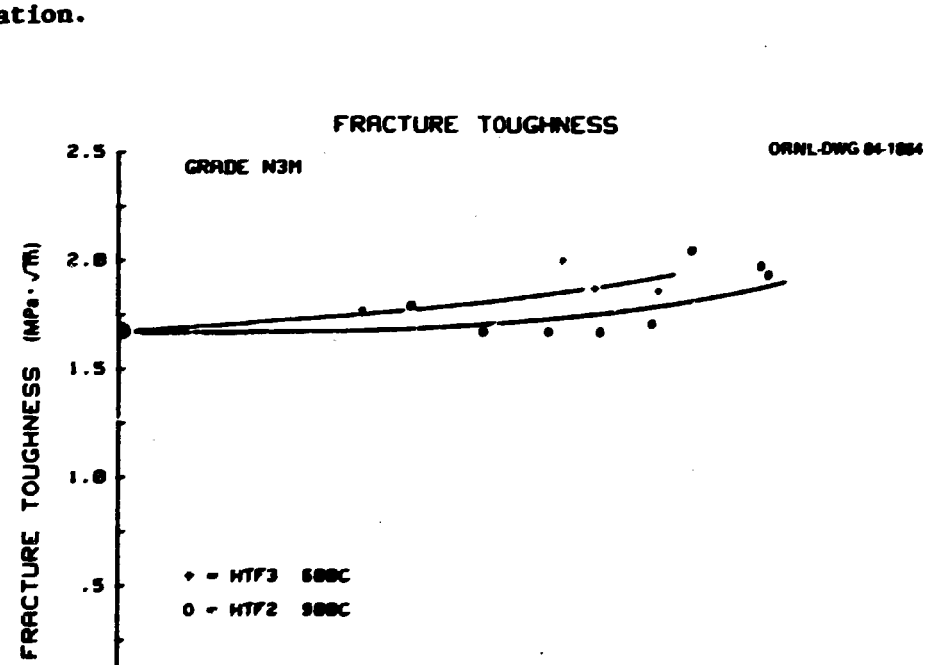

Fig. 10.7. Fracture toughness of grade GraphNOl N3M as affected by irradiation.

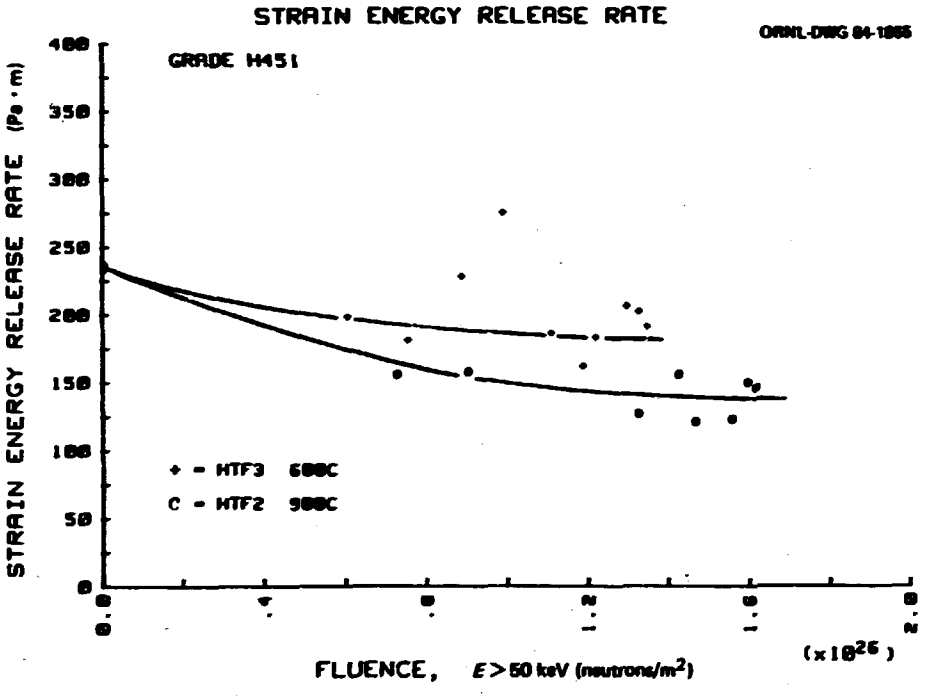

Fig. 10.8. Strain energy release rate of grade H451 graphite as affected by irradiation.

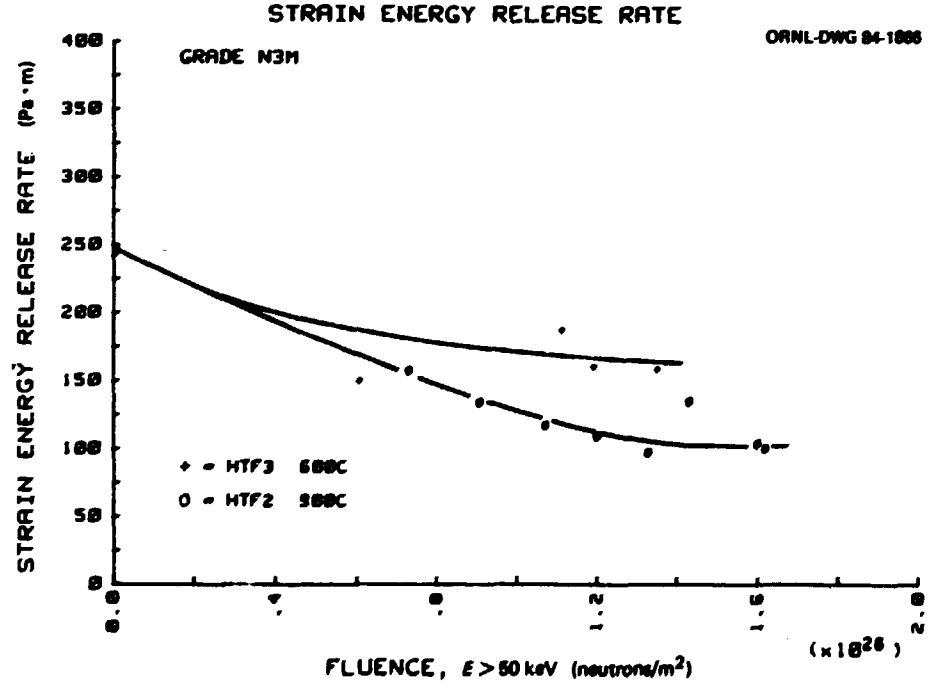

Fig. 10.9. Strain energy release rate of grade GraphNOL N3M as affected by irradiation.

this decreases toward the crystallite size as damage continues. One is tempted to associate this phenomenon with the thermal expansion voids. Concurrently, however, shear at boundaries by differential growth must initiate very early in damage and continue. Such weakened boundaries serve not only to reduce G_{IC} but eventually to produce a new and growing critical defect. This, then, leads to decreasing strength and eventual disintegration of the material.

The significance of these results is that the increase in fracture strength observed in graphite does not occur with an equal increase in fracture toughness K_{IC}. Therefore, one cannot simply take credit for the increase in strength, particularly in components with high-stress concentration factors. Each case must be considered individually and on its own merit. We also showed that the current concepts describing fracture as affected by irradiation are incorrect and require modification. We clearly demonstrated that G_{IC} does not remain constant, thus requiring a reexamination of effects of irradiation on the pore structure and its effect on fracture.

10.3 GRAPHITE EVALUATIONS

10.3.1 Basic Fracture Mechanics Studies — C. R. Kennedy

The development of a high-strength moderator graphite necessitates small-size filler particles to reduce the defect size. An increase in strength will be achieved only if the reduced particle size graphites retain the same fracture toughness and strain energy release rates. To examine the effect of particle size on fracture, a series of special experimental graphites fabricated at ORNL under carefully controlled conditions was evaluated. These graphites were made from green Robinson filler coke for which the particle size of each molding was controlled within 10% of the mean. The graphites achieved densities from 1.8 to 1.98 g/cm^3 without or with one pitch impregnation. The strength, elastic modulus, electrical resistance, and CTE of these graphites normalized to 1.85 g/cm^3 density have been reported.[2] We have now fracture-toughness tested these graphites with a particle size range from 90 to 720 μm by use of the short-rod-type specimen with a 12.7-mm diameter.

The results of fracture toughness testing these graphites and normalizing the fracture toughness for a 1.85 g/cm^3 density are given in Table 10.3.

Table 10.3. Fracture toughness testing results on Robinson-coke graphite normalized to 1.85 g/cm^3

Particle size (μm)	Fracture toughness K_{IC} [(MPa·m)$^{1/2}$]	Brittle ring fracture strength (MPa)	Young's modulus (GPa)	Strain energy release rate G_{IC} (Pa·m)	Critical defect size 2a (μm)
725	1.55	46.2	10.3	233	717
430	1.59	52.4	11.3	224	586
180	1.65	68.3	12.3	221	372
170	1.55	71.0	13.0	185	303
125	1.54	79.0	13.2	180	242
110	1.62	81.4	13.4	196	252
100	1.63	84.1	13.7	194	239
90	1.62	86.9	13.4	172	195

These results show a very slight increase in K_{IC} with decreasing particle size; however, Young's modulus also increases. Thus, we show that the calculated value for the strain energy release rate decreases with decreasing particle size. These results actually indicate that the fracture characteristics are relatively insensitive to particle size over a wide range. Also note that the strength variation is about a factor of 2 without much change in K_{IC} or G_{IC}. Shown in Fig. 10.10 are the calculated critical defect sizes compared with the particle size. The solid line was drawn parallel to the dashed line of equality and represents a displacement of 125 μm. This is fairly strong evidence that the effective crack growth is common, about 125 μm, for each of the graphites with the exception of the much larger 725-μm material. This very likely results from the small specimen thickness of 3.81 mm compared with 0.73-mm particle size. Our overall conclusion from these results is that a reduced particle size for increased strength will not adversely affect the overall fracture characteristics of the graphite.

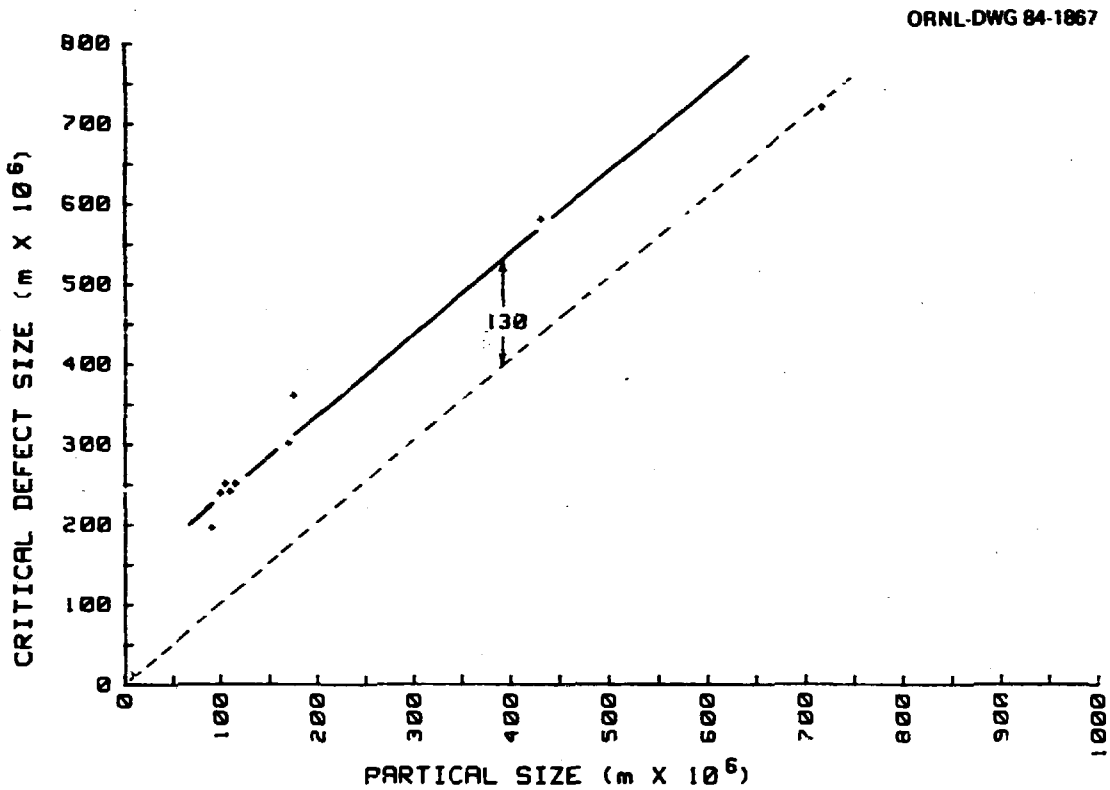

Fig. 10.10. Calculated defect size compared with particle size of Robinson graphites.

10.3.2 Improved Moderator Graphite, H451I — C. R. Kennedy

The program to develop a moderator graphite with improved mechanical properties has continued through a second phase. The graphites, made at GLRC are destructively tensile tested at GA Technologies (GA). Our effort at ORNL was to assist in evaluating the experimental graphites by nondestructive techniques, with the dual purpose of screening the experimental graphites and of eventually using these techniques for quality assurance of full-scale billets for reactor use.

The nondestructive characterization (NDC) procedures were in two steps: (1) inspection of the subsize experimental billet as a whole (as received from GLRC) and (2) inspection of smaller cutup sections. The initial NDC of the whole block was to gain experience for valid evaluations of future full-scale blocks. The NDC of the sections was to determine the

variability within the billet and to have a more direct comparison of the NDC with destructive tensile test results performed at GA. Inspection of the blocks included

1. bulk density,
2. measurement of longitudinal and shear wave velocities in both the axial and radial directions,
3. measurement of the ultrasonic attenuation of the longitudinal wave in the block,
4. measurement of the eddy-current response, and
5. low-voltage radiograph of a 19.05-mm-thick center slab cut from each block.

All the measurements were referenced to a 25.4-mm grid scribed on the ends of each block and at 25.4-mm intervals at azimuths of 0, 90, 180, and 220° down the cylindrical sides. After the full billet was examined, it was sectioned and reexamined.

A central 19.05-mm slab was removed from each block and radiographed. The resulting radiographs, contact printed for ease of overall examination, clearly indicated concentrations of high-Z contamination within the blocks. They also clearly indicated structural irregularities due to preferred orientation of pores from fabrication as well as evidence of density gradients both from impregnation and, on a finer scale, from mix-ball retention. The radiographs yield a quick overall relative estimate of block quality. The results of the sonic and eddy-current testing for the phase II blocks are given in Tables 10.4 and 10.5. These results indicate that the quality of virtually all the blocks was lower than that of those from phase I. The parameter $(E/\alpha)^{1/2}$ used to estimate tensile strength was low for the phase II blocks. Not only was the mean value for $(E/\alpha)^{1/2}$ fairly low, but the variability was also very large. The sonic testing also indicated large disparate populations in several of the blocks, which were confirmed by radiography and later by tensile testing. The axial attenuation was very high in contrast with attenuation measurements in the radial direction, implying an oriented defect structure. In general,

Table 10.4. Eddy-current and sonic velocity measurements made on full blocks

Block	Eddy-current results						Sonic velocities (km/s)										Attenuation (dB/mm)		Bulk density (g/cm³)
	Top		Bottom		Side		Axial				Radial								
							Long		Shear		Long		Shear		Shear				
	$\bar{x}$	s	$\bar{x}$	s	$\bar{x}$	s	$\bar{x}$	s	$\bar{x}$	s	$\bar{x}$	s	$\bar{x}$	s	$\bar{x}$	s	$\bar{x}$	s	
2MB1-1	166	4	167	5	147	3	2.24	0.03	1.47	0.05	2.43	0.01	1.59	0.01	1.51	0.01	0.131	0.035	1.766
2MB2-1	163	2	170	5	150	3	2.34	0.03	1.46	0.04	2.44	0.01	1.58	0.01	1.51	0.02	0.139	0.027	1.764
2MB2-2	161	8	164	2	151	4	2.35	0.04	1.44	0.04	2.44	0.02	1.59	0.01	1.51	0.02	0.165	0.023	1.752
2MB3-1	173	4	166	2	152	4	2.35	0.04	1.41	0.09	2.45	0.02	1.59	0.01	1.52	0.03	0.158	0.036	1.763
2MB3-2	163	3	167	4	149	4	2.36	0.03	1.51	0.07	2.45	0.02	1.60	0.01	1.52	0.02	0.137	0.030	1.775
2MB5-2	163	[illegible]	171	4	154	8	2.35	0.03	1.52	0.04	2.46	0.01	1.61	0.01	1.54	0.01	0.145	0.022	1.797
2MB1-3	141	[illegible]	140	3	133	3	2.40	0.03	1.56	0.02	2.48	0.03	1.58	0.02	1.56	0.02	0.113	0.019	1.753
2MB1-4	137	4	150	4	133	6	2.42	0.03	1.57	0.02	2.43	0.01	1.58	0.01	1.53	0.02	0.135	0.014	1.754
2MB4-3	144	4	146	3	136	3	2.41	0.06	1.55	0.06	2.44	0.04	1.58	0.02	1.56	0.03	0.153	0.022	1.797
2MB4-4	149	4	142	4	137	4	2.44	0.04	1.47	0.05	2.45	0.02	1.60	0.01	1.58	0.02	0.159	0.018	1.793
2MB7-1	138	4	144	3	130	3	2.33	0.04	1.51	0.05	2.49	0.02	1.60	0.01	1.53	0.04	0.148	0.024	1.747
2MB7-2	135	3	139	4	124	3	2.31	0.04	1.54	0.02	2.44	0.02	1.59	0.01	1.55	0.03	0.155	0.015	1.745
2MB8-1	140	6	138	[illegible]	129	3	2.34	0.04	1.54	0.04	2.47	0.02	1.59	0.01	1.54	0.02	0.150	0.031	1.741
2MB8-2	142	4	137	3	126	4	2.34	0.03	1.56	0.04	2.43	0.01	1.59	0.01	1.53	0.02	0.154	0.021	1.753
2MB9-1	134	5	140	4	129	3	2.41	0.03	1.47	0.07	2.47	0.03	1.58	0.02	1.55	0.02	0.173	0.037	1.746
2MB10-1	144	4	137	3	133	3	2.40	0.04	1.56	0.02	2.45	0.02	1.59	0.01	1.56	0.03	0.161	0.015	1.788
2MB1-5	126	8	112	15	113	4	2.35	0.01	1.54	0.003	2.44	0.01	1.58	0.02	1.52	0.01	0.154	0.010	1.742
2MB2-3	138	4	139	8	130	7	2.32	0.02	1.53	0.01	2.40	0.02	1.56	0.01	1.49	0.02	0.171	0.012	1.727
2MB4-5	135	2	133	8	124	3	2.36	0.05	1.48	0.03	2.39	0.02	1.56	0.01	1.50	0.01	0.206	0.033	1.775
2MB4-6	134	3	119	6	124	3	2.39	0.04	1.50	0.04	2.43	0.02	1.57	0.02	1.52	0.02	0.206	0.035	1.773
2MB4-7	147	8	108	20	144	6	2.38	0.04	1.52	0.05	2.45	0.03	1.59	0.01	1.52	0.03	0.222	0.018	1.784
2MB4-8	153	5	143	3	141	4	2.39	0.02	1.57	0.004	2.46	0.02	1.60	0.01	1.54	0.01	0.167	0.011	1.795
2MB4-9	150	3	155	3	139	4	2.36	0.04	1.50	0.05	2.40	0.03	1.57	0.01	1.50	0.02	0.220	0.031	1.757
2MB5-3	130	4	135	3	122	3	2.40	0.04	1.55	0.04	2.43	0.02	1.58	0.01	1.52	0.02	0.204	0.020	1.768
2MB5-4	149	5	133	6	141	3	2.41	0.01	1.57	0.004	2.46	0.02	1.61	0.01	1.55	0.02	0.167	0.016	1.794
2MB9-2	148	4	127	6	140	4	2.41	0.03	1.55	0.01	2.42	0.03	1.58	0.02	1.53	0.02	0.203	0.017	1.765
2MB113	153	2	145	3	140	4	2.39	0.03	1.55	0.04	2.39	0.04	1.54	0.04	1.51	0.02	0.203	0.023	1.758
2MB114E	145	3	145	3	136	16	2.36	0.03	1.51	0.06	2.37	0.02	1.57	0.02	1.48	0.03	0.206	0.037	1.743

Table 10.5. Results of testing full blocks of H451I

Block	Density (g/cm^3)	E_{33} (GPa)	E_{11} (GPa)	E_{44} (GPa)	E_{66} (GPa)	$-S_{12}/S_{11}$	$-S_{13}/S_{11}$	$-S_{13}/S_{33}$	$(E/\alpha)^{1/2}$		Eddy-current resistivity ($\mu\Omega\cdot m$)		Ratio of top to bottom eddy-current readings
									$\bar{x}$	s	With grain	Against grain	
2MB1-1	1.766	8.57	9.93	3.92	4.48	0.11	0.19	0.16	8.40	1.25	7.91	9.02	0.99
2MB2-1	1.764	8.78	9.85	3.89	4.41	0.12	0.21	0.19	8.07	0.80	7.91	8.84	0.96
2MB2-2	1.752	8.69	9.75	3.81	4.41	0.10	0.23	0.20	7.31	0.55	8.01	8.66	0.98
2MB3-1	1.763	8.71	9.81	3.81	4.56	0.10	0.23	0.21	7.53	0.82	7.82	8.81	1.04
2MB3-2	1.775	9.13	10.10	4.08	4.51	0.12	0.19	0.17	8.28	0.92	7.94	8.85	0.98
2MB5-2	1.797	9.29	10.37	4.20	4.65	0.12	0.18	0.16	8.15	0.67	7.89	8.62	0.95
2MB1-3	1.753	9.52	10.14	4.25	4.37	0.16	0.16	0.15	9.57	0.74	8.63	9.08	1.01
2MB1-4	1.754	9.66	9.86	4.22	4.37	0.13	0.16	0.15	8.54	0.53	8.55	9.18	0.91
2MB4-3	1.797	9.84	10.21	4.35	4.50	0.14	0.16	0.15	8.09	0.57	8.50	9.04	0.99
2MB4-4	1.793	9.77	10.10	4.16	4.59	0.10	0.20	0.20	7.75	0.35	8.57	8.99	1.05
2MB7-1	1.747	8.86	10.19	4.05	4.47	0.14	0.18	0.16	7.88	0.66	8.62	9.29	0.96
2MB7-2	1.745	8.91	9.97	4.15	4.42	0.13	0.14	0.13	7.69	0.38	8.75	9.52	0.98
2MB8-1	1.741	8.97	10.05	4.11	4.41	0.14	0.16	0.15	7.94	0.85	8.68	9.67	1.01
2MB8-2	1.753	9.17	9.96	4.18	4.44	0.12	0.15	0.14	7.90	0.63	8.66	9.49	1.04
2MB9-1	1.746	9.20	9.90	3.99	4.35	0.14	0.20	0.19	7.34	0.83	8.74	9.22	0.96
2MB10-1	1.788	9.78	10.22	4.34	4.54	0.13	0.16	0.15	7.85	0.41	8.63	9.08	1.05
2MB1-5	1.742	9.03	9.83	4.06	4.32	0.14	0.17	0.15	7.77	0.26	9.29	9.67	1.13
2MB2-3	1.727	8.78	9.44	3.92	4.20	0.13	0.17	0.16	7.28	0.29	8.69	9.24	0.99
2MB4-5	1.775	9.09	9.60	3.94	4.34	0.11	0.19	0.18	6.71	0.55	8.83	9.44	1.02
2MB4-6	1.773	9.31	9.83	4.02	4.39	0.12	0.20	0.19	6.81	0.63	9.05	9.21	1.13
2MB4-7	1.784	9.33	10.12	4.13	4.52	0.12	0.19	0.17	6.54	0.30	9.02	8.07	1.36
2MB4-8	1.795	9.70	10.36	4.33	4.58	0.13	0.16	0.15	7.72	0.27	8.42	8.83	1.07
2MB4-9	1.757	9.08	9.57	3.96	4.30	0.11	0.18	0.18	6.51	0.48	8.29	9.08	0.97
2MB5-3	1.768	9.54	9.87	4.16	4.39	0.12	0.17	0.17	6.91	0.37	8.87	9.52	0.96
2MB5-4	1.794	9.84	10.36	4.35	4.63	0.12	0.17	0.16	7.76	0.36	8.62	8.62	1.12
2MB9-2	1.765	9.63	9.82	4.19	4.40	0.12	0.16	0.16	6.95	0.34	8.72	8.57	1.17
2MB113	1.758	9.54	9.50	4.11	4.14	0.15	0.16	0.16	6.91	0.46	8.39	8.92	1.06
2MB114E	1.743	9.03	9.33	3.90	4.29	0.09	0.18	0.18	6.74	0.64	8.50	9.04	1.00

these blocks are not high quality and do not represent the potential of the H451I graphite as a moderator material. Effort is necessary to determine the cause of this deterioration in the overall quality.

The oriented porosity and lack of good axial tensile strength in these blocks was confirmed by GA tensile testing. This porosity-type defect structure is very attenuating to the sound waves in the axial direction. In most cases the defect structure occurred in bands rather than uniformly throughout the block. Therefore, the axial attenuation was significantly increased in contrast with the average properties in the block. Also, the strength in the radial direction is mildly affected by this type of oriented defect. Thus, it was found that, for graphites with this type of defect structure, the attenuation was a good estimator of strength in the parameter $(E/\alpha)^{1/2}$. Although the measurement of attenuation in the radial direction may be questionable because of the curved surfaces, these measurements appear to more truly indicate the quality of the graphite. Also, because of the preferred orientation of the flaw structure, it appears that the axial and radial strengths must be compared separately. The use of the radial attenuation along with the elastic moduli to estimate the tensile strengths are given in Figs. 10.11 and 10.12. These data can be compared with the conventional methods of estimating strength from Young's modulus shown in Fig. 10.13. The parameter $(E/\alpha)^{1/2}$ is obviously far superior to the $(E)^{1/2}$ for strength estimation. Although the blocks from phase II are certainly not the type of material that eventually will be used for moderator material, they yield a chance to further our ability to define nondestructive parameters that will estimate the quality of the graphite. These studies clearly indicate the potential of NDC to assure quality.

10.3.3 Statistical Analysis of H451 Tensile Strengths — W. P. Eatherly

In the attempt to produce a statistical analysis procedure that would permit billet-by-billet quality control of nuclear graphite, we have used variance homogeneity as a justification for pooling and identifying outliers. If the starting hypotheses (normality, fixed variance components)

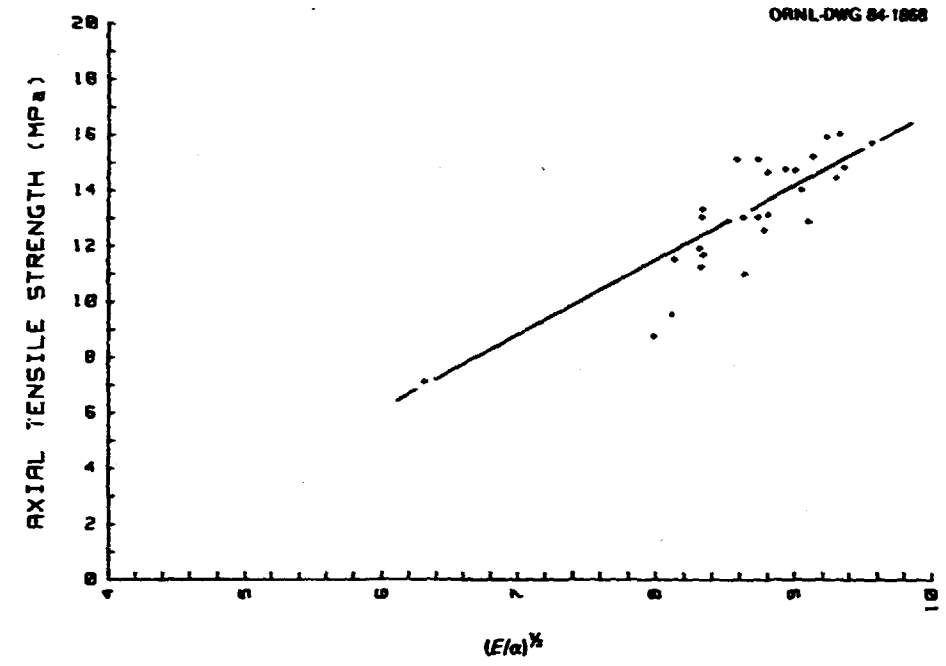

Fig. 10.11. Correlation of the measured axial strength with the parameter $(E/\alpha)^{1/2}$. Here E is the axial sonic modulus and α, the radial sonic attenuation.

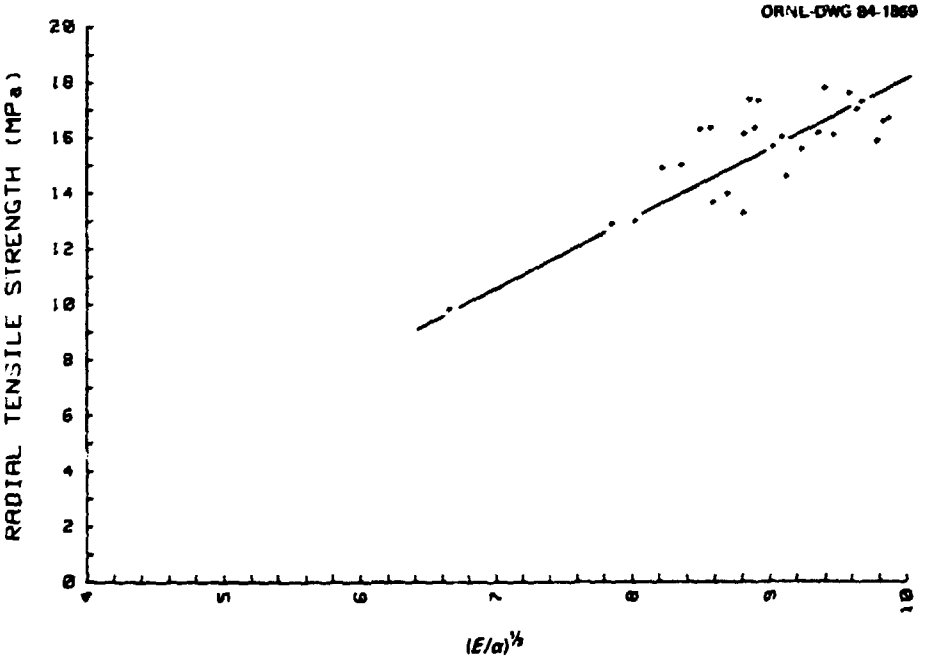

Fig. 10.12. Correlation of the measured radial strength with the parameter $(E/\alpha)^{1/2}$. Here E is the axial sonic modulus and α, the radial sonic attenuation.

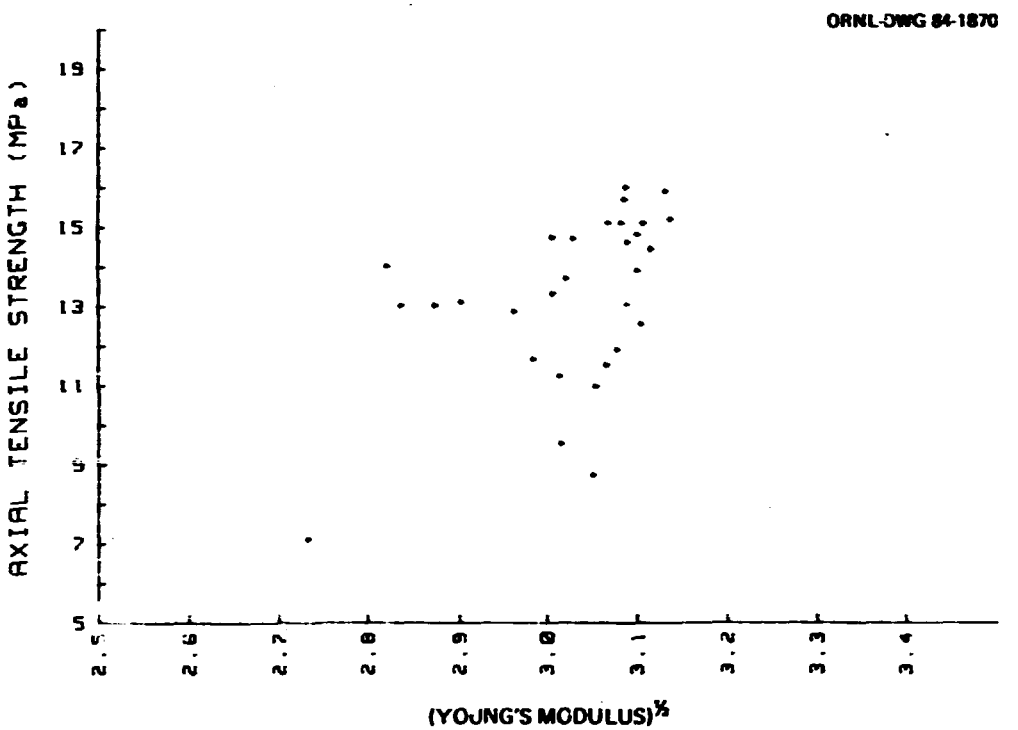

Fig. 10.13. Lack of correlation between axial tensile strength and the square root of axial sonic modulus.

are valid, the removal of outliers by a prescribed procedure and the homogeneity test should be concurrently satisfied. Implicit in this approach is the fact that disparate flaws demonstrably exist and should appear as outliers.

Because no use has been made in this procedure of the higher moments, they become available as an independent test for normality. To understand the nature of these tests and their bearing on our problem, we remind the reader that the definition of the normalized central moments of a distribution with probability density function $f(x)$ is given by

$$\mu_k = \sigma^{-k} \int (x - \mu)^k f(x)\, dx \quad k > 0 ,$$

where μ is the mean and σ^2 the variance of $f(x)$. The sample moment is given by

$$M_k = \hat{s}^{-k}\, n^{-1} \sum (x_i - \bar{x})^k ,$$

where x_i is the ith observation, $\bar{x}$ the observed mean, $\hat{s}^2$ the maximum-likelihood estimator of σ^2, and n the sample size. In Pearson's notation, the skewness $\sqrt{b_1}$ and kurtosis b_2 measures are given by

$$\sqrt{\beta_1} \equiv |\mu_3| \qquad \beta^2 \equiv \mu_4$$

with analogous definitions for the sample

$$\sqrt{b_1} = |M_3| \qquad b_2 = M_4 \ .$$

For a normal distribution, $\sqrt{\beta_1} = 0$ and $\beta_2 = 3$. Pearson has calculated upper and lower one-sided 1 and 5% points for sample $\sqrt{b_1}$ and b_2 at various sample sizes n (ref. 3). These are obtained by moment fitting to the so-called Pearson-type distributions and treat $\sqrt{b_1}$ and b_2 as stochastically independent variables. These tests have very poor powers for samplings of less than perhaps 400 data points and, hence, require either a very large sampling or a pooling of samples to achieve high resolution. That is, the conclusion from observed $\sqrt{b_1}$ and b_2 that a distribution is indeed normal may be overturned as the sample size increases, for the simple and obvious reason that large fluctuations in the higher moments are not rare.

We have interpolated the Biometrika Tables[4] to obtain the percentiles of the $\sqrt{\beta_1}$ and β_2 distributions used in the following tables.

In Table 10.6 we list the observed values of the skewness $\sqrt{b_1}$ and the 5% points for the $\sqrt{\beta_1}$ distribution for the various lots and orientations and poolings thereof. In the last column we provide a superficial decision that the underlying distribution is either skewed or normal and arrive uniformly at the decision that all samplings may be considered "normal" after truncation. It must be remembered, however, that the very act of truncation reduces the fluctuations in $\sqrt{b_1}$ and the conclusion toward "normality" even if such does not exist. In general, however, the observed $\sqrt{b_1}$ is so small compared with the 5% point that we can feel fairly safe in concluding that the distributions are normal under a skewness test alone.

The conclusion shifts sharply, however, when we consider the kurtosis, presented in Table 10.7. Here the data are marginally platykurtic* even before truncation and become markedly so as truncation proceeds.

---

*Platykurtic: platy (flat) + kurt (bulged) (i.e., the distribution is too flat in the center, and the tails are largely missing).

Table 10.6. Test of observed skewness $\sqrt{b_1}$ against one-sided 5% point of expected skewness for sample of size n against a normal distribution

Lot	Orientation	n	Two-sided truncation	$\sqrt{b_1}$	One-sided 5% point	Decision
472	Axial	111	None	−0.349	−0.371	Normal
		108	First	−0.080	−0.376	Normal
		100	Second	−0.001	−0.389	Normal
	Radial	56	None	−0.076	−0.508	Normal
478	Axial	439	None	−0.541	−0.191	Skewed
		400	First	−0.191	−0.200	Normal
		389	Second	−0.096	−0.203	Normal
	Radial	224	None	−0.239	−0.265	Normal
		214	First	+0.072	+0.271	Normal
		211	Second	+0.104	+0.273	Normal
482	Axial	224	None	−0.338	−0.265	Skewed
		213	First	−0.173	−0.272	Normal
		205	Second	−0.114	−0.277	Normal
	Radial	112	None	−0.236	−0.369	Normal
		105	First	+0.033	+0.380	Normal
		94	Second	−0.068	−0.401	Normal
All	Axial	774	None	−0.475	−0.144	Skewed
		721	First	−0.176	−0.149	Skewed
		694	Second	−0.096	−0.152	Normal
	Radial	392	None	−0.240	−0.201	Skewed
		375	First	+0.035	−0.206	Normal
		361	Second	+0.011	−0.210	Normal
All	Both	1166	None	−0.395	−0.118	Skewed
		1096	First	−0.110	−0.122	Normal
		1055	Second	−0.066	−0.124	Normal

Here again, the same remarks for the case of skewness apply: the very act of truncation would tend to remove fluctuations and cause b_2 to tend toward negative values on that basis alone. Furthermore, our outlier criterion at the 5% level alone drives b_2 to. rd values of 2.5. Consequently, we can at this point conclude only that the truncation has been overly severe regardless of the true nature of the underlying distribution.

Table 10.7. Test of observed kurtosis b_2 against one-side 5% point of expected kurtosis for sample of size n against a normal distribution

Lot	Orientation	n	Two-sided truncation	b_2	One-sided 5% point	Decision[a]
472	Axial	111	None	−1.73	−2.38	Plat.
		108	First	−1.18	−2.37	Plat.
		100	Second	−0.77	−2.35	Plat.
	Radial	56	None	−1.48	−2.19	Plat.
478	Axial	439	None	−2.79	−2.65	Normal
		400	First	−2.13	−2.64	Plat.
		389	Second	−2.13	−2.64	Plat.
	Radial	224	None	−2.82	−2.53	Normal
		214	First	−1.74	−2.52	Plat.
		211	Second	−1.37	−2.52	Plat.
482	Axial	224	None	−2.44	−2.53	Plat.
		213	First	−2.02	−2.52	Plat.
			Second	−1.86	−2.51	Plat.
	Radial	112	None	−2.22	−2.38	Plat.
		105	First	−1.91	−2.36	Plat.
		94	Second	−1.23	−2.33	Plat.
All	Axial	774	None	−2.67	−2.73	Plat.
		721	First	−2.05	−2.72	Plat.
		694	Second	−1.90	−2.72	Plat.
	Radial	392	None	−2.76	−2.63	Normal
		375	First	−1.95	−2.63	Plat.
		361	Second	−1.37	−2.62	Plat.
All	Both	1166	None	−2.70	−2.77	Plat.
		1096	First	−2.02	−2.77	Plat.
		1055	Second	−1.77	−2.77	Plat.

[a]Plat. = platykurtic.

Bowman and Shenton point out that $\sqrt{b_1}$ and b_2 are correlated and provide 5 and 10% points for the bivariate distribution.[5] Their contours for various sampling levels n are basically obtained by a Monte Carlo calculation, and we reproduce their curves in Fig. 10.14 for the 90% level. Superimposed on this are the three observed values for no truncation (on the $n = 200$ contour) and for the first and second truncations for the totally pooled data. For this entire data set, $n \approx 1100$. If we thus consider the area within $n = 1000$ as a normal distribution plateau, we have

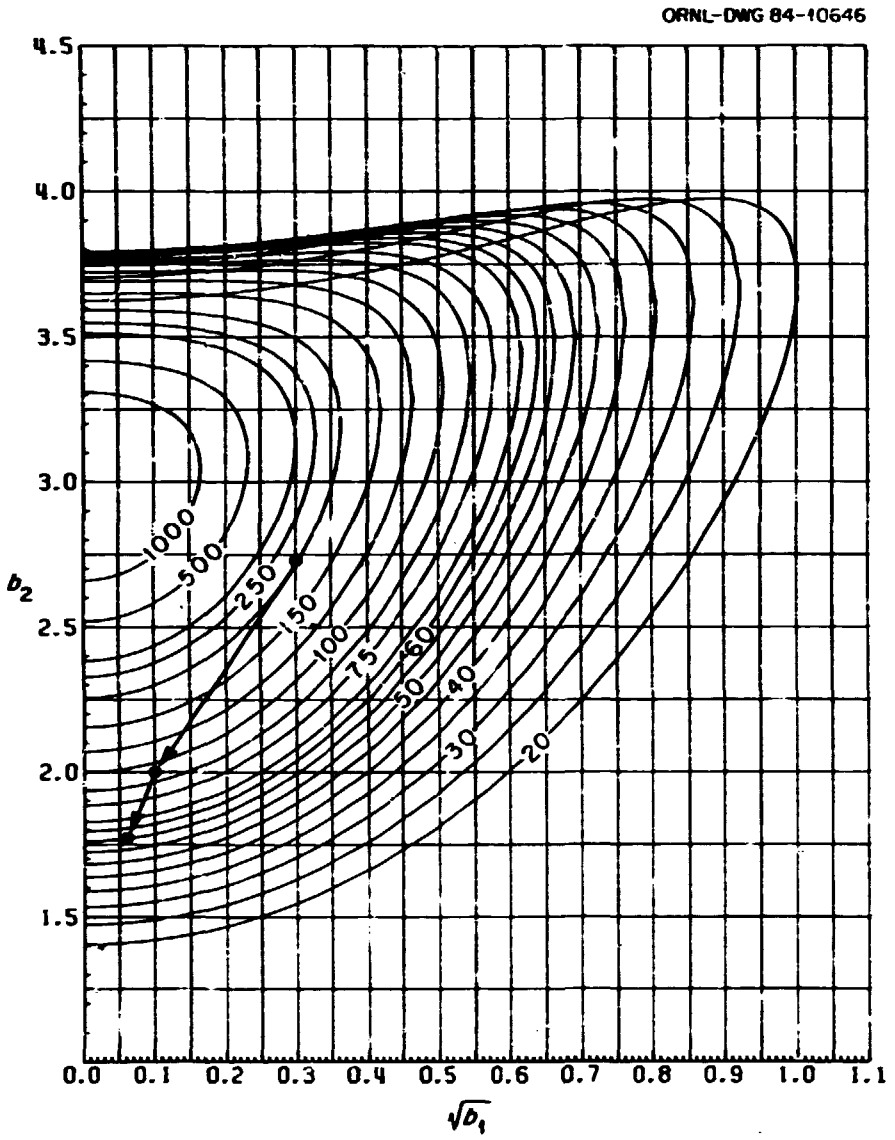

Fig. 10.14. Bivariate skewness-kurtosis contours with observed values superimposed for the untruncated and truncated complete samplings ($n \approx 1100$). Values on the contours are for various assumed values of n.

slid downhill away from normality with each truncation. We again caution that the application of the Nair criterion as a truncating method drives us toward

$$(\sqrt{b_1}, b_2) \rightarrow (0, 2.5)$$

and is sufficient alone to drive us off the plateau if we had ever been on it.

It is premature at this point to argue that our distributions are indeed nonnormal or that our truncation has been oversevere. This problem is still under study.

10.3.4 Higher Moments of the Weibull Distribution* — W. P. Eatherly

We have demonstrated that the background flaw field in H451 graphite most certainly is characterized by a Weibull distribution. With the increasing appearance of graphitic and ceramic materials in high-technology applications, it becomes increasingly obvious that the Weibull statistic must be put on a firm basis similar to that of the Gaussian (normal) statistic. Although some beginnings toward this goal have been made, most obviously for the determination of the Weibull exponent m as it depends on sample size, the general behavior of the sample moments and the tolerance limits remain unsolved. In general, they will be accessible to us only through Monte Carlo techniques and, thus, should be studied as a group.

The question of a choice between Weibull or normal statistics to represent data has never been carefully explored, and the choice becomes even more difficult if we elect to choose between Weibull and a bimodal normal distribution. Generally, the preference has been to take a normal model when faced with compounded variances and to take a Weibull model when dealing with brittle materials. In general, no tests for goodness of fit are yet available to assist in a choice.

Here we begin a study of the use of the bivariate moment test as a means of differentiating between the choices of model. We point out first the essential differences between the two statistics. For the normal distribution, we have two independent statistical parameters, the true mean μ and the true variance σ^2. In Weibull statistics we have only one, the exponent m. To this, however, are added scaling factors, a shifted origin, and a volume dependence. The essential fact is that the Weibull distribution makes two claims on the data: first, the coefficient of variance σ/μ is given by

---

*The work reported here is jointly sponsored by the High-Temperature Reactor Program and the Ceramic Technology for Advanced Heat Engines Program (Office of Vehicle and Engine Research and Development), Conservation and Renewable Energy, Department of Energy.

$$\frac{\sigma}{\mu} = \frac{\left[\Gamma\left(1 + \frac{2}{m}\right) - \Gamma^2\left(1 + \frac{1}{m}\right)\right]^{1/2}}{\Gamma\left(1 + \frac{1}{m}\right)},$$

where Γ is the gamma (factorial) function; thus, σ/μ depends only on the parameter m. The second claim is that

$$\log \mu = c - \frac{1}{m} \log V ,$$

where c is a constant and V is the volume under stress. Both claims must be satisfied by the data to justify the statement that the statistics are indeed Weibull.

The moments of the Weibull distribution are given by

$$\frac{\mu_n}{\theta^n} = \sum_{k=1}^{n} (-1)^k \binom{n}{k} \Gamma\left(1 + \frac{k}{m}\right) \Gamma^{n-k}\left(1 + \frac{1}{m}\right),$$

where the parameter θ is defined in terms of the mean by

$$\mu = \theta \, \Gamma\left(1 + \frac{1}{m}\right).$$

The skewness and kurtosis are, by definition,

$$\sqrt{\beta_1} = \frac{|\mu^3|}{\sigma^{3/2}} \qquad \beta_2 = \frac{\mu^4}{\sigma^2} .$$

The calculation of $\sqrt{\beta_1}$ and β_2 are extremely difficult for the Weibull distribution in that

$$\lim_{m \to \infty} \mu_n = 0 \qquad \lim_{m \to \infty} \sigma = 0 ,$$

so that extremely delicate techniques are necessary as m becomes large.

In Table 10.8 we give values for the moments β_1 and β_2 as a function of m up to 25. These values are calculated from ten-place tables by use of quartic interpolation. Although the values are given to six decimal places, they can as yet be considered correct for β_2 only up to $m = 14$. Values for $\sqrt{\beta_1}$ should be good up to $m = 25$.

Table 10.8. Moments of the Weibull distribution for various values of the exponent m

[Here, μ is the mean, σ the standard deviation, $\sqrt{\beta_1}$ the normalized third moment (skewness), and β_2 the normalized fourth moment (kurtosis)]

m	μ/θ	σ/μ	$\sqrt{\beta_1}$	β_2
1	1.0	1.0	2.0	9.0
2	0.886227	0.522723	0.631111	3.245089
3	0.892980	0.363447	0.168103	2.729464
4	0.906402	0.280544	−0.087237	2.747830
5	0.918169	0.229053	−0.254110	2.880290
6	0.927719	0.193774	−0.373261	3.035452
7	0.935438	0.168022	−0.463190	3.187182
8	0.941743	0.148369	−0.533727	3.327676
9	0.946965	0.132863	−0.590657	3.455209
10	0.951351	0.120310	−0.637637	3.570164
12	0.958286	0.101216	−0.710743	3.766969
14	0.963510	0.087371	−0.765089	3.927768
16	0.967580	0.076866	−0.807121	4.060756
18	0.970838	0.068621	−0.840626	4.172422
20	0.973504	0.061976	−0.867966	4.267202
25	0.978438	0.049902	−0.918457	4.451174

It is possible to express the moments in terms of the Riemann zeta function, and we have employed these to obtain an asymptotic series for μ_n up to the eighth power of $1/m$. This is sufficient to complete Table 10.8 at intermediate values of m, but the table will be extended as the asymptotic series is extended.

These calculations are being performed as a basis for Monte Carlo calculations on finite samplings from the Weibull distribution. Dr. C. A. Johnson of General Electric, among others, has performed such calculations for the mean and shown that large sample sizes are required to obtain good values of m. And we are aiming at similar conclusions in regard to the moment test. In Fig. 10.15 we plot the values of $\sqrt{\beta_1}$, β_2 as functions of m but superimpose them on the sample statistics $\sqrt{b_1}$, b_2 for the normal

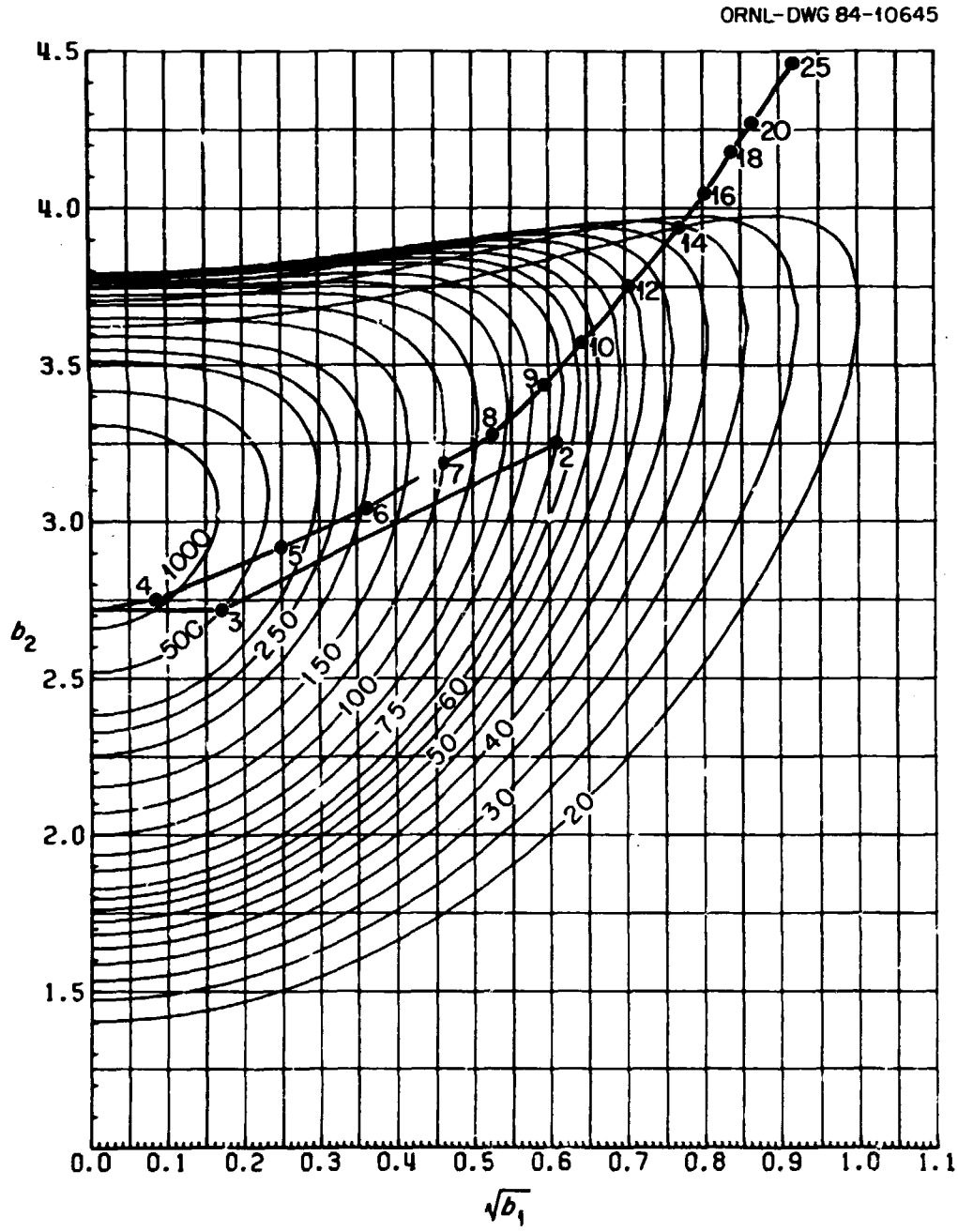

Fig. 10.15. Values of the moments $\sqrt{\beta_1}$ and β_2 of the Weibull distribution superimposed on the 90% significance contours of the bivariate moments for the normal distribution. Figures on the contours are the sample size from the normal distribution. Figures on the points are the values of the Weibull exponent m. The upper branch of the curve has negative skewness.

distribution at the 90% significance level. We note that at $m = 7$ we would not begin to differentiate between normal and Weibull statistics even with a sampling of 150. Only as m exceeds 15 do small samplings differentiate, and this only for a unimodular normal distribution. The Monte Carlo calculation will produce similar contours centered around each value of m, so the confusion factor will be much greater than suggested by Fig. 10.15.

10.4 REFERENCES

1. C. R. Kennedy, "Fracture Toughness Testing," pp. 100–105 in *High-Temperature Gas-Cooled Reactor Technology Development Program Progress Report for Period Ending December 31, 1982*, ORNL-5960, June 1983.

2. E. P. Kennedy and C. R. Kennedy, "Dependence of Strength on Particle Size in Graphite," pp. 303–15 in *Fracture Mechanics: 13th Conference*, ASTM STP 743, American Society for Testing and Materials, Philadelphia, 1981.

3. E. S. Pearson, "Tables of Percentage Points of b-1 and b-2 in Normal Samples; A Rounding Off," *Biometrika* 52, 282–85 (1965).

4. E. S. Pearson and H. O. Hartley, eds., *Biometrika Tables for Statisticians*, vol. 1, 3d ed., University Press, Cambridge, England, 1966, Tables 34A and 34B.

5. K. O. Bowman and L. R. Shenton, *Moment* $(\sqrt{b_2}, b_2)$ *Techniques*, ORNL/CSD-83, August 1981.

11. INTERNATIONAL TECHNOLOGY TRANSFER (WBS 3690.01)

W. P. Eatherly, M. J. Kania, and P. L. Rittenhouse

11.1 INTRODUCTION

A large number of activities and interests are common to the gas-cooled reactor programs being pursued in the United States and in Europe. This task involves the transfer of technology in the areas of fuels, fission products, graphites, and materials between the United States and European programs. Transfer of information in the first three areas above is covered under the U.S.—Federal Republic of Germany (FRG) Fuel, Fission Product, and Graphite Subprogram; materials technology transfer is handled through the U.S.—FRG-Switzerland (CH) Materials Subprogram.

11.2 FUELS — M. J. Kania

Irradiated fuels from experiments FRJ2-P23/compact 14; FRJ2-P25/compacts 13, 21, 27, and 32; and DR-56/compacts 19 and 22 (set 2 fuels under Project Work Statement FD-20 of the U.S.-FRG Fuel, Fission Product, and Graphite Subprogram) were subjected to irradiated microsphere gamma analyzer (IMGA) examinations. The results of these are reported in Chap. 7 of this report.

11.3 GRAPHITE — W. P. Eatherly

11.3.1 High-Pressure (HOVA) Loop Tests — W. P. Eatherly

Some 20 specimens each of graphite grades H451 and 2020 have been machined and shipped to Kernforschungsanlage Jülich (KFA) GmbH for oxidation testing in the Hochdruck-Oxidations-Versachs-Anlage (HOVA) loop. These tests are designed to study oxidative penetration as a function of

pressure over the range 0.4 through 5.0 MPa absolute (4–50 bar). The specimens were machined from characterized stock. The H451 specimens were removed from material adjacent to specimens used in the ORNL + 0.1 MPa (1-atm) laboratory loop. The parent billet had been certified by GA Technologies. The 2020 specimens came from the first experimental lot of nuclear-grade material supplied by Stackpole Carbon, and the particular specimens supplied to KFA are from a section characterized for both density and chemical purity. Similar specimens will be oxidized at Oak Ridge National Laboratory (ORNL) in the summer of 1984.

11.3.2 Fracture Mechanics of Irradiated Graphite — C. R. Kennedy

Graphite grade ASR-1RS was included in High Flux Isotope Reactor (HFIR) experiments HTF-2 and -3, designed to run at 900 and 600°C, respectively. The experimental design and the short-rod fracture-toughness specimen were described in the past annual.[1] Each experiment included four specimens of ASR-1RS, irradiated to different fluences up to 1.5×10^{26} neutrons/m^2 ($E > 50$ keV). The resulting dimensional changes are shown in Fig. 11.1, comparing the effects of temperature. As observed in the figure, the specimens irradiated at 900°C exceeded the fluence necessary for maximum densification and began to expand, while the 600°C specimens were still increasing in density.

The fracture toughness K_{IC} results are shown in Fig. 11.2. In both cases there is a slight initial increase in the fracture toughness; however, the 900°C specimens began to experience a volume expansion and a decreasing K_{IC}. The strain energy release rates G_{IC} are calculated from the fracture toughness values and the sonic elastic modulus E by

$$G_{IC} = (K_{IC})^2/E ,$$

shown in Fig. 11.3. Irradiation at both 600 and 900°C causes a loss in G_{IC} with fluence, with that at 900°C having a greater effect. These results are in general agreement with the results obtained from testing grades H451 and N3M specimens irradiated in the same experiments.

The overall implication is that the increase in fracture strength observed in graphite does not occur with an equal increase in K_{IC}.

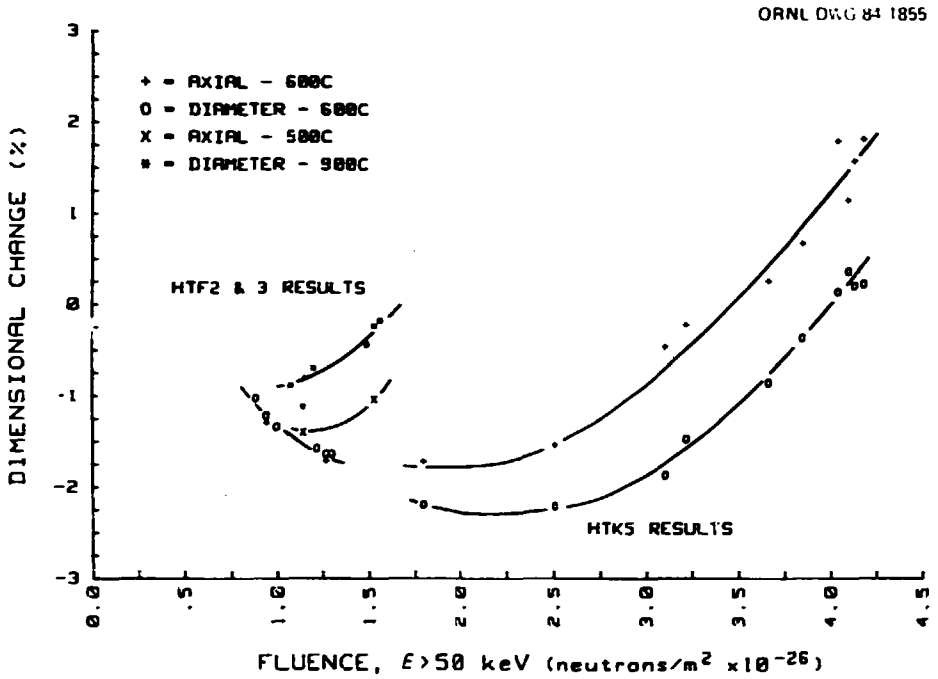

Fig. 11.1. Dimensional behavior of grade ASR-1RS graphite as determined from High Flux Isotope Reactor capsules HTF-2 and HTF-3.

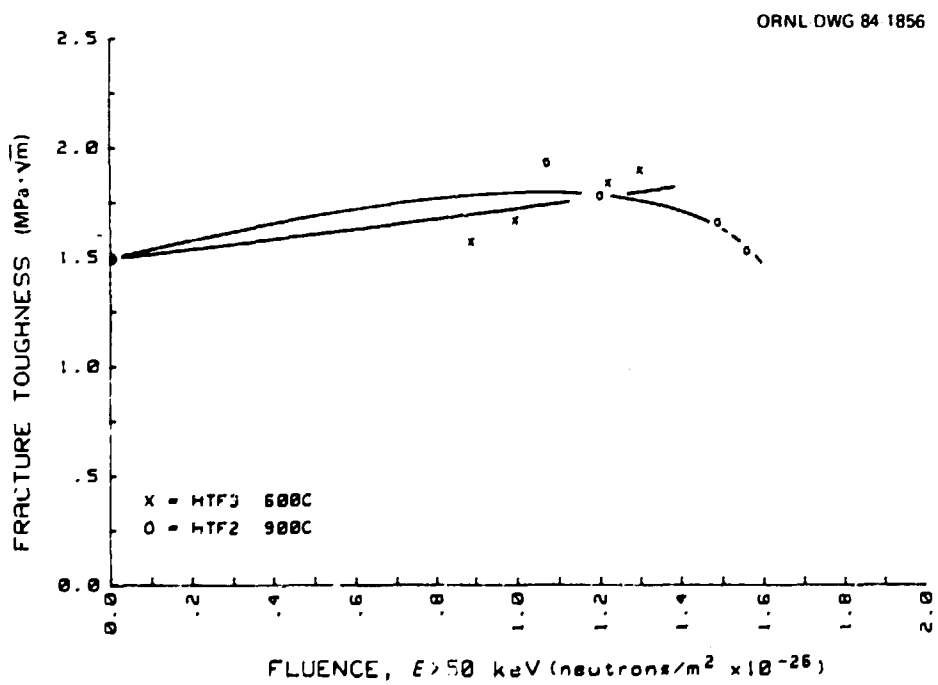

Fig. 11.2. Fracture toughness as a function of fluence for grade ASR-1RS graphite. Curves are shown as a guide to the eye and should not be taken literally.

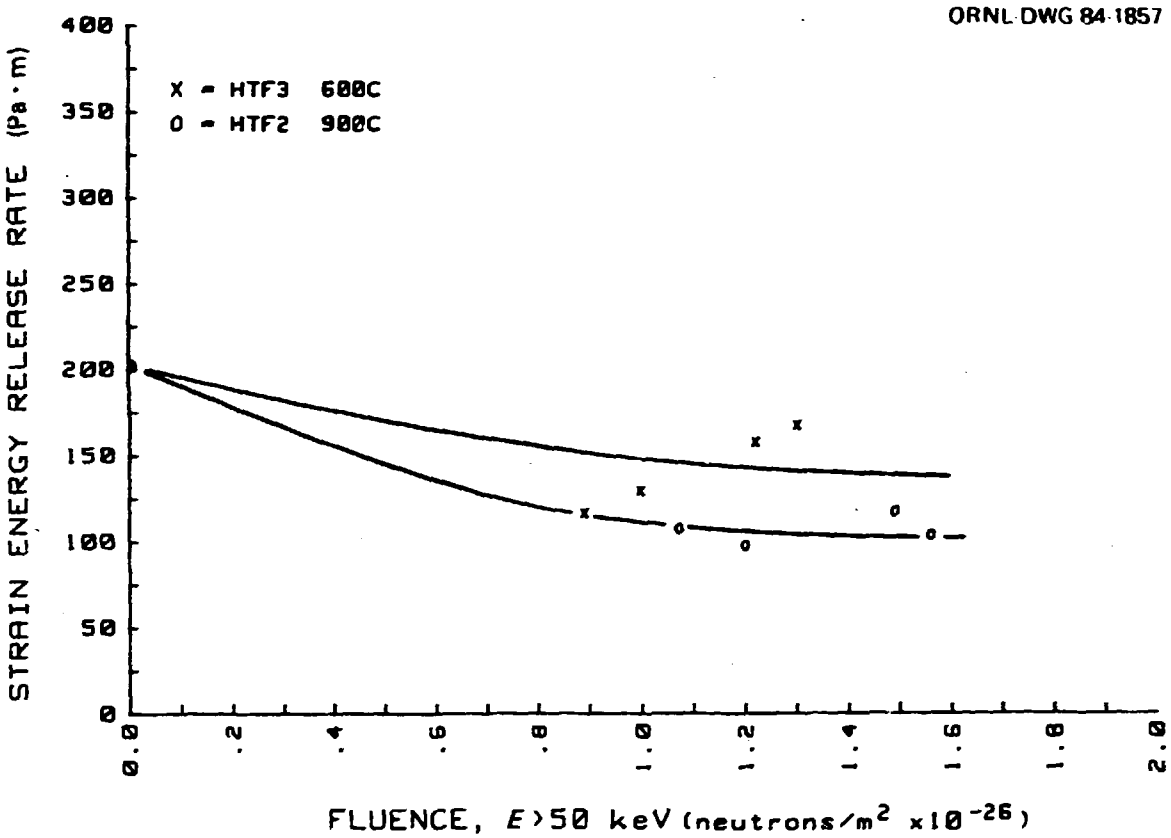

Fig. 11.3. Strain energy release rate as a function of fluence on grade ASR-1RS graphite. Curves are shown as a guide to the eye and should not be taken literally.

Therefore, one cannot simply take credit for the increase in strength, particularly in components with high stress concentrations. The present concepts of describing fracture as affected by irradiation by using the assumption that G_{IC} remains constant must also be reexamined.

11.4 MATERIALS — P. L. Rittenhouse

Agreement on and approval for international cooperation on gas-cooled reactor structural materials under the US-FRG-CH Materials Subprogram was achieved during the year. Work covered is defined in 13 project work statements addressing various aspects of corrosion, surface effects, mechanical properties, and high-temperature design. The participants in the United States are GA Technologies, General Electric Company,

and ORNL; cooperative organizations overseas are Gessellschaft für Hochtemperatur-Technik mbH/Interatom GmbH, Hochtemperatur-Reaktorbau GmbH, Kernforschunsanlage Jülich GmbH, Eidgenoessisches Institut für Reaktorforschung, and associated partners of the foregoing. Special round-robin testing activities were initiated in the areas of low-cycle fatigue and fracture toughness.

11.5 REFERENCE

1. C. R. Kennedy, "German Irradiation Program," pp. 93–98 in *High-Temperature Gas-Cooled Reactor Technology Development Program Progress Report for Period Ending December 31, 1982*, ORNL-5060, June 1983.

12. ADVANCED REACTOR SYSTEMS ENGINEERING (WBS 4108.03)

J. C. Cleveland, H. I. Bowers, B. A. Worley, and P. R. Kasten

12.1 INTRODUCTION

This effort is primarily a peer review of modular High-Temperature Reactor (HTR) concept development activities performed by General Electric, GA Technologies, Combustion Engineering, and Bechtel under the coordination of Gas-Cooled Reactor Associates. Areas of review included design and economic ground rules and criteria, capital and fuel cycle cost estimates, reactor performance, and safety behavior. Oak Ridge National Laboratory (ORNL) personnel attended several modular reactor system technical coordination meetings and provided comments on input. Also, detailed comments were prepared on the draft FY 1983 design and cost summary report. Finally, specific technical analyses were performed to evaluate important issues. Two of these are summarized.

12.2 CALCULATIONS OF FUEL TEMPERATURES DURING DEPRESSURIZED CORE HEATUP ACCIDENTS IN MODULAR HTRs

This work was carried out by Mary Ann Savage of Pennsylvania State University during a practicum performed under separate (non-DOE) funding. The purpose of this work was to compare the heat transfer mechanisms during a depressurized loss of forced-circulation heatup transient in prismatic and pebble-bed HTRs.

A one-dimensional model was developed to evaluate the heat removal capabilities of both core types during depressurized heatup transients. General features of the code include:

1. steady state or transient,
2. cylindrical or rectangular coordinates (one-dimensional),
3. convective and radiative conditions at the outer boundary,

4. up to 20 different regions — some of which may be void regions,
5. up to 20 different materials,
6. temperature-dependent thermal properties,
7. time- and space-dependent internal heat generation rate,
8. graphite conductivity dependent on temperature and neutron fluence, and
9. radiation and conduction within a pebble-bed region.

During a depressurized core heatup transient little or no heat is removed by convection; the primary heat transfer mechanisms are conduction and radiation to the outer pressure vessel surface. In the prismatic core the heat is conducted through the graphite blocks; in the pebble-bed core the heat is transferred by both conduction between and through the pebbles and radiation across the voids between pebbles.

Figure 12.1 is a plot of effective thermal conductivity versus temperature for two heat transfer mechanisms: conduction through solid graphite and heat transfer through a bed of graphite pebbles of given geometry and composition. The curve for effective conductivity for the pebble bed accounts for both conduction and radiation effects. As can be seen, in the lower temperature range, the conduction of heat through graphite blocks is more effective than is the combination of conduction and radiation in the pebble bed. However, at higher temperatures, radiation becomes the dominant process, and heat can be removed more effectively from the pebble bed.

A representative modular reactor was modeled with both a pebble-bed and a prismatic block core. For the core power, diameter, and height given in Table 12.1 and for the same initial conditions (fluence, power density, and temperature distributions), the peak temperature of the heatup transient was slightly higher for the pebble bed and occurred much sooner after initiation of the transient. The heat transfer mechanism was less effective in the pebble-bed core during initial stages of the transient, but, as transient temperatures rose above about 1750°C, thermal radiation in the pebble bed became a more effective heat removal mechanism than conduction in the prismatic core. The net effect was that the peak temperature was only slightly higher for the pebble-bed core for the specific conditions selected for this study.

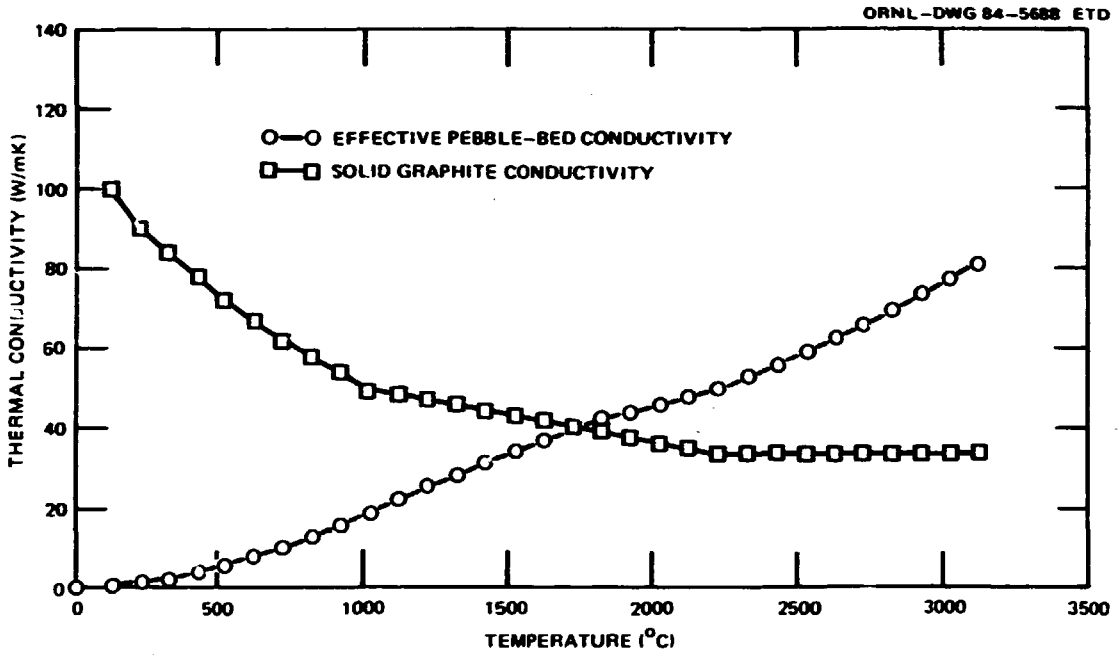

Fig. 12.1. Effective thermal conductivities for two heat transfer mechanisms.

Table 12.1. Design data and peak transient temperature

Reactor power, MW(t)	250.0
Core diameter, m	3.49
Core height, m	6.34
Average core power density, MW(t)/m^3	4.12
Average pebble volume fraction	0.61

	Solid-block core	Pebble-bed core
Peak transient temperature, °C	2152	2172
Time to peaking, h	24	38

12.3 ACCIDENT SOURCE TERM ISSUES

An assessment was performed to determine whether a no-confinement option for the modular HTR could be supported on the basis of current knowledge about fission product release from fuel and the primary circuit during core heatup and depressurization accident conditions. The primary

conclusion was that fission product retention factors beyond the particle coating need to be experimentally determined to estimate releases from the fuel and the primary system resulting from accident conditions. The acceptability of the no-confinement option cannot be supported by the simplistic approach of assuming that the total fission product inventory of the fuel particles that fail during the accident is released directly from the primary circuit; rather, retention factors beyond the particle coating need to be considered.

Specifically, ORNL concluded that:

- Based on thermal cycling data, fuel heatup to 1600°C is not expected to result in a large increase in fuel failure fraction (probably less than a factor of 10) relative to normal operation. Development of fuel capable of limiting fuel particle failure caused by core heatup (to 1600°C) to 10^{-4} (based on noble gas release-to-birth fraction) of the total core fuel particle inventory appears achievable. This requires development and experimental verification.
- Fuel particle release from the primary circuit (circulating activity and liftoff) as a result of depressurization will not be a problem if liftoff is very low. Krypton-88 circulating activity is not a problem; however, ^{131}I and ^{90}Sr liftoff fractions must be verified to be very low.
- For core-heatup-induced failures, scoping analyses imply that additional barriers beyond the particle coatings are necessary to limit releases to values within Title 10, *Code of Federal Regulations*, Part 100, criteria.
- Retention factors beyond the particle coatings for depressurization and heatup conditions must be determined. Holdup by matrix graphite, structural graphite, and steel surfaces must be experimentally determined.
- Finally, a mechanistic analysis of fission product transport resulting from depressurized core heatup accidents is required.

13. MARKET DEFINITION AND APPLICATION ASSESSMENT (WBS 4151.02)

W. R. Gambill

13.1 INTRODUCTION

The intent of the subject study was to relate High-Temperature Reactor (HTR) applications of various types to national needs and to project the relationship to the years 2020 to 2025. The following is a brief summary of this assessment.

Conventional energy projections nearly always indicate growth rates that decrease monotonically with time and historically ignore observable fluctuations in energy growth. An alternative, and preferable, projection methodology has been described by Stewart in his book concerning transitional energy policies and in two of his papers.[1-3] His approach is based on the observation that the growths of both total energy and electrical energy consumption in the United States (since 1850 for the former and 1905 for the latter) have exhibited a cyclic variation about a median logistic growth curve.

Stewart applied the cyclic pattern of energy growth to projections of future energy consumption according to what he calls the cycle-adjusted-logistic (CAL) growth. The result is a relatively flat total energy consumption until about the year 2000, with electrical energy growing at about 2.5% per annum during the same period.[2] The CAL projection, however, forecasts a very rapid energy growth rate between 2000 and 2025, which will more than make up for the relative stagnation between 1980 and 2000.

13.2 NATIONAL NEEDS STUDY

13.2.1 Electrical Energy and the HTR

The CAL projections indicate increasing electrification, the portion of energy used for electricity generation increasing from the current

level of about 34% to almost 50% by 2000 and to about 63% by 2025, ultimately saturating at 68 to 70%. Stewart produced growth projections for U.S. nuclear energy[3] by combining the total energy growth projected by the CAL methodology with the results of Marchetti's energy substitution data for fractional market penetration.[4-5] A revised and updated version is presented here as Table 13.1, in which:

- Base data are for December 1982.
- Average nuclear plant load factors are taken as 55% through 1990 and as 65% for later years.
- All additional light-water reactors (LWRs) are 3800-MW(t) reactors [currently ~1260 MW(e)].
- The number of HTRs is linked directly to water use considerations, that is, to the need for power plants with advanced (dry or hybrid) cooling in water-deficient areas, a potential market for which the HTR, with its high thermal efficiency, is well suited. A study conducted by Hanford Engineering Development Laboratory (HEDL) for Gas Cooled Reactor Associates (GCRA) indicates that this need from 2000 through 2020 will be 179 GW(e) [June 1982 updated (reduced) estimate], of which 96% is for western U.S. sites. For a minimum market share of 33%, this estimated need corresponds to 70 HTRs of 3360 MW(t) each.[6] For the western section of the United States, it seems improbable that more than two-thirds of the projected capacity addition, if that, could be met by coal-fired plants or LWRs in an environmentally acceptable manner. A 33% market share corresponds to HTRs representing 11% of nuclear additions after the year 2000. This value has been used in Table 13.1 to project the number of HTRs [of 3360 MW(t) each] that would be built.

Table 13.1 projects a total of 106 power-producing HTRs over the next 46 years if the nuclear market share were 11%. If the HTR share of the nuclear power market were doubled after the year 2000 from 11 to 22%, 212 large HTRs would be in use by the year 2030, or a total of 609 HTRs of 1170 MW(t) each. These values represent the high estimate for electrical energy generation.

Table 13.1. Electrical energy growth projections for the United States[a]

Year	Total energy[b]		Fraction of total energy		Generating capacity			Total LWRs[e]	Total HTRs[f]
	(EJ/year)	(quads/year)	Electricity input	Nuclear input	Total[c] [GW(e)]	Revised nuclear[d] [GW(e)]	Nuclear (%)		
1990	71	67	0.42	0.07	700	94	13	99	1
2000	76	72	0.49	0.10	930	132	14	129	2[g]
2010	103	98	0.57	0.24	1490	434	29	371	31
2020	139	132	0.61	0.34	2270	876	39	725	70
2030	154	146	0.64	0.43	2770	1288	47	1055	106

[a]A partial revision and extension of the projection of H. B. Stewart, "Economic Growth as Affected by Technologies," paper presented at Gas-Cooled Reactor Associates Annual Meeting, San Diego, Calif., September 1981.

[b]1981 projection.

[c]Assumes total system load factor of 45% and average thermal efficiency that increases from 33% (1990) to 40% (2030).

[d]With average nuclear load factors stated previously and thermal efficiency given in footnote *c*.

[e]If all nuclear reactors were light-water reactors (LWRs) [3800 MW(t) each for additions]; 59 GW(e) and 76 LWRs + 1 HTR in 1982.

[f]For 11% of nuclear additions of 3360 MW(t) each beginning in 2001; HTRs, High-Temperature Reactors.

[g]Fort St. Vrain Reactor + 1 new unit.

13.2.2 Nonelectrical Energy and the HTR

Because of its potential high core-exit coolant temperature of up to 1000°C (1800°F), the HTR permits the application of nuclear energy to nonelectrical processes currently using fossil fuels. These processes are of four general types: resource recovery (tar sands and heavy crude oil); synthetic fuels production (from coal and oil shale); chemicals production (*e.g.*, H_2, ammonia, and methanol by initially steam reforming natural gas); and delivery of process heat, primarily as high-temperature, high-pressure process steam (either directly by pipeline or by indirect, onsite generation using, for example, pumped molten salt). In each category, the useful production rate per unit of fossil fuel consumption is raised compared with the all fossil fuel processes.

Low and high estimates were made of the number of HTRs that might suitably by applied by 2020 to 2025 in each of the four categories. A

conservative HTR load factor of 70% was assumed for these nonelectrical applications. The resulting energy totals were then compared with projected nonelectrical energy needs derived by the CAL methodology.

13.3 PROJECTED TOTALS

Although individual future HTRs might have power ratings ranging from 200 to 3360 MW(t), the totals given here for the year 2020 are expressed as the equivalent number of 1170-MW(t) reactors. The totals were obtained by summation of the preceding sectoral projections.

Case	Total [GW(t)]	Total HTRs	Electric power (%)	Nonelectric power [GW(t)]
Low estimate	338	289	70	103
Mid-range estimate	584	499	60	234
High estimate	825	705	56	362

For nonelectrical energy applications only, these projections are compared below with third-quarter 1982 estimates made by General Electric (GE), GCRA, and GA Technologies (GA) (for the year 2020),[6] expressed as numbers of 1170-MW(t) HTRs:

GE	GCRA	GA	This report		
771	510	363	200 (mid)	88 (low)	309 (high)

The estimates arrived at in this report and those of an earlier GA report[7] are in reasonable agreement. The GA report addresses only nonelectrical applications; the numbers of 1170 MW(t) HTRs (year 2020) are compared below:

Case	GA (ref. 7)	This report
Low estimate	101	88
Mid-range estimate	290	200
High estimate	478	309

13.4 COMPARISON WITH CAL GROWTH PROJECTION FOR NONELECTRICAL ENERGY

The CAL methodology projects the nonelectrical energy component to remain fairly constant to the year 2025, at about 58 EJ (55 quads) per

year. The nonelectrical uses include transportation, comfort heat, and industrial process heat. About 90% of these demands are currently met by oil and natural gas. We assumed, as did Stewart in 1980 (ref. 2), that the available supply of economically recoverable (conventional) gas and oil will be reduced by 50% by the year 2025. Although somewhat arbitrary, this projection is similar both to that of the Department of Energy (DOE) for the United States and to that of the International Institute of Applied Systems Analysis for the world.[8] The latter organization, for example, has forecast that in 2025 about 50% of total global oil consumption will be conventional petroleum. Given this projection, about 26 EJ (25 quads) of energy for nonelectrical uses now supplied by oil and gas must by 2025 be supplied by alternative thermal energy sources such as nuclear, coal, and solar energy.

The total HTR nonelectrical capacity of 103 GW(t) (low case) corresponds to an 8.7% share of the substituted 26 EJ (25 quads) and to only 3.9% of the 58 EJ (55 quads) of total nonelectrical energy. The high-case HTR nonelectrical capacity of 362 GW(t) represents a 30.3% share of the substituted 26-EJ (25-quad) and 13.8% of the 58-EJ (55-quad) total.

13.5 REFERENCES

1. H. B. Stewart, *Transitional Energy Policy, 1980–2030, Alternative Nuclear Technologies*, Pergamon Press, New York, 1981.

2. H. B. Stewart, "Energy Growth Projections and the Role of the HTGR," paper presented at Gas-Cooled Reactor Associates Annual Meeting, San Diego, Calif., October 1980.

3. H. B. Stewart, "Economic Growth as Affected by Technologies," paper presented at Gas-Cooled Reactor Associates Annual Meeting, San Diego, Calif., September 1981.

4. C. Marchetti, "Glimpses into the Pre-Programmed Society: On Energy, Invention, Innovation, and Other Things," IIASA paper, International Institute for Applied Systems Analysis, Laxenburg, Austria, 1980.

5. C. Marchetti, "Society as a Learning System: Discovery, Invention, and Innovation Cycles Revisited," IIASA Publ. RR-81-29, International Institute for Applied Systems Analysis, Laxenburg, Austria, November 1981.

6. *Industrial Process Heat Market Assessment, An Update*, GCRA 82-015, Gas-Cooled Reactor Associates, San Diego, Calif., September 1982, pp. 5-3–5-7.

7. G. R. Hopwood et al., *HTGR Application Comparative Assessment Study*, GA-A16525, General Atomics, San Diego, Calif., April 1982.

8. W. Häfele, *Energy In a Finite World*, two volumes and Executive Summary, International Institute for Applied Systems Analysis, Laxenburg, Austria, Ballinger Publishing Co., Cambridge, Mass., 1981.

14. ADVANCED SYSTEMS ALLOYS (WBS 4604.01)

P. L. Rittenhouse

14.1 INTRODUCTION

New nickel-base superalloys and new classes of alloys will be required to reach the full potential for process heat applications of advanced High-Temperature Reactors (HTRs). The Oak Ridge National Laboratory (ORNL) efforts toward the materials development goal involve the evaluation of new and modified wrought nickel-base alloys and assessment of the behavior of a new class of alloys based on the ordered Ni_3Al intermetallic compound.

14.2 MECHANICAL PROPERTIES OF ADVANCED NICKEL-BASE ALLOYS — H. E. McCoy

Several nickel-base alloys with varying amounts of Cr, Ti, and Al are being creep tested in HTR-He. The role of chromium is to modify the tendency toward carburization in HTR-He by modifying the activity of carbon; aluminum and titanium affect the permeability of the oxide formed on the surface and hence reduce the amount of carbon that can enter the underlying metal. Most of the alloys being examined are modifications of the Inconel 617 composition and form only trace amounts of brittle gamma prime. These modifications have been effective in reducing the amount of carburization but do not result in alloys with high-temperature strength greater than that of Inconel 617.

An alloy development approach by GA Technologies has been to add sufficient aluminum and titanium to form an adherent low-permeability oxide. The levels of aluminum and titanium present cause the formation of amounts of gamma prime sufficient to give excellent creep strength at elevated temperatures and very low ductility at ambient temperature. Two materials containing 2% each of aluminum and titanium are being tested, and both are quite strong and very resistant to carburization.

14.3 NICKEL-ALUMINIDE ALLOYS — H. Inouye and C. T. Liu

A large effort aimed at the development and commercialization of ductile high-strength alloys based on the Ni_3Al composition is in progress at ORNL. The work is sponsored by a number of offices within the Department of Energy (DOE), other government agencies, and several industrial firms. The commercialization of such alloys could be of significant benefit to HTR advanced systems. For example, the creep strength of several Ni_3Al compositions is two orders of magnitude better than that of Hastelloy X at 760°C, the highest temperature investigated to date. Because of this potential, a modest study was initiated to assess the applicability of these materials under HTR conditions.

As the first part of this study, the experimental alloys listed in Table 14.1, all with the approximate formula Ni_3Al, are being fabricated to bar type tensile specimens and will then be exposed to simulated HTR-He containing about 50.5 (500) H_2/5.1 (50) CH_4/5.1 (50) CO [Pascals (μatm)] for 2500 h at 950°C. On the basis of corrosion results of conventional alloys, the aluminides are expected to be highly resistant to carburization by virtue of the dense continuous Al_2O_3 film that forms in oxidizing environments. It is also anticipated that, because of their high aluminum contents, the aluminides will not exhibit internal oxidation characteristic of many conventional alloys.

Table 14.1. Experimental aluminides scheduled for corrosion tests in HTR-He

Alloy	Composition (at. %)
IC-15-9	Ni–24 % Al–0.2 % B
IC-50-4	Ni–23.5 % Al–0.5 % Hf–0.2 % B
IC-63-1	Ni–20 % Al–10 % Fe–0.5 % Hf–0.5 % Mn–0.2 % B

15. HIGH-TEMPERATURE DESIGN CRITERIA (WBS 4605.03)

J. A. Clinard

15.1 INTRODUCTION

The objective of this task is to carry out an assessment of the applicability of ASME Code Case N-47 to very high-temperature reactor (VHTR) components and to identify shortcomings and development needs.

Given its charge at the beginning of FY 1984, this task remained in its infancy in 1983. Thus, this reporting deals mainly with background information and with summary statements concerning the approach being followed and the results expected later in the fiscal year.

15.2 REVIEW OF WORK AREA

The current design methodology for class-1 high-temperature reactor systems components is embodied in the criteria of ASME Code Case-N-47 (ref. 1) and in the design requirements and guidance of Department of Energy NE standards F 9-4T (ref. 2) and F 9-5T (ref. 3). This methodology is currently limited to temperatures not exceeding 649 to 760°C (1200–1400°F) and primarily to Liquid Metal Fast Breeder Reactor (LMFBR) materials, types 304 and 316 stainless steels, 2 1/4 Cr-1 Mo steel, and alloy 800H. In general, the methodology is based on a design-by-analysis concept addressing the several possible failure modes in high-temperature service: (1) ductile rupture from short-term loadings, (2) creep rupture from long-term loadings, (3) creep-fatigue failure, (4) gross distortion due to incremental collapse and ratchetting, (5) loss of function due to excessive deformation, (6) buckling due to short-term loadings, and (7) creep buckling due to long-term loadings. The methodology includes many contributions in terms of both development and validation from the High-Temperature Structural Design Technology Program of Oak Ridge

National Laboratory. The approach taken in task WBS 4605.03 is to develop further the existing LMFBR high-temperature design methodology for the particular alloys and conditions of interest in the VHTR. First, the adequacy of the framework itself must be assessed. This will be accomplished in concert with the task force on very high-temperature structural design established in March 1983 within the ASME Code organization. The primary goal for 1984 is completion of that assessment. The assessment will identify areas needing modification and areas in which additional rules will be required to cover new failure modes and effects.

Once this assessment of Code Case N-47 is completed, the key issues will be known, and specific activities to address them can be formulated.

15.3 REFERENCES

1. "Class 1 Components in Elevated Temperature Service," Sect. III, Div. 1, *ASME Boiler and Pressure Vessel Code, Case Interpretations, Code Case N-47-21*, American Society of Mechanical Engineers, New York, Dec. 11, 1981.

2. NE Standard F 9-4T, *Requirements for Construction of Class 1 Elevated Temperature Nuclear System Components*, Supplement to ASME Code Case N-47, American Society of Mechanical Engineers, New York, February 1984.

3. NE Standard F 9-5T, *Guidelines and Procedures for Design of Class 1 Elevated Temperature Nuclear System Components*, American Society of Mechanical Engineers, New York, March 1981.

16. ADVANCED SYSTEMS INTERNATIONAL COOPERATION (WBS 4607.01)

J. C. Cleveland and P. R. Kasten

16.1 INTRODUCTION

The efforts in this project, carried out during the latter half of 1983, focused on planning and establishing a cooperative effort between Arbeitsgemeinschaft Versuchs-Reaktor (AVR)-GmbH-Kernforschungsanlage (KFA)-Jülich GmbH and Oak Ridge National Laboratory (ORNL) in High-Temperature Reactor (HTR) physics, performance, and safety. This cooperative effort is being established within the framework of the U.S.—Federal Republic of Germany (FRG) Umbrella Agreement. A mutually acceptable project work statement (PWS) was prepared by AVR-KFA and ORNL, and in November 1983 the Department of Energy (DOE) gave verbal approval for ORNL to begin work on the various tasks defined in the PWS.

An important basis for the project derives from the potential contribution to a second generation of nuclear plants offered by the modular HTR. Reactor dynamic and safety experiments at the AVR reactor are of special interest because the modular HTR concept has many design features that are similar to AVR design features and because the predicted safety performance of modular HTRs has many similarities with AVR safety performance.

The objective of this project is to further the understanding of HTR performance and safety and to compare predictions of reactor behavior with experimental data. Planned efforts include reactor physics, dynamics, and safety evaluations of small pebble-bed reactors (PBRs). Reactor performance and inherent features will be investigated through analysis of experiments performed at the AVR. The possibility of gaining significant additional reactor performance and safety information through further experimentation at the AVR will be investigated. The project will also

include benchmarking computational methods and exchanging ideas on improving reactor analysis techniques, on simulating reactor accident behavior, and on design approaches for modular systems.

Our interests in this cooperative program include analyzing HTR dynamic and safety experiments, investigating the possibilities for additional knowledge on HTR performance and safety through further AVR experiments, benchmarking computational tools, exchanging ideas on code improvements, and gaining information useful in evaluating modular HTR systems. Arbeitsgemeinschaft Versuchs-Reaktor-GmbH and KFA-Jülich GmbH are mainly interested in an independent check of nuclear and thermal hydraulic calculations and in ORNL's investigation of possibilities for additional knowledge about reactor performance and safety from further AVR experiments.

In summary, the tasks planned by ORNL in this program are to

1. perform an independent analysis of the AVR response to a depressurized core heatup accident;
2. perform an independent analysis of the response of the AVR to sharp reductions in coolant flow and to reactivity perturbations by use of ORNL computational tools and compare predicted response with measured data;
3. investigate possibilities for obtaining additional information about inherent features of the AVR from further AVR dynamic experiments and participate in planning such experiments;
4. analyze the accident response of modular HTRs;
5. compute few-group cross sections, reaction rates, k-infinite, and temperature coefficients for AVR high-enriched uranium (HEU)—Th and low-enriched uranium (LEU) fuel with a one-dimensional transport "cell" model and compare results obtained by use of ORNL nuclear data derived primarily from Evaluated Nuclear Data Files (ENDF)/B-IV and data derived from ENDF/B-V; and
6. perform multidimensional core calculations to determine various core parameters.

The tasks planned by AVR and KFA are to

1. provide results of experimental measurements for AVR flow reduction experiments and for control rod insertion and withdrawal experiments,
2. provide the THERMIX/KONVEK code (for core thermal hydraulic analyses) and a sample problem,
3. provide AVR fuel and core data required for ORNL calculation of core nuclear parameters,
4. evaluate decay heat production in PBRs, and
5. analyze accident response of modular HTRs.

16.2 BRIEF DESCRIPTION OF THE AVR

The AVR is a 15-MW(e) HTR steam cycle demonstration plant in Jülich, West Germany. The AVR began generating electricity in December 1967. Its purpose is to demonstrate the feasibility of an HTR with pebble fuel elements and high operating temperatures. The primary system of the AVR is shown in Fig. 16.1. Technical data are summarized in Table 16.1, and physical characteristics are summarized in Table 16.2. A key feature of the AVR is its on-line refueling. During operation fuel pebbles (6 cm diam) are withdrawn from the bottom of the reactor, and other pebbles are added at the top of the core so that a continuous circulation of pebbles occurs. The burnup of the discharged pebbles is measured. On the basis of the burnup of each pebble, it is decided whether to discharge it or to return it to the top of the bed. Discharged elements are replaced by fresh elements.

The steam generator is located above the core in the reactor vessel. It is shielded from core radiation by a 50-cm-thick graphite top reflector and two additional 50-cm-thick carbon stone layers. The helium is circulated by two blowers located in the lower part of the vessel.

The inner reactor vessel is enclosed concentrically in a second reactor vessel. A biological shield is located between the vessels. The space between the vessels is cooled with helium at a slightly higher pressure than that of the primary coolant. About 2% of nominal thermal power is removed by the interspace coolers. The double vessel system is surrounded by a containment vessel and by a 1.5-m-thick concrete building.

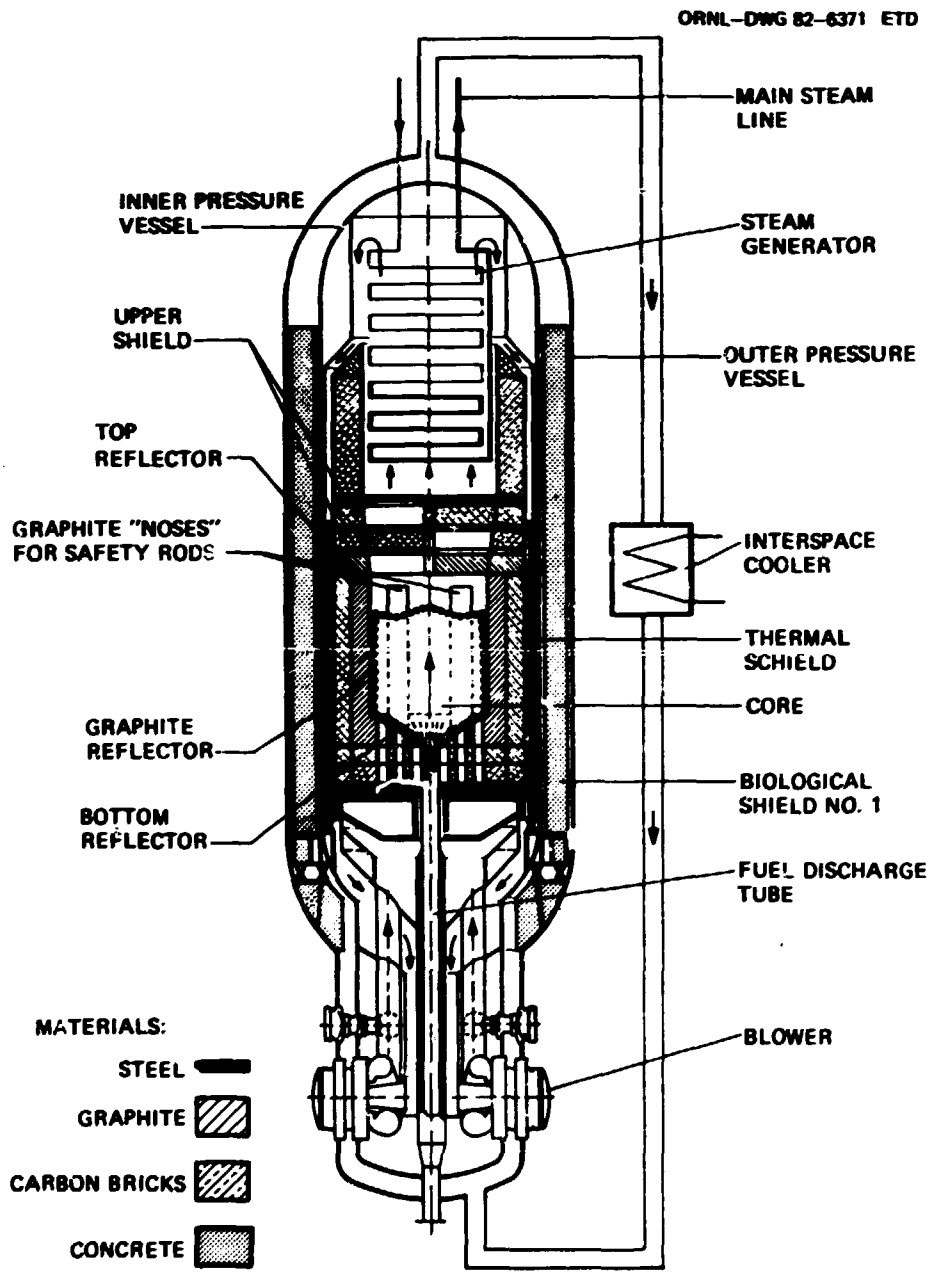

Fig. 16.1. The AVR 15-MW(e) pebble-bed reactor.

Table 16.1. Technical data for the Arbeitsgemeinschaft Versuchs-Reaktor

Thermal power rating, MW	46.0
Electrical power, gross, MW	15.0
Electrical power, net, MW	13.0
Net efficiency, %	28
Core power density, MW/m^3	2.5
Core inlet temperature, °C	275
Core outlet temperature, °C	950
Maximum fuel temperature, °C	1150
Maximum fuel element surface temperature, °C	1090
Maximum hot gas temperature, °C	1040
Primary system pressure, MPa	1.08
Steam conditions:	
Pressure, MPa	7.3
Temperature, °C	505
Reactor vessel type	Steel
Core helium flow direction	Up
Number and location of heat exchangers	One steam generator above core in same vessel
Absorber rods	
Number in core	0
Number in reflector noses	4

Table 16.2. Physical characteristics of Arbeitsgemeinschaft Versuchs-Reaktor components

Core diameter, m	3.0
Side reflector thickness, m	
Graphite	0.5
Carbon brick	0.5
Gap: core barrel, thermal shield, cm	14
Thermal shield thickness, cm	15
Thermal shield material	Steel
Gap: thermal shield, inner vessel, cm	4
Inner vessel thickness, cm	4
Inner vessel material	Steel
Inner vessel outside diameter, m	5.78
Gap: inner vessel, biological shield, cm	7
Biological shield thickness, m	0.75
Biological shield material	Limonite-magnetite granules
Gap: biological shield, outer vessel, cm	3
Outer pressure vessel outer diameter, m	7.60
Outer pressure vessel thickness, cm	3
Outer pressure vessel material	Steel
Top carbon brick thickness, m	1.0
Top graphite reflector thickness, m	0.5
Void between top of pebble bed and lower surface of upper reflector, m	1.0
Height of cylindrical portion of core, m	2.5
Height of conical portion of core, m	0.7
Bottom graphite reflector thickness, m	1.0

16.3 AVR PERFORMANCE AND SAFETY EXPERIMENTS

Arbeitsgemeinschaft Versuchs-Reaktor experiments of interest relative to verification of computational tools used to predict reactor performance and safety are of four types:

1. termination of all forced circulation, without insertion of control rods;
2. sharp reductions in primary coolant flow through blower speed reduction while maintaining control rod position;
3. insertion of control rods to reduce reactor power, followed by rod withdrawal; and
4. possible future experiments to demonstrate safe response to a depressurized loss of forced circulation accident.

Each of these types of experiments is described in the following.

16.3.1 Experiments Involving Reactor Shutdown by Stopping Forced Circulation

The AVR-GmbH recently provided ORNL with a summary of experimental results obtained during a test in the mid-1970s, in which forced coolant circulation was completely stopped, resulting in reactor shutdown without insertion of control rods. More information was obtained in recent discussions at the AVR with the personnel involved in the experiments. Just before the experiment, the reactor was operating at full power [46 MW(t)] with a hot gas temperature of 770°C and the helium circulators at full speed. The transient was initiated by removing the electric generator from the grid, stopping both circulators, and closing both main circuit coolant valves. In the discussions with the AVR personnel, we learned that these valves were closed to provide more severe conditions to the reactor core by essentially preventing natural convection through the *normal* gas flow loop. Because of the strongly negative temperature coefficient of reactivity, the reactor became subcritical without control rod insertion, and the power generation dropped to afterheat levels. Under the conditions established by termination of forced circulation, heat was removed from the core by natural convection processes to the steam

generator (which was fed with a reduced feedwater flow during the transient) and by natural heat transport mechanisms through the reflector, thermal shield, pressure vessels, and biological shield.

Core temperature measurements were made at the top and at the axial midplane of reflector "noses," which protrude into the pebble-bed region. (Temperatures in the pebble bed itself were not measured.) All core temperature measurements (combined with supplementary calculations to estimate pebble temperatures) indicated that fuel temperatures remained well below temperatures at which fuel damage and fission product release would occur.

About 15 h after initiation of the transient, core temperature had decreased enough to cause recriticality. This produced a power peak of about 1.85 MW(t) (or about 4% full power), with the reactor finally achieving an equilibrium power of about 370 KW(t) (less than 1% full power). The experiment was terminated by inserting the control rods.

Unfortunately the collection of experimental data for these experiments was not as extensive as it was for those described in the following sections.

16.3.2 Experiments Involving Sharp Reductions in Primary Coolant Flow with Continued Power Operation

Five experiments involving sharp reductions in coolant flow with continued power generation have been performed in the past year and one-half. The first three of these were performed with an all highly enriched uranium with thorium (HEU-Th) core, and the latter were performed as increasing amounts of low-enriched uranium (LEU) fuel had been added.* The experiments are important checks of the predicted changes in fuel temperature coefficient of reactivity as HEU-Th fuel is replaced by LEU fuel (important from the standpoint of shutdown reactivity margin) as well as an overall check of dynamic analysis tools. The experiments will be repeated as the LEU fuel content in the core increases.

---

*Since the beginning of 1983 the AVR has been converting from an all HEU-Th core to a part LEU core. It is planned that by the end of 1983 the core will contain approximately 40% LEU fuel and that by the end of 1984 it will contain approximately 70% LEU fuel.

The first experiment was performed on April 16, 1982, with the reactor initially at full power. To initiate the transient, the blower speed was reduced to 50% in about 1 min, and the feedwater to the steam generator was reduced to about 50%. The negative temperature coefficient caused a decrease in reactor power to 43% in 150 s, with the power leveling out at 53%. Later forced-helium flow was stopped completely for about 1 h, but the measured core temperatures did not increase significantly.

Similar experiments involving blower speed reductions were performed on March 3 through 7, 1983. By that date about 10% of the fuel elements in the core were LEU.

16.3.3 Experiments Involving Insertion and Withdrawal of Control Rods

An experiment performed on August 2, 1982 (before insertion of a significant amount of LEU fuel), involved insertion of about -60 milliniles of reactivity in 5 s, with the reactor initially at full power. After 20 min, the rods were withdrawn over about 120 s (to avoid a reactor trip signal from a high rate of change in neutron flux). On insertion of the control rods, measured results showed that the neutron flux decreased to 80% in 20 s, peaked at 101% in 120 s, and leveled out at 97%.

Experiments similar to the above were performed with the part LEU core from March 3 to 7, 1983, and additional experiments will be performed as the LEU fuel fraction in the core increases.

16.3.4 Possible Depressurized Loss of Forced-Circulation Experiments

Within Germany there is considerable interest in passively safe modular HTRs (containing features similar to the AVR) that could be sited in highly populated areas to produce process heat and electricity. To achieve this passive safety, a design goal is to maintain peak fuel temperature below a fission product release limit of 1600°C in all conceivable accidents.

It would therefore be very worthwhile to demonstrate the passively safe response of the AVR to an accident involving complete loss of forced circulation *and* depressurization (loss of coolant) because such an accident would produce the most severe fuel temperatures. To date, no loss of

forced-circulation experiments have been performed at the AVR with the reactor *depressurized*. However, AVR-GmbH is giving consideration to proposing for licensing approval an experiment simulating such an accident. One of ORNL's tasks is to analyze the response of the AVR to a depressurized core heatup accident.

Analyses of such hypothetical accidents generally assume instantaneous depressurization and loss of forced circulation of primary coolant. The AVR-GmbH analyses (as well as preliminary ORNL analyses) have predicted that fuel temperatures would stay well below the 1600°C limit during such an accident. These analyses have shown that the peak fuel temperatures occur 15 to 25 h after the accident.

To carry out the depressurization for the actual experiment by available (normal) procedures will require more than 1 d. However, during this time the afterheat will decrease to a level insufficient to simulate an accident. Therefore, AVR is considering performing the experiment in the following manner. First, the reactor would be shut down to cold conditions and depressurized by the standard procedure. Next, the reactor would be brought critical (while still depressurized), and the core would be heated to normal operating temperature with nuclear heat. To simulate an accident from full-power conditions, the time dependence of the afterheat curve (from "time zero") would then be reproduced with nuclear heat. This technique has the appealing feature that the experiment could be stopped at any time by simply inserting the control rods with little or no additional core heatup caused by the very low level of actual afterheat present. A low feedwater flow would be supplied to the steam generator to protect it from overheating. One of the concerns that remains to be evaluated is the accuracy of the AVR flux measurement device at low flux levels and with changing reflector temperatures.

16.4 ANALYSES OF AVR RESPONSE TO SELECTED TRANSIENTS

Some limited calculations of AVR transient response were conducted with ORNL methods during the planning stages of this cooperative project. The purpose of these scoping calculations was to identify initial

questions and information needs regarding completed and planned AVR experiments and to become more familiar with specific design details of the AVR. Because of a lack of detailed information available to ORNL during this planning stage, some assumptions and approximations regarding conduct of the experiments were necessary.

16.4.1 Analyses of Flow Reduction and Control Rod Insertion and Withdrawal

Dynamic models developed under Nuclear Regulatory Commission (NRC) sponsorship in ORNL's HTR Safety Studies Program were modified and used to perform analyses of PBRs. As noted in Sect. 16.3.2, one recent AVR experiment involved a 50% flow reduction over about 1 min from initial full-power conditions. The strongly negative temperature coefficient of reactivity caused a decrease in reactor power to about 43% in 150 s, followed by power equilibration at about 53%. The ORNL scoping calculations predicted a decrease in power to 36% in 140 s (for an assumed instantaneous 50% decrease in core flow) and a final power level of 52%.

As discussed in Sect. 16.3.3, other experiments were performed to measure system response to control rod insertion followed by withdrawal. As discussed, in one such experiment with the reactor initially at full power, -60 milliniles was inserted over 5 s, followed by 20 min with no rod motion.

Our calculations for this transient assumed an instantaneous reactivity insertion, rather than the 5-s ramp. The results predicted a flux decrease to 76% in 30 s, followed by a flux peak of 103% after 130 s and an equilibrium flux of 95%. Measured results showed the flux decreasing to 80% in 20 s, peaking at 101% after 120 s, and leveling out at 97%.

Results of these calculations encouraged us to conclude that existing ORNL dynamics models for operational transients (i.e., with the reactor at power under forced-convection conditions) can be adapted for PBR analyses.

16.4.2 Analysis of AVR Depressurized Core Heatup Accident

The accident analyzed here assumes a loss of forced circulation and a depressurization with the reactor initially at full power. A reactor scram is assumed at accident initiation. Under these accident conditions,

afterheat can be removed from the reactor core by conduction and radiation processes through the core, reflector, pressure vessel, and concrete biological shield to a second pressure vessel that surrounds the biological shield. For these analyses, we assumed that the outer surface of the pressure vessel surrounding the biological shield remained at 90°C.

During such an accident the outer surface of the outer reactor vessel would be cooled by natural convection of air within the containment. In the last resort, containment cooling would be accomplished by a passive system that is available to cool the outer surface of the steel containment with a water spray using water normally stored above this containment vessel.

The analyses were performed in r-z geometry with the HEATING6 code.[1] The analyses were very limited in scope but served to illustrate ORNL's depressurized core heatup analysis capabilities and to identify information needs for a more thorough analysis.

The several computed radial temperature distributions through the core, reflector, thermal shield, inner pressure vessel, biological shield, and outer pressure vessel during the transient are shown in Fig. 16.2. The radial profiles are plotted for the axial plane in which the highest core temperature occurs. For this reference case, a peak fuel temperature of 1335°C occurred at about 17 h and decreased very slowly thereafter. For this initial scoping analysis a decay heat curve for the AVR was not available to ORNL. In the above reference case, a decay heat curve in use at ORNL for analysis of Fort St. Vrain (FSV) was used.[2]

A PBR decay heat curve was obtained from General Electric (GE) (ref. 3). The GE curve is more than 40% lower than the FSV curve. When the GE decay heat curve was used in the AVR core heatup analysis, a peak fuel temperature of 1187°C occurred at about 15 h into the transient.

After these initial analyses were performed, decay heat curves in use by the AVR staff were provided to ORNL. These are shown in Fig. 16.3 along with the GE curve and the FSV curve. The curve labeled "AVR with 4-year reactor operating time" is very close to the GE curve. Thus, we conclude that a peak fuel temperature of about 1187°C could be expected and that the results shown in Fig. 16.3 are based on a very conservative

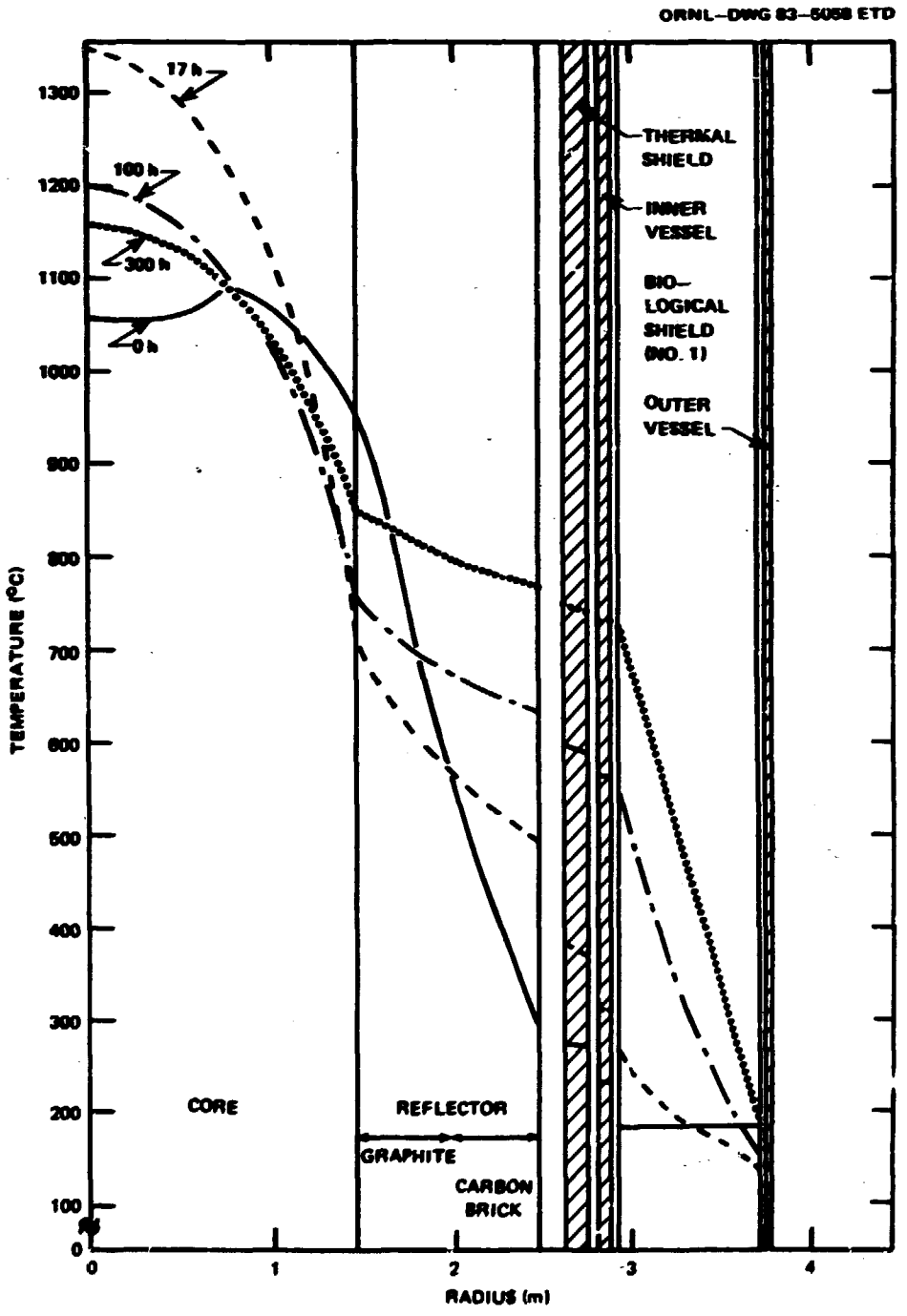

Fig. 16.2. Temperature distribution during depressurized core heatup accident.

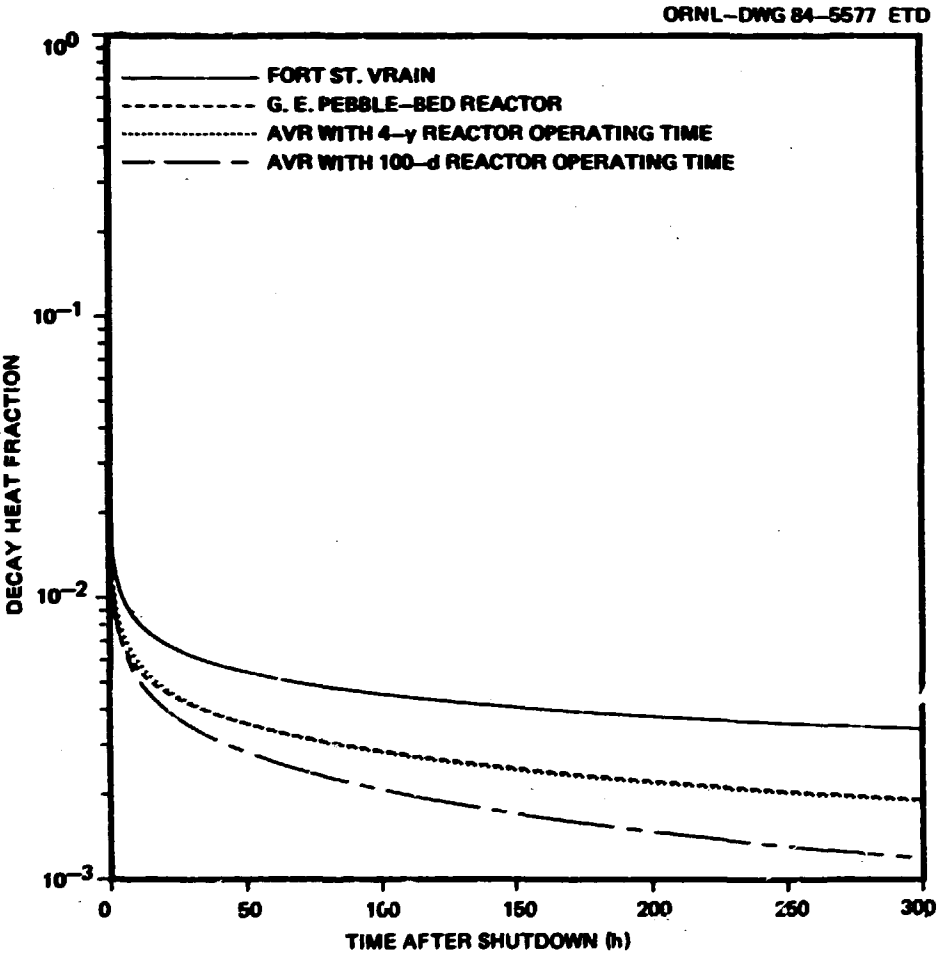

Fig. 16.3. Decay heat fraction as a function of time following reactor shutdown.

representation of decay heat. In any event, based on these analyses, the peak fuel temperature during this accident remains well below the 1600°C limit recommended by ORNL as a design limit for peak fuel temperature.[4] No assessment of possible damage to the reactor vessel from the high temperature was performed. This should be considered in the more detailed analysis of this accident.

For these ORNL analyses, there was a fair uncertainty in the thermal properties (conductivity and heat diffusivity) of the biological shield between the two reactor vessels. However, the results show that these thermal properties are quite important, as there is a large temperature

drop across this structure. Because of the importance of the thermal properties of this structure, ORNL will suggest experimental methods for determining these properties (see Sect. 16.5).

16.5 INITIAL IDEAS ON POTENTIAL FUTURE EXPERIMENTS TO FURTHER INVESTIGATE AND DEMONSTRATE INHERENT FEATURES OF THE AVR

Some initial ideas have been identified by ORNL for possible future experiments to investigate and demonstrate inherent features of the AVR. These, and possibly others, will be further investigated by ORNL during this project. Some are summarized below.

1. A staged approach to the AVR depressurized loss of forced-circulation core heatup experiment. Such an approach could help assure the licensing authorities that the actual experiment on a totally depressurized core cooled only by natural processes would produce satisfactory results. The "intermediate" experiments might be performed on a partially depressurized core and/or with afterheat removal by an active vessel interspace cooling system (i.e., the system that normally cools the first biological shield). Agreement between analytical predictions and measured results for these less severe heatup experiments would strongly support the plans for a fully depressurized and nonactively cooled experiment. An additional step that may be desirable would be a separate dynamics experiment to determine the thermal properties of the first biological shield because these properties have an important effect on the peak vessel temperature.

2. An investigation of the possibility of obtaining accurate estimates of important reactor parameters (e.g., core average heat transfer coefficient and/or the change in temperature coefficient of reactivity as the fraction of LEU fuel increases) through comparison of frequency response test results with predicted (model) frequency response curves. Efficient frequency response testing and analysis techniques for determining parameters that are otherwise difficult to measure by more straightforward steady-state methods have been developed by ORNL and the University of Tennessee and applied at several U.S. reactors, including a large pressurized-water reactor (PWR).

16.6 REACTOR PHYSICS ANALYSIS

A significant portion of ORNL's work in this cooperative effort will involve computation of various nuclear parameters as outlined in Sect. 16.1. These parameters (few-group cross sections, burnup-dependent reaction rates, $k_{infinite}$, temperature coefficient, etc.) will be computed by use of different nuclear data files (ENDF/B-IV and ENDF/B-V), and results will be compared.

Preliminary efforts during the planning stages focused on selecting methods for computing resonance integrals and for treating the double heterogeneity effects of the fuel. Details on methods to be used are reported in Chap. 4.

An effort was also made in locating and securing copies of documents reporting the results of critical experiments and physical constant testing on LEU fuel systems. Data have been obtained for HITREX-1 and -2, CESAR-II, KAHTAR, and Dragon LEU measurements. Some of these data will be used to provide experimental benchmarks, which could be analyzed in conjunction with the AVR HEU-Th and LEU fuel loadings.

16.7 REFERENCES

1. D. C. Elrod et al., "HEATING6: A Multidimensional Heat Conduction Analysis with the Finite Difference Formulation," in *SCALE: A Modular Code System for Performing Standardized Computer Analyses for Licensing Evaluation*, ORNL/NUREG/CSD-2, July 1980.

2. S. J. Ball, *ORECA-1: A Digital Computer Code for Simulating the Dynamics of HTGR Cores for Emergency Cooling Analyses*, ORNL/TM-5159, 1976.

3. G. R. Pflasterer, General Electric, Sunnyvale, Calif., letter to C. McDonald, GA Technologies, San Diego, Calif., subject, "GE MRS-Pebble Bed Core Data," Apr. 7, 1983.

4. F. J. Homan and P. R. Kasten, "Permissible Fuel Temperatures Under Accident Conditions for Modular HTR," pp. 207-9 in *High-Temperature Gas-Cooled Reactor Technology Development Program Annual Progress Report for Period Ending December 31, 1982*, ORNL-5960, June 1983.

GAS-COOLED REACTOR PROGRAMS

JANUARY 1, 1984

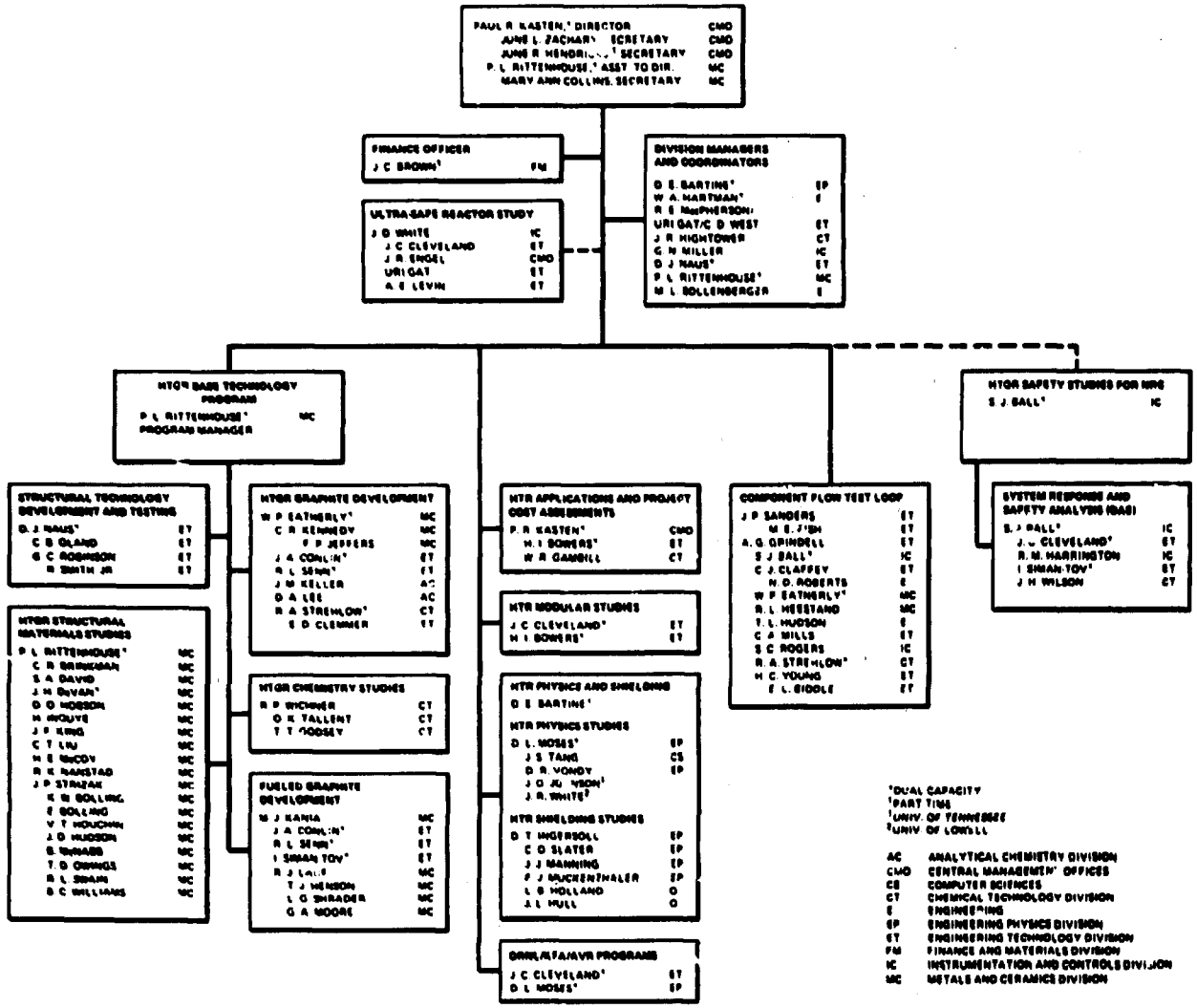

*DUAL CAPACITY
†PART TIME
‡UNIV. OF TENNESSEE
§UNIV. OF LOWELL

AC	ANALYTICAL CHEMISTRY DIVISION
CMD	CENTRAL MANAGEMENT OFFICES
CS	COMPUTER SCIENCES
CT	CHEMICAL TECHNOLOGY DIVISION
E	ENGINEERING
EP	ENGINEERING PHYSICS DIVISION
ET	ENGINEERING TECHNOLOGY DIVISION
FM	FINANCE AND MATERIALS DIVISION
IC	INSTRUMENTATION AND CONTROLS DIVISION
MC	METALS AND CERAMICS DIVISION

ORNL-6053
Distribution
Category UC-77

INTERNAL DISTRIBUTION

1–2. Central Research Library
3. Document Reference Section
4–5. Laboratory Records Department
6. Laboratory Records, ORNL RC
7. ORNL Patent Section
8. P. Angelini
9. D. E. Bartine
10. J. J. Blass
11. H. I. Bowers
12. I. H. Brogden
13. S. J. Chang
14. C. J. Claffey
15. J. C. Cleveland
16. C. W. Collins
17. J. M. Corum
18–20. W. P. Eatherly
21. U. Gat
22. T. T. Godsey
23. W. A. Hartman
24. J. R. Hightower
25. L. B. Holland
26. T. L. Hudson
27. D. T. Ingersoll
28. M. A. Janney
29–33. M. J. Kania
34–43. P. R. Kasten
44. C. R. Kennedy
45. J. F. King
46. W. J. Lackey
47. R. J. Lauf
48. D. A. Lee
49. Y. L. Lin
50. F. C. Maienschein
51. R. W. McClung
52. H. E. McCoy
53. S. E. Moore
54. D. L. Moses
55. D. J. Naus
56. C. B. Oland
57. A. R. Olsen
58. H. Postma
59–63. P. L. Rittenhouse
64. G. C. Robinson
65–69. J. P. Sanders
70. A. C. Schaffhauser
71. R. L. Senn
72. C. O. Slater
73. G. M. Slaughter
74. J. O. Stiegler
75. J. P. Strizak
76. O. K. Tallent
77–79. P. T. Thornton
80. D. R. Vondy
81. G. D. Whitman
82. R. P. Wichner
83. J. H. Wilson
84. B. A. Worley
85. R. G. Wymer
86. G. T. Yahr
87. H. C. Young

EXTERNAL DISTRIBUTION

88–92. DOE, DIVISION OF HTR DEVELOPMENT, Washington, DC 20545

J. E. Fox
I. L. Helms
A. C. Millunzi
G. A. Newby
R. Ng

93. DOE, OFFICE OF CONVERTER REACTOR DEPLOYMENT, Washington, DC 20545

Director

94. DOE, SAN-SAN DIEGO, 110 West A Street, Suite 460, San Diego, CA 92101

Manager

95. DOE, OAK RIDGE OPERATIONS OFFICE, P.O. Box E, Oak Ridge, TN 37830

Office of Assistant Manager for Research and Development

96. Director, Nuclear Research and Development Division, P.o. Box E, Oak Ridge, TN 37830

97–214. DOE, TECHNICAL INFORMATION CENTER, P.O. Box 62, Oak Ridge, TN 37830

For distribution as shown in TID-4500 Distribution Category, UC-77 (Gas-Cooled Reactor Technology)

U.S. GOVERNMENT PRINTING OFFICE: 1983-746-081/4071